Amorphous and nanocrystalline soft magnetic materials: from design to application

A thesis undertaken at the

Tyndall National Institute and Trinity College Dublin

And presented to the

University College Cork

In partial fulfilment of the
requirements for the degree of ***Doctor of Philosophy (PhD)***

by

Hasan Ahmadian Baghbaderani

Supervisors: Dr. Paul McCloskey, Prof. Plamen Stamenov

Advisor: Dr. Ansar Masood

2021

I would like to dedicate this thesis to my loving family and the readers of this work.

Declaration

I hereby declare that except where specific reference is made to the work of others, the contents of this dissertation are original and have not been submitted in whole or in part for consideration for any other degree or qualification in this or any other university. This dissertation is the result of my own work. Most parts of this work have been published as peer-reviewed journal articles.

Hasan Ahmadian Baghbaderani

2021

Acknowledgements

After working for more than four years on my thesis, I would like to take this opportunity to express my gratitude to several individuals. I would like to thank Dr. Paul McCloskey and Dr. Santosh Kulkarni for giving me the opportunity to undertake a PhD programme of study in the Integrated Magnetics Group at Tyndall as a PhD student. During each step of my project, I had Paul's unwavering help and support. Our scientific discussions provided me with invaluable insights. I have been deeply inspired by his approach towards research, as he was always open to new ideas, as well as group management. When there was a problem, I could always count on him as he was very supportive and understanding. He has been very welcoming to new ideas and collaboration opportunities. I thank Dr. Ansar Masood as my advisor for those insightful discussions on amorphous alloys and their soft magnetic properties. He has my admiration for his passion for science and his profound insights. Publishing several peer-reviewed articles could not be possible without Ansar's help and guidance.

I owe my deepest gratitude to Professor Plamen Stamenov owing to his extraordinary scientific talent as a scientist and excellent guidance as a mentor. I truly appreciate that Professor Stamenov and Professor Coey gave me the opportunity to come to Magnetism and Spin Electronics Group at Trinity College Dublin and experience three wonderful years towards the end of my PhD. I would like to thank Plamen for being both a mentor and a friend. He gave me time, space, research independence, and meanwhile inspiration and encouragement. His high standards of quality have influenced and encouraged me to pursue the perfection of work. I was further intrigued by Tuesday group meetings, first in SNIAM's conference room and then online. Additionally, I would like to thank Dr. Karl Ackland, who taught me excellent experimental skills in arc melting and melt spinning. I would like to appreciate the help of Dr. Niclas Teichert in training me on MOKE imaging on melt-spun ribbons.

I would also like to thank Dr. Kenny Alvarez and Dr. José Manuel Martín from CEIT for being great collaborators. Our collaboration dates back to the Intermag 2018 conference in Singapore, where I met José Manuel. I'm very grateful for our fruitful collaborations over the past few years on thermal (DSC) and structural (TEM) characterisations of the ribbons in addition to the fabrication and characterisation of gas atomised powder and soft magnetic

composites. My friendship with Kenny has started from this collaboration, and thanks to the research, we are friends for life now!

My gratitude also goes to the members of my thesis committee. I would like to thank Dr. James Rohan and Professor Cian O'Mathuna. They made the yearly review meetings on my thesis very enlightening with their valuable comments.

Finally, I must express my profound gratitude to my parents, Nader and Fereshteh, and brothers, Amir Hossein and Amir Sepehr, for providing me with unfailing support and continuous encouragement throughout my years of study and research. This accomplishment would not have been possible without them.

Thank you!

سپاس گزارم!

Abstract

Advanced soft magnetic materials are required to match high-power density and switching frequencies made possible by advances in wide band-gap semiconductors. Magnetic materials capable of operating at higher operating frequencies have the potential to reduce the size of power converters significantly. Amorphous magnetic alloys lack long-range atomic order and consequently exhibit high electrical resistivity, no macroscopic magnetocrystalline anisotropy and no microstructural discontinuities, e.g., grain boundaries or precipitates, on which magnetic domain walls can be pinned. Consequently, they show excellent performance in DC and AC magnetic fields due to their low hysteresis and eddy current losses. Much work on this class of materials has been carried out, yet there are some critical issues in design, fabrication and optimisation that need to be addressed.

First, one of the main challenges is producing amorphous alloys with a lower content of non-magnetic elements. The alloys comprising more abundant magnetic elements show low amorphisation capability, so non-magnetic metals have been added to these alloys to tackle this issue. However, adding these elements can significantly reduce the saturation magnetisation and increase the cost of alloy. To overcome these hurdles, kinetic, thermodynamic and topological parameters have been exploited to predict and tune the amorphisation capability of Co-Fe-B alloys. Based on this, seven alloys with very attractive magnetic properties have been designed and fabricated by melt spinning. Five out of seven alloys are amorphous, highlighting the efficiency of the design procedure, among which there is an alloy with ultra-low coercivity, 2.9 A/m. This substantiates the efficiency of the amorphous alloy design policy. Additionally, the crystallisation behaviour of alloys correlates significantly with their amorphisation ability. In this regard, the eutectic mode of crystallisation can be a sign of higher amorphisation ability, whereas alloys that crystallise through other mechanisms can offer lower amorphisation ability.

Two *in-situ* crystallised alloys offer low power loss and high saturation magnetisation. The surface crystallised alloy exhibits not only very low coercivity but also surprisingly 20% lower power loss compared to the best amorphous sample. The mechanism behind this observation is investigated in more detail. The surface crystallisation can be used to induce anisotropy and decrease the power loss of melt-spun ribbons, eliminating the need for magnetic annealing. In addition, it has been shown that the amorphisation capability of an alloy can be tuned, based

on the as-mentioned parameters in order to produce an *in-situ* nanocrystallised alloy with remarkable B_s = 1.57 T. The precipitation of the kinetically-favoured metastable Co_7Fe_3 nanocrystalline phase in the amorphous matrix is responsible for the high B_s of this alloy. The atomic structure of the amorphous matrix is evaluated based on Mössbauer spectroscopy, and the distribution of the hyperfine magnetic field implies that cobalt atoms form clusters and boron atoms undergo only short-range ordering. Therefore, designing alloy compositions using the as-mentioned predictive parameters can give one the opportunity to manipulate the microstructure of alloys to greatly benefit from their optimised properties.

To further lower the cost of amorphous alloys, ultra-thin soft magnetic amorphous ribbons are fabricated via a single-step rapid-quenching process. The ribbons, with the thicknesses of 5.5 µm, fabricated by a high speed melt spinner offer ultra-soft magnetic properties. It is shown that *in-situ* thinning process results in a substantial reduction in the cost of the material. It also eliminates the need for post-processing steps, providing the opportunity for mass production of high-performance soft magnetic amorphous ribbons at a relatively low cost.

Despite the low hysteresis and eddy current loss of amorphous metals, the measured losses, especially at high frequencies, are often in excess of these classical loss contributions. To gain a better understanding of this observation, the measured total power loss is resolved into hysteresis, eddy current, and anomalous losses. It is found that the main contributor to the power loss is the anomalous loss that can be reduced substantially through annealing in a transverse magnetic field at temperatures lower than the ribbons crystallisation temperature. It has been shown that transverse magnetic annealing not only alters the mechanism of magnetisation, from domain wall motion to magnetisation rotation, but it results in domain pinning due to the increased number of domains by decreasing their width. The latter promotes the magnetisation rotation mechanism. These effects account for a 75% decline in the total power loss in the melt-spun ribbons, making them desirable candidates for power converters working at mid- and high frequency.

In addition, soft magnetic nanocomposites can be produced through annealing the amorphous ribbons, with a specific composition, at temperatures higher than crystallisation temperature. The nanocrystallisation of $Co_{23}B_6$, with network-like FCC structure, in the amorphous matrix, leads to substantial progress in DC and AC magnetic properties of ribbons. These metastable complex phases with 116 atoms per unit cell are not well understood. Therefore, it is essential to investigate the kinetics and thermodynamics of this kind of phase

transformation in order to identify the substantial effects of the resulting phase on magnetic properties. This has been done using CALPHAD and nucleation theory. As a result of transverse magnetic annealing leading to the combined effects of nanocrystallisation and coherent magnetisation rotation, the anomalous loss declines by 70% in the ribbons annealed at 525 °C. Therefore, this soft magnetic nanocomposite can be utilised as the core of efficient power convertors.

Contents

List of Publications

Journal articles

1. **H. Ahmadian Baghbaderani**, A. Masood, K.L. Alvarez, C. Ó. Mathúna, P. McCloskey, P. Stamenov, CALPHAD-assisted development of in-situ nanocrystallised melt-spun Co-Fe-B alloy with high B (1.57 T), J. Alloys Compd. 877 (2021) 160194. https://doi.org/10.1016/j.jallcom.2021.160194.

2. A. Masood, **H. Ahmadian Baghbaderani**, V. Ström, P. Stamenov, P. McCloskey, C. Ó. Mathúna, S. Kulkarni, Fabrication and soft magnetic properties of rapidly quenched Co-Fe-B-Si-Nb ultra-thin amorphous ribbons, J. Magn. Magn. Mater. 483 (2019) 54–58. https://doi.org/10.1016/j.jmmm.2019.03.079.

3. **H. Ahmadian Baghbaderani**, A. Masood, Z. Pavlovic, K. L. Alvarez, C. Ó. Mathúna, P. McCloskey, P. Stamenov, On the mechanisms limiting power loss in amorphous CoFeB-based melt-spun ribbons, J. Magn. Magn. Mater. 502 (2020) 166535. https://doi.org/10.1016/j.jmmm.2020.166535.

4. **H. Ahmadian Baghbaderani**, A. Masood, Z. Pavlovic, N. Teichert, C. Ó. Mathúna, P. McCloskey, P. Stamenov, Improved magnetic performance of Cobalt-based ribbons by nanocrystallisation through magnetic annealing, J. Magn. Magn. Mater. 503 (2020) 166630. https://doi.org/10.1016/j.jmmm.2020.166630.

5. A. Masood, **H. Ahmadian Baghbaderani**, K. L. Alvarez, J. M. Blanco, Z. Pavlovic, V. Ström, P. Stamenov, C. Ó. Mathuna, P. McCloskey, High-frequency power loss mechanisms in ultra-thin amorphous ribbons, J. Magn. Magn. Mater. 519 (2021) 167469. https://doi.org/10.1016/j.jmmm.2020.167469.

6. K. L. Alvarez, **H. Ahmadian Baghbaderani**, J. M. Martín, N. Burgos, M. Ipatov, Z. Pavlovic, P. McCloskey, A. Masood, J. Gonzalez, Novel Fe-based amorphous and nanocrystalline powder cores for high-frequency power conversion, J. Magn. Magn. Mater. 501 (2020) 166457. https://doi.org/10.1016/j.jmmm.2020.166457.

7. K. L. Alvarez, **H. Ahmadian Baghbaderani**, J. M. Martín, N. Burgos, P. McCloskey, J. González, A. Masood, Novel predictive methodology of amorphisation of gas-atomised Fe-Si-B alloy powders, J. Non. Cryst. Solids. 574 (2021) 121151. https://doi.org/https://doi.org/10.1016/j.jnoncrysol.2021.121151.

International conference papers

1. Cathal Sheehan, A. Masood, Z. Pavlovic, **H. Ahmadian Baghbaderani**, P. McCloskey. High-flux Density Nanocrystalline Materials for High-Frequency Power Applications. APEC2019 Applied Power Electronics Conference (Oral Presentation).

2. Cathal Sheehan, **H. Ahmadian Baghbaderani**, A. Masood, Z. Pavlovic, P. McCloskey. High-flux Density Amorphous Materials for High-Frequency Power Applications. PCIM2019 (Oral Presentation).

3. Ansar Masood, Zoran Pavlovic, **H. Ahmadian Baghbaderani**, Valter Ström, Plamen Stamenov, Paul McCloskey, Cian Ó. Mathúna, Santosh Kulkarni. Ultra-high performance Co-Fe-B-Si-Nb amorphous alloys for high-frequency applications. JEMS2019 (Oral Presentation).

4. **H. Ahmadian Baghbaderani**, Ansar Masood, Zoran Pavlovic, Valter Ström, Plamen Stamenov, Paul McCloskey, Cian Ó. Mathúna, Rapidly quenched ultra-thin soft magnetic amorphous ribbons for high-frequency power applications. JEMS2018 (Oral Presentation).

5. **H. Ahmadian Baghbaderani**, D. J. Cronin, Paul McCloskey, Cian Ó. Mathuna. Fabrication and development of miniaturised efficient power converters using ultra-soft magnetic ribbons. 2018 IEEE International Magnetic Conference (INTERMAG), DOI: 10.1109/INTMAG.2018.8508478 (Poster Presentation).

Chapter 1 Introduction

Ultra-fast progress in technology has been pushing materials science boundaries towards Advanced Materials. These are systematically designed, fabricated and post-processed materials that deliver the properties needed for demanding applications [1]. Such materials offer a distinct superiority in performance when compared to conventional materials. To gain such an advantage, one method can be the fabrication and/or post-processing of materials under non-equilibrium conditions. Therefore, a variety of non-equilibrium techniques have been developed to address this demand. Rapid Solidification Processing (RSP) is amongst these techniques [2].

Alloys with no long-range atomic order have been fabricated via RSP methods from the gas or liquid phases. In these fabrication procedures, the solidification takes place so rapidly that the atoms are frozen in their liquid configuration. In other words, as a fundamental aspect of all rapid solidification methods, the heat released during solidification must be transferred with sufficient rapidity to a heat sink to preclude crystallisation [3]. Based on the structure and different properties of rapidly solidified materials, the atoms can undergo short-range ordering, but there is no long-range atomic order [4]. Although there have been many studies in the field of amorphous metals from 60 years ago [5–9], this field of research is relatively novel compared to the history of metals.

Humanity has started to use metals, with mainly crystalline atomic structure, since 8000 years ago. Historically, the fabrication of a range of non-crystalline metallic alloys, via vapour deposition, was first reported by Kramer *et al.* in 1934 [10]. In the same year, Brenner *et al.* [11] claimed the electrodeposition of amorphous alloys containing nickel or cobalt and 15 at.% of phosphorus from phosphite solutions. They confirmed the amorphous structure of the fabricated alloys by observing only one broad diffuse peak in the X-ray scattering pattern. This

class of alloys have been used for many years as wear- and corrosion-resistant coatings. Afterwards, Duwez *et al.* [5] produced $Au_{75}Si_{25}$ with a liquid-like structure in 1960. Regarding the non-crystalline ferromagnetic alloys, the fabrication of CoP alloy was first reported in 1965 [12]. Subsequently, Duwez's group splat-quenched Fe-C-P and Pd-Co-Si alloys with attractive soft ferromagnetic properties [13,14]. The research and development on amorphous magnetic alloys have subsequently increased dramatically [15]. Since then, a large variety of non-crystalline metals have been developed.

It seems that technological advances have outpaced progress in materials science, so that the performance of materials can limit their technological applications. Therefore, new materials and processing methods should be developed to meet the ever-increasing high-tech criteria. From the first studies on non-crystalline alloys, it was recognised that they exhibit properties attractive for structural, chemical and magnetic applications. Furthermore, they were important in showing a characteristic that was not universally expected at the time, namely that crystallinity is not a prerequisite for ferromagnetism [15]. With their excellent soft-magnetic properties, Fe- and Co-based melt-spun ribbons were among the first non-crystalline materials to be exploited on a large commercial scale. In addition, their physical, mechanical, and corrosion-resistant properties can also be highly attractive. They may not be applicable on the largest scales associated with structural steels, but on the scales associated with personal items such as sports equipment down to micro- and nano-devices, they have so much to offer [2,15]. As the goal of this study is to design the composition, characterise and optimise the properties of soft magnetic rapidly solidified alloys, first, the parameters related to the amorphisation capability of the alloys are explained, and then the soft magnetic properties of such alloys are scrutinised in more detail.

1.1 Glassy and amorphous alloys

Glass can be defined as a solid with a frozen-in liquid structure. It is also referred to as a 'supercooled liquid', which can be fabricated using RSP methods [16]. Accordingly, to understand the formation of the glass, the alterations in some physical properties during the cooling procedure should be evaluated. In this regard, Figure 1 illustrates the variation of the

specific volume of an alloy as a function of temperature. The specific volume of the molten alloy declines when it is cooled down. At the solidification/melting point, T_m, there is an abrupt drop in the specific volume of the alloy down to the value characteristic of the solid crystalline alloy (black line). Further decrease in temperature below T_m results in a slow reduction in the volume of the metal, depending on its thermal expansion behaviour [17–19].

Prior to crystallisation, instead of the as-mentioned sudden decline in the specific volume, a liquid typically undercools. It means that the liquid state can be maintained at temperatures well below the melting temperature before crystallisation can begin (purple line in Figure 1). The activation energy barrier of the formation of the solid nuclei is the main reason for undercooling, and this barrier is smaller when the undercooling is larger. The actual value of undercooling varies for different metals, but generally, the value is at best only a few tens of degrees [17–19].

Even in the undercooling region, the volume still declines to the point that the liquid gets frozen in. This state can be defined as when the viscosity of the liquid reaches a value of 10^{12} Pa.s. [2]. The temperature at which the liquid undergoes this state is traditionally named glass transition temperature, T_g. It should be mentioned that the glass transition temperature can be changed by changing the cooling rate. Therefore, Kauzmann *et al.* [20] preferred to call this phase transition a 'glass transformation interval' [17–19]. Based on this observation, higher T_g can be achieved by increasing the cooling rate (Figure 1). In the as-mentioned procedure, the size of the undercooling region, T_m - T_g, can be deemed as the main parameter to distinguish a glass-forming alloy. Furthermore, more details on the other effective parameters are given in the next section.

Different terms have been used for the solid with a lack of crystallinity. Non-crystalline, amorphous and glassy all refer to the solid state atomic arrangement in which there is no long-range order. These terms have been used interchangeably, which resulted in some confusion. To avoid this ambiguity, it is better to differentiate such names in this thesis. First, non-crystalline material can refer to any solid material that does not possess crystallinity. As a more general term, it can include amorphous and glassy materials [2]. In addition, in contrast to amorphous alloys, the glassy materials exhibit glass transition temperature and the undercooling region.

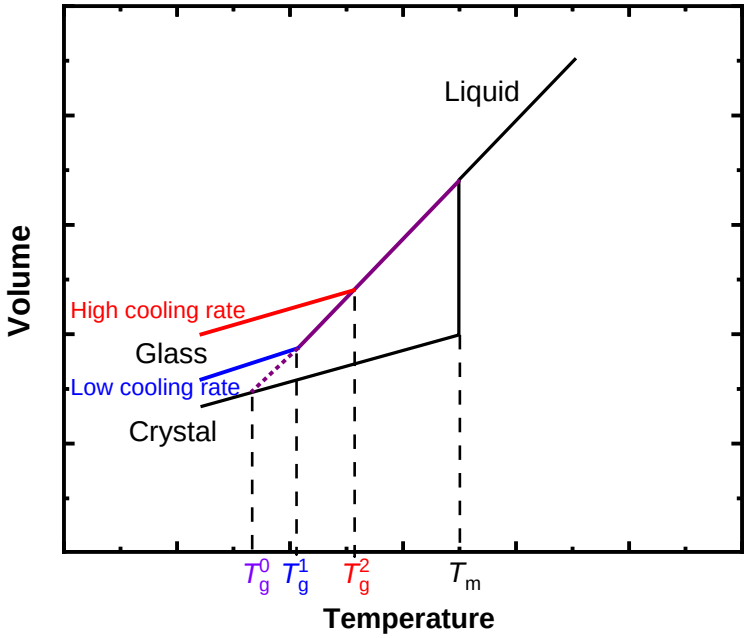

Figure 1. Specific volume as a function of temperature for a non-glass forming (black line) and a glass forming alloy (purple line), reproduced from [2].

1.1.1 Amorphisation capability

In order to produce non-crystalline alloys, it is essential to understand the effective parameters leading to glassy/amorphous phase formation from the liquid. The ability of a metallic liquid to transform into a glassy state can be defined as glass forming ability (GFA). In addition, if the resulted phase is amorphous, this parameter can be called amorphisation capability (AMC). In this regard, GFA evaluation of bulk metallic glasses (BMGs) has received much attention in the last forty years [21–24]. BMGs are those non-crystalline solids obtained by continuous cooling from the liquid state, which have a section thickness of at least a few millimetres. It should be mentioned that the major criteria that have been developed to evaluate the non-crystalline phase formation behaviour in bulk metallic glasses (BMGs) are equally applicable to the amorphous alloys, so GFA and AMC terms can be used interchangeably [2].

From the early years of research on non-crystalline alloys produced by RSP methods, several empirical criteria have been proposed to explain the AMC of alloys. The most fundamental and, at the same time, simple criterion proposed is the minimum cooling rate at which the liquid can be vitrified, which depends on the alloy composition. However, as an experimentally determined parameter, producing the alloys in different cooling rates and evaluating their microstructure would be not only time-consuming, but having a variety of cooling rates would be an involved process as well. Thus, other theoretical, semi-empirical and empirical criteria have been proposed to explain glass formation in a variety of alloy systems [21,25,26].

As a case in point, Inoue [22] had formulated three basic empirical rules to predict the formation of BMGs based on the extensive data on the synthesis of BMGs for over a decade. These rules can be listed as follows:

i. the alloy must contain at least three components. The formation of glass becomes easier with the increasing number of elements in the alloy system

ii. the constituent elements should have a significant atomic size difference. It is suggested that the atomic size differences should be above ∼12% among the main constituent elements

iii. the heat of mixing among the (major) constituent elements in the alloy system should be negative

These rules have helped researchers to design alloy compositions with higher GFA. However, some glass forming alloy systems do not follow Inoue's rules. For instance, the formation of binary BMGs have been reported in Ca–Al [27], Cu–Hf [24], Cu–Zr [28], Ni–Nb [29] and Pd–Si [30] alloy systems. Thus, in addition to the as-mentioned general rules, a variety of new criteria have been discovered and developed. These criteria can be categorised as follows [31–38]:

1. Topological criteria: These criteria are based on the geometrical arrangement of atoms, bonding, and atomic size effects. The electronegativity of the constituents, first and second Inoue's rules, and atomic mismatch factors can be considered as topological criteria [7,39–41]. The latter is explained in more detail in Chapters 2 and 3, in addition to Appendix A.

2. Thermodynamic criteria: These are on the basis of thermodynamic properties of the system, e.g., liquidus temperature and equilibrium crystalline phases after

crystallisation [39,40,42–44]. Among these criteria, liquidus temperature is taken into account to predict AMC of alloys in Chapters 2 and 3, in addition to Appendix A, where the equilibrium crystalline phase is considered as another parameter to evaluate AMC.

3. Thermal criteria: In these parameters, the thermal properties of the alloy system, e.g., reduced glass transition temperature, are taken into account [27,31,34]. This parameter is taken into account in AMC analysis of Fe-Si-B alloys in Appendix A.

4. Kinetic criteria: These parameters are related to the cooling rate in an RSP method relative to the kinetics of crystallisation. The heat of mixing, as Inoue's third rule, can be considered as one of the kinetic parameters [41,46,47], which is explained in more detail in Chapters 2 and 3.

5. Other criteria: Recently, there have been some studies showing the correlation between the magnetic properties and the electronic structure of the glassy alloys with their GFA [48,49].

It has been established that AMC of different alloy systems can be analysed or predicted by evaluating a set of criteria from different categories [50].

It should be noted that thermodynamics can predict the product of phase transformations in different alloy systems but in equilibrium conditions. In this regard, local atomic arrangements are essentially determined by the thermodynamics of interatomic interactions. Therefore, by calculating the Gibbs free energy of different possible phases in an alloy system, the most stable phase is the one with the minimum Gibbs free energy. The system is supposed to be under the equilibrium condition in such calculations. However, the RSPs include different procedures which are far from equilibrium, e.g., rapid heat removal by the spinning wheel, rapid solidification front velocity in copper mould casting, or high energy solid-state treatment in ball milling. In some of the as-mentioned processes, the time needed for diffusion to transform the melt to the equilibrium crystalline state exceeds the time needed to reach the metastable state. Hence during RSPs, the kinetics of the fabrication process itself can override the tendency of the atoms for ordering [15]. Thus, having the knowledge of the basic thermodynamic properties of the alloy can be useful to predict the AMC, but those properties related to the kinetics of crystallisation during RSP should be taken into account, as well. AMC of alloy systems in Chapters 2 and 3, in addition to Appendix A, has been predicted using a combination of structural, thermodynamic and kinetic criteria.

1.2 Nanocrystalline alloys

When the size of crystals, at least in one dimension, in a polycrystalline alloy is less than 100 nm, the alloy can be called nanocrystalline. These materials show unique properties because a large volume fraction of atoms is located at the grain boundaries [3,51]. This class of alloys can be fabricated mainly using two different strategies. One approach can be quenching the melt at a rate that is not high enough to vitrify the alloy. More details on this method are provided in Chapter 3. In the second approach, the amorphous precursor can be heat-treated above its crystallisation temperature with a long-range diffusion-controlled crystal growth which is the focus of Chapter 6 [52]. In this case, the amorphous matrix has a different composition compared to that of the parent amorphous alloy [3]. The atomic diffusion, leading to crystal growth during heat treatment can be restrained by increasing the heating and cooling rate. In addition, Yoshizawa *et al.* [53] discovered that minor addition of Cu and Nb results in nanocrystallisation of 10-15 nm FeSi grains in FeSiB-based glasses after heat treatment. The nanocrystalline alloys can be distinguished by their relatively high resistivity, mechanical strength, and saturation magnetisation. They also exhibit low magnetocrystalline anisotropy. With such properties, the nanocrystalline alloys have great potential as soft magnets [54]. Some of these properties will be explained in more detail in the following sections.

1.3 Magnetic properties of rapidly solidified alloys

Several studies have been carried out on magnetic amorphous and nanocrystalline alloys. They have been attracting considerable interest due to their excellent soft magnetic properties to be used in diverse applications. As a case in point, the amorphous ribbons can be mainly utilised as the core of transformers [55–58]. In addition, this type of material has been increasingly used as the fundamental component of magnetic actuators [59], magnetic sensors [60], flux concentrators [61], and magnetic shieldings [62] (Figure 2).

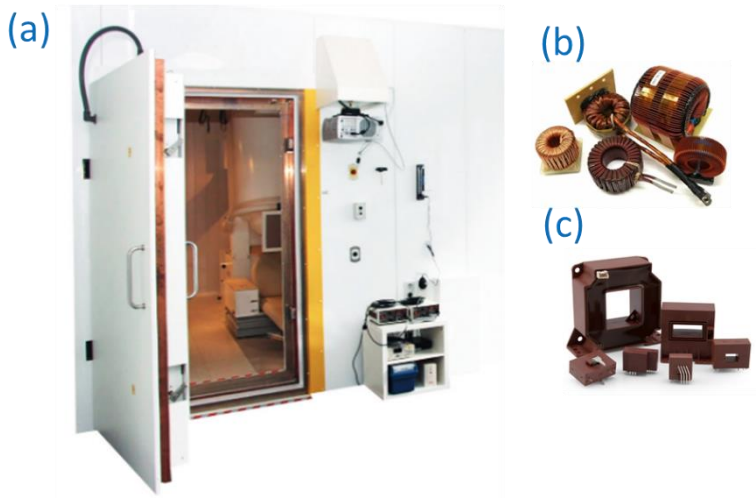

Figure 2. Application examples of rapidly quenched soft magnetic materials in (a) a magnetically shielded room, (b) toroidal inductors, and (c) closed-loop current sensors.

Amorphous alloys can be classified in several ways. The ones of magnetic interest are based on either 3d transition metals (e.g., Fe, Co, Ni) or rare-earth metals (e.g., Nd, Sm). The former types are generally soft magnetic materials, while the latter alloys can be considered as semi-hard to hard magnets [15]. Amorphous alloys can also be classified into two categories: metal-metalloid and metal-metal alloys. In the former, the 3d transition metal atoms constitute about 80% and the metalloid atoms (typically B, C, P, and Si) about 20% [15]. The metal and metalloid atoms may be of one type or a combination of different metals and metalloids. As mentioned before, the difference in the atomic radii can help amorphisation, so the metalloid atoms, with a much smaller radius than that of Fe, Co, and Ni act as glass formers. The introduction of the metalloids also decreases the liquidus temperature of the alloy, which helps amorphisation to take place [63]. On the other hand, there is no such compositional restriction in the case of metal-metal type non-crystalline alloys. The second metal component, which is from early transition metals of 4d or 5d type (e.g., Zr, Nb, Hf), can be as small as 9–10 at.% or as large as nearly 50 at.% [2,15]. Therefore, in both classes, the composition of the alloy can be widely manipulated to achieve the desired ferromagnetic properties for a specific application [64]. In the following sections, first, the ferromagnetic materials, hysteresis phenomenon, and then the magnetic properties of amorphous alloys are reviewed.

1.3.1 Ferromagnetism

A ferromagnetic material has spontaneous magnetisation even in the absence of an external field. Exchange interactions between atomic moments result in the long-range ordering, which is responsible for magnetisation [15,65]. The spontaneous, long-range magnetisation exists just below the magnetic ordering temperature, Curie temperature T_C. Above T_C, thermal perturbations deteriorate the spontaneous magnetic order, and the material behaves like a paramagnet. Weiss was the first to postulate the existence of magnetic domains as regions over which all moments are parallel to each other. Based on the modern theory of magnetism, the minimisation of internal energy is the main reason for the formation of domains. If there were no domains in a ferromagnetic material, a large region with constant magnetisation would produce an enormous stray field and requires a lot of magnetostatic energy. To reduce the energy, this region can split up into smaller magnetised regions called magnetic domains, which results in diminishing the stray field. Domain walls are separating domains, so the orientations of the magnetic moment change abruptly through the width of the domain wall, which can range from 5 nm to several hundred nanometers on going from hard to soft magnetic materials. The domains are magnetised in different directions, so the summation of the magnetisation vectors of the domains in the sample would be zero [15].

1.3.2 Origin of ferromagnetism in the amorphous state

To understand the origin of ferromagnetism in amorphous alloys, the theory of the ferromagnetic order should be explained. Based on quantum mechanics, the interaction between spins leads to ferromagnetism [66], so in a ferromagnetic material, the macroscopic moment is a result of the parallel alignment of several spins in one direction. This alignment is due to the exchange coupling between neighbouring electrons, which can be formulated as:

$$H = -\frac{1}{2}\sum J_{ij}.\vec{S}_i.\vec{S}_j \qquad (1)$$

where H denotes the Hamiltonian operator, and J_{ij} stands for the exchange integral. In addition, $\vec{S}_i$ and $\vec{S}_j$ are the spin operators of two neighbouring electrons [66]. It is worth mentioning that

the exchange couplings between all neighbour pairs are taken into account in Eq. (1). In ferromagnetic materials, the exchange integral is positive, so the Hamiltonian operator becomes minimum when the spins of the electrons are parallel and pointing to the same direction. However, in the anti-ferromagnets, the exchange integral is negative, so the orientation in which spins are parallel but pointing to opposite directions is energetically favourable. Then, volume magnetisation can be defined as the vectorial sum of all magnetic moments relative to the entire volume of the ferromagnetic body. Consequently, the fundamental characteristics of magnetic materials such as magnetic moments and Curie temperature mainly depend on the interaction in the atomic scale. Thus, the absence of long-range order does not deteriorate the large scale magnetic properties of amorphous alloys. In addition, the decreased values of saturation magnetisation and Curie temperature of 3d-transition metal-based amorphous alloys can be the consequence of the presence of nonmagnetic glass-formers in the structure [15,63]. Thus, the effect of the absence of long-range order on the magnitude of the local magnetic moment is negligible [15]. In addition to high saturation magnetisation, amorphous and nanocrystalline alloys also show high relative permeability, low coercivity and high electrical resistivity. These properties are the best properties of any soft magnetic material. The exceptional soft magnetic properties of these classes of alloys are characterised and analysed in the rest chapters of this thesis.

1.3.3 Magnetic Hysteresis and Magnetisation Reversal

As an essential characteristic, when a cyclic magnetic field is applied to a ferromagnet, it shows hysteresis behaviour. This behaviour is the result of the irreversible nonlinear response of magnetisation, M, to an applied magnetic field, H [67]. The detailed mechanism of magnetisation of a ferromagnetic material can be explained accordingly.

Figure 3 depicts the magnetisation curve, including four sequential steps. At $H = 0$, the ferromagnetic material is in a virgin state, where the domains are magnetised in different directions [15]. By applying a weak magnetic field ($0 < H < H_R$, $H_R < 0.1H_c$), the domains, with the largest component of M along with H, would grow by domain wall motion (region I). At this stage, the initial slope of the loop can be defined as initial permeability, μ_i. It should be mentioned that the magnetisation would generate a magnetic field inside a magnetic material,

B, which can be formulated as $B= \mu_0(H+M)$. By increasing H ($0.1H_c < H < H_c$), B increases sharply, and as a result, the permeability reaches its maximum value, μ_{max} (region II). In this region, magnetisation occurs through large irreversible Barkhausen jumps. By the end of stage II, the domains within which the magnetisation direction is along H has grown to their maximum size. The remained unaligned domains are narrow domain regions such as closure domains, with non-zero components of magnetisation at right angles to the applied field direction. In region III, when $H_c < H < H_k$, mainly rotational processes in addition to minor domain wall motions change the magnetisation direction of these domains towards the applied field. The magnetisation in these domains must be rotated into the field direction to minimise the potential energy. More energy is needed in this stage as the magnetisation should rotate away from the easy axis. In region IV ($H > H_k$), magnetisation approaches its saturation (M_s) which occurs by microscopic reversible rotations in the areas around defects where spin states are inhomogeneous. At saturation, all magnetic domains are aligned with the applied field direction, and magnetisation is maximal and $B_s = \mu_0(H + M_s)$ [15,68].

After reaching H_{max}, the field starts to decline ($H_k < H < H_{max}$), implying that the domains rotate back to their easy direction. As mentioned before, this rotation is mainly a lossless reversible process, which is equivalent to non-hysteresis rotation; however, by a further decrease in H ($0 < H < H_k$), the domain wall jumps from a local energy minimum to the next, which is a lossy irreversible procedure. Actually, the lines of the B-H loop diverge when the field is decreasing, owing to the as-mentioned lossy processes (Figures 3 and 4). At $H = 0$, the ferromagnet is in a metastable remanent state with a non-zero magnetisation, M_R. In other words, increasing H in the opposite direction to the magnetisation triggers the process of magnetisation reversal, which can be evaluated by the point at which $M = 0$, known as coercivity, H_c, in which domains are oriented to cancel net magnetisation (Figure 4). This parameter can be used to evaluate the magnetic softness/hardness of the material. It should be mentioned that it is more difficult to magnetise a ferromagnet with a high H_c (hard magnets) compared to the ones with low H_c (soft magnets). Thus, by applying a cyclic magnetic field, the ferromagnetic materials respond in a way that can be illustrated as a B-H loop (Figure 4) [15]. Different features of B-H loops are analysed and compared for different samples in the

rest chapters. Therefore, as H_c is the core of many discussions in this thesis, the effect of different parameters on H_c can be summarised in the following section.

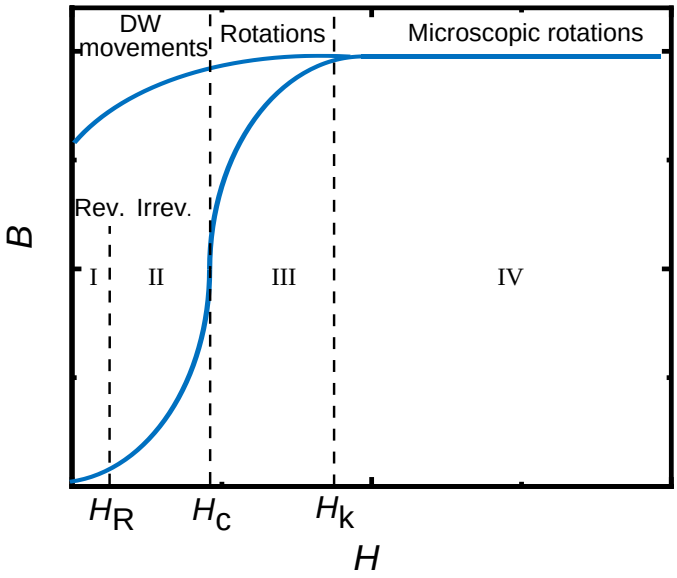

Figure 3. Schematic magnetisation curve including four subsequent mechanisms of magnetisation process, reproduced from [68].

1.3.4 Magnetic anisotropy

Low magnetic anisotropy is the fundamental condition for a material to have the properties of a good soft magnet with a narrow hysteresis loop (Figure 4). Magnetic anisotropy can be defined as the energy density required to rotate the magnetisation vector out of its energetically preferred orientation which is called the magnetic easy-axis. Taking into account its origin, there are several types of anisotropy, such as shape (arisen from geometrical characteristics of the ferromagnetic material), magnetoelastic (arisen from the internal coupling between elastic and magnetic properties), and exchange (arisen from the interaction among magnetic atoms/species within the material) anisotropies [15]. There are several types of anisotropy, such as shape, magnetoelastic and exchange anisotropies. Nonetheless, among these different types, the magnetocrystalline anisotropy, as an intrinsic property, can have the greatest contribution. Thus, the magnetisation process is different when the field is applied along with different

crystallographic directions, so the anisotropy reflects the crystal symmetry. This type of anisotropy stems from the crystal-field interaction, spin-orbit coupling, or interatomic dipole-dipole interaction [67]. In the polycrystalline structure with the structural length (grain size) of *D*, each of the grains have their preferred magnetic orientation. Therefore, the magnetisation behaviour of the material depends on the local magnetocrystalline anisotropy constant, *K*, of the grains.

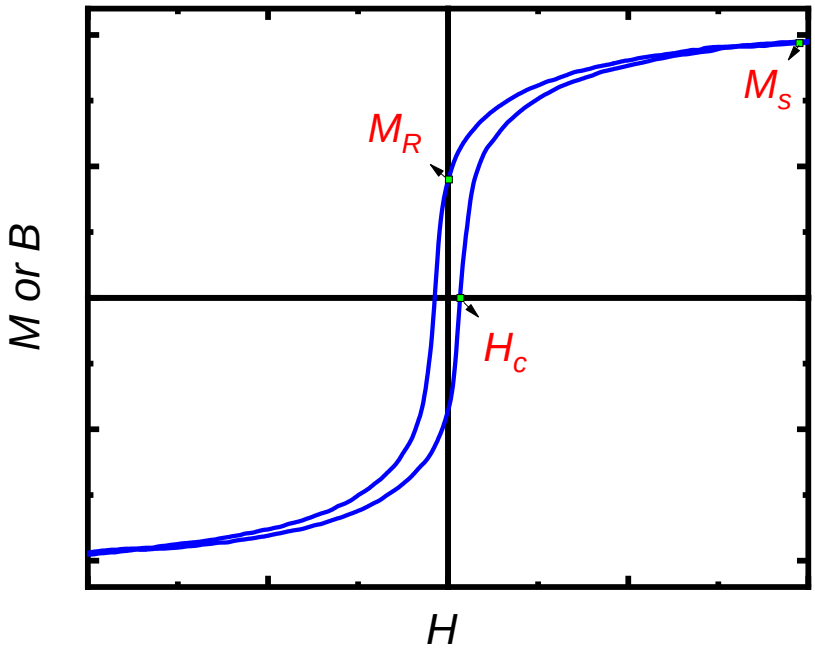

Figure 4. Magnetic hysteresis loop of a soft ferromagnetic material.

There are different methods to minimise magnetocrystalline anisotropy. First, it is established that the materials with large grains and/or cubic atomic structures demonstrate lower anisotropy. In addition, a textured structure with an easy axis parallel to the direction of the magnetic field, like silicon steels, can be another example of low-anisotropy materials [64]. However, in the case of materials with a small correlation length, the mechanism of

magnetisation with respect to magnetocrystalline anisotropy is different. This mechanism can be explained through the random anisotropy model in section 1.3.5.1.

1.3.5 Coercivity

As an extrinsic property, coercivity is a function of the structure of the material. In other words, any structural features which influence the domain wall motion can change the coercivity. To have a better understanding of this parameter, it is useful to analyse the movement of a domain wall with respect to its interaction with the structure. In this regard, the gradient of the potential energy of a moving domain wall determines the ease or difficulty of its motion. The application of a magnetic field exerts pressure on a 180° domain wall, equal to $2M_sH\cos\theta$, where θ is the angle between the applied field and the magnetisation directions [3]. By applying this pressure, a domain wall can reversibly move in its potential valley. By increasing the intensity of the applied field, the potential energy of a domain wall exceeds the maximum intensity that it can have in the current valley. If the pressure is such as to move the wall to a position of larger wall energy density, the field pressure will be opposed by the wall energy density gradient, $d\sigma_{dw}/dx$. Thus, the domain jumps irreversibly, which implies that its potential energy reached the peak of the next potential valley. These irreversible jumps cause the hysteresis behaviour and determine the significance of the coercivity [3,68]. Accordingly, the greater the fluctuations in wall energy with position, the higher the field needed to move the wall, so H_c is proportional to $(2/M_s).d\sigma_{dw}/dx$. On the other hand, if the potential energy of a domain wall was independent of its position in the structure, the wall could move by applying a relatively weak field. However, structural defects can result in the dependence of wall energy on its position in the structure, so in most materials higher field is needed to move domain walls [15]. This effect can lead to domain wall pinning.

Structural defects should have two conditions to be able to pin the domain wall. First, they should show very different magnetic properties compared to the matrix. In addition, their dimensions must be comparable to the domain wall width [15]. For very small defects, the wall

energy gradient varies linearly with defect size divided by domain wall width [3], indicating that the defect cannot pin the domain wall.

Based on these conditions, there can be several pinning centres in the structure. For instance, defects in different dimensions, e.g., line (dislocations), planar (grain boundaries), and bulk defects (inclusions) can pin the domain walls. On a larger scale, local anisotropies in the grains also can hinder the motion of domain walls. This effect will be discussed in more detail in the following section. Additionally, surface features, e.g., roughness or scratches, can also act as pinning centres, especially in the case of melt-spun ribbons. As many of these structural features can be characterised in a ferromagnet, in the case of domain wall pinning, they function simultaneously. However, depending on the structure of the material, some of these mechanisms can be considered as dominant mechanisms [3].

As far as structural features effective on pinning procedure are concerned, there are not many pinning centres in the amorphous structure, e.g., there are no grain and grain boundaries. In addition, as these alloys are fabricated through quenching the melt, there is not enough time for diffusion and precipitation of crystalline phases. Thus, amorphous materials are structurally homogenous, which implies that the size of possible defects, 2-3 nm, is much less than the size of the wide domain walls, 5-10 nm for Co-based and 20-40 nm for Fe-based alloys [3]. Therefore, the domain can easily move in the amorphous structure, resulting in low coercivity and high permeability of these materials. However, the coercivity of nanocrystalline alloys can change in a wide range depending on the magnetocrystalline anisotropy of individual grains, grain size and the structure of grain boundaries [3]. The dependence of coercivity on grain size is explained through the random anisotropy model in the following section. In addition, coercivity is a DC magnetic characteristic that is also effective on AC magnetic behaviour of the material through hysteresis loss which is discussed in the 1.3.3 section.

1.3.5.1 Random anisotropy model

Magnetic anisotropy as a result of long-range atomic order is not obviously the case in amorphous alloys. Hence, no fundamental anisotropy constant attributed to a specific amorphous alloy, of a particular composition, has been defined. Nevertheless, the same local

field which leads to magnetocrystalline anisotropy in crystalline alloys contributes to the soft magnetic properties of non-crystalline materials on a scale of a few nanometers [69]. However, the local atomic order of amorphous magnetic alloys, which varies randomly in direction, gives rise to a random anisotropy that plays an essential role in their magnetic properties. As the local atomic order in amorphous alloys varies randomly, the orientation and strength of the so-called local field depend on its position, which is the reason why this type of anisotropy has been called random anisotropy. Although this kind of anisotropy might be averaged out in some soft magnetic materials, the mechanism of averaging and the magnitude of this anisotropy on the macroscopic magnetic behaviour of this class of materials should be evaluated [15].

The random anisotropy model stems from minimising two competing mechanisms in the free energy equation. The first mechanism, exchange interaction, promotes long-range correlation in the magnetisation direction, and the second one, magnetic anisotropy, favours short-range fluctuations in the magnetisation direction [64]. It is assumed that the ferromagnetic material is composed of structural building blocks, with the size of D, in which the magnetic anisotropy axes is in the same direction, e.g., grains in nanostructured materials. The exchange interaction is effective in orienting the local magnetisation of the structural features towards the direction of the magnetic field on a scale smaller than $L_{0,}$ which can be calculated as [64]:

$$L_0 = \varphi_0\sqrt{A/K_1} \tag{2}$$

where K_1 is the local anisotropy constant, A as the exchange stiffness constant represents the intensity of exchange interactions among the local magnetic moments, $\varphi_0 = \alpha\sqrt{8/(3\beta)}$, including α and β as dimensionless factors, where α corresponds to the average angle between the easiest axes of adjacent exchange-coupled regions, and β is related to the symmetry of the random anisotropy axis, so φ_0 is a dimensionless parameter of the order of one. This basic ferromagnetic correlation length (L_0) represents the characteristic minimum scale below which the direction of magnetisation cannot vary appreciably. It determines, for example, the magnitude of the domain wall width for grains larger than L_0. The ferromagnetic correlation length for Co-based and Fe-based alloys are 5-10 nm and 20-40 nm, respectively. It can be concluded that amorphous, with $D \approx$ atomic scale, and nanocrystalline, with $D \approx$ 5–40 nm,

alloys fall into the regime where the structural correlation length (D) is smaller than ferromagnetic correlation length (L_0) and exchange interactions can average the local randomly oriented anisotropies of nanograins (Figure 5) [64].

Based on the random anisotropy model, the magnetisation direction is kept constant by exchange interactions in the volume of $V_{ex} = L_{ex}^3$ in which L_{ex} is exchange correlation length. The average anisotropy over the randomly oriented anisotropies of the $N = (L_{ex}/D)^3$ grains in the exchange-coupled volume is determined by statistical fluctuations. The average anisotropy constant $\langle K_1 \rangle$ hence scales as [64]:

$$\langle K_1 \rangle = K_1/\sqrt{N} = K_1.(D/L_{ex})^{3/2} \quad (3)$$

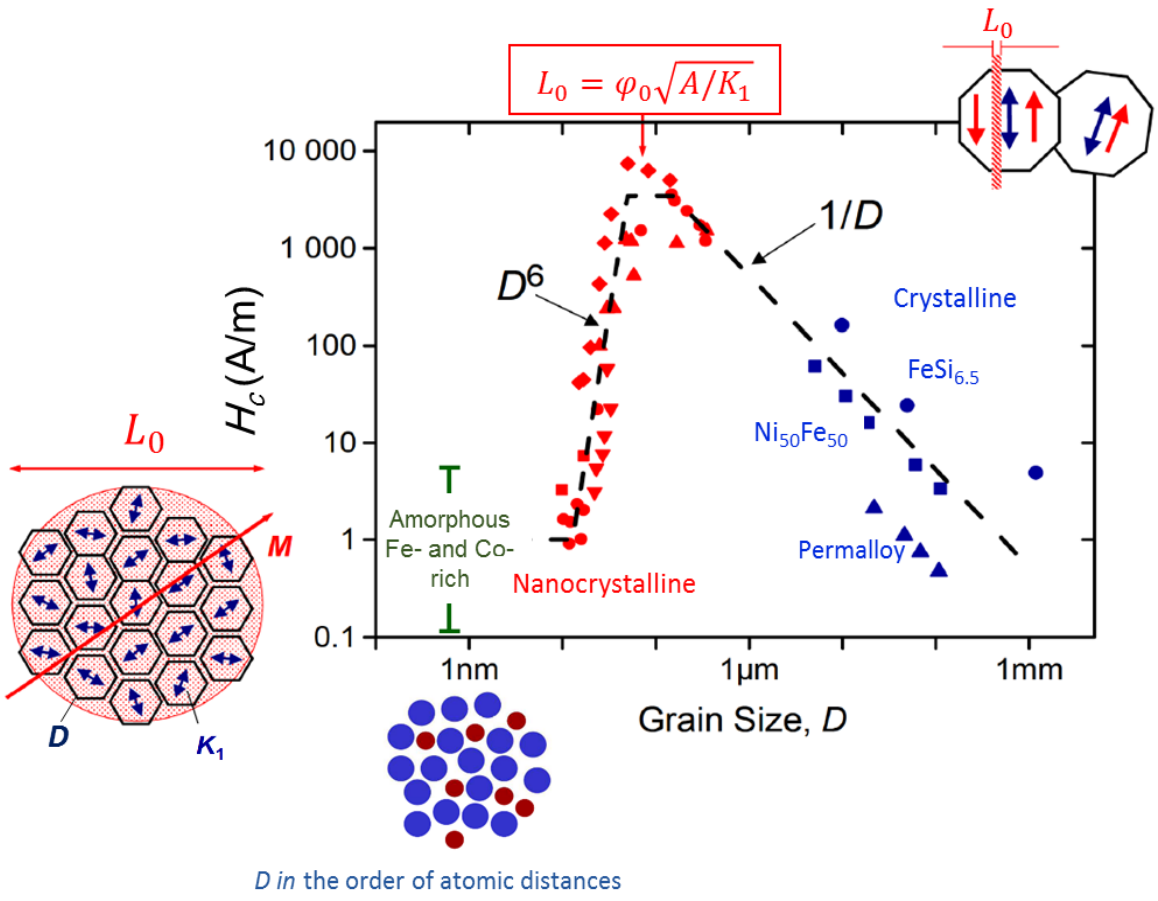

Figure 5. Coercivity, H_c, versus structural correlation length, D, for a variety of soft magnetic amorphous, nanocrystalline and crystalline alloys, reproduced from [99–101].

By replacing K_1 in Eq. (2) with $\langle K_1 \rangle$, L_{ex} can be calculated as:

$$L_{ex} = \varphi_0 \sqrt{A/\langle K_1 \rangle} \quad (4)$$

Thus, based on these calculations, when $D < L_0$, the anisotropy can be averaged out by exchange interactions, and as a result, L_{ex} can be calculated in which $L_0 < L_{ex}$, implying that the exchange interactions are effective over a larger area. Therefore, the average anisotropy constant $\langle K_1 \rangle$ for the local anisotropy constant K_1 can be calculated as [64]:

$$\langle K_1 \rangle = K_1 (D/L_0)^6 \quad (5)$$

When anisotropies of structural features are averaged out through random anisotropy model, coercivity and initial permeability, μ_i, can be calculated as:

$$H_c = p_c \frac{K_1 D^6}{J_s {L_0}^6} \quad (6)$$

$$\mu_i = p_\mu \frac{J_s^2 {L_0}^6}{\mu_0 K_1 D^6} \quad (7)$$

where J_s is the average saturation polarisation of the material, p_c and p_μ are dimensionless pre-factors of the order of unity, and μ_0 is the vacuum permeability. Therefore, based on Equation 6, coercivity increases abruptly with grain size when the grain size is less than the ferromagnetic correlation length. It is worth mentioning that, due to the effect of exchange interactions in averaging out the anisotropy constant, the renormalised exchange length, L_{ex}, is almost two orders of magnitude larger than the basic ferromagnetic exchange length L_0 [15]. This effect can be reflected in the domain size of amorphous materials. Based on this, in amorphous metals, the weak local anisotropies, like short-range ordered regions, can barely disturb the exchange interactions between magnetic moments, and, as a result, this kind of materials have domain sizes in the micrometre scale, which is confirmed by the magnetic domain images in Chapters 4, 5 and 6. This effect can be illustrated in the dependence of H_c on the structural correlation length (Figure 5). In this regard, amorphous materials with the smallest structural correlation lengths, in the scale of atomic distance, offer the lowest

coercivities. In the nanocrystalline materials, the anisotropies can be averaged out when $D < L_0$, but with an increase in D, H_c varies as the sixth power of the grain size based on Equation 6 [70]. Then, the coercive force reaches its maximum value when L_{ex}/D decreases toward unity, where the orientation of the local anisotropies constrains the magnetisation vector more effectively. The $1/D$ dependence of coercivity for large grain sizes reflects the conventional rule that good soft magnetic properties require very large grains ($D > 100$ μm) through which domain walls can move easily without being hindered or pinned [15].

1.3.6 AC magnetic properties

Amorphous materials mainly target power conversion applications at higher frequencies. An increase in switching frequency reduces the required energy to be stored in power converters. This satisfies the need for a smaller footprint, better manufacturability, and higher performance power electronics [57]. However, devices, passive components, and circuit designs are required which can operate efficiently at the necessary frequencies [71]. In this regard, the efficiency of the device comprised of the magnetic material is one of the most frequently stated problems with high-frequency passive components. In other words, the advances in power conversion technologies have outpaced the progress in soft magnetic materials. This has made this class of magnetic materials the main pitfall in the miniaturisation of devices [72,73]. In this respect, although amorphous and nanocrystalline alloys usually exhibit excellent soft magnetic properties under quasistatic conditions; however, these characteristics degrade rapidly with increasing frequency [15]. This degradation can be estimated by evaluating the magnetic loss of these materials, which will be explained in more detail in Chapters 2, 5 and 6.

The magnetic loss can be defined as the summation of different energy dissipation mechanisms taking place when a magnetic material is subject to a time-varying external field $H(t)$, by which magnetic flux density of $B(t)$ is induced. Because of the inherent irreversible nature of magnetisation processes, part of the energy injected into the system by the external

field is irrecoverably transformed into heat. In a cyclic field of frequency *f*, the loss per cycle, that is, the energy per unit volume converted into heat, is given by [68]:

$$W = \int H \frac{dB}{dt} dt \tag{8}$$

Magnetic losses are often expressed per cycle ($P = f \times W$), in which case they have units W/m^3 or W/kg. As mentioned before, during the magnetisation process, various mechanisms can contribute to magnetic loss. A major issue in the evaluation of magnetic materials is understanding and predicting their complex loss behaviour with respect to these mechanisms. In this regard, the total power loss (P_t) can be separated into three different mechanisms, namely hysteresis loss (P_h), eddy current loss (P_{ec}) and anomalous loss (P_a) [63,72,74]:

$$P_t = P_h + P_{ec} + P_a \tag{9}$$

1.3.6.1 Hysteresis loss

Hysteresis loss is related to the irreversibility of the quasistatic B-H loop. The area inside the B-H loop is the energy per unit volume lost per cycle in magnetising the material, which is called hysteresis loss. Several models have been proposed to calculate different constituents of power loss [75–78]. In AC applications, the hysteresis loss can be calculated as the frequency times the loop area [15]. An empirical method can also be used to estimate the hysteresis loss [72]:

$$P_h = 4 f B_{ac}^2 \frac{H_c}{B_s} \tag{10}$$

where B_{ac} represents the applied AC flux density, and B_s is the saturation magnetic flux density. As can be seen in Eq. (10), the smaller the coercivity, the smaller is the hysteresis loss. This loss is a result of the interaction between the applied alternating magnetic field and the microstructure of the material. As it is described in the 1.3.3 section, the domain wall motion can be hindered or pinned by different types of defects, and by increasing the pressure of the

magnetic field on the pinned domain wall, it can jump over the defect through the Barkhausen mechanism. Local eddy current arises from each of such jumps as the abrupt change in the magnetic induction takes place. The local eddy current is the main mechanism responsible for heat dissipation in metallic systems. The amount of heat depends on the height of the energy barrier created by the pinning obstacle. Thus, the hysteresis loss is the sum of the heat dissipated during all Barkhausen jumps in a magnetic material [68].

1.3.6.2 Eddy current loss

The coercivity increases when the B-H loop is measured at high frequencies which can be due to other mechanisms of power loss rather than just hysteresis loss. Based on Faraday's law, when the magnetic flux changes at higher frequencies, a voltage is induced in the magnetic material. Then, the direction of the induced voltage is such that the resulting current opposes the initial flux change based on Lenz's law [15]. Such currents flow in the cross-section of the magnetic core perpendicular to the magnetic induction vector and are named eddy currents [79].

Alternating current cannot be distributed homogenously in a conductor. Also, when it comes to a magnetic material exposed to an AC field, the intensity of the field is maximum on the surface and decreases with greater depth inside the material, which can be defined as skin effect. The limitation in the penetration depth of the flux arises from eddy currents. Accordingly, the skin depth δ can be estimated as the depth where B falls to 1/e of its value at the surface [15,67,68]:

$$\delta = \sqrt{\frac{\rho}{\pi \mu_{\mathrm{r}} \mu_0 f}} \tag{11}$$

where ρ is the resistivity, μ_r denotes the relative permeability of the material, μ_0 is the permeability of free space, and f is the AC frequency in hertz. As a case in point, electrical steel, $Fe_{94}Si_6$, shows electrical resistivity of 50 μΩ.cm and relative permeability of 20000. The skin depth of this type of material is 0.36 mm and 3.6 μm at 50 Hz and 500 kHz, respectively [67]. If the skin depth is appreciably smaller than the sample dimension, perpendicular to the

dimension of the applied field, then a significant volume fraction of the magnetic material is unresponsive to the field, and, effectively, the permeability is reduced [15]. For this case, the classical eddy current loss increases significantly as frequency rises. Thus, the magnetic cores are generally composed of insulated magnetic particles, flakes or laminations where the thickness of the magnetic material is chosen to be less than δ, at the application frequency, so that the applied field can penetrate each one [67].

According to John Barranger's model [80], classical eddy current loss can be calculated as:

$$P_e = \frac{\omega^2 B_{\mathrm{ac}}^2 b\delta}{8\rho l}\left(\frac{sinh\left(\frac{t}{\delta}\right) - sin\left(\frac{t}{\delta}\right)}{cosh\left(\frac{t}{\delta}\right) + cos\left(\frac{t}{\delta}\right)}\right) \tag{12}$$

where t is the thickness of the lamination, δ is the skin depth, b and l are the width and length of the lamination, ω is the excitation radian frequency, and ρ is the resistivity of the material. Once the magnetic component thickness is less than one skin depth, its classical eddy current loss can be simplified to

$$P_e = \frac{(\pi t f B_{\mathrm{ac}})^2}{6\rho} \tag{13}$$

Based on these equations, the eddy current loss can be diminished by decreasing the thickness of the magnetic component or using highly resistive magnetic material. Both of these physical and electrical properties have been documented in soft magnetic melt-spun ribbons. In the case of the latter, the high electrical resistivity of amorphous materials (of the order of 120 μΩ.cm), is due to the very short mean free paths of the order of one or two atomic spacings in the disordered structure [81]. Therefore, apart from Ferrites, magnetic cores of devices are not usually made of bulk soft magnetic materials [68], and the amorphous ribbons are attractive for higher frequency operation [3,15]. The value of the actual measured AC loss is always greater than the summation of hysteresis and classical eddy current losses, the sum of which can be called classical loss. The excess of the measured loss over the classical loss is called the anomalous loss [15].

1.3.6.3 Anomalous loss

As mentioned before, the increase in B-H loop area, resulting from increased frequency of the applied magnetic field, is understood to be not only because of classical but also excess or anomalous loss. The origin of the anomalous loss is eddy currents induced around the active walls involved in the magnetisation process [79]. Having many active domain walls in the structure of the material can limit the domain wall motion. However, the density of domains in the magnetic structure of amorphous alloys and single crystals is low due to the shortage of domain nucleation sites. Thus, the soft magnetic behaviour of such materials degrades when frequency increases. Given that the number of active domain walls can be increased by inducing anisotropy and/or changing the microstructure of amorphous alloys, making them attractive for higher-frequency applications [15]. As a case in point, the precipitated crystals in the amorphous matrix can act as domain nucleation sites. However, the size and anisotropy of the crystals should be such that their benefits in terms of decreasing the anomalous loss by domain wall nucleation and pinning outweigh their negative effect on hysteresis loss through domain wall pinning and enhanced magneto-crystalline anisotropy. Additionally, the volume density of the crystalline phase should be small (1-2 vol%) as the excessive portion of such phase leads to stresses and domain wall pinning, degrading both DC and AC properties by raising the hysteresis loss and declining the permeability. Consequently, the limited nanocrystallisation of the low-anisotropy phase that strains the amorphous matrix only weakly can improve both the DC and AC properties of the amorphous alloys. This effect will be explained in detail in Chapter 6.

In addition, the arrangement of domain walls can substantially affect anomalous loss. As mentioned in section 1.3.3, magnetisation proceeds through different mechanisms. The initial mechanism of magnetisation, in a low intensity applied field, is domain wall movement which contributes to the hysteresis and anomalous loss. Through this movement, the concentrated flux change is induced in the narrow area of the domain wall, and the magnetic response of the material away from the domain wall is zero. That is why this magnetisation mechanism can be considered inhomogeneous. The rearrangement of the domain walls from the easy axis to the

hard axis of the material can change the mechanism of magnetisation more towards homogenous domain rotation [15]. In Chapters 5 and 6, this effect is observed and discussed further. Consequently, the size and arrangement of magnetic domains can determine the magnitude of anomalous loss. As previously stated, a finer domain structure results in a lower anomalous loss. This kind of loss can be neglected when the domain width is much smaller than the specimen thickness or when magnetisation changes homogeneously by rotation, as is the case for flat-type hysteresis loops with small B_r/B_s ratios. The square B-H loop of soft magnetic materials can be changed to the flat loop by inducing anisotropy perpendicular to the direction along which the magnetic field will be applied.

A model in which the statistical approach was used to investigate losses in the whole volume of bulk material was proposed by Bertotti [75]. According to this model, it was concluded that in many magnetic materials, the number of movable domain walls linearly increases with the frequency. Additionally, the distance between domain walls is inversely proportional to the number of simultaneously movable domain walls in the cross-section of the sample [79]. Based on this model, the anomalous loss under sinusoidal flux can be calculated as [68]:

$$P_{an} = 8.8\sqrt{GSV_0/\rho}(B_{ac}f)^{3/2} \quad (14)$$

where S is the cross-sectional area of the material, G and V_0 are variables dependant on the material and magnetization. The numerical constant is a function of waveform shape, for example for a triangular waveform, it can be set as 8.

Based on total power loss separation, it is established that there are several important parameters that determine the behaviour of the magnetic material in a cyclic magnetic field, including B_{max}, f, ρ, and the size of the material perpendicular to the applied magnetic field [15]**.** These parameters can be categorised, based on power loss mechanisms, as structural parameters effective on domain wall pinning (hysteresis loss), geometrical and electrical resistivity (eddy current loss), and the number of active domain walls (anomalous loss). In addition, as the purpose of the power loss decomposition is the evaluation of the high-frequency behaviour of the magnetic material, the frequency dependence of the power loss mechanisms

should be taken into account. Based on Eq. (10), the hysteresis loss per cycle is directly proportional to frequency. In contrast, the anomalous loss is proportional to frequency to the power of 1.5 (Eq. (14)) and eddy current losses are proportional to frequency to the power of 2 (Eq. (13)) and hence are the major contributors to the total power loss at higher frequencies. More specifically, the anomalous loss becomes the main mechanism of power loss with increasing the frequency in the melt-spun ribbons, which will be discussed in Chapters 5 and 6.

1.3.7 Figures of merit

Miniaturisation has been essential to a variety of latest technological advances. With the ongoing trend toward miniaturisation of mechanical, optical, and electronic devices, ever smaller power convertors are needed [82]. In this regard, the high saturation flux density and permeability of the magnetic material implies that a lower amount of such material is needed for making a power converter magnetic core with a specific value of inductance. This can result in a decrease in the convertors' weight-to-performance ratio. Additionally, ultra-soft magnetic materials are needed to satisfy the increasing global demand for efficient electrical power distribution and generation. Thus, saturation flux density, permeability and coercivity of the magnetic materials can be considered as figures of merit, and they are evaluated for different kinds of such materials as follows.

In Figure 6, ferromagnetic materials are classified based on their coercivity and saturation flux density (B_s). Hence these materials can be divided into soft, semi-hard and hard categories based on their coercivity. In this regard, hard magnetic materials exhibit coercivities above 50 kA/m, whereas this value is below 1 kA/m for soft magnets. As illustrated in the figure, amorphous Co-based alloys offer $H_c \leq 1$ A/m, while the magnitude of this property is one order of magnitude higher in the case of amorphous Fe-based alloys. Furthermore, Fe-based alloys exhibit 50% higher B_s compared to Co-based alloys. In general, it can be pinpointed from Figure 6 that amorphous alloys can be deemed as the softest magnetic materials available [83].

Nevertheless, Fe and FeSi, with relatively high H_c and B_s (Figure 6), in comparison with other soft magnets, have obtained about 80% of the market share of soft magnetic materials.

These materials have been exploited mostly in the generation and distribution of electrical energy such as inductors, transformers and motors. As the eddy current losses might limit the application of these alloys at high frequencies, soft MnZn and NiZn ferrites have been utilised for frequency ranges of 1-1000 kHz and 1-1000 MHz, respectively. Compared to other soft magnets, ferrites offer high H_c and low B_s (Figure 6), which confines their efficiency and volume to performance ratio. In addition, CoFe and NiFe alloys can be identified as materials with lower H_c, much higher B_s and permeability compared to ferrites. Nonetheless, the high value of loss in such crystalline materials is the main issue when it comes to their high-frequency applications. Although cores made from soft magnetic metals are often assembled

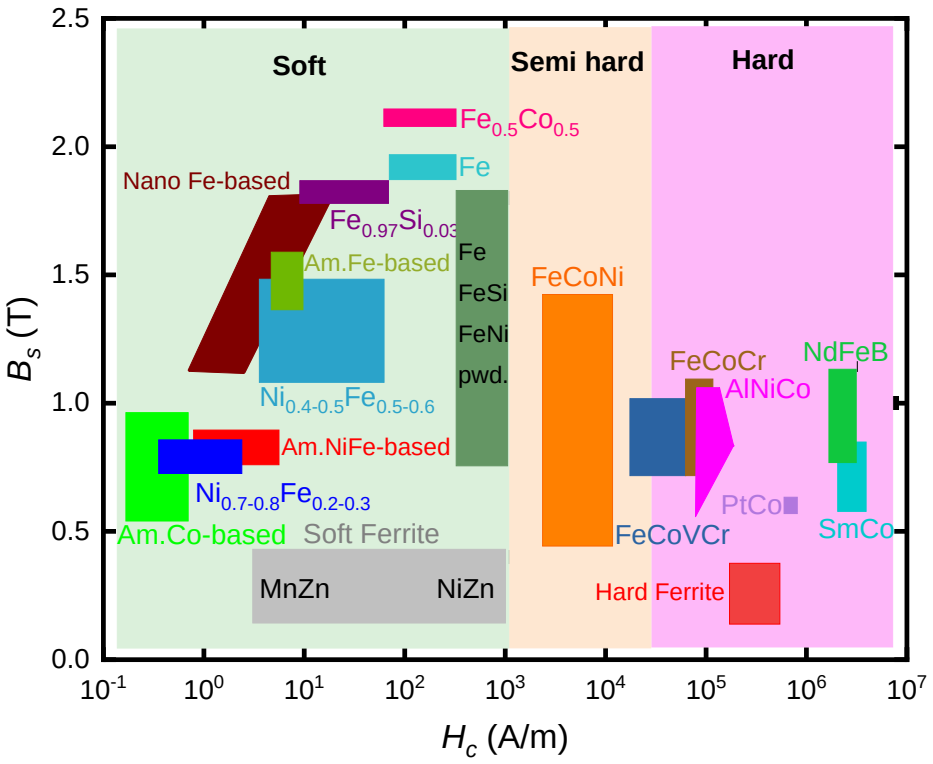

Figure 6. Coercive field vs saturation flux density for a variety of magnetic materials, reproduced from [83].

from a stack of insulated laminations to decrease the total loss, their low resistivity and limitation in fabricating ultra-thin laminations still constraint their high-frequency applications.

To bridge this gap, amorphous and nanocrystalline soft magnets with higher resistivity and lower eddy current losses have been developed [64]. Based on this, Fe-Si-based magnetic components can be replaced with their amorphous/nanocrystalline counterparts.

Figure 7 illustrates the effective permeability, μ_e (measured at 1 kHz) versus saturation flux density, B_s, for soft magnetic materials. FeCo-based alloys exhibit particularly interesting magnetic properties, with high Curie temperatures, the highest saturation magnetisations, and relatively good mechanical properties [84]. Nevertheless, they show lower permeability compared to other crystalline counterparts such as ferrites and FeSi steels. Although FeSi steels offer much higher B_s in comparison with MnZn ferrites, their permeability can be lower than ferrites and much lower than amorphous/nanocrystalline alloys.

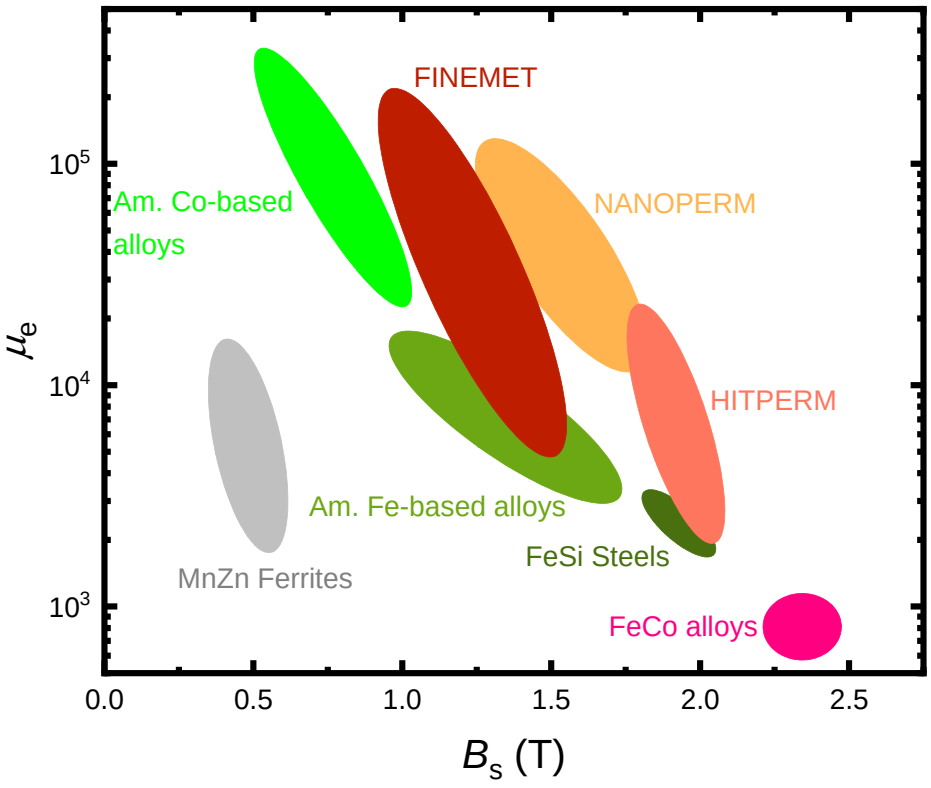

Figure 7. Effective permeability, μ_e (at 1 kHz) vs saturation flux density, B_s, for soft magnetic materials, reproduced from [54].

Amorphous and nanocrystalline alloys offer the highest achievable permeability and simultaneous high saturation flux density. These types of soft magnets allow an extensive range of property variation through alloying. For instance, based on the alloy system, their permeability can be varied continuously by more than two orders of magnitude from 1×10^3 to 3×10^5 (Figure 7) [85]. Compared to amorphous Fe-based alloys, Co-based alloys offer higher permeability but lower B_s. Additionally, nanocrystallisation in the case of Fe-based alloys results in the enhancement of μ_e and B_s due to the formation of soft magnetic Fe-Si solid solutions, whereas the formation of cobalt borides increase the H_c of amorphous Co-based alloys during nanocrystallisation. The optimised properties of three nanocrystalline Fe-based alloys are listed in Table 1 [54].

In addition to the exceptional magnetostatic properties of amorphous and nanocrystalline alloys, their high frequency soft magnetic properties have also generated considerable interest in this type of materials [64]. These properties are favourable for more efficient power conversion [89–91]. For instance, the excellent high-frequency behaviour of these materials is comparable to MnZn ferrites [86,92]. It should be stated that due to lower B_s of ferrites compared to amorphous/nanocrystalline alloys, ferrites do not suit the requirements for miniaturised devices.

Table 1. Optimised magnetic properties and nanocrystalline phases in three nanostructured Fe-based alloys.

Name	**Alloy**	**Optimised properties**	**Nanocrystalline phase**	**Ref.**
FINEMET	Fe-Si-B-Nb-Cu	High B_s, low H_c	α-FeSi DO_3	[53,86]
NANOPERM	Fe-M-B-Cu (M= Zr, Nb, Hf)	Low magnetostriction, high μ_e	α-Fe BCC	[87]
HITPERM	(Fe,Co)-M-B-Cu (M= Nb, Hf, Zr)	High B_s, high μ_e, high T_C	B2–FeSi, (B2)-FeCo	[88]

1.4 Motivation and scope of thesis

This study has enhanced our understanding of the design, fabrication, characterisation and optimisation of amorphous and nanocrystalline soft magnetic alloys, which are primarily used for power conversion

The evaluation of amorphisation capability and crystallisation behaviour of the soft magnetic alloys by fundamental topological, thermodynamic and kinetic criteria can be used as a guideline to design the alloy compositions with optimised AMC and soft magnetic properties. Despite many criteria to predict the amorphisation ability of alloys, it has been challenging to distinguish certain alloys with high amorphisation ability. As a case in point, to calculate some of the criteria, the thermal properties of the amorphous or glassy alloys are needed, which are not predictable before the fabrication of such alloys. In addition, some of the new criteria seem to be limited to a few alloy systems. Therefore, a multi-faceted predictive model is needed to predict the AMC in different alloy systems. This model, which considers topological, kinetic and thermodynamic parameters, can estimate the AMC of alloys without performing any experiments. Using this predictive model will eliminate many laborious 'trial and error' experiments needed to find an alloy composition with high amorphisation capability.

Moreover, such a predictive model is more crucial as the alloys made of more abundant elements tend to show low AMC. In such cases, nonmagnetic metals are added to these compositions to overcome the low AMC problem. However, the presence of such metals can substantially decrease the saturation magnetisation of amorphous alloys, whereas high M_s is essential for the miniaturisation of power convertors. In addition, using these metallic elements can substantially increase the cost of amorphous alloys compared to the existing competing materials such as ferrites. Thus, optimising the AMC of ternary alloys is both interesting scientifically and very valuable, as one of the most important considerations for manufacturers is the cost of the material involved.

In addition, most studies have tended to focus on the magnetic properties of Fe-based amorphous alloys, and just a few studies have been reported on the cobalt-rich ones, which is the focus of Chapters 2-6. Further, having the information regarding the magnetic properties of different alloys in Co-Fe-B system can give the opportunity to find the compositions in

which there is a balance between saturation magnetisation and power loss for power converter applications. As there hasn't been a significant step-change in decreasing the power loss of soft magnetic materials, especially for high-frequency devices, there is a need for a detailed investigation of different mechanisms of power loss (Chapters 5 and 6) and their contribution to the total power loss. This can serve as a guide for researchers to optimise the microstructure of soft magnets based on effective parameters, which mostly contribute to the power loss of the material. Additionally, investigation of the Co-rich side of Co-Fe-B phase diagram by one of the furthest from equilibrium fabrication methods, melt spinning, as well as studying their crystallisation, can shed light on the thermodynamic, kinetic and structural behaviour of soft magnetic alloys to be exploited in a variety of applications. This behaviour of the alloys in the case of amorphisation capability and soft magnetic properties can be extrapolated to the other regions of this phase diagram and even to other alloy systems.

The cost of rapidly quenched materials limits their application. Therefore, producing more cost-effective materials is also addressed in this thesis. The alloys with excellent DC and AC magnetic properties are fabricated in a ternary Co-Fe-B system, without using any costly element, in Chapters 2 and 3. This has a direct impact on the cost of melt-spun ribbons used as power convertors' cores. Ultra-thin soft magnetic amorphous ribbons of Co-Fe-B-Si-Nb alloy have been synthesised by a single step rapid-quenching approach to acquire the advantage of improved material performance and lower costs over commercial amorphous alloys in Chapter 4. It has been suggested that the *in-situ* thinning process of amorphous ribbons significantly reduces the basic material cost and eliminates the need for post-processing steps; hence it provides the opportunity for mass production of high-performance soft magnetic amorphous ribbons at relatively lower costs for high-frequency applications. Therefore, this study focuses on filling the gaps in the research, and as a publication-based thesis, each chapter and appendix include a published article or a submitted manuscript, which will be summarised one by one as follows.

In the second chapter, a novel multi-faceted model based on kinetic and thermodynamic parameters, Calculation of Phase Diagram (CALPHAD), combined with a topological instability parameter, is proposed to predict the amorphisation ability of Co-based alloys. Based on the Prediction of the model, seven Co-based alloys are designed and fabricated via melt-

spinning, among which five of them are amorphous. The structural, DC and AC magnetic properties of the alloys are investigated. A detailed Mössbauer study is performed confirming the alloys structural features. It is proposed that the alloy with the limited surface nanocrystallisation can perform better than other amorphous alloys at higher frequencies due to induced out-of-plane anisotropy and domain wall pinning as a result of surface nanocrystallisation, which constraints the anomalous loss.

The as-mentioned model, in Chapter 3, is experimentally evaluated, in order to optimise *in-situ* nanocrystallisation of rapidly quenched CoFeB alloys, with remarkable B_s = 1.57 T, by designing an alloy with the moderate amorphisation ability [93]. The formation of the metastable nanocrystalline Co_7Fe_3 phase is confirmed by XRD, TEM, and nucleation theory. Based on Mössbauer study, it is asserted that cobalt atoms form clusters, as they attract each other to form ordered structures, and boron atoms undergo only short-range ordering, likely due to covalent bond formation governed by the size and electronegativity differences with the atoms in the amorphous matrix. The design of nanostructured alloys based on the proposed model provides a practical approach to develop novel functional alloys with the desired combination of coercivity and saturation magnetisation.

After working on the design of the amorphous and nanocrystalline alloys, the fabrication of ultra-thin Co-Fe-B-Si-Nb amorphous ribbons is explored in Chapter 4 [94]. The ultra-thin ribbons, with good surface quality, show ultra-soft magnetic properties. Thus, it is concluded high performance soft magnetic ribbons can be produced using the *in-situ* thinning process, through high-speed melt spinning, at relatively lower costs. The ultra-thin amorphous ribbons are continuous without any pores over a large scale and retain excellent soft magnetic properties. The thickness-dependent magnetic properties of the amorphous ribbons are largely attributed to the surface inhomogeneities and voids produced during the quenching process.

To gain a deeper understanding of the AC magnetic behaviour of melt-spun ribbons, the mechanisms that limit their power loss performance at frequencies in the range 50 kHz – 1 MHz, have been analysed in Chapter 5 [95]. The total power loss is decomposed into hysteresis, eddy current, and anomalous losses. It is deduced that the anomalous loss is the main contributor to total power loss, and it is decreased substantially through transverse magnetic

annealing. The mechanism of this observation is studied in detail using magneto-optic Kerr effect (MOKE) microscopy and domain wall energy calculations based on magnetisation data. Thus, heat treatment of CoFeBSiNb amorphous ribbons in a transverse magnetic field at a temperature in the range of 450-500 $^{\circ}$C can render them ideal candidates for power applications, with a smaller footprint alternative to ferrites.

The aim of Chapter 6 of this research is to further the current knowledge of phase transformation driven soft magnetic properties of cobalt-based amorphous alloys [96]. In this regard, a combination of structural, magnetothermal and domain imaging techniques coupled with related calculations are used to evaluate AC/DC magnetic properties of amorphous and different nanocrystalline ribbons. The nucleation of different nanocrystalline phases, including $Co_{23}B_6$, Co_2B and Co_3B, during magnetic annealing at different temperatures, is also studied in detail using thermodynamic modelling and nucleation theory. It can be concluded that the limited nucleation of favourable phases with low magnetocrystalline anisotropy can optimise the magnetic properties of Co-rich ribbons. In addition, the knowledge of soft magnetic nanocrystalline Co-based systems is largely based on very limited data, and this study shows that this type of alloys offers an interesting engineering trade-off between the extreme properties of amorphous and fully crystalline soft magnets. The main conclusions of the dissertation and outlook for future work in described in Chapter 7.

An evaluation of the amorphisation capability of gas atomised amorphous powders is outlined in Appendix A. A set of predictive criteria, similar to the ones mentioned in Chapters 2 and 3, are taken into account to predict amorphisation ability in Fe-Si-B gas atomised powders. In this research, different empirical and theoretical parameters are implemented to propose a model to predict the amorphisation capability. No one to date has put forward such a comprehensive model in the case of gas atomised powders. Given a production method with a characteristic average cooling rate, this model can be used to design alloys with a high enough amorphisation ability to be gas atomised.

In Appendix B, the high-frequency core loss performance of Fe-based amorphous and nanocrystalline gas-atomised powder cores is investigated [98]. The soft magnetic composite cores exhibit excellent loss performance due to the ultra-low coercivity obtained upon

nanocrystallisation, and negligible eddy currents loss, owning to efficient insulation of small soft magnetic particles. These cores can be used in high-frequency power conversion applications, such as voltage regulator (VR), and resonant converters, in the automotive industry and data storage centres.

The present study aimed to explore the design, fabrication, characterisation and optimisation of amorphous and nanocrystalline soft magnets. Through this multi-faceted piece of work, alloys with optimised amorphisation capability, ultra-soft DC and AC magnetic properties are designed, fabricated, characterised and heat treated in order to achieve the optimised properties. The crystallisation and power loss behaviour of alloys are investigated in detail. The findings of this research have improved the knowledge about amorphous and nanocrystalline soft magnets from the design of their composition to their low and high frequencies applications as the core of power converters.

1.5 References

[1] D. Bloor, R.J. Brook, M.C. Flemings, S. Mahajan, F. Disalvo, The Encyclopedia of Advanced Materials, Pergamon, 1995. https://doi.org/10.1063/1.2808264.

[2] C. Suryanarayana, A. Inoue, Bulk metallic glasses: Second edition, CRC, New York, 2017. https://doi.org/10.1201/9781315153483.

[3] M.A. Otooni, Elements of rapid solidification : fundamentals and applications, Springer Berlin Heidelberg, 1998. https://books.google.ie/books?id=Xn1vMAEACAAJ.

[4] F.E. Luborsky, Amorphous metallic alloys, in: Amorph. Met. Alloy., Butterworth-Heinemann, 1983: pp. 1–7. https://doi.org/10.1016/b978-0-408-11030-3.50006-6.

[5] W. Klement, R.H. Willens, P. Duwez, Non-crystalline structure in solidified Gold-Silicon alloys, Nature. 187 (1960) 869–870. https://doi.org/10.1038/187869b0.

[6] D. Raskin, C.H. Smith, Applications of amorphous metals: progress and prospects, in: Amorph. Met. Alloy., Butterworth-Heinemann, 1983: pp. 381–400. https://doi.org/10.1016/b978-0-408-11030-3.50025-x.

[7] T. Egami, Y. Waseda, Atomic size effect on the formability of metallic glasses, J. Non. Cryst. Solids. 64 (1984) 113–134. https://doi.org/10.1111/j.1442-2026.1994.tb00449.x.

[8] R.C. O'Handley, Fundamental magnetic properties, in: F.E. Luborsky (Ed.), Amorph. Met. Alloy., Butterworth-Heinemann, 1983: pp. 257–282. https://doi.org/10.1016/b978-

0-408-11030-3.50019-4.

[9] D.E. Polk, The structure of glassy metallic alloys, Acta Metall. 20 (1972) 485–491. https://doi.org/10.1016/0001-6160(72)90003-X.

[10] J. Kramer, Über nichtleitende Metallmodifikationen, Ann. Phys. 411 (1934) 37–64. https://doi.org/10.1002/andp.19344110104.

[11] A. Brenner, D.E. Couch, E.K. Williams, Electrodeposition of alloys of phosphorus with nickel or cobalt, J. Res. Natl. Bur. Stand. (1934). 44 (1950) 109. https://doi.org/10.6028/jres.044.009.

[12] S. Mader, A.S. Nowick, Metastable cosingle bond signau alloys: Example of an amorphous ferromagnet, Appl. Phys. Lett. 7 (1965) 57–59. https://doi.org/10.1063/1.1754298.

[13] C.C. Tsuei, P. Duwez, Metastable amorphous ferromagnetic phases in palladium-base alloys, J. Appl. Phys. 37 (1966) 435. https://doi.org/10.1063/1.1707858.

[14] P. Duwez, S.C.H. Lin, Amorphous ferromagnetic phase in iron-carbon-phosphorus alloys, J. Appl. Phys. 38 (1967) 4096–4097. https://doi.org/10.1063/1.1709084.

[15] R.C. O'Handley, Modern magnetic materials - principles and applications, Wiley, New York, 2000. https://doi.org/10.1109/mei.2005.1490004.

[16] N. Mattern, Structure formation in liquid and amorphous metallic alloys, J. Non. Cryst. Solids. 353 (2007) 1723–1731. https://doi.org/10.1016/j.jnoncrysol.2007.01.042.

[17] C. Suryanarayana, A. Inoue, Iron-based bulk metallic glasses, Int. Mater. Rev. 58 (2013) 131–166. https://doi.org/10.1179/1743280412Y.0000000007.

[18] K. Russew, L. Stojanova, Glassy Metals, Springer Berlin Heidelberg, 2016. https://doi.org/10.1007/978-3-662-47882-0.

[19] M. Miller, P. Liaw, Bulk metallic glasses: An overview, Springer US, 2008. https://doi.org/10.1007/978-0-387-48921-6.

[20] W. Kauzmann, The Nature of the Glassy State and the Behavior of Liquids at Low Temperatures, Chem. Rev. 43 (1948) 219–256. https://doi.org/10.1021/cr60135a002.

[21] C. Suryanarayana, A. Inoue, Iron-based bulk metallic glasses, Int. Mater. Rev. 58 (2013) 131–166. https://doi.org/10.1179/1743280412Y.0000000007.

[22] A. Inoue, Stabilization of supercooled liquid and opening-up of bulk glassy alloys, Proc. Japan Acad. Ser. B Phys. Biol. Sci. 73 (1997) 19–24. https://doi.org/10.2183/pjab.73.19.

[23] W.H. Wang, Roles of minor additions in formation and properties of bulk metallic glasses, Prog. Mater. Sci. 52 (2007) 540–596. https://doi.org/10.1016/j.pmatsci.2006.07.003.

[24] L. Xia, D. Ding, S.T. Shan, Y.D. Dong, The glass forming ability of Cu-rich Cu-Hf

binary alloys, J. Phys. Condens. Matter. 18 (2006) 3543–3548. https://doi.org/10.1088/0953-8984/18/15/002.

[25] A. Inoue, High Strength Bulk Amorphous Alloys with Low Critical Cooling Rates (Overview), Mater. Trans. JIM. 36 (1995) 866–875. https://doi.org/10.2320/matertrans1989.36.866.

[26] A. Inoue, A. Takeuchi, Recent development and application products of bulk glassy alloys, Acta Mater. 59 (2011) 2243–2267 https://doi.org/10.1016/j.actamat.2010.11.027.

[27] F.Q. Guo, S.J. Poon, G.J. Shiflet, CaAl-based bulk metallic glasses with high thermal stability, Appl. Phys. Lett. 84 (2004) 37–39. https://doi.org/10.1063/1.1637940.

[28] D. Xu, B. Lohwongwatana, G. Duan, W.L. Johnson, C. Garland, Bulk metallic glass formation in binary Cu-rich alloy series - Cu 100-xZrx (x=34 , 36, 38.2, 40 at.%) and mechanical properties of bulk Cu64Zr36 glass, Acta Mater. 52 (2004) 2621–2624. https://doi.org/10.1016/j.actamat.2004.02.009.

[29] L. Xia, W.H. Li, S.S. Fang, B.C. Wei, Y.D. Dong, Binary Ni-Nb bulk metallic glasses, J. Appl. Phys. 99 (2006) 26103. https://doi.org/10.1063/1.2158130.

[30] K.F. Yao, F. Ruan, Pd-Si binary bulk metallic glass prepared at low cooling rate, Chinese Phys. Lett. 22 (2005) 1481–1483. https://doi.org/10.1088/0256-307X/22/6/051.

[31] Z.Z. Yuan, S.L. Bao, Y. Lu, D.P. Zhang, L. Yao, A new criterion for evaluating the glass-forming ability of bulk glass forming alloys, J. Alloys Compd. 459 (2008) 251–260. https://doi.org/10.1016/j.jallcom.2007.05.037.

[32] Z.P. Lu, C.T. Liu, A new glass-forming ability criterion for bulk metallic glasses, Acta Mater. 50 (2002) 3501–3512. https://doi.org/10.1016/S1359-6454(02)00166-0.

[33] W.J. Botta, F.S. Pereira, C. Bolfarini, C.S. Kiminami, M.F. De Oliveira, Topological instability and electronegativity effects on the glass-forming ability of metallic alloys, Philos. Mag. Lett. 88 (2008) 785–791. https://doi.org/10.1080/09500830802375622.

[34] X.H. Du, J.C. Huang, C.T. Liu, Z.P. Lu, New criterion of glass forming ability for bulk metallic glasses, J. Appl. Phys. 101 (2007) 86108. https://doi.org/10.1063/1.2718286.

[35] Z. Long, H. Wei, Y. Ding, P. Zhang, G. Xie, A. Inoue, A new criterion for predicting the glass-forming ability of bulk metallic glasses, J. Alloys Compd. 475 (2009) 207–219. https://doi.org/10.1016/j.jallcom.2008.07.087.

[36] K. Mondal, B.S. Murty, On the parameters to assess the glass forming ability of liquids, J. Non. Cryst. Solids. 351 (2005) 1366–1371. https://doi.org/10.1016/j.jnoncrysol.2005.03.006.

[37] J.H. Kim, J.S. Park, H.K. Lim, W.T. Kim, D.H. Kim, Heating and cooling rate dependence of the parameters representing the glass forming ability in bulk metallic glasses, J. Non. Cryst. Solids. 351 (2005) 1433–1440.

https://doi.org/10.1016/j.jnoncrysol.2005.03.020.

[38] A. Hrubý, Evaluation of glass-forming tendency by means of DTA, Czechoslov. J. Phys. 22 (1972) 1187–1193. https://doi.org/10.1007/BF01690134.

[39] D.D.E. Brennhaugen, H. Mao, D. V. Louzguine-Luzgin, L. Arnberg, R.E. Aune, Predictive modeling of glass forming ability in the Fe-Nb-B system using the CALPHAD approach, J. Alloys Compd. 707 (2017) 120–125. https://doi.org/10.1016/j.jallcom.2016.12.049.

[40] S.M. Liang, R. Schmid-Fetzer, Evaluation of Calphad Approach and Empirical Rules on the Phase Stability of Multi-principal Element Alloys, J. Phase Equilibria Diffus. 38 (2017) 369–381. https://doi.org/10.1007/s11669-017-0577-0.

[41] M. Zhang, L.G. Hector, Y. Guo, M. Liu, L. Qi, First-principles search for alloying elements that increase corrosion resistance of Mg with second-phase particles of transition metal impurities, Comput. Mater. Sci. 165 (2019) 154–166. https://doi.org/10.1016/j.commatsci.2019.04.018.

[42] D. Kim, B.J. Lee, N.J. Kim, Prediction of composition dependency of glass forming ability of Mg-Cu-Y alloys by thermodynamic approach, Scr. Mater. 52 (2005) 969–972. https://doi.org/10.1016/j.scriptamat.2005.01.038.

[43] A. Tabeshian, H. Mao, L. Arnberg, R.E. Aune, Investigation of glass forming ability in the Zr-rich part of the Zr-Fe-Al ternary system, J. Appl. Phys. 125 (2019) 8–15. https://doi.org/10.1063/1.5066554.

[44] P. Gao, W. Tu, P. Li, L.M. Wang, Variation in entropies of fusion driven by mixing in binary glass forming eutectics, J. Alloys Compd. 736 (2018) 12–16. https://doi.org/10.1016/j.jallcom.2017.11.103.

[45] B.S. Rao, J. Bhatt, B.S. Murty, Identification of compositions with highest glass forming ability in multicomponent systems by thermodynamic and topological approaches, Mater. Sci. Eng. A. 448–451 (2007) 211–214. https://doi.org/10.1016/j.msea.2005.12.092.

[46] A. Takeuchi, A. Inoue, Calculations of mixing enthalpy and mismatch entropy for ternary amorphous alloys, Mater. Trans. JIM. 41 (2000) 1372–1378. https://doi.org/10.2320/matertrans1989.41.1372.

[47] J. Bhatt, W. Jiang, X. Junhai, W. Qing, C. Dong, B.S. Murty, Optimization of bulk metallic glass forming compositions in Zr-Cu-Al system by thermodynamic modeling, Intermetallics. 15 (2007) 716–721. https://doi.org/10.1016/j.intermet.2006.10.018.

[48] E. Babić, R. Ristić, I.A. Figueroa, D. Pajić, Skoko, K. Zadro, Electronic structure and glass forming ability in early and late transition metal alloys, Philos. Mag. 98 (2018) 693–709. https://doi.org/10.1080/14786435.2017.1415467.

[49] A. Masood, L. Belova, V. Ström, On the correlation between glass forming ability

(GFA) and soft magnetism of Ni-substituted Fe-based metallic glassy alloys, J. Magn. Magn. Mater. 504 (2020) 166667. https://doi.org/10.1016/j.jmmm.2020.166667.

[50] M. Miller, P. Liaw, Bulk metallic glasses: An overview, Springer US, US, 2008. https://doi.org/10.1007/978-0-387-48921-6.

[51] C. Suryanarayana, Nanocrystalline materials, Int. Mater. Rev. 40 (1995) 41–63. https://doi.org/10.1179/imr.1995.40.2.41.

[52] A. Inoue, D. V. Louzguine, Bulk nanocrystalline and nanocomposite alloys produced from amorphous phase, in: S.H.B.T.-N.M. and A. Whang (Ed.), Nanostructured Met. Alloy. Process. Microstruct. Mech. Prop. Appl., Woodhead Publishing, 2011: pp. 152–177. https://doi.org/10.1533/9780857091123.1.152.

[53] Y. Yoshizawa, S. Oguma, K. Yamauchi, New Fe-based soft magnetic alloys composed of ultrafine grain structure, J. Appl. Phys. 64 (1988) 6044–6046. https://doi.org/10.1063/1.342149.

[54] M.E. McHenry, M.A. Willard, D.E. Laughlin, Amorphous and nanocrystalline materials for applications as soft magnets, Prog. Mater. Sci. 44 (1999) 291–433. https://doi.org/10.1016/S0079-6425(99)00002-X.

[55] A.M. Leary, P.R. Ohodnicki, M.E. Mchenry, Soft magnetic materials in high-frequency, high-power conversion applications, Jom. 64 (2012) 772–781. https://doi.org/10.1007/s11837-012-0350-0.

[56] D.J. Perreault, J. Hu, J.M. Rivasy, Y. Han, O. Leitermann, R.C.N. Pilawa-Podgurski, A. Sagneri, C.R. Sullivan, Opportunities and challenges in Very High Frequency power conversion, in: Conf. Proc. - IEEE Appl. Power Electron. Conf. Expo. - APEC, 2009: pp. 1–14. https://doi.org/10.1109/APEC.2009.4802625.

[57] C.Ó. Mathúna, N. Wang, S. Kulkarni, S. Roy, Review of integrated magnetics for Power Supply on Chip (PwrSoC), IEEE Trans. Power Electron. 27 (2012) 4799–4816. https://doi.org/10.1109/TPEL.2012.2198891.

[58] V.R.V. Ramanan, Metallic glasses in distribution transformer applications: An update, J. Mater. Eng. 13 (1991) 119–127. https://doi.org/10.1007/BF02995816.

[59] S. Tsunashima, M. Jimbo, Y. Imada, K. Komiyama, Spin valves using amorphous magnetic layers, J. Magn. Magn. Mater. 165 (1997) 111–114. https://doi.org/10.1016/S0304-8853(96)00483-0.

[60] I. Škorvánek, J. Marcin, M. Capik, M. Varga, J. Kováč, I. Janotova, P. Švec, B. Idzikowski, Soft Magnetic Melt-Spun Ribbons for Energy and Sensor Applications, Acta Electrotech. Inform. 13 (2013) 45–48. https://doi.org/10.2478/aeei-2013-0009.

[61] I.G. Trindade, D.C. Leitão, Y. Pogorelov, J.B. Sousa, R.C. Chaves, S. Cardoso, P.P. Freitas, Control of hysteretic behavior in flux concentrators, Appl. Phys. Lett. 94 (2009) 73501. https://doi.org/10.1063/1.3081012.

[62] P. Murugaiyan, A. Mitra, A.K. Panda, A.S. Kumar, R.K. Roy, K. Manna, S.K. Srivastava, Electromagnetic interference shielding effectiveness of amorphous and nanocomposite soft magnetic ribbons, Phys. B Condens. Matter. 568 (2019) 13–17. https://doi.org/10.1016/j.physb.2019.05.017.

[63] G. Bertotti, F. Fiorillo, Magnetic Losses, Ref. Modul. Mater. Sci. Mater. Eng. (2016) 1–13. https://doi.org/10.1016/b978-0-12-803581-8.02799-5.

[64] G. Herzer, Modern soft magnets: Amorphous and nanocrystalline materials, Acta Mater. 61 (2013) 718–734. https://doi.org/10.1016/j.actamat.2012.10.040.

[65] S. Blundell, D. Thouless, Magnetism in Condensed Matter, OUP Oxford, 2003. https://doi.org/10.1119/1.1522704.

[66] W. Heisenberg, Zur Theorie des Ferromagnetismus, Zeitschrift Für Phys. 49 (1928) 619–636. https://doi.org/10.1007/BF01328601.

[67] J.M.D. Coey, Magnetism and magnetic materials, Cambridge University Press, Cambridge, 2010. https://doi.org/10.1017/CBO9780511845000.

[68] H. Kronmuller, S. Parkin, eds., Handbook of Magnetism and Advanced Magnetic Materials, Volume 1:, John Wiley & Sons, 2007. https://doi.org/10.1002/9780470022184.hmm404.

[69] R. Harris, M. Plischke, M.J. Zuckermann, New model for amorphous magnetism, Phys. Rev. Lett. 31 (1973) 160–162. https://doi.org/10.1103/PhysRevLett.31.160.

[70] Y. Matsuoka McClain, Handbook of Modern, 1981. https://doi.org/10.1007/978-1-4615-4917-8.

[71] Y. Han, G. Cheung, A. Li, C.R. Sullivan, D.J. Perreault, Evaluation of magnetic materials for very high frequency power applications, IEEE Trans. Power Electron. 27 (2012) 425–435. https://doi.org/10.1109/TPEL.2011.2159995.

[72] S. Kulkarni, D. Li, N. Wang, S. Roy, C.O. Mathuna, G. Young, P. McCloskey, Low Loss Magnetic Thin Films for Off-Line Power Conversion, IEEE Trans. Magn. 50 (2014) 1–4. https://doi.org/10.1109/TMAG.2013.2288791.

[73] C.R. Sullivan, D. Yao, G. Gamache, A. Latham, J. Qiu, (Invited) Passive Component Technologies for Advanced Power Conversion Enabled by Wide-Band-Gap Power Devices, ECS Trans. 41 (2019) 315–330. https://doi.org/10.1149/1.3631508.

[74] S. Flohrer, G. Herzer, Magnetization loss of nanocrystalline soft magnets, J. Phys. Conf. Ser. 144 (2009). https://doi.org/10.1088/1742-6596/144/1/012075.

[75] G. Bertotti, General Properties of Power Losses in Soft Ferromagnetic Materials., IEEE Trans. Magn. 24 (1987) 621–630. https://doi.org/10.1109/20.43994.

[76] H.J. Williams, W. Shockley, C. Kittel, Studies of the propagation velocity of a ferromagnetic domain boundary, Phys. Rev. 80 (1950) 1090–1094.

https://doi.org/10.1103/PhysRev.80.1090.

[77] R.H. Pry, C.P. Bean, Calculation of the energy loss in magnetic sheet materials using a domain model, J. Appl. Phys. 29 (1958) 532–533. https://doi.org/10.1063/1.1723212.

[78] J.E.L. Bishop, The influence of a random domain size distribution on the eddy-current contribution to hysteresis in transformer steel, J. Phys. D. Appl. Phys. 9 (1976) 1367–1377. https://doi.org/10.1088/0022-3727/9/9/013.

[79] E.A. Périgo, B. Weidenfeller, P. Kollár, J. Füzer, Past, present, and future of soft magnetic composites, Appl. Phys. Rev. 5 (2018). https://doi.org/10.1063/1.5027045.

[80] H. Zangl, M.J. Moser, T. Bretterklieber, A. Fuchs, et al. Holler, Hysteresis and Eddy-Current Losses of a Transformer Lamination Viewed As an Application of the Poynting Theorem, National Aeronautics and Space Administration, 2010.

[81] R. Cochrane, Resistivity of amorphous metallic alloys, J. Phys. Colloq. 39 (1978). https://doi.org/10.1051/jphyscol:19786597.

[82] Z. Jiang, J. Zhao, H. Xie, Scaling Laws, in: Z. Jiang, J. Zhao, H.B.T.-M.T. Xie (Eds.), Microforming Technol., Academic Press, 2017: pp. 53–71. https://doi.org/10.1016/b978-0-12-811212-0.00003-0.

[83] P. Tiberto, M. Baricco, E. Olivetti, R. Piccin, Magnetic properties of bulk metallic glasses, Adv. Eng. Mater. 9 (2007) 468–474. https://doi.org/10.1002/adem.200700050.

[84] T. Sourmail, Near equiatomic FeCo alloys: Constitution, mechanical and magnetic properties, Prog. Mater. Sci. 50 (2005) 816–880. https://doi.org/10.1016/j.pmatsci.2005.04.001.

[85] D. Chu, H. Lashgari, Y. Jiang, M. Ferry, K. Laws, S. Xie, H. Sun, S. Li, Recent progress in high Bs and low Hc Fe-based nanocrystalline alloys, Nanotechnol. Rev. 3 (2014) 153–159. https://doi.org/10.1515/ntrev-2013-0030.

[86] Y. Yoshizawa, K. Yamauchi, T. Yamane, H. Sugihara, Common mode choke cores using the new Fe-based alloys composed of ultrafine grain structure, J. Appl. Phys. 64 (1988) 6047–6049. https://doi.org/10.1063/1.342150.

[87] A. Makino, A. Inoue, T. Masumoto, Nanocrystalline soft magnetic fc-m-b (m = zr, hf, nb)"nanoperm," fc-m-o (m = zr, hf, rare earth)alloys and their applications, Mater. Res. Soc. Symp. - Proc. 577 (1999) 457–468. https://doi.org/10.1557/proc-577-457.

[88] H. Iwanabe, B. lu, M.E. Mchenry, D.E. Laughlin, Thermal stability of the nanocrystalline Fe–Co–Hf–B–Cu alloy, J. Appl. Phys. 85 (1999) 4424–4426. https://doi.org/10.1063/1.369805.

[89] G. Herzer, H.R. Hilzinger, Recent developments in soft magnetic materials, Phys. Scr. 1988 (1988) 22–28. https://doi.org/10.1088/0031-8949/1988/T24/003.

[90] R. Hasegawa, D. Azuma, Impacts of amorphous metal-based transformers on energy

efficiency and environment, J. Magn. Magn. Mater. 320 (2008) 2451–2456. https://doi.org/10.1016/j.jmmm.2008.04.052.

[91] T. Fukao, A. Chiba, M. Matsui, Test Results On A Super-Highspeed Amorphous-Iron Reluctance Motor, IEEE Trans. Ind. Appl. 25 (1989) 119–125. https://doi.org/10.1109/28.18881.

[92] J. Petzold, Applications of nanocrystalline softmagnetic materials for modern electronic devices, Scr. Mater. 48 (2003) 895–901. https://doi.org/10.1016/S1359-6462(02)00624-3.

[93] H. Ahmadian Baghbaderani, A. Masood, K.L. Alvarez, C.Ó. Mathúna, P. McCloskey, P. Stamenov, CALPHAD-assisted development of in-situ nanocrystallised melt-spun Co-Fe-B alloy with high B (1.57 T), J. Alloys Compd. 877 (2021) 160194. https://doi.org/10.1016/j.jallcom.2021.160194.

[94] A. Masood, H.A. Baghbaderani, V. Ström, P. Stamenov, P. McCloskey, C. Mathúna, S. Kulkarni, Fabrication and soft magnetic properties of rapidly quenched Co-Fe-B-Si-Nb ultra-thin amorphous ribbons, J. Magn. Magn. Mater. 483 (2019) 54–58. https://doi.org/10.1016/j.jmmm.2019.03.079.

[95] H. Ahmadian Baghbaderani, A. Masood, Z. Pavlovic, K. L. Alvarez, C. ÓMathúna, P. McCloskey, P. Stamenov, On the mechanisms limiting power loss in amorphous CoFeB-based melt-spun ribbons, J. Magn. Magn. Mater. 502 (2020) 166535. https://doi.org/10.1016/j.jmmm.2020.166535.

[96] H. Ahmadian Baghbaderani, A. Masood, Z. Pavlovic, N. Teichert, C. Ó. Mathúna, P. McCloskey, P. Stamenov, Improved magnetic performance of Cobalt-based ribbons by nanocrystallisation through magnetic annealing, J. Magn. Magn. Mater. 503 (2020) 166630. https://doi.org/10.1016/j.jmmm.2020.166630.

[97] A. Masood, H.A. Baghbaderani, K.L. Alvarez, J.M. Blanco, Z. Pavlovic, V. Ström, P. Stamenov, C.O. Mathuna, P. McCloskey, High-frequency power loss mechanisms in ultra-thin amorphous ribbons, J. Magn. Magn. Mater. 519 (2021) 167469. https://doi.org/10.1016/j.jmmm.2020.167469.

[98] K.L. Alvarez, H.A. Baghbaderani, J.M. Martín, N. Burgos, M. Ipatov, Z. Pavlovic, P. McCloskey, A. Masood, J. Gonzalez, Novel Fe-based amorphous and nanocrystalline powder cores for high-frequency power conversion, J. Magn. Magn. Mater. 501 (2020) 166457. https://doi.org/10.1016/j.jmmm.2020.166457.

[99] G. Herzer, The Random Anisotropy Model, Prop. Appl. Nanocrystalline Alloy. from Amorph. Precursors. 184 (2005) 15–34. https://doi.org/10.1007/1-4020-2965-9_2.

[100] G. Herzer, Magnetic materials for electronic article surveillance, J. Magn. Magn. Mater. 254–255 (2003) 598–602. https://doi.org/10.1016/S0304-8853(02)00930-7.

[101] G. Herzer, On the theoretical understanding of nanocrystalline soft magnetic materials, J. Mater. Eng. Perform. 2 (1993) 193–197. https://doi.org/10.1007/BF02660285.

Chapter 2 Composition engineering of ultra-soft-magnetic Co-based alloys

Abstract

In the present study, the liquidus temperature, mixing enthalpy, and atomic mismatch factor are used to predict and empirically evaluate the amorphisation capability of Co-Fe-B alloys fabricated by melt spinning. Based on this approach, five out of seven alloys have an amorphous structure, confirming the capability of the proposed model in predicting the alloy compositions with higher amorphisation ability in a ternary alloy system in the absence of any costly elements, such as Nb, Mo and Zr. X-ray diffraction, TEM and Mössbauer results show that the other two alloys exhibit different *in-situ* crystallisation behaviour. In one case, only the free-side crystallises, whereas the crystallisation occurs through the entire thickness of the ribbon in the other alloy. The lower amorphisation ability exhibited by these alloys in relation to the predictive parameters has been evaluated. Additionally, there is a strong correlation between amorphisation ability and crystallisation behaviour of alloys. Alloys, which crystallise through eutectic mode, are more likely to exhibit high amorphisation capability, whereas crystallisation via the primary mechanism can be the sign of lower amorphisation ability. The output of the alloy design process is five amorphous alloys compositions, among which one is magnetically ultra-soft, H_c = 2.9 A/m; a surface crystalline alloy, with 50% lower power loss, at high frequencies, compared to the best amorphous ribbons, due to the *in-situ* induced out-of-plane anisotropy of the crystalline phase on the surface; and a nanocrystalline sample with a very high saturation flux density, B_s = 1.57 T. The surface crystallisation can eliminate the need for inducing transverse anisotropy by magnetic annealing. Therefore, optimising the alloy composition through this method can be a universal strategy of composition design for the fabrication of alloys with excellent properties, to be utilised in both high-M_s and low-H_c applications.

Keywords: Alloy design, CALPHAD, Amorphisation capability, Nanostructured alloys, soft magnetic properties, Rapid quenching, Mössbauer studies

2.1 Introduction

Wide-bandgap (WBG) semiconductors permit devices to operate at much higher frequencies. This reduces the size requirements for passive components as a result of the decrease in the

required energy to be stored in power converters. However, current soft magnetic materials constrain the potential of WBG-based devices [1]. The pre-requisite for soft magnetic materials for use in these applications are high magnetisation, low coercivity and low power loss at high frequencies [2]. In this regard, due to the elimination of magnetocrystalline anisotropy, the coercivity is drastically reduced in amorphous Fe- and Co-based alloys. Thus, melt-spun ribbons are gaining adoption in high-frequency power electronic devices due to their low losses. Despite the higher initial cost of these alloys compared to silicon steel, these advanced alloys can diminish the total lifetime costs of power converters on account of their low losses. However, the saturation magnetisation (M_s) of this class of alloys is still lower than that of crystalline counterparts [3–5].

The main reason for the lower M_s of amorphous alloys is the presence of non-magnetic elements in their composition. These elements have been introduced in the compositions to stabilise the amorphous state and thus enhance the Amorphisation Capability (AMC). More importantly, AMC criteria are mostly either qualitative (e.g., Inoue's empirical rules [6]) or a posteriori (e.g., parameters based on glass transition temperature, T_g, and liquidus temperature, T_l), so one has to produce the amorphous alloy to obtain the necessary values of T_g and T_l. The optimisation of composition design using these benchmarks is quite time-consuming [3,7]. Therefore, it is preferable to choose calculable, quantifiable *a priori* parameters like enthalpy of mixing (ΔH_{mix}) [8,9], liquidus temperature (T_l) [10], and atomic size mismatch factor (λ) [11] to predict the AMC of alloys. This strategy can be exploited to keep the glass former contents as low as possible in order to retain the high M_s of the designed alloy, which is beneficial to drive device miniaturisation. Additionally, using a combination of these parameters can help us to engineer the AMC of Co- and Fe-based alloys leading to the manipulation of the microstructure of the alloys and achieve specific magnetic properties from their unique microstructure, which can be amorphous or partially crystalline.

In this regard, to optimise the power loss behaviour of the as-quenched ribbons, transverse anisotropy should be induced via magnetic annealing [12]. Apart from the brittle nature of as-annealed ribbons, which makes further processing and core fabrication difficult, the coercivity of the amorphous ribbons can be susceptible to processing conditions and adversely can increase upon annealing due to possible oxidation or crystallisation. It is possible, however, to

straightforwardly design an alloy composition with moderate AMC to fabricate partially crystallised ribbons, which can offer lower power loss [13]. Yet, instead of being a prejudicial factor, properly controlled *in-situ* crystallisation and resulting induced magnetic anisotropies can be a powerful tool for tuning the magnetic properties of melt-spun ribbons, according to the application requirements [4].

In this work, the relationship between the predictive AMC parameters, composition and the properties of Co-based alloys is systematically investigated. It is demonstrated that the amorphous-forming ability and, as a result, the microstructure of these alloys can be quantitatively estimated by implementing AMC parameters in the composition design procedure. Using this strategy has led to the development of three kinds of alloys comprising ultra-soft magnetic amorphous and *in-situ* surface crystallised alloys, in addition to a bulk *in-situ* crystallised alloy with high saturation magnetisation. Although surface and bulk crystallisation is reported in Fe-based alloys [14–19], there are no reports on such crystallisation in Co-based samples in which results in superior DC and AC magnetic properties. Besides, one must take into account that the alloys with excellent DC and AC magnetic properties are fabricated in the ternary Co-Fe-B system in the absence of any costly elements. Therefore, this study is beneficial for the understanding of the correlations between AMC parameters, the structure and properties of the designed alloys, such as the effect of surface and bulk *in-situ* crystallisation on their soft magnetic properties.

2.2 Experimental methods

The equilibrium phase diagram of Co-Fe-B is thermodynamically modelled using Pandat^{TM} software (version 2019). The cobalt-based thermodynamic software database is utilised to predict the liquidus temperature of seven Co-based alloys in the Co-Fe-B system (Table 1). More details about the principles of Calculation of Phase Diagram (CALPHAD) method can be found in Appendix A of this Chapter. The starting materials, including Co pieces 99.5% trace metals basis (TMB), Fe chips 99.98% (TMB), and boron crystalline pieces 99.7%, all sourced from Sigma Aldrich, are used to prepare the 5 g arc-melted ingots. During arc melting, the material is heated up by an electric arc created between a copper electrode and sharp

welding tip (2% thoriated red-tungsten) in high purity argon. The elements to be melted are contained within a water-cooled copper hearth. The ingots are flipped and re-melted eight times to ensure homogeneity and a uniform lustre. As a precaution, high purity titanium (in a separate hearth) is used for the absorption of oxygen.

Ribbons are subsequently fabricated by induction melting and melt-spinning the arc-melted ingots (in 1 g batch) in an argon atmosphere. The detailed explanation of melt spinning procedure can be found in Appendix B of this Chapter. An argon jet (at an overpressure of 0.7 bar) is used to eject the molten liquid contained in a fused silica vial. Typical experimental parameters and conditions applied are quartz vial of 60 mm length, 8 mm inner diameter and 0.5 mm diameter orifice, a nozzle to wheel angle of 10 degrees from the perpendicular, a nozzle to wheel separation of ~ 0.1 mm, wheel diameter of 90 mm and a wheel speed of 80 m/s. Using the as-mentioned conditions, ribbons of ~ 12-14 μm thickness and ~ 1 mm width are obtained. The thermal behaviour of the ribbons before any annealing treatment is evaluated by Differential Scanning Calorimetry (DSC) in TA Instrument DSC 2920. DSC experiments are performed on 20 mg of ribbons, at the heating rate of 10 K/min in the Ar atmosphere. Based on crystallisation temperatures observed in the DSC traces, the ribbons are thermally annealed at different temperatures with the heating rate of 10 K/min for 1 h to correlate the DSC peaks with the crystallised phases.

The X-ray powder diffraction (XRD) data of the melt-spun ribbons are collected using a Phillips PANalytical X'pert Pro diffractometer, with an operational wavelength of 1.5405 Å (Cu-Kα anode and a Ni filter). For transmission electron microscopy (TEM) analysis, each selected ribbon is first processed using a focused ion beam microscope (FEI Quanta 3D FEG). A protective metallic (Pt-based) layer is deposited on the surface before milling to create an ultrathin lamella, and two stair-step FIB trenches are cut at both sides of the area of interest. Next, the specimen is further thinned to less than 1 μm in thickness. The obtained lamellae are then removed using a micromanipulator and welded onto a Cu grid suitable for transmission electron microscopy (TEM) analysis. Final milling down to less than 100 nm is carried out by employing successively lower voltages down to 2 kV. TEM imaging of the ultrathin lamellae is performed using a JEOL JEM-2100F (S) TEM microscope operating at 200 kV with a LaB_6 filament. In addition, the coercivity and anisotropy field of the ribbons, along their length, is

measured using a B-H loop tracer (at a fixed f = 10 Hz) with a maximum magnetic field of 0.1 Tesla. Additionally, the magnetic hysteresis loops of the samples are studied by superconducting quantum interference device (SQUID-based) magnetometry (MPMS 5XL, Quantum Design, USA) at RT in fields of up to $\mu_0 H \leq 5$ T. Room temperature transmission Mössbauer spectra are collected using a conventional constant acceleration spectrometer with ^{57}Co source sealed in the Rh matrix. In this geometry, the γ-ray direction is perpendicular to the ribbon plane. The description and principle of the transmission Mössbauer can be seen in Appendix C of this Chapter.

2.3 Results and discussions

2.3.1 Alloy design

The critical cooling rate has been defined as the lowest possible cooling rate that the disordered atomic structure in metallic alloys can be retained. This is one of the primary methods to evaluate the AMC of rapidly quenched metallic systems. Additionally, several criteria have been established to evaluate this ability [6]. In this study, the following three predictive parameters are scrutinised to design the alloys with tuned AMC.

2.3.1.1 Liquidus temperature

The ratio of the glass transition temperature, T_g, to the liquidus temperature, T_l, also well-known as reduced glass transition temperature, T_{rg} (Equation 1), can be a good indicator of the AMC. The higher the value of T_{rg}, the higher is the viscosity of the melt, and therefore the alloy melt is more easily solidified into the amorphous state at a lower critical cooling rate. In other words, an alloy composition with a high value of T_g and a low value of T_l is more capable of amorphisation.

$$T_{rg} = \frac{T_g}{T_l} \tag{1}$$

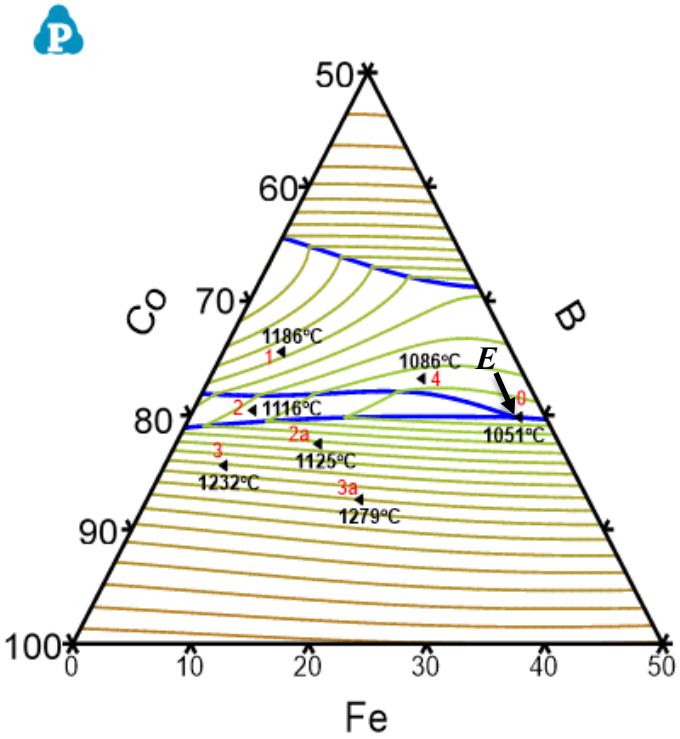

Figure 1. Liquidus surface projection of the Co-Fe-B phase diagram in the Co-rich zone calculated by CALPHAD. Parallel lines show isotherms with a difference of 25 ºC, decreasing toward the eutectic point (Alloy 0). Seven studied alloy compositions and their liquidus temperatures are labelled in the figure.

The dependance of T_g and T_l on alloy composition can be studied in more detail. It has been experimentally proven that the value of T_g changes slowly with solute content. On the other hand, T_l decreases with increasing solute content in most of the alloy systems. Particularly, phase diagrams of some alloy systems show that liquidus curves drop very steeply with solute content [20]. In this regard, an alloy with a eutectic temperature significantly lower than the melting points of the individual elements is referred to as a 'deep' eutectic point. In such cases, the T_{rg} value around the 'deep' eutectic composition is a strong function of the alloy composition and exhibits the highest value at the eutectic composition. Therefore, based on this parameter, the deep eutectic alloy should demonstrate high AMC. Based on these criteria, seven alloy compositions in the Co-Fe-B system have been judiciously chosen. Figure 1 illustrates the liquidus projection in the Co-Fe-B phase diagram in which the liquidus isotherms

are shown every 25 ºC decreasing towards the eutectic point. The alloys compositions are chosen to have different liquidus temperatures, ranging from the eutectic point (*E* point in Figure 1), at 1051 ºC in Alloy 0, to 1279 ºC in Alloy 3a.

2.3.1.2 Thermodynamics of mixing

It has been suggested that a significant negative heat of mixing, ΔH_{mix}, would lead to an increase in the energy barrier at the liquid-solid interface and a decrease in the atomic diffusivity, which in turn increases the melt viscosity. Thus, the more negative the ΔH_{mix}, the higher the AMC of an alloy [2,4]. This parameter is calculated based on the extended regular solution model as [8]:

$$\Delta H_{\mathrm{mix}} = \Omega_{\mathrm{CoFe}} c_{\mathrm{Co}} c_{\mathrm{Fe}} + \Omega_{\mathrm{CoB}} c_{\mathrm{Co}} c_{\mathrm{B}} + \Omega_{\mathrm{FeB}} c_{\mathrm{Fe}} c_{\mathrm{B}} \quad (2)$$

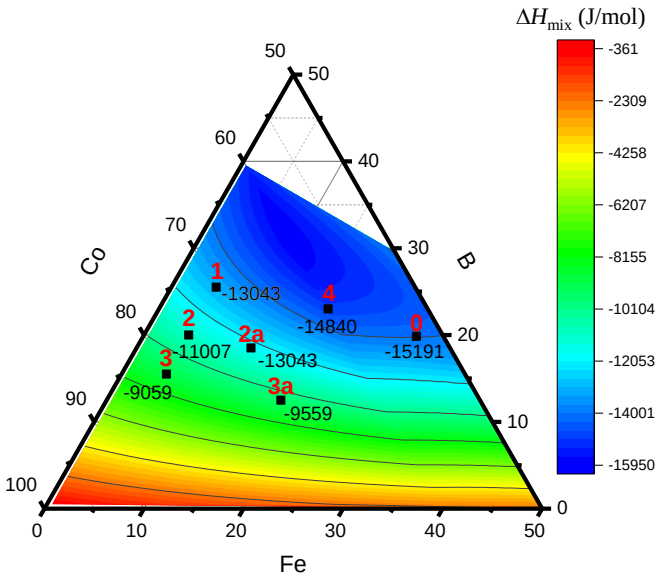

Figure 2. Colourmap of enthalpy of mixing (ΔH_{mix}) in the Co-rich zone in the Co-Fe-B system. The studied alloys and their enthalpy of mixing are illustrated in the ternary diagram.

where Ω_{ij} is the regular solution interaction parameter between *i* and *j* elements, which can be expressed by the mixing enthalpy of binary alloys ($\Omega_{\mathrm{ij}} = 4\Delta H_{\mathrm{mix}}^{ij}$), and c_i is the molar fraction of the *i* element [22]. A ternary diagram of enthalpy of mixing in the Co-Fe-B system is

presented in Figure 2. The labelled alloy compositions demonstrate different values of enthalpy of mixing, from -15,191 J/mol in Alloy 0 to -9,059 J/mol in Alloy 3.

2.3.1.3 Atomic mismatch factor

In addition to the above thermodynamic parameters, a topological criterion has also been taken into account to predict the amorphisation capability. Preliminarily, it has been proposed that the alloys in which constituent atoms have at least a 12% size difference show higher AMC. This is due to the fact that a critical lattice strain caused by the volumetric mismatch of the species is required to suppress crystallisation. This concept was developed by Sá Lisboa *et al.* [11] in 2005 through the atomic mismatch factor, λ, in multicomponent systems as [23]:

$$\lambda = \sum_{i=B}^{Z} c_i \left| \left(\frac{r_i}{r_A} \right)^3 - 1 \right| \quad (6)$$

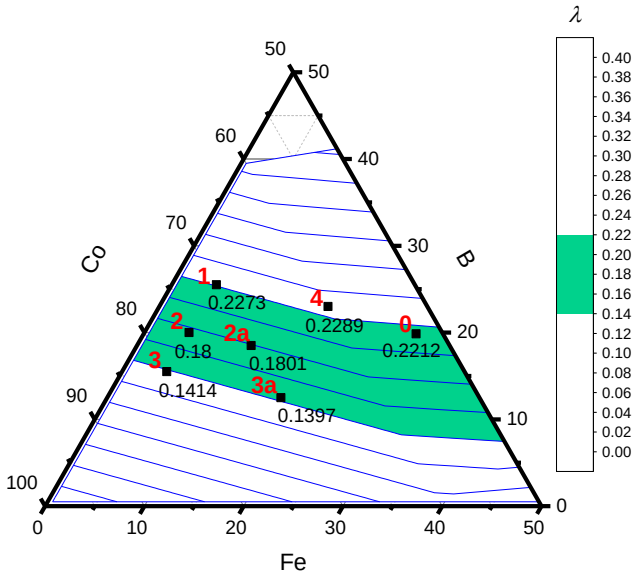

Figure 3. Variation of atomic mismatch factor (λ) in the Co-rich zone of the Co-Fe-B system. Compositions on the blue lines have the same λ. The green region represents the compositions with optimal amorphisation capability according to [25]. The studied alloys and their λ are illustrated in the ternary diagram.

where *i* denotes the different solutes *B* through *Z* in matrix *A*, c_i is the concentration of solute *i* in matrix *A* (mol.%), r_i is the solute atomic radius (nm), and r_A is the solvent atomic radius (nm).

Yan *et al.* [24] noted that optimal glass-forming ability happens at $\lambda = 0.18$ for several multicomponent alloys based on atomic packing efficiency. When assuming that an amorphous material is made up of numerous clusters of icosahedra, the packing efficiency of these is shown to be at its peak at $\lambda = 0.18$. It can also be inferred from [25] that several alloy systems suggest a reasonably high AMC when $\lambda = 0.18 \pm 0.04$. Thus, as can be seen in Figure 3, in which the λ-lines are superimposed in the Co-Fe-B phase diagram, to tune AMC to fabricate amorphous or nanocrystalline ribbons, the alloy compositions are chosen to have different values of λ, ranging from 0.1397 in Alloy 3a to 0.2289 in Alloy 4.

By combining information on the compositional regions with high and middle-range liquidus temperatures, enthalpy of mixing, and knowledge of the optimum atomic mismatch factor to form the amorphous microstructure, a predictive model can be proposed, which encompasses thermodynamic, kinetic and topological effects.

2.3.2 Structural and thermal characterisations

The designed alloys are fabricated via melt spinning. Figure 4 shows the X-ray diffraction patterns of the Co-Fe-B melt-spun ribbons. Five out of seven alloys exhibit a broad and diffuse peak indicative of their amorphous nature. This observation confirms the capability of the proposed model in predicting the alloy compositions with higher amorphisation ability. It should be mentioned that the XRD data is collected from both sides of the ribbons. Except Alloy 4, the XRD patterns of both sides of the ribbons in the other six alloys are similar.

There are crystalline peaks of Co_7Fe_3 and $(Co,Fe)_{23}B_6$ in the XRD pattern of the free side of Alloy 4, whereas no such peaks can be seen in the XRD pattern of the wheel side of the same alloy (Figure 4). In this regard, the TEM micrograph of a sample taken from the centre of Alloy 4 shows only a black and white contrast (Figure 5a). Even at this high resolution, one

does not see any evidence of crystallinity in the centre of the sample. The broad and diffuse halo in the diffraction pattern of the TEM image also confirms the amorphous nature of the bulk of this alloy. Therefore, the XRD crystalline peaks, observed only on the free side, and the absence of any crystals in the TEM image from the central part of Alloy 4 suggest that only the free-side surface is *in-situ* crystallised, whereas the bulk and wheel side are still in the amorphous state. This is because the free side experiences a lower cooling rate during the melt spinning procedure than the ribbon's bulk and wheel side.

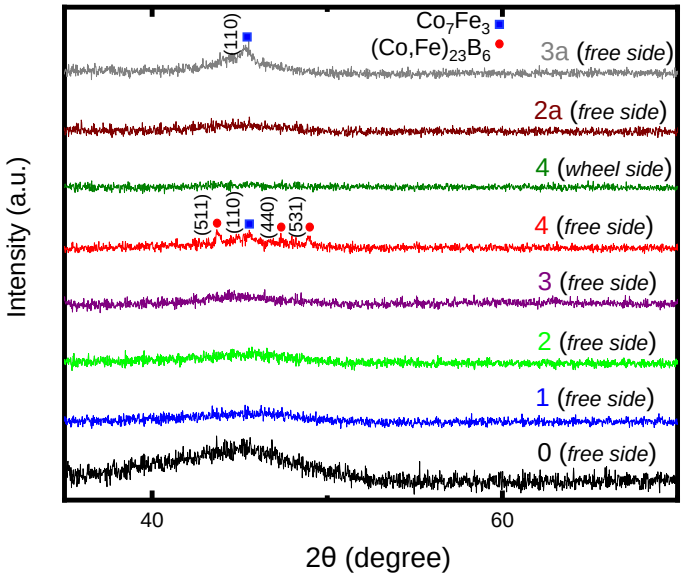

Figure 4. XRD patterns taken from the free side of ribbons with seven different compositions, and the wheel side of Alloy 4 ribbons.

In addition to the crystalline peaks on the free side of Alloy 4, a sharp Bragg peak at 45.27° <110> can be seen in the XRD pattern of Alloy 3a, which represents the Co_7Fe_3 phase. The crystallisation of this phase is investigated in more detail as follows. As can be seen in the TEM image of this sample (Figure 5b and Figure 5c), the morphology of the crystals is composed of heavily twinned polycrystals (Figure 5c). Due to ultra-rapid cooling of the molten alloy during melt spinning, Co_7Fe_3 crystals grow, with no long-range diffusion, into an isotropic medium. Therefore, their external shapes would be a function of only the crystallographic dependence

of the growth rate, resulting in such highly-faulted morphology [26]. Based on these pieces of evidence, it suggests that the Co_7Fe_3 crystallises in a polymorphous transformation which is one of the simplest crystallisation reactions. A more detailed investigation of Co_7Fe_3 *in-situ*

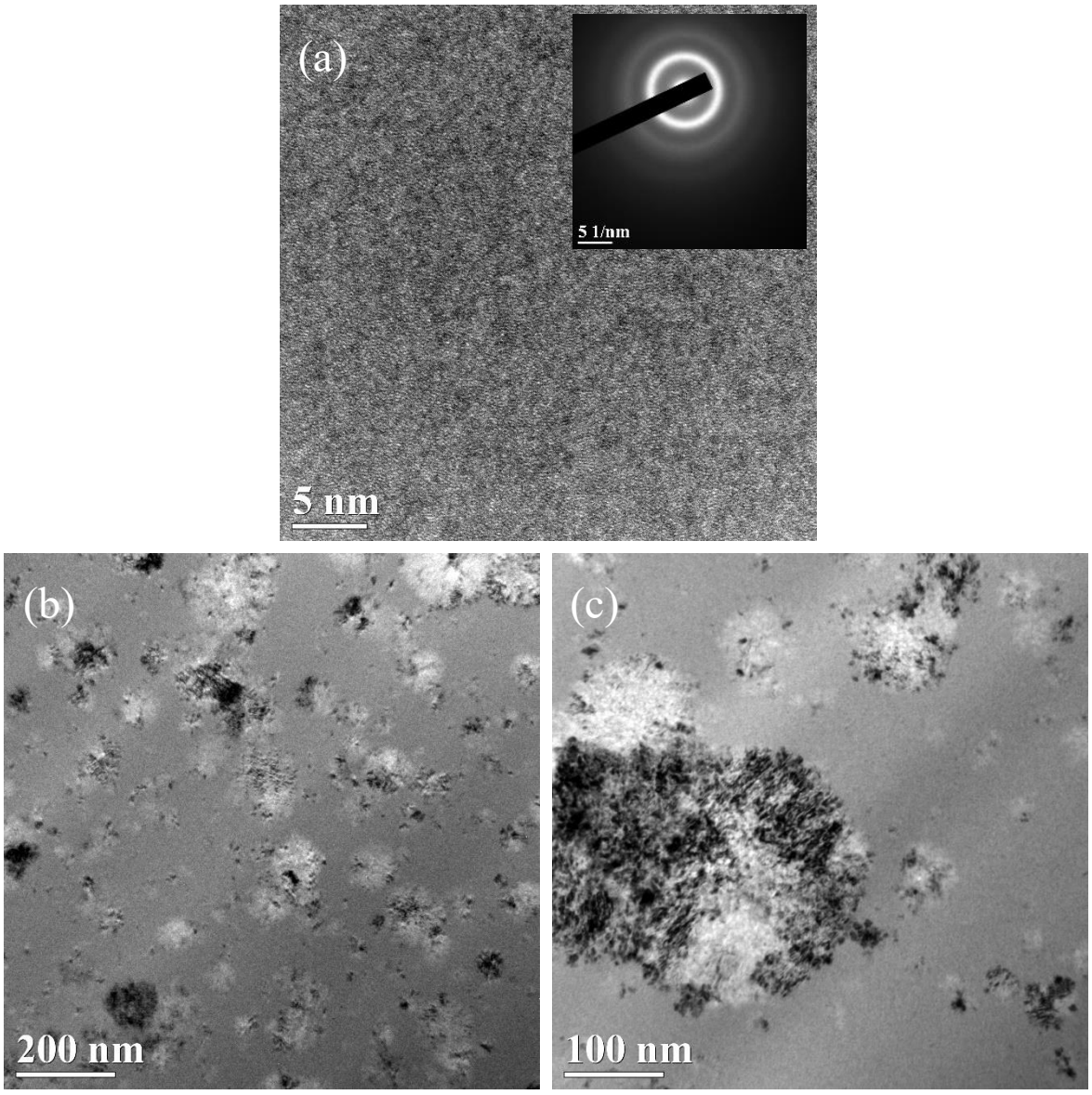

Figure 5. TEM micrographs of Alloy 4 including the SAED pattern (a), and Alloy 3a (b) and (c).

crystallisation and its effect on structural and magnetic properties of Alloy 3a can be found in our recently published article [9].

From structural analysis, it can be concluded that Alloys 3a and 4 exhibit lower AMC compared to the other five alloys. This observation can be evaluated based on the AMC criteria used to design the alloy compositions. It appears that the atomic mismatch factor of Alloy 4, which is a bit higher than the maximum value of the optimum λ (Figure 3), leads to lower AMC of this alloy and as a result, surface crystallisation occurs. In Alloy 3a, the main reasons for this can be its high T_l (Figure 1) and its enthalpy of mixing (Figure 2), which is the second highest in these seven alloy compositions.

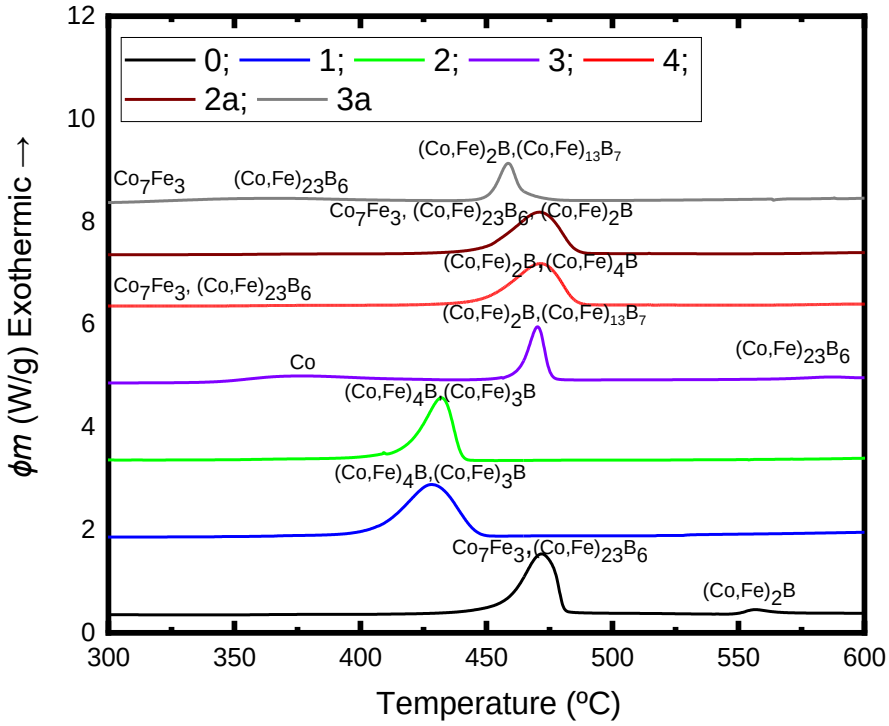

Figure 6. Differential scanning calorimetry (DSC) trace of seven Co-based melt-spun alloys. The crystallisation peaks are correlated to the phase formed after annealing the ribbons at the required temperature (Table 2).

2.3.3 Amorphisation capability and crystallisation behaviour

Additionally, one of the first experiments that can be performed to identify the AMC behaviour of different alloys involves characterising their crystallisation behaviour under dynamic heat

treatment conditions by monitoring their heat evolution and correlating it to detect transformations. The dynamic DSC traces at 10 K/min for seven alloys series are collated in Figure 6. The temperatures that characterise the crystallisation processes, including T_x and T_p as the onset and the peak temperature of crystallisation, for each of the alloys are also mentioned in Table 1. Alloys 0, 3, and 3a crystallise in multiple steps, whereas there is a single peak of crystallisation in the rest of the alloys.

Table 1. DSC results of the melt-spun ribbons. T_X: crystallisation temperature; T_P: crystallisation peak temperature; ΔH_C: total crystallisation enthalpy (accumulative area of exothermic crystallisation peaks).

Alloy	**Composition**	**First peak**		**Second peak**		**Third peak**		**ΔH_C (J/g)**
		T_{X1} (ºC)	**T_{P1} (ºC)**	**T_{X2} (ºC)**	**T_{P2} (ºC)**	**T_{X3} (ºC)**	**T_{P3} (ºC)**	
0	$Co_{52.69}Fe_{27.45}B_{19.85}$	456.85	471.82	549.52	556.63	---	---	127.31
1	$Co_{70}Fe_{4.5}B_{25.5}$	406.13	428.33	---	---	---	---	155.60
2	$Co_{75.5}Fe_{4.5}B_{20}$	417.23	432.06	---	---	---	---	121.50
3	$Co_{80}Fe_{4.5}B_{15.5}$	343.56	374.09	462.6	470.28	586.12	569.79	96.73
4	$Co_{60}Fe_{17}B_{23}$	449.13	471.48	---	---	---	---	112.90
2a	$Co_{70}Fe_{11.5}B_{18.5}$	440.44	450.82	---	---	---	---	105.40
3a	$Co_{70}Fe_{17.5}B_{12.5}$	302.97	362.03	451.02	485.61	---	---	80.21

Amorphisation ability can be looked at as an indication of the resistance of a liquid alloy to crystallisation during quenching in order to produce an amorphous solid. Thus, the amorphous structure always has the potential to transform to more stable states and ultimately to the equilibrium crystal structure(s), as can be seen in the DSC traces (Figure 6). Therefore, the resistance of the amorphous alloy to crystallisation can be correlated with its thermal stability [6]. However, just as AMC cannot be described entirely by a single parameter, neither can thermal stability. In addition, T_x is not an intrinsic property of an alloy, unlike the melting

point, since crystallisation is influenced by transformation kinetics. In addition, T_x does not have a constant value, as it is time and temperature dependent, i.e., given sufficient time, crystallisation will occur at any temperature. Therefore, it must be noted that T_x is useful only in determining the comparative ease of crystallisation of different alloy compositions under certain experimental conditions [27]. Thus, T_x will be used to evaluate the AMC of the alloys.

Furthermore, the specific nature of the reaction mechanisms that compete for the transformation and the associated temperature dependence of their nucleation and growth kinetics greatly influence the thermal stability and AMC of amorphous alloys. In this regard, the driving force for any transformation is the free energy difference between the initial and final states. The investigations into the crystallisation sequence of amorphous alloys suggested that the transformation proceeds through a series of progressively more stable phases until final equilibrium is reached, rather than directly to the equilibrium phases [27]. Therefore, based on the characteristic crystallisation peaks in the DSC traces, annealing experiments have been designed to target temperatures in the interval of phase transitions in order to trace the crystalline phases formed at different temperatures and correlate the phase transformation with AMC (Table 2 and Figure 6).

There is a strong correlation between AMC and the crystallisation behaviour of alloys. It seems that as a result of annealing, the alloys crystallise in primary and eutectic modes. The nature of the reaction depends on the composition of the alloy, the thermodynamic driving force for crystallisation, and the activation barrier for each reaction. In this regard, Alloys 3 and 3a, in which the first event of crystallisation is the primary one, show lower T_x compared to other alloys. As there is no competition between different phases to be crystallised, the primary formation of Co and $(Co,Fe)_{23}B_6$ crystals need less driving force compared to other eutectic reactions, resulting in the formation of tiny peaks with the lowest T_x at 343.6 and 303 °C in Alloys 3 and 3a respectively. In both alloys, the primary crystallisation events are followed by the eutectic crystallisation of $(Co,Fe)_2B$ and $(Co,Fe)_{13}B_7$ evidenced by intense peaks. On the other hand, Alloys 0, 1, 2 and 2a seems to be kinetically suited for amorphous phase formation as their crystallisation takes place through a eutectic mechanism, which is complex enough to hinder the rearrangement of atoms from the disordered configuration into strict lattice positions during rapid solidification [28].

Based on T_x, Alloy 0 shows the highest AMC, which can be evaluated based on both the predictive factors and the crystallisation behaviour of this alloy. In the former, Alloy 0, as the eutectic composition in Co-Fe-B system (Figure 1), offers the lowest T_l along with the most negative ΔH_{mix} (Figure 2) indicative of its high AMC. In addition, the eutectic crystallisation of this alloy leads to the formation of Co_7Fe_3 and $(Co,Fe)_{23}B_6$ phases (Table 2). Since the aforementioned crystalline phases compete for nucleation and growth, liquid crystallisation requires extensive rearrangement of different types of atoms, particularly to form the highly ordered Co_7Fe_3 phase [29,30]. Similarly, high AMC of Alloy 2a can be because the crystallisation of this alloy takes place through simultaneous eutectic nucleation of Co_7Fe_3, $(Co,Fe)_{23}B_6$, $(Co,Fe)_2B$ (Table 2). However, in the procedure of crystallisation of Alloy 3, there is no competition between different phases to crystallise, which leads to its lowest thermal stability (lowest T_x) and AMC in comparison with other amorphous alloys.

Regarding the crystallisation behaviour of partially *in-situ* crystallised alloys, Alloys 4 and 3a, it should be mentioned that similar to Alloys 0 and 2a, Co_7Fe_3 and $(Co,Fe)_{23}B_6$ crystallise simultaneously on the surface of Alloy 4 ribbons during ultra-rapid quenching and thus the crystallisation of these two phases can be considered eutectic. At higher temperatures in the DSC trace of this alloy, the diffusion path for the elements to form $(Co,Fe)_2B$ is long enough to enhance the required temperature for the next crystallisation event, T_x, to 449 °C. In Alloy 3a, there is 11.5% less B in the alloy composition compared to Alloy 4, which makes the *in-situ* crystallisation of $(Co,Fe)_{23}B_6$ more difficult, but this phase is the first phase to be crystalised at a relatively low T_x= 302.9 °C (Table 1 and Figure 6), which confirms the similar crystallisation behaviour of Co_7Fe_3 and $(Co,Fe)_{23}B_6$ phases. Additionally, the small enthalpy of crystallisation (ΔH_C) of Alloy 3a (Table 1) confirms that the substantial portion of the amorphous phase, about 33%, has already transformed to Co_7Fe_3 through *in-situ* crystallisation (observed in TEM and XRD of this sample in [9]). In addition, due to the presence of Co_7Fe_3 nanocrystals in the microstructure of this alloy, the nucleation mainly occurs heterogeneously on Co_7Fe_3 nanocrystals [7]. However, ΔH_C in Alloy 4 is comparable with amorphous alloys indicating that the crystallisation in this sample has been limited to its surface, which is also confirmed by XRD and TEM (Figures 4 and 5).

As previously mentioned, Co_7Fe_3, $(Co,Fe)_{23}B_6$ phases crystallise simultaneously in Alloys 1, 4 and 2a. Additionally, in Alloy 3a, which comprises Co_7Fe_3 nanocrystals, $(Co,Fe)_{23}B_6$ crystallises at 303 °C, which is the minimum crystallisation temperature among all of the alloys. All of these observations confirm the similar crystallisation behaviour of Co_7Fe_3 and $(Co,Fe)_{23}B_6$ phases. It has been established in two of our published articles [9,31] that according to classical nucleation theory [32], the activation thresholds for the formation of a critical nucleus of these two phases are lower than other possible equilibrium phases in this alloy system.

Table 2. Annealing temperatures of the melt-spun ribbons and the resulting crystalline phases.

Alloy	**Composition**	T_a (°C)	**Phases in annealed samples**
0	$Co_{52.69}Fe_{27.45}B_{19.85}$	500	Co_7Fe_3, $(Co,Fe)_{23}B_6$
		600	Co_7Fe_3, $(Co,Fe)_2B$
1	$Co_{70}Fe_{4.5}B_{25.5}$	500	$(Co,Fe)_4B$, $(Co,Fe)_3B$
2	$Co_{75.5}Fe_{4.5}B_{20}$	500	$(Co,Fe)_4B$, $(Co,Fe)_3B$
3	$Co_{80}Fe_{4.5}B_{15.5}$	425	Co
		500	Co, $(Co,Fe)_2B$, $(Co,Fe)_{13}B_7$
		600	Co, $(Co,Fe)_2B$, $(Co,Fe)_{13}B_7$, $(Co,Fe)_{23}B_6$
4	$Co_{60}Fe_{17}B_{23}$	25	Co_7Fe_3, $(Co,Fe)_{23}B_6$
		500	Co_7Fe_3, $(Co,Fe)_2B$, $(Co,Fe)_4B$
2a	$Co_{70}Fe_{11.5}B_{18.5}$	500	Co_7Fe_3, $(Co,Fe)_{23}B_6$, $(Co,Fe)_2B$
3a	$Co_{70}Fe_{17.5}B_{12.5}$	25	Co_7Fe_3
		425	Co_7Fe_3, $(Co,Fe)_{23}B_6$
		500	Co_7Fe_3, $(Co,Fe)_{23}B_6$, $(Co,Fe)_{13}B_7$, $(Co,Fe)_2B$

2.3.4 Mössbauer analysis

A further study with Mössbauer spectroscopy provides more detailed information about the local structure of amorphous and *in-situ* crystallised ribbons. Figure 7 presents the Mössbauer transmission spectra of amorphous and crystalline ribbons, along with the respective distribution of Hyperfine Magnetic Field (HMF), $P(B_{hf})$. The shape of the spectra for all samples is characteristic of a ferromagnetic arrangement with a typical form of the Zeeman spectrum, consisting of 6 asymmetric absorption lines. The lines are more broadened in the case of fully amorphous samples, Alloys 1 and 2. The hyperfine parameters change from nucleus to nucleus because of structural and chemical disorder in amorphous Alloys 1 and 2, and this distribution of different environments results in many spectral lines which overlap in an unresolved B_{hf}-broadened spectrum (Figure 7a and b) [33]. It can also be inferred from the HMF distribution of amorphous samples that the sample with a higher amount of cobalt, Alloy 2, shows a higher average B_{hf} compared to Alloy 1 (Table 3), which is the result of the presence of more cobalt atoms in the closest neighbourhood of iron atoms.

Table 3. Hyperfine interactions parameters of amorphous, crystalline and surface-crystalline melt-spun ribbons where B_{ave}, B_{min} and B_{max} are average, least and most probable hyperfine magnetic field inductions.

Alloy	Crystalline structure	B_{min} (T)	B_{max} (T)	B_{avr} (T)
1	Amorphous	15.5	34	24.76
2	Amorphous	15.5	36	26.04
4	Surface-crystalline	15.5	36	27.22
3a	Crystalline	14	36	28.09

Hyperfine Magnetic Field distribution of amorphous and nanocrystalline samples can be compared, as well. As can be seen, the peaks of $P(B_{hf})$ in amorphous samples, Alloys 1 and 2, are more toward the lower B_{hf}, compared to the peaks in nanocrystalline samples, Alloys 4 and 3a, in which the peaks are more towards the higher B_{hf}. This effect can be evaluated based on B_{avr} of the samples (Table 3). The relatively high B_{avr} in Alloy 3a is due to the strong hyperfine interactions between Co and Fe atoms in the ordered Co_7Fe_3 phase [34]. In Alloy 4, the

aforementioned interaction is less as the limited formation of Co_7Fe_3 is just observed on the surface (Figure 4). For more details, the reader is advised to refer to the recently published article of authors on the correlation between $P(B_{hf})$ - B_{hf} of Alloy 3a with the atomic neighbourhood of Fe atoms in Co_7Fe_3 [9]. However, it seems that lower B_{avr} in the amorphous alloys suggests that in the disordered amorphous structure of Alloys 1 and 2, iron atoms have B atoms in their closest neighbourhood, strongly lowering the internal magnetic field. In other words, this closer to a normal distribution of $P(B_{hf})$ - B_{hf} can also be attributed to the higher amorphisation capability of Alloys 1 and 2.

2.3.5 DC magnetic properties

The saturation flux density, B_s, and coercivity, H_c, of the ribbons measured along their axis are presented in Table 4. There is a general linear trend between the portion of the magnetic element and the value of B_s as an intrinsic property, so due to the dilution of the main magnetic components in Alloys 1 and 4, they exhibit lower B_s. However, Alloys 0 and 3a exhibit exceptionally high B_s in comparison to the other alloys. A larger percentage of Fe leads to this effect in Alloy 0. In addition, the ordered nature of Co_7Fe_3 grains in Alloy 3a results in its high B_s [34]. High B_s of Co_7Fe_3 can also be inferred from the high hyperfine magnetic field interactions of the Fe nuclei in the nanocrystals of Co_7Fe_3 [9]. In other words, the hyperfine interaction between Fe and Co atoms can represent the magnitude of the interactions between these atoms and the effective density of states. Therefore, the higher exchange interaction can lead to higher B_s of the alloys. Based on this, there is a direct relationship between the average hyperfine field (Table 3) and B_s of the alloys (Table 4). It should be mentioned that as there is a more variety of Fe atoms, with respect to their atomic neighbourhoods, in the fully amorphous alloys (Alloys 1 and 2) compared to the partially crystalline ones, the deeps in the Mössbauer spectra of such alloys are broader (Figure 7a and 7c) compared to their counterparts in the partially crystalline alloys (Figure 7e and 7g). This effect makes the fitting of the Mössbauer spectra of fully amorphous alloys more challenging, as can be noticed in the first and last deeps of the Mössbauer spectra in Figure 7a and 7c, resulting in possible experimental error in extracting the Hyperfine Magnetic Field distribution of these alloys.

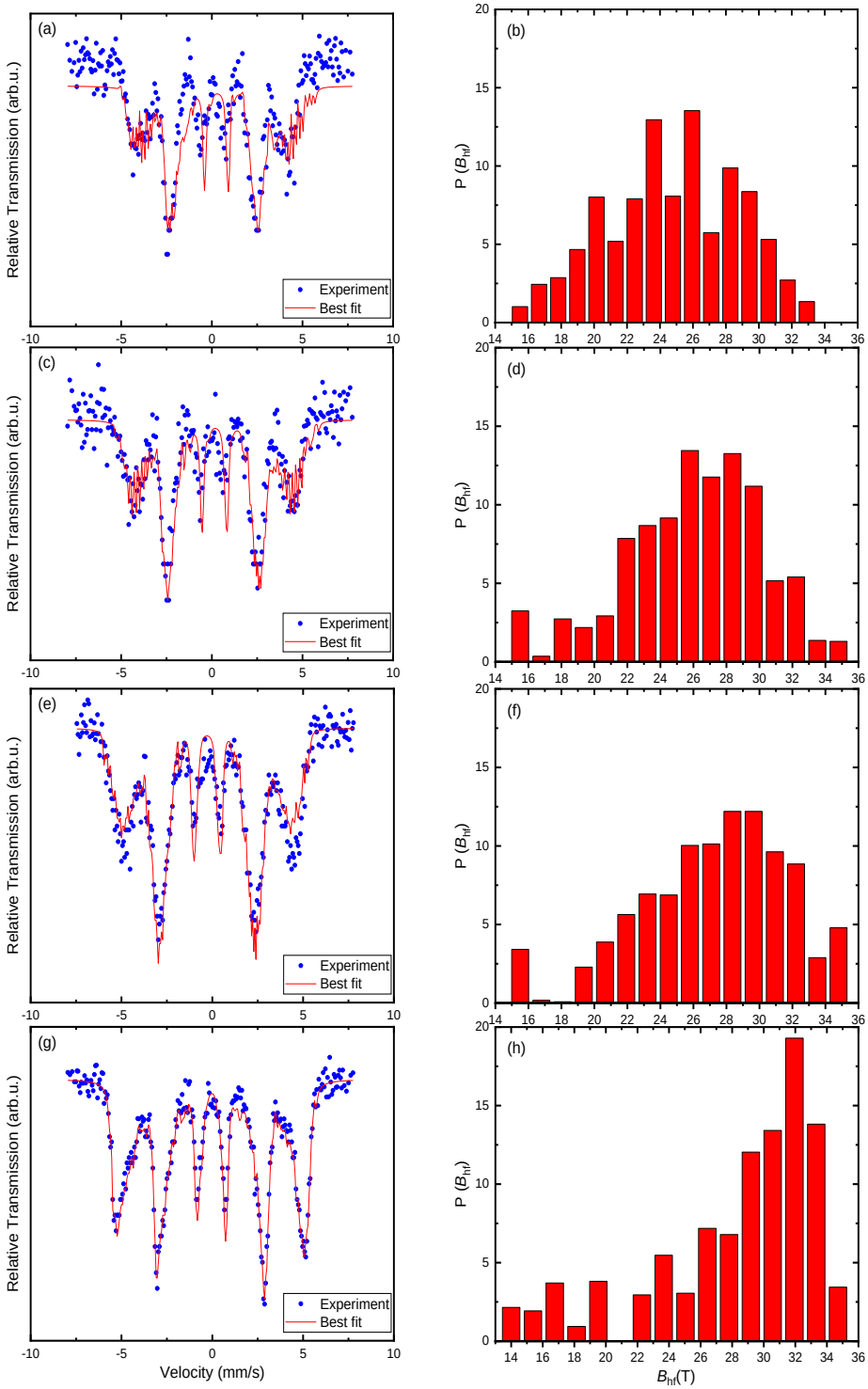

Figure 7. Room-temperature Mössbauer spectra of alloys 1 (a), 2 (c), 4 (e) and 3a (g), and hyperfine magnetic field distributions of alloys 1 (b), 2 (d), 4 (f) and 3a (h).

Table 4. DC magnetic properties of melt spun ribbons including saturation flux density, B_s and Coercivity, H_c.

Alloy	**Composition**	B_s **(T)**	H_c **(A/m)**
0	$Co_{52.69}Fe_{27.45}B_{19.85}$	1.44	30.2
1	$Co_{70}Fe_{4.5}B_{25.5}$	0.96	2.9
2	$Co_{75.5}Fe_{4.5}B_{20}$	1.21	13
3	$Co_{80}Fe_{4.5}B_{15.5}$	1.29	8.1
4	$Co_{60}Fe_{17}B_{23}$	1.19	19.7
2a	$Co_{70}Fe_{11.5}B_{18.5}$	1.29	13.7
3a	$Co_{70}Fe_{17.5}B_{12.5}$	1.57	381.5

In general, amorphous materials exhibit low coercivity, which is essentially due to the absence of bulk effective magnetocrystalline anisotropy. There is a direct relationship between H_c and the percentage of Fe in Alloys 0, 1, 2, 3 and 2a, with the amorphous structure (Table 4). Because the magnetocrystalline anisotropy of amorphous alloys is zero, most soft magnetic properties are controlled by stress and by the magnetostriction coefficient. Generally, in CoFe-based alloys, as the Co:Fe ratio is varied, the magnetostriction goes from negative (Co-rich) to positive (Fe-rich), and in a specific Co-rich composition, it becomes zero implying the lowest coercivity. Thus, by decreasing the percentage of Fe in the alloy composition, the coercivity diminishes, due to lower magnetostriction of the alloys. The ultra-low coercivity of Alloy 1, 2.9 A/m, is among the lowest reported in the ternary Co-Fe-B system.

In the case of partially crystalline samples, they exhibit different magnetic hysteresis behaviour as crystallisation takes place differently in these alloys. In the case of Alloy 4, crystallisation is limited to the surface of the melt-spun ribbon, and the main crystallised phase is $(Co,Fe)_{23}B_6$ with low magnetocrystalline anisotropy [31], whereas as a bulk phenomenon, crystallisation of the ordered Co_7Fe_3 phase with high anisotropy occurs in the whole volume of Alloy 3a resulting in its much higher coercivity, owing to the combination of the magnetocrystalline anisotropy of the nanocrystalline phase and its effect on the pinning domain walls, due to the large size of grains, compared to the ferromagnetic exchange correlation

length, and different magnetocrystalline anisotropy of this phase compared to the one for the amorphous matrix [9].

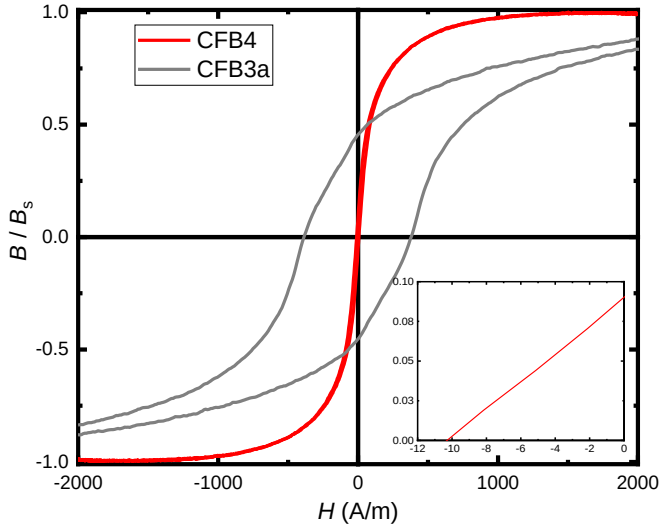

Figure 8. Hysteresis loops of surface crystallised, Alloy 4, and crystallised, Alloy 3a, melt-spun ribbons, measured along their length. The inset shows the linear shape of Alloy 4 loop close to the origin.

In order to analyse the magnetisation reversal mechanism, it is crucial to have a closer look at the hysteresis loops measured along the easy axis of the ribbons. For the thin crystalline surface layer in Alloy 4, the hysteresis loop is predominantly governed by magnetisation processes in the amorphous bulk system. As can be seen in the inset of Figure 8, magnetisation runs almost linearly from its remnant value B_r to zero, with an average slope minimally different from rotational bulk permeability. The magnetisation between $H = 0$ and $-H_c$ varies almost reversibly with the applied magnetic field. This indicates that the magnetisation reversal is closely correlated with rotational processes in the amorphous bulk in Alloy 4. For the bulk crystalline sample, Alloy 3a, the role of crystalline grains becomes more significant. Due to the random distribution of highly ordered grains of Co_7Fe_3 (Figure 5b) with high anisotropy in Alloy 3a, magnetisation now is reversed by domain wall displacements, in which the irreversible jumps of domains are needed, resulting in non-linear *B*-*H* behaviour of sample from $H = 0$ to $-H_c$ (Figure 8) [13].

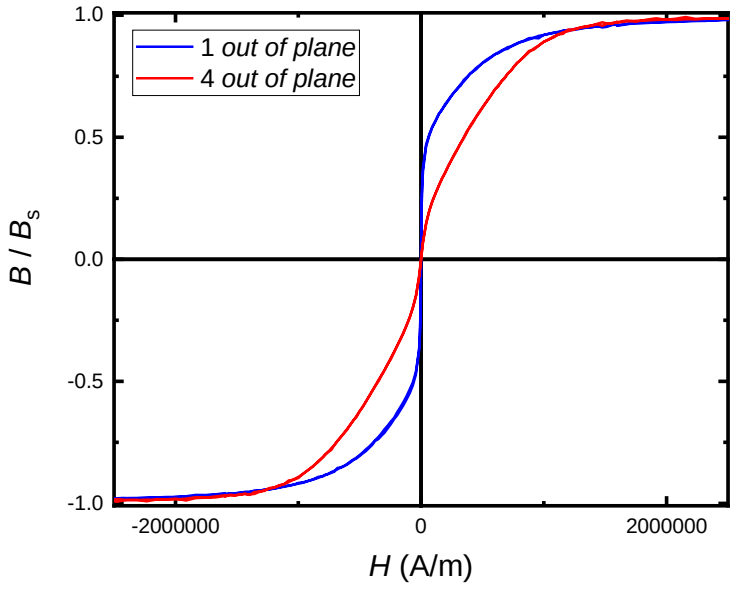

Figure 9. Hysteresis loops of amorphous, Alloy 1, and surface-crystallised, Alloy 4, melt-spun ribbons, measured along their thickness (out of plane).

Therefore, within the crystallised surface of Alloy 4, the domain walls are subject to strong pinning forces at the crystalline precipitates. Hence, surface magnetisation is hardly influenced in small magnetic fields *H*, whereas spontaneous magnetisation in the amorphous bulk can immediately follow *H* through rotation. Thus, the coercivity in Alloy 4 can be understood as the magnetic field required to rotate the bulk magnetisation in order to compensate for the remanent magnetisation of the crystalline surface layers. For the bulk crystalline sample, Alloy 3a, however, pinning forces are overcome before this compensation is completed, resulting in irreversible magnetisation jumps [13].

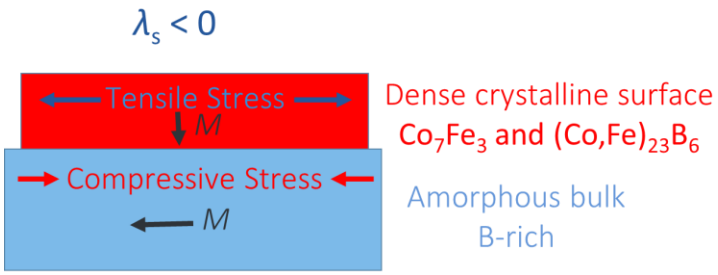

Figure 10. Schematic of types of stress and the direction of magnetisation (*M*) in Co-based surface crystalline ribbons with a negative magnetostriction (λ_s).

The magnetic properties of amorphous and surface crystalline samples can be compared accordingly. As can be seen in Figure 9, the out of plane hysteresis loop flattens noticeably with surface crystallisation on Alloy 4 compared to Alloy 1, which is the softest magnetic alloy. This clearly indicates the establishment of a magnetic anisotropy perpendicular to the ribbon axis. However, no magnetic field has been applied during the melt spinning. The origin of the perpendicular anisotropy is the compressive stress from the formation of higher-density crystalline surface layers. As illustrated in Figure 10, the compressive stress in the bulk amorphous region forces the magnetic moments to align along the ribbon plane through negative magnetostriction in Co-based alloys. On the other hand, the partially crystallised surface-layers are under tensile stress, which forces the magnetisation inside the layers to be perpendicular to the ribbon plane, thus leading to the out-of-plane anisotropy [13,35]. Due to the induced in-plane anisotropy, in total, Alloy 4 exhibits a low value of H_c.

2.3.6 AC magnetic properties

Figure 11 illustrates the power loss behaviour of samples as a function of magnetic induction at different frequencies, 100 kHz - 2 MHz. Total power loss density increases with AC magnetic induction (B_{AC}) and frequency. The low coercivity of Alloys 1 and 3 (Table 4), which stems from their amorphous structure, leads to their low hysteresis loss, which can be correlated with their lower power loss at 100 kHz compared to the partially crystalline alloys, Alloys 3a and 4. However, surface crystalline Alloy 4 offers the lowest power loss at higher frequencies, 500 kHz and 2 MHz. The reason for this observation is the difference in the contribution of three main mechanisms of power loss at different frequencies. In addition to hysteresis loss, eddy current and anomalous losses also contribute to total power loss [36]. It is known that the anomalous loss contributes mostly to the total power loss at higher frequencies [31,37–39]. Therefore, the induced out-of-plane anisotropy as a result of surface crystallisation in the crystallised layers and the possible pinning of the domains, in the amorphous portion, by the crystalline-amorphous interface, enhances the contribution of the magnetisation rotation mechanism in Alloy 4, which leads to a lower anomalous loss. It can be seen that controlling the crystallisation of the ribbons to take place just on the surface by tuning their amorphisation

ability can result in ultra-soft magnetic ribbons, with excellent performance at higher frequencies.

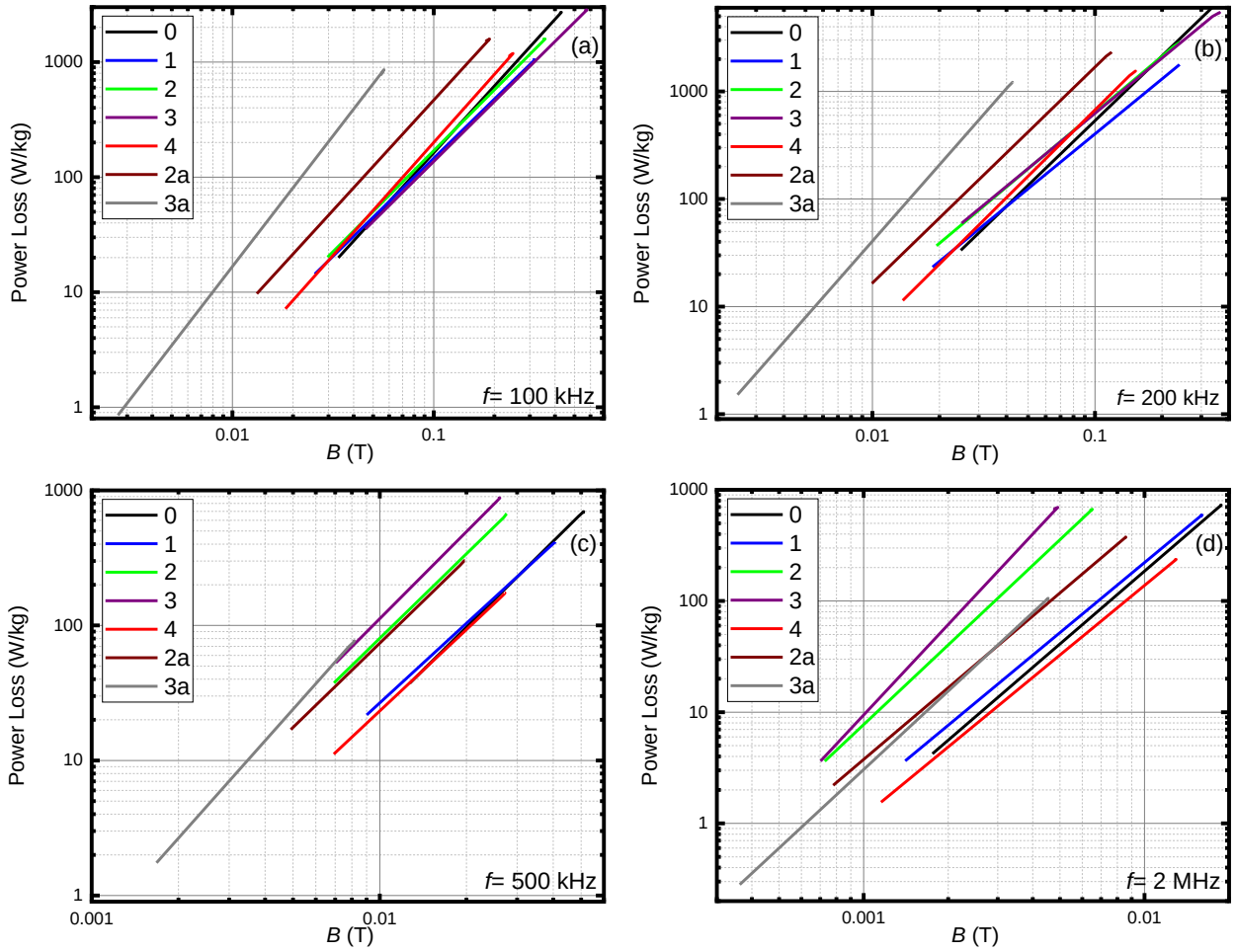

Figure 11. Power loss density of Co-based melt spun ribbons with different compositions as a function of the intensity of the applied magnetic induction at different frequencies; (a) 100 kHz, (b) 200 kHz, (c) 500 kHz, and (d) 2 MHz.

2.4 Conclusions

A thermodynamics-based approach, using the Calculation of Phase Diagram (CALPHAD), combined with the topological mismatch factor, is proposed and experimentally evaluated in order to tune the amorphisation ability of Co-based alloys. The model is highly adept at predicting the compositions of amorphous alloys (five out of seven) with a large percentage of magnetic content and the absence of any costly elements. The *in-situ* surface and bulk crystallinity of two alloys are characterised by XRD, TEM and Mössbauer spectroscopy. It appears that the high magnitude of the atomic mismatch factor is responsible for surface crystallisation in Alloy 4, whereas high liquidus temperature and mixing enthalpy results in bulk crystallisation in Alloy 3a. In addition, the crystallisation behaviour of these alloys is investigated. It is shown that the alloys with a eutectic mode of crystallisation exhibit higher amorphisation ability compared to the alloys which crystallise through the primary mechanism.

Regarding magnetic properties, the ultra-low coercivity of amorphous Alloy 1, 2.9 A/m, is among the lowest reported coercivities in the ternary Co-Fe-B system. Two alloys with different levels of crystallinity show excellent magnetic properties, as well. The induced out of plane anisotropy in the surface crystalline alloy enhances the contribution of the magnetisation rotation mechanism, which leads to lower anomalous losses. Transverse magnetic annealing has been used to decrease the contribution of this important part of power loss, specifically at high frequencies. Herein, 50% lower power loss of surface crystalline sample at 2 MHz, compared to the best amorphous alloy, is a result of *in-situ* surface crystallisation. In addition, the bulk crystalline sample exhibits very high saturation flux density, B_s = 1.57 T. Therefore, tunning the amorphousity level of rapidly quenched alloys using this methodology can result in the fabrication of soft magnets with optimised properties, which are excellent candidates for a wide range of applications, from low-loss high-frequency transformers to surge-arrestors.

Appendix A

Knowledge of phase equilibria or phase diagrams and thermodynamic properties is important in alloy design and materials-processing simulation. In principle, stable phase equilibrium is uniquely determined by the thermodynamic properties of the system, such as the Gibbs energy

functions of the phases. PANDAT, a computer software package for multicomponent phase diagram calculation, was developed under the guidance of this principle.

The thermodynamic equilibrium of a system at constant pressure is given by the minimum of the Gibbs energy, *G*. For multiphase equilibria this means that the sum of the molar Gibbs energies for the stable phases is at a minimum:

$$G = \sum_{\varphi} n^{\varphi} G_m^{\varphi} = minimum \quad (1)$$

where n^{φ} is the number of moles and G_m^{φ} is the molar Gibb energy of phase φ.

The Gibbs energy and other properties of phases can be described with the CALPHAD method as functions of temperature, pressure and composition. The formalism used for representing the composition dependence of the functions gives the CALPHAD method the ability to extrapolate the properties to higher-order systems after accurately defining the needed binary, ternary, and when necessary quaternary systems. This makes the CALPHAD method a powerful tool for alloy development and process design. A variety of experimental data and first principles results are used as inputs by the CALPHAD method to fit the Gibbs energy, diffusion mobility and other property functions of lower order system which are then combined into databases for multicomponent systems. The currently available thermodynamic databases are used in a wide range of applications to predict material properties and microstructure evolution. The development of auxiliary property databases will increase the range of applications.

Appendix B

Melt-spinning method consist of melting a small quantity of the alloy inside a crucible, and then ejecting the molten alloy by pressurization through a fine nozzle onto a fast-rotating copper wheel (Figure 1). Every one of these parameters can be carefully controlled to obtain the desired size, shape, and thickness of the ribbon. The crucible material is chosen based on its chemical compatibility with the melt, its temperature handling capability, its resistance to thermal shock, its low thermal conductivity, and its low porosity. Dense alumina and quartz

are the most common crucible materials used. In this study the quartz nozzle circular in cross section with diameter of 500 μm is used. The ejection pressures is 0.7 bar in this study. The required ejection pressure increases as the nozzle diameter decreases [6].

The primary purpose of the copper wheel is to extract the heat from the ribbon as quickly as possible, while allowing the puddle to wet the wheel and form the ribbon. Cooling of the wheel is desirable for long runs. The outer surface of the wheel is generally polished to remove any surface roughness since the wheel side of the cast ribbon is almost an exact replica of the wheel surface. The wheel speed is an important parameter in determining the thickness of the ribbon; the faster the wheel rotates, the thinner is the ribbon [6].

The melt-spinning operation is carried out in vacuum, air, or inert atmosphere, or reactive gas depending on the chemical and physical properties of the charge. Alloys susceptible to oxidation can be cast in vacuum or inert gas environment. The solidification rates achieved in this process are typically about 10^5–10^6 K s^{-1}. Because of the high solidification rates, it will be possible to produce most alloys of appropriate composition in the glassy state by this technique. But the downside is that the section thickness is limited. The width of the ribbons can, however, be increased using the planar flow casting method, in which the nozzle has a rectangular cross section and occasionally more than one nozzle is also used to ensure overlap of the melt puddle to increase the width of the ribbon. But, the thickness cannot be increased much by any of the known melt-spinning methods [6].

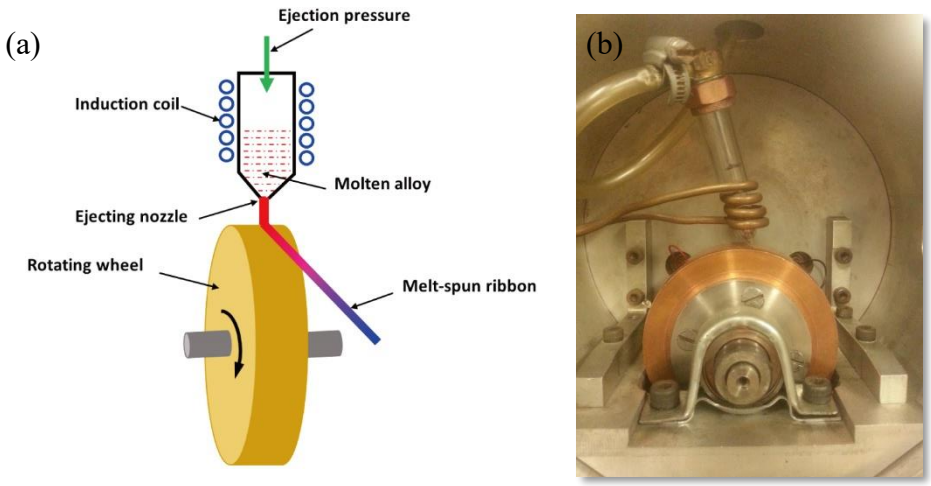

Figure 1. (a) A schematic of a melt spinner and (b) the melt spinner used in this thesis.

Appendix C

Mössbauer spectroscopy is based on resonant absorption of γ-radiation by atomic nuclei. The γ-photons originate from nuclear decay of a radioactive mother isotope. The decay cascade in the Mössbauer source passes through the excited nuclear state of the corresponding Mössbauer isotope. In the case of ^{57}Fe spectroscopy which has been performed in this thesis, the source isotope is ^{57}Co, which decays by so-called K-capture with a lifetime of 270 days. In these events, an electron from the K-shell reacts with a proton of the nucleus, yielding ^{57}Fe in a meta-stable excited state. The decay of this state yields a cascade of γ-transitions, the lowest of which has quantum energy E_0 = 14.4 keV.

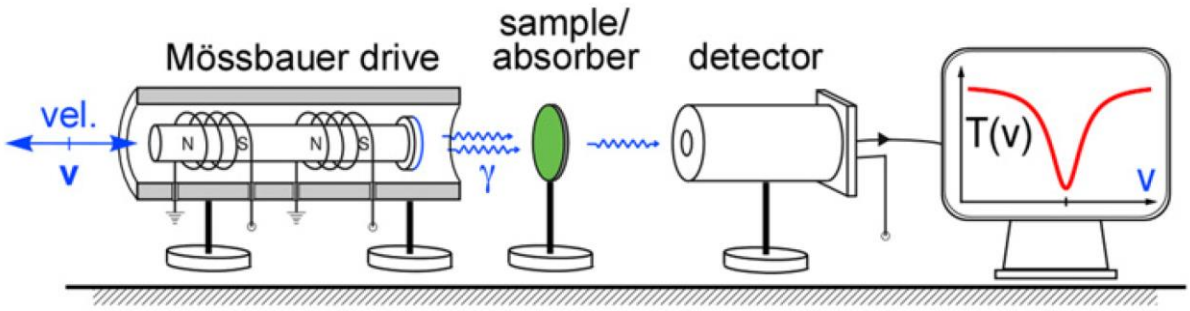

Figure 2. Transmission Mössbauer set-up .

In the transmission Mössbauer setup which is utilised in this thesis, γ-ray is coming from the Mössbauer source and passes through the absorber, which is the sample under investigation (Figure 2). The sample in this thesis consists of two layers of sets of melt spun ribbons which cover 1 × 2 cm^2 of a sticky tape. The source is mounted on the moving part of a Mössbauer drive system. For recording the spectrum, the number of γ-rays passing the absorber is counted with a γ-counter and detection system that is tuned to discriminate the 14.4 KeV Mössbauer photons from other radiation, which get electronically rejected from counting. During the measurement, the radioactive source is periodically moved with controlled Doppler velocities, +v towards and -v away from the absorber (Figure 2). The counting system is synchronised with the velocity control of the driving system such that the full velocity range ±v is divided into a number of discrete velocity increments, vi, for storing the detected data (so-called

channels). The numbers of counts, T(v), arriving at the detector and detected in each channel represent the Mössbauer spectrum.

In the case of paramagnetic Fe nucleus, the typical Mössbauer spectrum is composed of either a single line (cubic symmetry) or a quadrupole doublet whereas a Zeeman sextet corresponds to a magnetically ordered iron moment. When the sample contains different iron phases or different iron sites in each phase, the spectrum results from the superimposition of several subspectra, and their intensity depends upon the recoil-free fraction of nuclear decay events. Consequently, the relative amount of Fe in each site is taken proportional to the absorption area of the corresponding subspectrum [33].

The main relevant Mössbauer parameters are the following: isomer shift, quadrupolar splitting, hyperfine field, quadrupolar shift, linewidth at a half height of Lorentzian line, asymmetry parameter and in the case of monocrystalline samples, the angles which define the directions of γ-beam and of hyperfine field with respect to the electric field tensor axes. The isomer shift is sensitive to coordination number and valence state whereas the quadrupolar splitting is related to the spin-state and distortion geometry of iron site. The hyperfine field is proportional to the magnetic field experienced by nucleus and is close to be proportional to the magnetisation of the iron moment while the relative intensities of the sextet lines are related to the angle between the hyperfine field direction and the γ-ray direction. Finally, the width and the shape of Mössbauer lines may provide relevant information about the static disorder and/or the dynamics of either electronic or superparamagnetic relaxation. The analysis of Mössbauer spectra including the different fitting procedures are based on the use of usually discrete distributions, step functions, but also of analytical functions, binomial distribution, Window's and Fourier methods [33]. Based on as-mentioned effects and fittings, the probabilities of different values of hyperfine field (representing different neighbourhoods of Fe atoms) can be extracted from the Mössbauer spectrum.

Acknowledgement

The authors would like to thank Science Foundation of Ireland (SFI) for the financial support to perform the research work under the grant number of 2015/SIRG/3569, Starting Investigator Research Grant (SIRG).

2.5 References

[1] C.Ó. Mathúna, N. Wang, S. Kulkarni, S. Roy, Review of integrated magnetics for Power Supply on Chip (PwrSoC), IEEE Trans. Power Electron. 27 (2012) 4799–4816. https://doi.org/10.1109/TPEL.2012.2198891.

[2] P. Tiberto, M. Baricco, E. Olivetti, R. Piccin, Magnetic properties of bulk metallic glasses, Adv. Eng. Mater. 9 (2007) 468–474. https://doi.org/10.1002/adem.200700050.

[3] L. Shi, K. Yao, Composition design for Fe-based soft magnetic amorphous and nanocrystalline alloys with high Fe content, Mater. Des. 189 (2020) 108511. https://doi.org/10.1016/j.matdes.2020.108511.

[4] J.M. Silveyra, E. Ferrara, D.L. Huber, T.C. Monson, Soft magnetic materials for a sustainable and electrified world, Science. 362 (2018). https://doi.org/10.1126/science.aao0195.

[5] R.C. O'Handley, Modern magnetic materials - principles and applications, Wiley, New York, 2000. https://doi.org/10.1109/mei.2005.1490004.

[6] C. Suryanarayana, A. Inoue, Bulk metallic glasses: Second edition, CRC, New York, 2017. https://doi.org/10.1201/9781315153483.

[7] Q. Zheng, Y. Zhang, M. Montazerian, O. Gulbiten, J.C. Mauro, E.D. Zanotto, Y. Yue, Understanding Glass through Differential Scanning Calorimetry, Chem. Rev. 119 (2019) 7848–7939. https://doi.org/10.1021/acs.chemrev.8b00510.

[8] A. Takeuchi, A. Inoue, Calculations of mixing enthalpy and mismatch entropy for ternary amorphous alloys, Mater. Trans. JIM. 41 (2000) 1372–1378. https://doi.org/10.2320/matertrans1989.41.1372.

[9] H. Ahmadian Baghbaderani, A. Masood, K.L. Alvarez, C.Ó. Mathúna, P. McCloskey, P. Stamenov, CALPHAD-assisted development of in-situ nanocrystallised melt-spun Co-Fe-B alloy with high B (1.57 T), J. Alloys Compd. 877 (2021) 160194. https://doi.org/10.1016/j.jallcom.2021.160194.

[10] D.R. Gaskell, Introduction to the Thermodynamics of Materials (5th ed.), 5th ed., CRC Press, 2012. https://doi.org/https://doi.org/10.4324/9780203428498.

[11] R.D. Sá Lisboa, C. Bolfarini, W.J. Botta F., C.S. Kiminami, Topological instability as a criterion for design and selection of aluminum-based glass-former alloys, Appl. Phys. Lett. 86 (2005) 1–3. https://doi.org/10.1063/1.1931047.

[12] G. Herzer, Magnetic field-induced anisotropy in nanocrystalline Fe-Cu-Nb-Si-B alloys, J. Magn. Magn. Mater. 133 (1994) 248–250. https://doi.org/10.1016/0304-8853(94)90537-1.

[13] G. Herzer, H.R. Hilzinger, Surface crystallisation and magnetic properties in amorphous iron rich alloys, J. Magn. Magn. Mater. 62 (1986) 143–151.

https://doi.org/10.1016/0304-8853(86)90136-8.

[14] J.G. Wang, H. Zhao, C.X. Xie, C.T. Chang, S.M. Zhou, J.Q. Feng, J.T. Huo, W.H. Li, In-situ synthesis of nanocrystalline soft magnetic Fe-Ni-Si-B alloy, J. Alloys Compd. 790 (2019) 524–528. https://doi.org/10.1016/j.jallcom.2019.03.226.

[15] S. V. Thomas, M.A. Willard, A. Martone, M.J. Heben, V. Solomon, A. Welton, P. Boolchand, R.C. Ewing, C. Wang, S.L. Bud'ko, J. Song, D. Shi, Nanocrystallites via Direct Melt Spinning of Fe77Ni5.5Co5.5Zr7B4Cu for Enhanced Magnetic Softness, Phys. Status Solidi Appl. Mater. Sci. 217 (2020) 1–10. https://doi.org/10.1002/pssa.201900680.

[16] X.D. Fan, B.L. Shen, Crystallisation behavior and magnetic properties in High Fe content FeBCSiCu alloy system, J. Magn. Magn. Mater. 385 (2015) 277–281. https://doi.org/10.1016/j.jmmm.2015.03.033.

[17] F. Wan, T. Liu, F. Kong, A. Wang, M. Tian, J. Song, J. Zhang, C. Chang, X. Wang, Surface crystallisation and magnetic properties of FeCuSiBNbMo melt-spun nanocrystalline alloys, Mater. Res. Bull. 96 (2017) 275–280. https://doi.org/10.1016/j.materresbull.2017.01.026.

[18] E. Lopatina, I. Soldatov, V. Budinsky, M. Marsilius, L. Schultz, G. Herzer, R. Schäfer, Surface crystallisation and magnetic properties of Fe84.3Cu0.7Si4B8P3 soft magnetic ribbons, Acta Mater. 96 (2015) 10–17. https://doi.org/10.1016/j.actamat.2015.05.051.

[19] J. Zhang, F. Wan, Y. Li, J. Zheng, A. Wang, J. Song, M. Tian, A. He, C. Chang, Effect of surface crystallisation on magnetic properties of Fe82Cu1Si4B11.5Nb1.5 nanocrystalline alloy ribbons, J. Magn. Magn. Mater. 438 (2017) 126–131. https://doi.org/10.1016/j.jmmm.2017.04.086.

[20] (Asm Handbook) Asm-Alloy Phase Diagrams. Volume 3-ASM International (1992).pdf, (n.d.).

[21] J.W. Martin, Glasses and ceramics, in: J.W.B.T.-M. for E. (Third E. Martin (Ed.), Mater. Eng., Woodhead Publishing, 2006: pp. 133–158. https://doi.org/10.1533/9781845691608.2.133.

[22] J. Guo, X. Bian, X. Li, C. Zhang, Evaluation of liquid fragility for glass-forming alloys based on mixing enthalpy and mismatch entropy, Intermetallics. 18 (2010) 933–937. https://doi.org/10.1016/j.intermet.2010.01.004.

[23] D.D.E. Brennhaugen, H. Mao, D. V. Louzguine-Luzgin, L. Arnberg, R.E. Aune, Predictive modeling of glass forming ability in the Fe-Nb-B system using the CALPHAD approach, J. Alloys Compd. 707 (2017) 120–125. https://doi.org/10.1016/j.jallcom.2016.12.049.

[24] Z.J. Yan, J.F. Li, S.R. He, Y.H. Zhou, Evaluation of the optimum solute concentration for good glass forming ability in multicomponent metallic glasses, Mater. Res. Bull. 38 (2003) 681–689. https://doi.org/10.1016/S0025-5408(03)00010-2.

[25] T. Egami, Y. Waseda, Atomic size effect on the formability of metallic glasses, J. Non. Cryst. Solids. 64 (1984) 113–134. https://doi.org/10.1111/j.1442-2026.1994.tb00449.x.

[26] Butterworths Monographs in Materials, in: Amorph. Met. Alloy., Butterworth-Heinemann, 1983: p. ii. https://doi.org/10.1016/b978-0-408-11030-3.50001-7.

[27] M.A. Gibson, Crystallisation of metallic glasses, (1988).

[28] A. Tabeshian, H. Mao, L. Arnberg, R.E. Aune, Investigation of glass forming ability in the Zr-rich part of the Zr-Fe-Al ternary system, J. Appl. Phys. 125 (2019) 8–15. https://doi.org/10.1063/1.5066554.

[29] S. Amsarajan, B.R. Jagirdar, Air-stable magnetic cobalt-iron (Co7Fe3) bimetallic alloy nanostructures via co-digestive ripening of cobalt and iron colloids, J. Alloys Compd. 816 (2020) 152632. https://doi.org/10.1016/j.jallcom.2019.152632.

[30] M. Najafi, F. Hayati, A.A. Rafati, Effect of Current Frequency and Annealing on Magnetic Properties of [Co70Fe30]97Sn3 Nanowire Arrays, Int. Conf. Nanomater. Appl. Prop. 1 (2012) 04MFPN10-2. http://essuir.sumdu.edu.ua/retrieve/76719/princon_2012_1_4_27.pdf.

[31] H. Ahmadian Baghbaderani, A. Masood, Z. Pavlovic, N. Teichert, C. Ó. Mathúna, P. McCloskey, P. Stamenov, Improved magnetic performance of Cobalt-based ribbons by nanocrystallisation through magnetic annealing, J. Magn. Magn. Mater. 503 (2020) 166630. https://doi.org/10.1016/j.jmmm.2020.166630.

[32] D.A. Porter, K.E. Easterling, M.Y. Sherif, Phase transformations in metals and alloys, third edition, 2009.

[33] P. Mangin, G. Marchal, M. Piecuch, C. Janot, Mossbauer spectra analysis in amorphous system studies, J. Phys. B At. Mol. Phys. 9 (1976) 1101–1105. https://doi.org/10.1088/0022-3735/9/12/025.

[34] D.W. Clegg, R.A. Buckley, The disorder ⟶ order transformation in iron-cobalt-based alloys, Met. Sci. J. 7 (1973) 48–54. https://doi.org/10.1179/030634573790445541.

[35] Hang Nam Ok and A., Origin of the perpendicular anisotropy in amorphous Fes28t2Si& ribbons Hang, Phys. Rev. B. 23 (1981).

[36] S. Kulkarni, D. Li, N. Wang, S. Roy, C.O. Mathuna, G. Young, P. McCloskey, Low Loss Magnetic Thin Films for Off-Line Power Conversion, IEEE Trans. Magn. 50 (2014) 1–4. https://doi.org/10.1109/TMAG.2013.2288791.

[37] Z. Li, K. Yao, D. Li, X. Ni, Z. Lu, Core loss analysis of Finemet type nanocrystalline alloy ribbon with different thickness, Prog. Nat. Sci. Mater. Int. 27 (2017) 588–592. https://doi.org/10.1016/j.pnsc.2017.09.002.

[38] K.J. Overshott, The causes of the anomalous loss in amorphous ribbon materials, IEEE Trans. Magn. 17 (1981) 2698–2700. https://doi.org/10.1109/TMAG.1981.1061648.

[39] M.A. Willard, T. Francavilla, V.G. Harris, Core-loss analysis of an (Fe, Co, Ni)-based nanocrystalline soft magnetic alloy, J. Appl. Phys. 97 (2005) 84–87. https://doi.org/10.1063/1.1847333.

Chapter 3 CALPHAD-assisted development of in-situ nanocrystallised melt-spun Co-Fe-B alloy with high B_s (1.57 T)

Journal of Alloys and Compounds 877 (2021) 160194

Contents lists available at ScienceDirect

Journal of Alloys and Compounds

journal homepage: www.elsevier.com/locate/jalcom

CALPHAD-assisted development of *in-situ* nanocrystallised melt-spun Co-Fe-B alloy with high B_s (1.57 T)

Hasan Ahmadian Baghbaderani[a,b,*], Ansar Masood[a], Kenny L. Alvarez[c], Cian Ó Mathúna[a,d], Paul McCloskey[a], Plamen Stamenov[a,b]

[a] Microsystems Centre, Tyndall National Institute, University College Cork, Cork, Ireland
[b] School of Physics and CRANN, Trinity College, Dublin 2, Ireland
[c] CEIT-Basque Research and Technology Alliance (BRTA), Manuel Lardizabal 15, 20018 Donostia-San Sebastián, Spain
[d] School of Electrical and Electronic Engineering, University College Cork, Cork, Ireland

Abstract

A thermodynamics-based approach, Calculation of Phase Diagram (CALPHAD), combined with topological instability parameters are proposed and experimentally evaluated in order to optimise *in-situ* nanocrystallisation of rapidly quenched CoFeB alloys and exploit their remarkable B_s = 1.57 T. The high B_s of the alloy is attributed to the precipitation of the metastable Co_7Fe_3 nanocrystalline phase dispersed heterogeneously in the amorphous matrix. High B_s of Co_7Fe_3 phase can be inferred from the high hyperfine magnetic field of the Fe nuclei deduced from Mössbauer spectra. It is worth noting that the *in-situ* nanocrystallisation is a volume phenomenon, instead of surface crystallisation at the air-side of ribbons owing to lower cooling rates. We judge, based on nucleation theory, that the formation of the metastable phase is kinetically favoured, when compared to the equilibrium phases, hence promoting the high B_s, when compared with conventional Co-rich amorphous alloys. The local atomic order of nanocrystallised phase is confirmed by X-ray and electron diffraction techniques. Using Mössbauer spectroscopy and the extracted distribution of the hyperfine magnetic field, it is asserted that cobalt atoms form clusters, as they attract each other to form ordered structures, and boron atoms undergo only short-range ordering, likely due to covalent bond formation, governed by the size and electronegativity differences with the atoms in the amorphous matrix. We suggest the proposed CALPHAD-assisted design of nanostructured alloys, along with an *in-situ* nanocrystallisation, provides a practical scheme to develop novel functional alloys, with the best possible balance of coercivity and saturation, exclusively aimed for a high tech application.

Keywords: Alloy design, CALPHAD, Amorphisation capability, Nanostructured alloys, Nanocrystallisation, soft magnetic properties, Rapid quenching, Mössbauer studies.

3.1 Introduction

The design of multifunctional materials is always prompted by an ever-increasing demand for advanced systems functionality: such examples include miniaturised electronic devices, ultra-fast computational and communication capabilities, and ultra-high density data storage media. Sensors, actuators, and nano-micro-electromechanical systems (NEMS-MEMS) already

integrate multifunctional materials and smart structures [1,2]. In this context, state-of-the-art magnetic materials, ranging from ultra-soft (Fe- and Co-rich amorphous alloys) to semi-hard (FePt-based) to permanent magnets (NdFeB-type), play a vital role in designing smart and high-performance systems, including efficient power conversion [3–6], ultra-high density data storage media, and clean energy generation [7]. Amorphous magnetic alloys are well-known for their soft magnetic performance, high corrosion resistance, exceptional mechanical toughness and tensile strength, thanks to their unique disordered atomic structure to support this excellent combination of properties [8]. Particularly, CoFe-based alloys are of significant importance due to their broad range of industrial applications, including data storage (e.g., MRAM) and integrated power conversion (e.g., PwrSoc) concepts [9]. However, the random atomic distribution in CoFe amorphous alloys contributes to the lower M_s, which eventually reduces their functionality for high magnetic flux applications. It is envisaged that the formation of nanocrystalline ordered phase in CoFe alloys is beneficial to enhance the M_s. Particularly, chemically ordered Co_7Fe_3 with CsCl structure has remained a focus of extensive research due to its high M_s and good chemical stability [10,11]. However, bare CoFe bimetallic nanoparticles are highly pyrophoric in nature; exposing alloys to air results in the formation of the corresponding oxides. Thus, the ease of oxidation, their potential toxicity and intrinsically low relative density hinders their functionality and hence stimulate developing alternative routes to grow the nominal phase and to materialise the advantages of the high-flux density CoFe-based alloys [11].

One of the alternative routes to developing the nanocrystalline alloys is a post-annealing of rapidly quenched amorphous precursors at elevated temperatures. However, nanocrystallisation of amorphous alloys is a multi-step process and requires a special scheme (additives and cooling rate) to control the nucleation and grain growth process of a particular phase [12]. In a first step, high purity transition metals along with different glass formers are melt-spun to amorphous precursors. As a second step, heat treatment is performed in order to precipitate the nanocrystalline phases. However, the growth of a particular phase, with optimal performance is challenging. In addition, the heat treatment process (of nanocrystallisation) causes the embrittlement of the ribbons and, therefore, deteriorates the manufacturability in subsequent procedures [12]. An alternative approach is to synthesise nanostructured alloys

without post heat treatment is "*in-situ* nanocrystallisation" using rapid-quenching. However, this requires a careful design of alloy composition, with low or moderate amorphisation capability (AMC) to avoid both vitrification into a glassy state or precipitation into a fully crystalline state, during the rapid-quenching [13]. Further, the volumetric precipitation of the nanocrystalline phase is essential to promote, instead of surface crystallisation of the melt-spun ribbons, due to lower cooling rates at the air (gas-exposed)-side of the ribbons. To synthesise an optimised alloy, using the *in-situ* nanocrystallisation approach, the prediction of AMC by calculation of the phase diagram (CALPHAD), combined with the topological instability parameter (λ), based on configurational entropies, estimated by mismatch factors, is established as an essential tool. It is also well-proven in the optimisation of the glass forming ability of Fe- and Zr-based glassy alloys [14]. A number of glass-forming criteria, based on the different phase transition temperatures such as T_g (glass transition temperature), T_x (onset crystallisation temperature), T_l (onset liquidus temperature) and T_m (melting temperature), can be calculated and combined together with λ to predict the AMC of alloys. The room temperature amorphous phase is also thought to have the long-range disorder, which is mainly contributed by mismatch and configurational entropies, as estimated by mismatch factors [15]. Using a predictive modelling approach, one can design the alloys with moderate AMC, in order to fabricate nanocrystalline structures, when using rapid quenching, without post heat treatment. Thus, one can benefit from the high M_s of the bimetallic phase, in the form of Co_7Fe_3 nano-grains embedded in an amorphous matrix, formed *in-situ* with no consecutive thermal treatment.

In this work, thermodynamic parameters, predicted by the CALPHAD approach, and the topological instability criteria, λ, are considered to design the Co-Fe-B alloy with a moderate AMC and evaluate the formation of *in-situ* nanocrystalline structures of a CoFe-based alloy with high B_s using rapid-quenching. The very-high B_s (1.57 T) of the as-quenched alloy is clearly attributed to the formation of the Co_7Fe_3 nanostructured phase, which is dispersed heterogeneously in the amorphous matrix, throughout the volume of the melt-spun ribbons. The latter is subjected to detailed structural investigations, using XRD, TEM, and Mössbauer spectroscopy. Based on the compositional maps of the relevant parameters, a model is proposed

to enhance the probability of *in-situ* nanocrystallisation, by adjusting the different thermodynamic and topological parameters.

3.2 Experimental methods

The equilibrium phase diagram of Co-Fe-B is thermodynamically modelled using Pandat^{TM} software (version 2019). The cobalt-based thermodynamic database of the software is utilised to predict the enthalpy of mixing, the liquidus temperature and possible equilibrium and non-equilibrium phases at room temperature for $Co_{70}Fe_{17.5}B_{12.5}$ (atomic %) composition. To melt-spin the nominal alloy composition, first, the desired quantities (about 5 g per batch) of each element are weighed out using a standard microbalance to a precision of ~ 0.2 mg. The starting materials are Co pieces 99.5% trace metals basis (TMB), Fe chips 99.98% (TMB), and boron crystalline pieces 99.7%, all sourced from Sigma Aldrich. The alloy is prepared by arc melting in high purity argon. Heating up occurs from an electric arc, which is created between a copper electrode and a sharp welding tip (2% thoriated red-tungsten). The elements to be melted are contained within a water-cooled copper hearth. In general, the lower melting point elements are placed under those of higher melting point, except for boron, which is placed at the bottom of the hearth in an adjusted excess amount in order to retain stoichiometry. The ingots are flipped and re-melted eight times to ensure homogeneity and a uniform lustre. As a precaution, high purity titanium (in a separate hearth) is used as a getter for oxygen.

Ribbons are subsequently produced by induction melting and melt-spinning the arc-melted ingots (in 1 g batch) in an argon atmosphere. An argon jet (at an overpressure of 0.7 bar) is used to eject the molten liquid contained in a fused silica vial. Typical experimental parameters and conditions applied are quartz vial of 60 mm length, 8 mm inner diameter and 0.5 mm diameter orifice, a starting ingot mass of 1 gram, a nozzle to wheel angle of 10 degrees from the perpendicular, a nozzle to wheel separation of ~ 0.1 mm, wheel diameter of 90 mm and a wheel speed of 80 m/s. Using the as-mentioned conditions, ribbons of ~ 14 μm thickness and ~ 1 mm width are obtained.

The X-ray powder diffraction (XRD) data of the melt-spun ribbons are collected using a Phillips PANalytical X'pert Pro diffractometer, with an operational wavelength of 1.5405 Å

(Cu-Kα anode and a Ni filter). For transmission electron microscopy (TEM) analysis, each selected ribbon is first processed using a focused ion beam microscope (FEI Quanta 3D FEG). A protective metallic (Pt-based) layer is deposited on the surface before milling to create an ultrathin lamella, and two stair-step FIB trenches are cut at both sides of the area of interest. Next, the specimen is further thinned to less than 1 µm in thickness. Final milling down to less than 100 nm is carried out by employing successively lower voltages up to 2 kV. The obtained lamellae is removed using a micromanipulator and welded to a Cu grid suitable for transmission electron microscopy (TEM) analysis. TEM imaging of the ultrathin lamellae is performed using a JEOL JEM-2100F (S) TEM microscope operating at 200 kV with a LaB_6 filament. In addition, the coercivity and anisotropy field of the ribbons, along their length, is measured using a B-H loop tracer (at f = 10 Hz) with a maximum magnetic field of 0.1 Tesla. Additionally, the M_s of the sample is studied by superconducting quantum interference device (SQUID-based) magnetometry (MPMS 5XL, Quantum Design, USA) at RT in fields of up to $\mu_0 H \leq 2$ T. Room temperature transmission Mössbauer spectra are collected using a conventional constant acceleration spectrometer with ^{57}Co sealed in the Rh matrix source. In this geometry, the γ-ray direction is perpendicular to the ribbon plane. The electrical resistivity measurements were carried out at room temperature using a DC four-probe method with fixed distances (i.e., 1 mm) between the four probes. The potential drop is picked up on the 22 mm long specimen, with an equivalent resistance error of ± 0.001 Ω. All samples are measured at six different voltage levels, and the data is regressed upon in order to diminish the role of contact non-linearities and heating.

3.3 Results and discussions

3.3.1 CALPHAD-assisted alloy design

Several criteria have been established to evaluate the amorphisation capability of rapidly quenched metallic alloy systems [14], suggesting how the disordered atomic structure in metallic alloys can be preserved on vitrification with the lowest possible cooling rates (defined as critical cooling rate, a well-known measure of the AMC of the amorphous alloys) [14]. However, all parameters are empirical and based on trial-and-error. More recently, there has

been some interest in an alternative evaluation of the AMC criterion for the amorphous alloys, using the CALPHAD approach, augmented by the topological instability factor λ. This predictive model of amorphisation has worked well, in a couple of examples, hence suggesting a working alternative for the prediction of the glass forming ability of alloys [16,17]. Interestingly, this criterion can be useful, when there is an interest in the growth of metastable nanocrystalline structures using the rapid quenching process. The alloy composition can be tuned, in a particular region of the phase diagram, where λ is not favourable for high AMC, and hence, the chance of precipitation of the desired metastable phases would be increased, during vitrification. Keeping this in mind, the following thermodynamic parameters, along with λ, are scrutinised in a specific region of the phase diagram to regulate the moderate AMC and design an alloy, in which the metastable nanocrystalline phase precipitates during the melt spinning process.

3.3.1.1 Liquidus temperature (T_l)

When a liquid melt is cooled down from the liquid state to a temperature below the T_g, the viscosity of the melt increases to a high value, and consequently, glass is vitrified. The effective viscosity at T_g is known to be fixed at 10^{12} Pa.s, as initially suggested by Turnbull [18], which is originally based on the kinetics of crystal nucleation and the viscosity of the melts. It suggests that the ratio of T_g to the liquidus temperature, T_l, also well-known as reduced glass transition temperature, T_{rg}, can be a good indicator of the susceptibility to amorphisation of the alloys. The higher the value of T_{rg}, the higher is the viscosity, and therefore the alloy melt could easily be solidified into the amorphous state, at a lower critical cooling rate. In other words, an alloy composition with a high value of T_g and a low value of T_l is preferable to promote high amorphisation capability.

$$T_{rg} = \frac{T_g}{T_l} \tag{1}$$

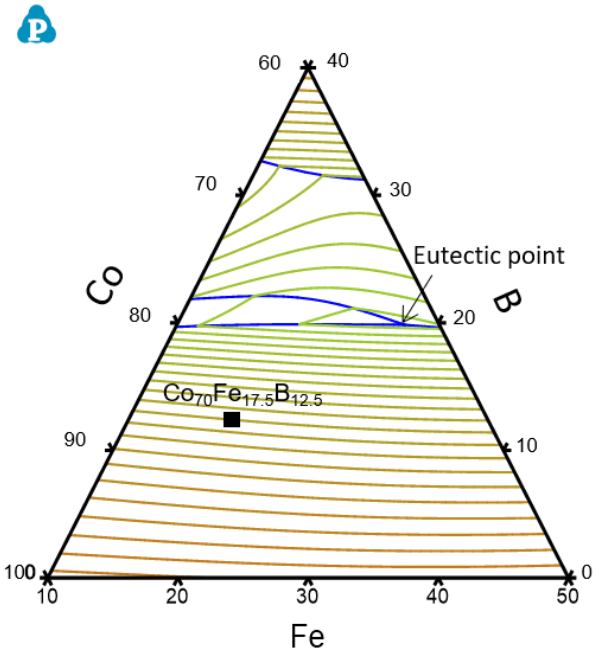

Figure 1. Liquidus surface projection of the Co-Fe-B phase diagram in the Co-rich zone calculated by CALPHAD. The red and green lines show isothermal lines with a difference of 25 ºC, decreasing toward the eutectic point.

Further, it has been experimentally proven that the value of T_g changes slowly with solute contents. On the other hand, T_l of an alloy usually decreases with increasing solute content in most of the alloy systems. Particularly, phase diagrams of some alloy systems show that liquidus curves drop very steeply with solute content [19]. Furthermore, an alloy with a eutectic temperature significantly lower than the melting points of the individual elements is referred to as a "deep" eutectic. In such cases, the T_{rg} value around the "deep" eutectic composition is a strong function of the alloy composition and exhibits its highest value at the eutectic composition. Therefore, it should be possible to quench this alloy composition easily into a glassy state.

On the other hand, if the liquidus temperature of an alloy also decreases slowly with the solute content, then the T_{rg} value at the eutectic composition may not be high. In such a situation, it will be challenging to produce such an alloy in a glassy state. Thus, the Turnbull criterion of high T_{rg} and deep eutectics converge at the deep eutectic compositions [14]. Fig. 1

illustrates the liquidus projection in the Co-Fe-B phase diagram, in which the liquidus isotherms are shown every 25 ºC decreasing towards the eutectic point. The composition is chosen to be in the region in which the liquidus temperature is approximately in the middle of the highest liquidus temperature, shown by brown and red coloured isotherms towards the horizontal axis, and the deep eutectic point at 1051 °C (Fig. 1). The main reason for choosing an alloy composition with middle-range T_l is to obtain a moderate AMC to *in-situ* nanocrystallise the alloy using melt-spinning.

3.3.1.2 Enthalpy of mixing

According to Inoue's empirical rule [20], the enthalpy of mixing, ΔH_{mix}, significantly favours the formation of an amorphous structure and is a good measure of the AMC. It has been suggested that a significant negative heat of mixing would lead to an increase in the energy barrier at the liquid-solid interface, and a decrease in the atomic diffusivity through the growth interface. The large mixing enthalpy would be expected to lower the effective mobilities of even the lightest species (i.e., boron) in the melt, which following Einstein's relation, would, in turn, increase the effective melt viscosity. Thus, the more negative the ΔH_{mix}, the higher the AMC of an alloy [2,4].

The chemical mixing enthalpy is calculated according to Equation (2) based on the extended regular solution model [22]:

$$\Delta H_{\mathrm{mix}} = \Omega_{\mathrm{CoFe}} c_{\mathrm{Co}} c_{\mathrm{Fe}} + \Omega_{\mathrm{CoB}} c_{\mathrm{Co}} c_{\mathrm{B}} + \Omega_{\mathrm{FeB}} c_{\mathrm{Fe}} c_{\mathrm{B}} \quad (2)$$

where Ω_{ij} is the regular solution interaction parameter between i and j elements, which can be expressed by the mixing enthalpy of binary alloys ($\Omega_{\mathrm{ij}} = 4\Delta H_{\mathrm{mix}}^{\mathrm{ij}}$), and c_{i} is the molar fraction of the i element [23]. Ternary diagram of enthalpy of mixing in the Co-Fe-B system is presented in Fig. 2. The labelled alloy composition is chosen to display an enthalpy of mixing, -9.56 kJ/mol, which is the region where this parameter is neither highly negative, towards the boron-rich alloys, nor extremely positive towards the Fe-rich alloy compositions. The moderate ΔH_{mix} could result in a moderate AMC, which can lead to the *in-situ* fabrication of nanocrystallised alloy.

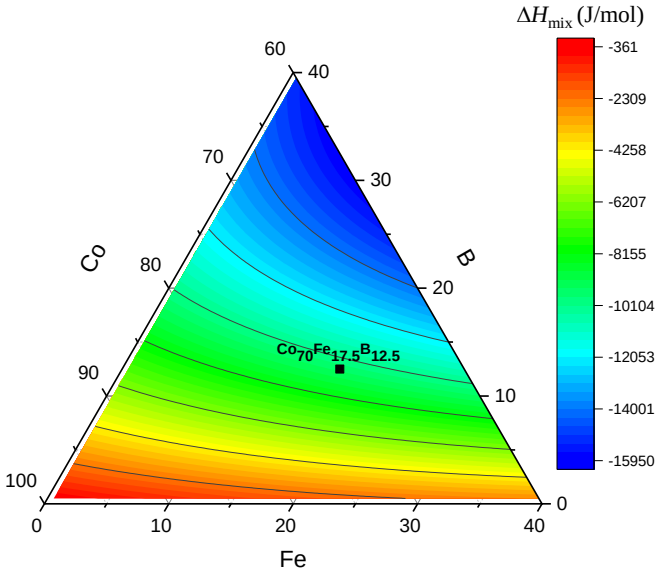

Figure 2. Colourmap of enthalpy of mixing in the Co-rich corner in the Co-Fe-B system.

3.3.1.3 Atomic mismatch factor

In addition to thermodynamic parameters, a topological parameter has also been used to predict the amorphisation capability of a metallic system. This effect has long been accounted for the empirical requirement for constituent atoms with at least a 12% size difference [14]. A more continuous approach to the question of topology has been linked to a critical lattice strain, caused by the volumetric mismatch of the species, required to suppress crystallisation. This concept was developed by Sá Lisboa *et al.* [24] through the atomic mismatch factor, λ in multicomponent systems [16],

$$\lambda = \sum_{\mathrm{i}=B}^{Z} c_{\mathrm{i}} \left| \left(\frac{r_{\mathrm{i}}}{r_{\mathrm{A}}} \right)^3 - 1 \right| \tag{3}$$

where i denotes the different solutes *B* to *Z* in matrix *A*, c_{i} is the concentration of solute i in matrix *A* (mol.%), r_{i} is the solute atomic radius (nm), and r_{A} is the solvent atomic radius (nm).

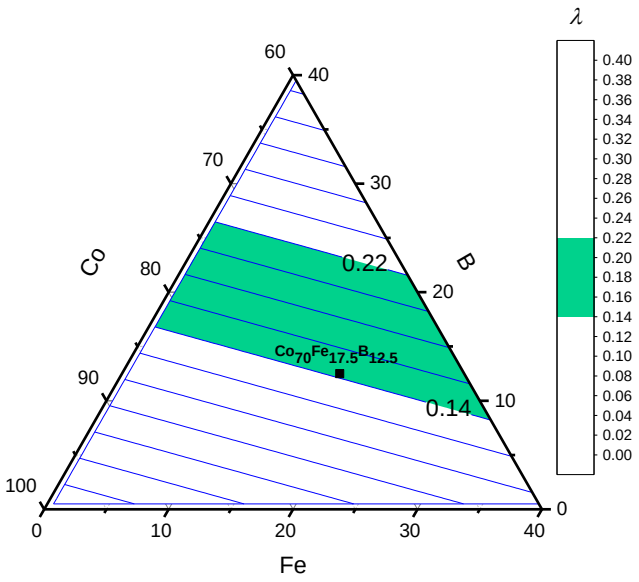

Figure 3. Variation of atomic mismatch factor in the Co-rich corner of the Co-Fe-B system. Compositions on the blue lines have the same λ. The green region represents the compositions with optimal glass-forming ability.

Yan *et al.* [25] noted that optimal glass-forming happens at $\lambda = 0.18$ for several investigated multicomponent systems. When assuming that an amorphous material is made up of numerous clusters of icosahedra, the packing efficiency of these peaks at $\lambda = 0.18$. It can also be inferred from [26] that $\lambda = 0.18 \pm 0.04$ can be considered as a region with a reasonably high AMC in several distinct alloy systems. Thus, the alloy composition is chosen on the boundary of the region with optimum λ to show moderate AMC, as shown in Fig. 3, where the λ-lines are superimposed in the Co-Fe-B phase diagram, to *in-situ* nanocrystalline the alloy during quenching. In other words, based on the λ parameter, the AMC of the alloy is lower as compared to the alloys inside the green region, but considerably higher when compared to the alloys outside the green region. This moderate (tuned) AMC can lead to *in-situ*-nanocrystallisation of the alloy during melt spinning.

Thus, the proposed predictive model of *in-situ* nanocrystallisation encompasses both the thermodynamic and topological aspects of the alloy system, and amalgamates the information on the compositional regions with middle-range T_l, enthalpy of mixing and atomic mismatch factor for the amorphous microstructure. It predicts moderate values of AMC, by identifying

the region of interest using T_l, ΔH_{mix}, and the λ-factor on the phase diagram. It will be shown that the rapid quenching of alloys with tuned AMC can result in an *in-situ* nanocrystallised alloy.

3.3.2 Structural characterisation

Fig. 4 shows the XRD pattern of the wheel-side of the as-quenched $Co_{70}Fe_{17.5}B_{12.5}$ ribbons. A sharp Bragg peak at 45.27° <110> and a broader diffused peak at 83.82° <211> can be seen in the XRD pattern, which both represent the Co_7Fe_3 phase formed on the side which experienced higher cooling rate (copper wheel side). Additionally, a sample from the middle region of the cross-section of the ribbons has been examined by TEM to corroborate the local nanocrystalline microstructure. Fig. 5a shows a typical TEM image of the nanocrystals in the glassy matrix. The Selected Area Electron Diffraction (SAED) pattern (Fig. 5c), shows the presence of a typical amorphous halo ring pattern, from the matrix, with discrete diffraction spots corresponding to {110}, {211}, and {220} reflections confirming the presence of the $Im\bar{3}m$ structured Co_7Fe_3 phase. Most of the equiaxed, rather than dendritic, nanocrystalline grains are smaller than 100 nm in size. These results confirm the *in-situ* formation of Co_7Fe_3 nanocrystals in $Co_{70}Fe_{17.5}B_{12.5}$ ribbons. It is worth noting that as XRD was performed on the wheel-side and the TEM sample was from the middle of the cross-section of the ribbon, the *in-situ* nanocrystallisation is a volumetric phenomenon, instead of surface crystallisation which possibly can start due to the lower cooling rates at the air-side of the ribbons. The surface crystallisation takes place when the alloy is not well designed with large AMC [27]. The volumetric formation of *in-situ* nanocrystallisation is essential to get the advantage of the high-flux density of the alloys.

In addition, a higher magnified TEM image of nanocrystals and corresponding SAED can be seen in Fig. 5d and e. The latter corresponds to [311]-bcc zone-axis pattern. Diffractions related to different atomic planes are indicated in Fig. 5e. The lattice parameter based on this lattice spacing between different atomic planes is in good agreement with the lattice parameter calculated from the Rietveld refinement analysis of the XRD pattern (Fig. 4). Thus, the observation of this pattern is also strong evidence of the existence of crystalline bcc-Co_7Fe_3 clusters in the as-quenched melt-spun $Co_{70}Fe_{17.5}B_{12.5}$ ribbon. It can also be noted that the

background noise seen in the SAED patterns comes from weak scattering by atomic clusters (several atoms in size) in the amorphous matrix surrounding crystalline clusters. Interestingly, the nanocrystalline structure yields to high electrical resistivity (168 μΩ.cm) of the alloy. The electrical resistivity of the nanocrystalline materials is higher than both coarse-grained polycrystalline metals and amorphous alloys due to the increased volume fraction of atoms lying at the grain boundaries [28].

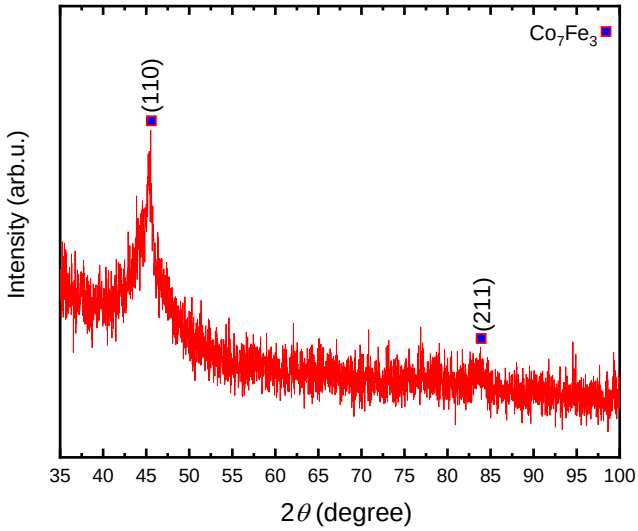

Figure 4. The X-ray diffraction pattern of the wheel-side of the as-quenched $Co_{70}Fe_{17.5}B_{12.5}$ ribbons.

Additionally, some thermodynamic and kinetic aspects of these phase transitions are studied below. First, the phase transitions are studied by evaluating the equilibrium and non-equilibrium solidification simulation of the alloy composition using the Pandat^{TM} software. As can be seen in Table 1, five different phases are predicted to crystallise as a result of equilibrium and non-equilibrium solidification of $Co_{70}Fe_{17.5}B_{12.5}$ alloy. Among these phases, $(CoFe)_3B$ has minimum Gibbs energy of formation, -30 kJ/mol. However, the nanocrystals of metastable Co_7Fe_3 form during melt-spinning, and they are stable at room temperature. Thus, this discrepancy between experiment and thermodynamic modelling should be addressed accordingly.

Table 1. Thermodynamically predicted equilibrium and non-equilibrium phases of $Co_{70}Fe_{17.5}B_{12.5}$ stable at room temperature.

	Equilibrium conditions		Non-equilibrium conditions	
	Phase	Percentage	Phase	Percentage
Stable phases at RT	$(CoFe)_3B$	44	$(CoFe)_3B$	49.97
	BCC (CoFe) S.S.*	34	FCC (CoFe) S.S.	50
	HCP (CoFe) S.S.	22	$(CoFe)_2B$	0.03

* S.S. stands for solid solution

The nucleation of a metastable phase could likely be kinetically-favoured compared to that of the stable phase [29]. According to classical nucleation theory [30], the activation threshold for the formation of a critical nucleus is ΔG^*, which is the free energy required to form the critical nucleus;

$$\Delta G^* = \frac{16\pi\sigma^3}{3\Delta G_v^2} f(\theta) \tag{4}$$

where $f(\theta)$ is the catalytic potency factor for heterogeneous nucleation, which depends on the wetting angle θ. ΔG_v is the Gibbs free energy difference between the liquid and the solid:

$$\Delta G_v = \Delta H_f \frac{T_m - T}{T_m} \tag{5}$$

where ΔH_f, T_m, and T denote the enthalpy of fusion, melting temperature, and undercooling temperature, respectively. The interface energy, σ, can be estimated by the model developed by Spaepen and Meyer [31]:

$$\sigma = \alpha \frac{\Delta S_f T}{(N_L V_m^2)^{1/3}} \tag{6}$$

where α is a factor dependent on the structure of the solid nucleus and ΔS_f, N_L; and V_m are the entropy of fusion, Avogadro's number, and the molar volume of the phase, respectively. Without the knowledge of the contact angle θ of the crystal nucleus to the substrate, the

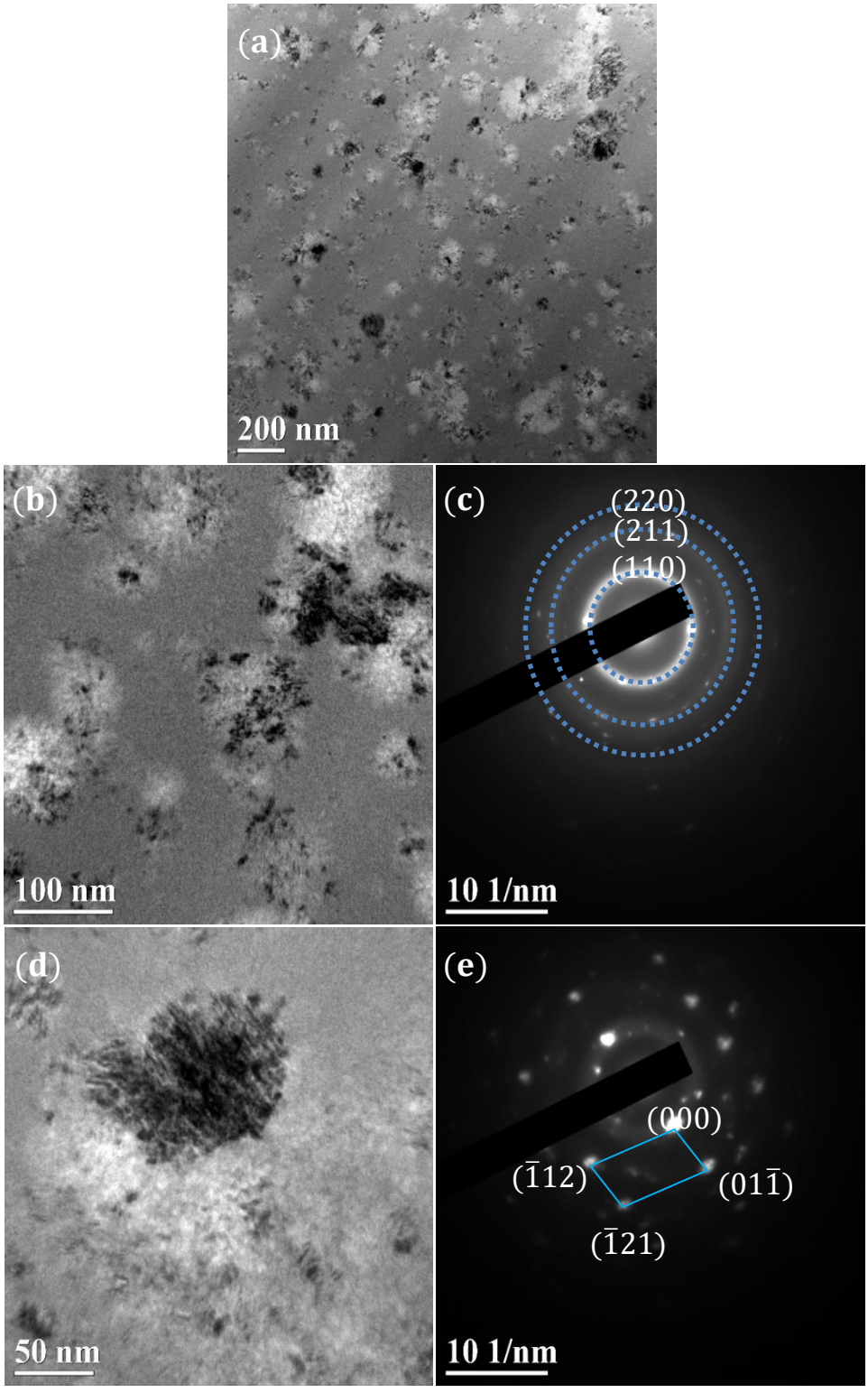

Figure 5. (a), (b), and (d): TEM micrographs of as-quenched nanostructured ribbons in different magnifications, (c) and (e) SAED pattern of (b) and (d) images.

nucleation is assumed to be homogenous. Based on this theory, the activation threshold of the

dominant stable and possibly metastable phases in this system is estimated and shown in Table 2. As can be seen, the necessary activation energy for the formation of Co_7Fe_3 is about three orders of magnitude less than the one for $(CoFe)_3B$. Therefore, from the kinetics point of view, the nucleation of this phase is more favourable.

Table 2. Gibbs free energy (ΔG_v) and interface energy (σ) difference between the liquid and solid, and the activation threshold for formation of a critical nucleus (ΔG^*) at room temperature.

Phase	ΔG_v (kJ/mol)	σ (J/m^2) ×10^5	ΔG^* (J) ×10^{23}	ΔG^* (meV)
$(CoFe)_3B$	52.34	1.99	4.85	0.3
Co_7Fe_3	12.55	1.39	0.003	0.00019

3.3.2.1 Mössbauer spectra of nanostructured alloy

Figure 6 presents the Mössbauer transmission spectra of $Co_{70}Fe_{17.5}B_{12.5}$ nanocomposite ribbons, along with respective distribution $P(B_{hf})$ of Hyperfine Magnetic Field (HMF). The shape of the spectra is characteristic of a nanocomposite structure with a ferromagnetic arrangement. Thus, both building blocks of the microstructure, nanocrystals and amorphous matrix, can be scrutinised based on the correlated distribution of HMF.

3.3.2.1.1 Local atomic order in nanocrystals

The hyperfine interaction distribution can be analysed based on the local environment model [32], which has been reported for different ternary systems [33–36]. In Fe–X, where X is treated as an impurity, and it can include different types of elements, every atom X which substitutes iron atom in the ith coordination sphere (or neighbour shell) of the ^{57}Fe isotope causes the change of the HMF at ^{57}Fe site by the value of ΔB_i. The changes in the HMF of iron, as ΔB_i, are additive. In practice, the contributions from the first and the second coordination spheres are considered, and the value $B(m,n)$ of the hyperfine magnetic field at ^{57}Fe site can be described as [37]:

$$B(m,n) = B(0,0) + m\Delta B_1 + n\Delta B_2 \quad (7)$$

where $B(0,0)$ denotes the value of the HMF at ^{57}Fe nucleus, which is surrounded only by Fe atoms in the first and the second coordination spheres; *m* the number of impurity atoms in the first sphere; *n* the number of impurity atoms in the second sphere; the changes of the HMF caused by impurity atoms in the first and the second neighbour shells, respectively. The values of ΔB_1 and ΔB_2 could be positive or negative. Relation (7) has been used for both disordered and ordered alloys in the broad range of impurity concentration [37].

In the FeCo, B2 structural type, there are eight cobalt atoms in the first sphere around an iron atom which is the same as the atomic orientation in Co_7Fe_3. However, there are just two iron atoms in the second sphere in Co_7Fe_3 compared to 6 iron atoms in the FeCo B2 structure. Thus, based on the fact that there are four fewer iron atoms in the second sphere in the Co_7Fe_3 phase and the as-mentioned local environment model, the HMF of Co_7Fe_3, based on its counterpart in FeCo, can be calculated as:

$$B_{\mathrm{Co_7Fe_3}} = B_{\mathrm{FeCo}} - 4\Delta B_{2,\mathrm{Fe}} \quad (8)$$

B_{FeCo} is mentioned to be 34.3 T [38] and ΔB for an iron atom in the second sphere is measured to be 0.77 T [39], so based on Equation 8, the HMF for an iron atom in Co_7Fe_3 is 31.22 T. This number is close to two peaks of the hyperfine field distributions, at 31 ($P(B_{\mathrm{hf}})$= 13.41%) and 32 ($P(B_{\mathrm{hf}})$= 19.29%) (Fig. 6b). The sum of probabilities for these two fields is 32.7, which agrees with the portion of nanocrystals formed in the amorphous matrix calculated based on the TEM image in Fig. 5a.

3.3.2.1.2 Local atomic order in the amorphous matrix

A relatively large portion of the structurally disordered matrix, about 70% (Fig. 5a), leads to the broadening of the experimental HMF peak and a significant contribution of low-field background in the total HMF distribution (Fig. 6b). For every HMF filed (B_{hf}), excluding the ones correlated to Co_7Fe_3 nanocrystals, the number of cobalt and boron atoms in the first sphere around the iron atom can be estimated based on the following Equation [33,37]:

$$B_{\mathrm{hf}} = B(0,0) + m\Delta B_{1,\mathrm{Co}} + n\Delta B_{1,\mathrm{B}} \quad (9)$$

where m and n denote the numbers of Co and B atoms in the first coordination sphere, while $\Delta B_{1,Co}$ and $\Delta B_{1,B}$ denote changes of the HMF caused by a single Co and B atoms respectively. Statistically, the probability of finding n of Co atoms and m of B atoms in the first coordination shell of ^{57}Fe in the amorphous matrix can be calculated using multinomial distribution [33,37]:

$$P(m,n) = \frac{N!}{m!\,n!\,(N-m-n)!} x^m y^n (1-x-y)^{N-m-n} \tag{10}$$

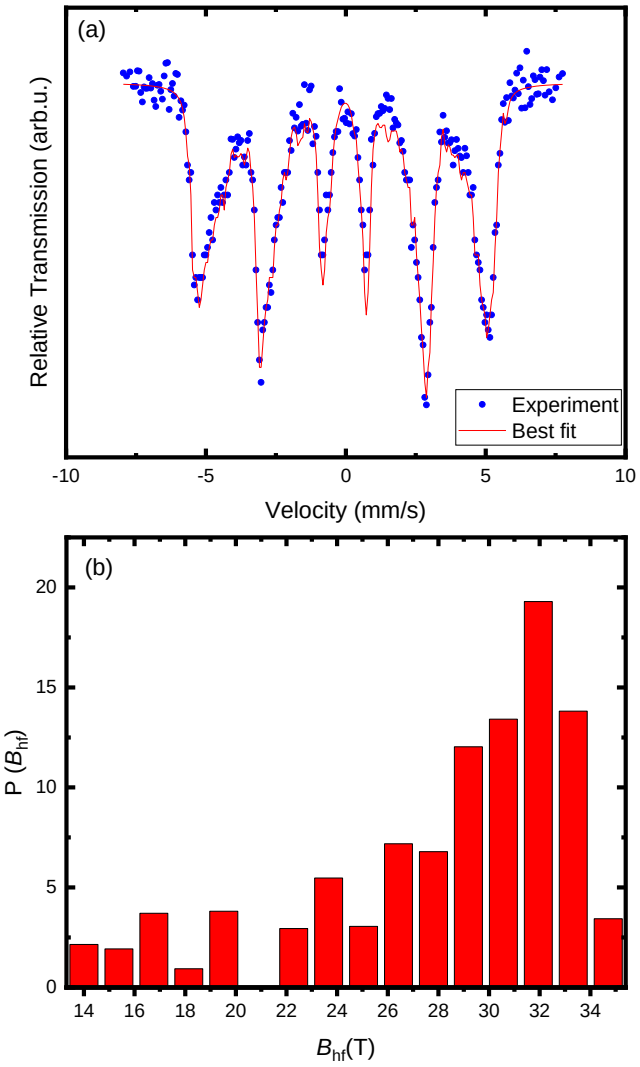

Figure 6. (a) Room-temperature Mössbauer spectra, and (b) hyperfine magnetic field distributions of as-quenched $Co_{70}Fe_{17.5}B_{12.5}$.

where *N* is the number of all atoms in the first coordination sphere, *x* and *y* denote the chemical concentration of the cobalt and boron in the amorphous matrix. Among different pairs of *m* and *n*, the ones with the highest $P(m,n)$ are chosen. Then $\langle m \rangle$ and $\langle n \rangle$ are calculated based on:

$$\langle m \rangle = \sum m P_{\mathrm{exp}}(m,n) \tag{11}$$

$$\langle n \rangle = \sum n P_{\mathrm{exp}}(m,n) \tag{12}$$

where P_{exp} denotes the probability of the configuration (m,n) of impurity atoms obtained from the analysis of the experimental Mössbauer spectra. Therefore, the Warren–Cowley parameters for cobalt (α_{Co}) and boron (α_{B}) atoms have the following form [33,37]:

$$\alpha_{\mathrm{Co}} = \frac{\langle m \rangle - 8x}{8(1-x)} \tag{13}$$

$$\alpha_{\mathrm{B}} = \frac{\langle n \rangle - 8y}{8(1-y)} \tag{14}$$

The interpretation of the values of the Warren–Cowley parameters is as follows: when $\alpha_{\mathrm{i}} = 0$ then the distribution of impurity atoms is random; if $\alpha_{\mathrm{i}} < 0$ the impurity atoms form clusters, i.e., they attract each other, and finally when $\alpha_{\mathrm{i}} > 0$; the impurity atoms undergo the short-range order (SRO) effect, i.e., they are attracted by the matrix atoms [33,37]. Based on this theory, cobalt atoms cluster as $\alpha_{\mathrm{Co}} = -1.17$. As the most stable local configuration of cobalt is highly dense hcp, this element shows the high tendency for clustering in a large variety of systems with either metallic or covalent bonding. The strong drive for clusterisation of the cobalt atoms, which leads to a local increase in their concentration, in addition to the tendency of boron atoms to undergo SRO leads to the nucleation of the ordered cobalt-rich Co_7Fe_3 phase (Fig. 4 and 5). Warren–Cowley parameter for boron atoms is 0.12, implying that they, indeed, undergo SRO. A repulsive potential between the small boron atoms and attraction between the boron atoms and large cobalt/iron atoms could lead to the formation of a tetrahedron of four

cobalt/iron atoms 'stuffed with boron', minimising the voids in the Bernal dense random packing structure [40], and thereby stabilising the structure against easy crystallisation.

3.3.3 Magnetic properties

The evolution of magnetisation, measured along the length of the ribbons, as a function of the applied magnetic field, is presented in Fig. 7. It can be seen that coercivity, $H_c = 381.5\ \mathrm{A/m}$, and anisotropy field, $H_k = 728.5\ \mathrm{A/m}$, are high, which could be attributed to the effect of magnetocrystalline anisotropy of the ordered nanocrystals of the Co_7Fe_3 phase. The as-mentioned effect can be measured quantitatively by the anisotropy energy (K_u), which is calculated based on the following Equation [41]:

$$K_u = \frac{H_k \mu_0 M_s}{2} \tag{15}$$

where μ_0 is the free space permeability. The anisotropy is related to directional atomic ordering along the direction of the local magnetisation to minimise the spin-orbit coupling energy [42]. The calculated anisotropy energy for the *in-situ* nanocrystalline alloy is 573 J/m^3, which is about twenty times larger than the values reported for similar amorphous alloys [3]. Furthermore, the B_s of the *in-situ* nanocrystalline alloy is 1.57 T. The relatively high B_s is due to the presence of the ordered Co_7Fe_3 phase, which is ~ 4% higher than its disordered counterparts [43]. Strong magnetic moment of Co_7Fe_3 can also be inferred from the high hyperfine magnetic field interactions of the Fe nuclei, in the nanocrystals of Co_7Fe_3 (Fig. 6b).

To understand the evolution of B_s of the alloy, it is necessary to take into account a few primary considerations concerning the electronic structure and magnetic properties of the 3d system. In this regard, the Slater-Pauling figure, which shows the relationship between the magnetic moment and the number of valence electrons per atom (e/a) is used. The e/a is estimated for Co_7Fe_3 nanocrystals, as 8.71, and for the amorphous matrix 7.72. Then, e/a for the nanocomposite is calculated based on the portion of the nanocrystals in the amorphous matrix. The magnitude of the magnetic moment for e/a of the nanocomposite is 1.64 μ_B which

is slightly higher than the magnetic moment of the nanocomposite estimated based on B_s, 1.47 μ_B. This difference can be due to the hybridisation effect, as a result of SRO of boron atoms, which is observed by Mössbauer spectroscopy in section 3.2.1.

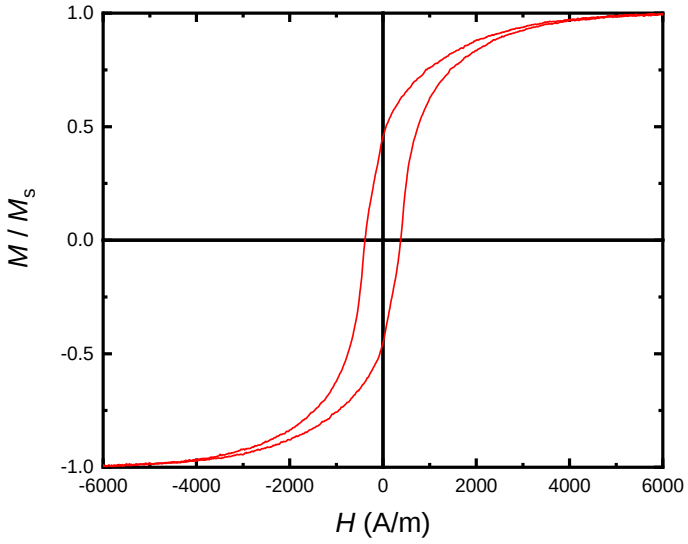

Figure 7. Hysteretic loop of as-quenched nanocrystalline $Co_{70}Fe_{17.5}B_{12.5}$ ribbons, $\mu_0 M_s$ = 1.57 T.

3.4 Conclusions

A $Co_{70}Fe_{17.5}B_{12.5}$ alloy, with a tuned amorphisation capability, has been designed, using a thermodynamics-based CALPHAD approach, together with a topological instability parameter, and experimentally confirmed to result in the fabrication of an *in-situ* nanocrystallised alloy. The proposed scheme works as a guideline for the tuning of AMC of alloys, to favour the formation of the desired ordered phase (Co_7Fe_3) nanocrystals throughout the volume of the alloys, during the rapid quenching process. This can be achieved without any post-spinning heat treatment, which is normally required in order to grow the necessary amount of nanocrystalline phase. The XRD and TEM results confirm the formation of the Co_7Fe_3 ordered phase, dispersed heterogeneously throughout the amorphous matrix. Furthermore, the

local atomic order of the nanocrystalline structures and the amorphous matrix has been investigated by the distribution of hyperfine magnetic field, using Mössbauer spectroscopy. In the latter, the Warren–Cowley parameter is negative for cobalt atoms showing their tendency to form ordered structures, and it is positive for boron atoms implying that they are prone to undergo short-range order due to their size and electronegativity difference with atoms in the amorphous matrix. The proposed approach of designing *in-situ* nanocrystalline alloys by rapid quenching, using both thermodynamic and topological parameters, is useful for the development of functional materials for a broad range of applications. Future research on the introduction of other elements, such as Nb or Cu, in order to increase the number of crystalline nuclei in the two-phase system (melt-solid) and therefore further decrease the grain size, may also benefit from the proposed predictive modelling approach.

Acknowledgement

The authors would like to thank Science Foundation of Ireland (SFI) for the financial support to perform the research work under the grant number of 2015/SIRG/3569, Starting Investigator Research Grant (SIRG).

3.5 References

[1] A.D.M. Charles, A.N. Rider, S.A. Brown, C.H. Wang, Multifunctional magneto-polymer matrix composites for electromagnetic interference suppression, sensors and actuators, Prog. Mater. Sci. 115 (2021) 100705. https://doi.org/10.1016/j.pmatsci.2020.100705.

[2] K.J. Overshott, Soft magnetic materials, Phys. Technol. 6 (1975) 280–281. https://doi.org/10.1088/0305-4624/6/6/409.

[3] H. Ahmadian Baghbaderani, A. Masood, Z. Pavlovic, K. L. Alvarez, C. ÓMathúna, P. McCloskey, P. Stamenov, On the mechanisms limiting power loss in amorphous CoFeB-based melt-spun ribbons, J. Magn. Magn. Mater. 502 (2020) 166535. https://doi.org/https://doi.org/10.1016/j.jmmm.2020.166535.

[4] K.L. Alvarez, H.A. Baghbaderani, J.M. Martín, N. Burgos, M. Ipatov, Z. Pavlovic, P. McCloskey, A. Masood, J. Gonzalez, Novel Fe-based amorphous and nanocrystalline powder cores for high-frequency power conversion, J. Magn. Magn. Mater. 501 (2020) 166457. https://doi.org/https://doi.org/10.1016/j.jmmm.2020.166457.

[5] A. Masood, H.A. Baghbaderani, V. Ström, P. Stamenov, P. McCloskey, C.Ó. Mathúna, S.

Kulkarni, Fabrication and soft magnetic properties of rapidly quenched Co-Fe-B-Si-Nb ultra-thin amorphous ribbons, J. Magn. Magn. Mater. 483 (2019) 54–58. https://doi.org/https://doi.org/10.1016/j.jmmm.2019.03.079.

[6] A. Masood, H.A. Baghbaderani, K.L. Alvarez, J.M. Blanco, Z. Pavlovic, V. Ström, P. Stamenov, C.O. Mathuna, P. McCloskey, High-frequency power loss mechanisms in ultra-thin amorphous ribbons, J. Magn. Magn. Mater. (2020) 167469. https://doi.org/10.1016/j.jmmm.2020.167469.

[7] O. Gutfleisch, M.A. Willard, E. Brück, C.H. Chen, S.G. Sankar, J.P. Liu, Magnetic materials and devices for the 21st century: Stronger, lighter, and more energy efficient, Adv. Mater. 23 (2011) 821–842. https://doi.org/10.1002/adma.201002180.

[8] D. Raskin, C.H. Smith, Chapter 20 - Applications of amorphous metals: progress and prospects A2 - LUBORSKY, F.E, in: Amorph. Met. Alloy., Butterworth-Heinemann, 1983: pp. 381–400. https://doi.org/https://doi.org/10.1016/B978-0-408-11030-3.50025-X.

[9] C.Ó. Mathúna, N. Wang, S. Kulkarni, S. Roy, Review of integrated magnetics for Power Supply on Chip (PwrSoC), IEEE Trans. Power Electron. 27 (2012) 4799–4816. https://doi.org/10.1109/TPEL.2012.2198891.

[10] M. Najafi, F. Hayati, A.A. Rafati, Effect of Current Frequency and Annealing on Magnetic Properties of [Co70Fe30]97Sn3 Nanowire Arrays, Int. Conf. Nanomater. Appl. Prop. 1 (2012)04MFPN10-2.http://essuir.sumdu.edu.ua/retrieve/76719/princon_2012_1_4_27.pdf.

[11] S. Amsarajan, B.R. Jagirdar, Air-stable magnetic cobalt-iron (Co7Fe3) bimetallic alloy nanostructures via co-digestive ripening of cobalt and iron colloids, J. Alloys Compd. 816 (2020) 152632. https://doi.org/10.1016/j.jallcom.2019.152632.

[12] J.G. Wang, H. Zhao, C.X. Xie, C.T. Chang, S.M. Zhou, J.Q. Feng, J.T. Huo, W.H. Li, In-situ synthesis of nanocrystalline soft magnetic Fe-Ni-Si-B alloy, J. Alloys Compd. 790 (2019) 524–528. https://doi.org/10.1016/j.jallcom.2019.03.226.

[13] S. V. Thomas, M.A. Willard, A. Martone, M.J. Heben, V. Solomon, A. Welton, P. Boolchand, R.C. Ewing, C. Wang, S.L. Bud'ko, J. Song, D. Shi, Nanocrystallites via Direct Melt Spinning of Fe77Ni5.5Co5.5Zr7B4Cu for Enhanced Magnetic Softness, Phys. Status Solidi Appl. Mater. Sci. 217 (2020) 1–10. https://doi.org/10.1002/pssa.201900680.

[14] A.I. C. Suryanarayana, Bulk Metallic Glasses, Second Edition, CRC, New York, 2012.

[15] J. Bhatt, W. Jiang, X. Junhai, W. Qing, C. Dong, B.S. Murty, Optimization of bulk metallic glass forming compositions in Zr–Cu–Al system by thermodynamic modeling, Intermetallics. 15 (2007) 716–721. https://doi.org/https://doi.org/10.1016/j.intermet.2006.10.018.

[16] D.D.E.E. Brennhaugen, H. Mao, D. V. Louzguine-Luzgin, L. Arnberg, R.E. Aune, Predictive modeling of glass forming ability in the Fe-Nb-B system using the CALPHAD approach, J. Alloys Compd. 707 (2017) 120–125. https://doi.org/https://doi.org/10.1016/j.jallcom.2016.12.049.

[17] A. Tabeshian, H. Mao, L. Arnberg, R.E. Aune, Investigation of glass forming ability in the Zr-rich part of the Zr-Fe-Al ternary system, J. Appl. Phys. 125 (2019) 8–15. https://doi.org/10.1063/1.5066554.

[18] D. Turnbull, Under what conditions can a glass be formed?, Contemp. Phys. 10 (1969) 473–488. https://doi.org/10.1080/00107516908204405.

[19] (Asm Handbook) Asm-Alloy Phase Diagrams. Volume 3-ASM International (1992).pdf, (n.d.).

[20] A. Inoue, High Strength Bulk Amorphous Alloys with Low Critical Cooling Rates (<I>Overview</I>), Mater. Trans. JIM. 36 (1995) 866–875. https://doi.org/10.2320/matertrans1989.36.866.

[21] J.W. Martin, 4 - Glasses and ceramics, in: J.W.B.T.-M. for E. (Third E. Martin (Ed.), Woodhead Publishing, 2006: pp. 133–158. https://doi.org/https://doi.org/10.1533/9781845691608.2.133.

[22] A. Takeuchi, A. Inoue, Calculations of mixing enthalpy and mismatch entropy for ternary amorphous alloys, Mater. Trans. JIM. 41 (2000) 1372–1378. https://doi.org/10.2320/matertrans1989.41.1372.

[23] J. Guo, X. Bian, X. Li, C. Zhang, Evaluation of liquid fragility for glass-forming alloys based on mixing enthalpy and mismatch entropy, Intermetallics. 18 (2010) 933–937. https://doi.org/10.1016/j.intermet.2010.01.004.

[24] R. Lisboa, C. Bolfarini, W. Botta, C. Kiminami, Topological instability as a criterion for design and selection of aluminum-based glass-former alloys, Appl. Phys. Lett. 86 (2005) 211904. https://doi.org/10.1063/1.1931047.

[25] Z.J. Yan, J.F. Li, S.R. He, Y.H. Zhou, Evaluation of the optimum solute concentration for good glass forming ability in multicomponent metallic glasses, Mater. Res. Bull. 38 (2003) 681–689. https://doi.org/10.1016/S0025-5408(03)00010-2.

[26] T. Egami, Y. Waseda, Atomic size effect on the glass forming ability of metallic alloys, J. Non. Cryst. Solids. 64 (1984) 113–134.

[27] J. Zhang, F. Wan, Y. Li, J. Zheng, A. Wang, J. Song, M. Tian, A. He, C. Chang, Effect of surface crystallisation on magnetic properties of Fe82Cu1Si4B11.5Nb1.5 nanocrystalline alloy ribbons, J. Magn. Magn. Mater. 438 (2017) 126–131. https://doi.org/10.1016/j.jmmm.2017.04.086.

[28] C. Suryanarayana, Nanocrystalline materials, Int. Mater. Rev. 40 (1995) 41–64. https://doi.org/10.1179/imr.1995.40.2.41.

[29] X.X. Wei, W. Xu, J.L. Kang, M. Ferry, J.F. Li, Metastable Co23B6 phase solidified from deeply undercooled Co79.3B20.7 alloy melt, J. Mater. Sci. 51 (2016) 6436–6443. https://doi.org/10.1007/s10853-016-9941-4.

[30] D.A. Porter, K.E. Easterling, M.Y. Sherif, Phase transformations in metals and alloys,

third edition, 2009.

[31] F. Spaepen, R.B. Meyer, The surface tension in a structural model for the solid-liquid interface, Scr. Metall. 10 (1976) 37–43. https://doi.org/10.1016/0036-9748(76)90323-9.

[32] M. Rubinstein, Hyperfine Field Spectra of Binary Fe-Co Alloys: Nuclear Magnetic Resonance of $^{57}\mathrm{Fe}$ and $^{59}\mathrm{Co}$, Phys. Rev. 172 (1968) 277–283. https://doi.org/10.1103/PhysRev.172.277.

[33] T. Pikula, Local atomic arrangement in mechanosynthesized CoxFe1−x−yNiy alloys studied by Mössbauer spectroscopy, Appl. Phys. A Mater. Sci. Process. 117 (2014) 1491–1498. https://doi.org/10.1007/s00339-014-8582-1.

[34] C. Djega-Mariadassou, L. Bessais, C. Servant, Nanocrystalline precipitates formed by aging of bcc disordered Fe-Ni-Mo alloys, Phys. Rev. B. 51 (1995) 8830–8840. https://doi.org/10.1103/PhysRevB.51.8830.

[35] J.M. Grenèche, Local structural order in disordered systems investigated by Mössbauer spectrometry, J. Non. Cryst. Solids. 287 (2001) 37–44. https://doi.org/https://doi.org/10.1016/S0022-3093(01)00634-2.

[36] J. Restrepo, G.A. Pérez Alcázar, Interpretation based on a binomial method of the hyperfine field distributions of disordered: Fe0.9−xMn0.1Alx alloys, J. Magn. Magn. Mater. 213 (2000) 135–142. https://doi.org/https://doi.org/10.1016/S0304-8853(99)00541-7.

[37] E. Jartych, Local atomic order in nanocrystalline Fe-based alloys obtained by mechanical alloying, J. Magn. Magn. Mater. 265 (2003) 176–188. https://doi.org/10.1016/S0304-8853(03)00263-4.

[38] Q. Samara, S.H. Mahmood, On the magnetic properties and hyperfine fields in Fe-containing alloys : A theoretical study, 3291 (2006) 3285–3291. https://doi.org/10.1002/pssc.200567119.

[39] Z. Klencsár, P. Németh, Z. Sándor, T. Horváth, I.E., Sajó, S. Mészáros, J. Mantilla, J.A.H. Coaquira, V.K. Garg, E. Kuzmann, G. Tolnai, Structure and magnetism of Fe-Co alloy nanoparticles, J. Alloys Compd. 674 (2016) 153–161. https://doi.org/10.1016/j.jallcom.2016.03.068.

[40] D.E. Polk, The structure of glassy metallic alloys, Acta Metall. 20 (1972) 485–491. https://doi.org/10.1016/0001-6160(72)90003-X.

[41] F. Johnson, C.Y. Um, M.E. McHenry, H. Garmestani, The influence of composition and field annealing on magnetic properties of FeCo-based amorphous and nanocrystalline alloys, J. Magn. Magn. Mater. 297 (2006) 93–98. https://doi.org/https://doi.org/10.1016/j.jmmm.2005.02.056.

[42] R.C. O'Handley, Modern Magnetic Materials: Principles and Applications, Wiley, 1999. https://books.google.ie/books?id=RKV1QgAACAAJ.

[43] D.W. Clegg, R.A. Buckley, The disorder ⟶ order transformation in iron-cobalt-based

alloys, Met. Sci. J. 7 (1973) 48–54. https://doi.org/10.1179/030634573790445541.

Chapter 4 Fabrication and soft magnetic properties of rapidly quenched Co-Fe-B- Si-Nb ultra-thin amorphous ribbons

Journal of Magnetism and Magnetic Materials 483 (2019) 54–58

Contents lists available at ScienceDirect

Journal of Magnetism and Magnetic Materials

journal homepage: www.elsevier.com/locate/jmmm

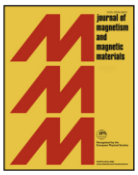

Research articles

Fabrication and soft magnetic properties of rapidly quenched Co-Fe-B-Si-Nb ultra-thin amorphous ribbons

Ansar Masood[a,*], Hasan Ahmadian Baghbaderani[a], Valter Ström[b], Plamen Stamenov[c], Paul McCloskey[a], Cian Ó. Mathúna[a], Santosh Kulkarni[a]

[a] Microsystems Centre, Tyndall National Institute, University College Cork, Cork, Ireland
[b] Materials Science and Engineering Department, KTH-Royal Institute of Technology, Stockholm, Sweden
[c] School of Physics and CRANN, Trinity College Dublin, Dublin 2, Ireland

Abstract

Ultra-thin soft magnetic amorphous ribbons of Co-Fe-B-Si-Nb alloy were synthesised by a single step rapid-quenching approach to acquire the advantage of improved material performance and lower costs over commercial amorphous alloys. The amorphous ribbons of approximately 5.5 µm thicknesses were quenched by a single roller melt spinner in a single-step production process and characterised for their structural and magnetic properties. The disordered atomic structure of amorphous ribbons was confirmed by X-ray diffraction. A surface morphology study revealed the continuity of ultra-thin ribbons without pores over a large scale. The amorphous alloy showed ultra-soft magnetic properties in the as-quenched state. The observed thickness dependency of the magnetic properties was attributed to the increased surface roughness and possibly due to a lack of densely packed atomic structure resulting from the extremely high cooling rates experienced by ultra-thin ribbons. We propose that the *in-situ* thinning process of amorphous ribbons significantly reduces the basic material cost and eliminates the need for post-processing steps; hence it provides the opportunity for mass production of high-performance soft magnetic amorphous ribbons at relatively lower costs.

Keywords: Amorphous metals, Ultra-thin ribbons, Soft-magnetic properties, High-frequency applications

4.1 Introduction

A significant advancement in cutting-edge efficient power switches at high-frequencies has enhanced the need for miniaturised magnetic components in the power converter industry [1-3]. A major challenge in the miniaturisation of power circuitry is the size of passive components which occupy a significant volume fraction (~30%) [4]. The large volume of passive components is due to the ferrite based magnetic cores which are widely used due to their high material loss performance and lower costs. Nevertheless, the low magnetic flux density (0.3-0.5 T) of ferrites is a key roadblock in miniaturising the passive component technology [1, 4]. The development of high-flux density low-cost soft magnetic materials to replace bulky ferrite

based passive components is a significant challenge to attain the miniaturised power switches at high-frequencies [1, 4].

High-flux density (B_s > 1.5 T), exceptionally low coercivity (H_c < 10 A/m), and high resistivity (> 100 μΩ cm) of amorphous ribbons make them a potential candidate for high switching frequency applications [5]. The amorphous metal ribbons are typically produced by a rapid-quenching technique and are commercially available in the range of 20-30 μm thickness [6-8]. It is widely known that as the operating frequency (f) increases, the eddy-current loss (W_e α f^2) increases more sharply than the hysteresis loss (W_h α f), and the total core loss dominates by W_e at f > 100 kHz [1, 4]. Eddy currents not only deteriorate the overall magnetic properties but also generate tremendous heat energy, which complicates the design and engineering of the device [1, 6]. The eddy current losses can be significantly reduced by either eliminating the electrically conducting path by using ultra-thin insulated stacks or significantly increase the electrical resistivity of the magnetic material [4]. To get an advantage of eliminated eddy current loss at high frequencies, the thickness of the magnetic material must be smaller than the skin depth δ ($= \sqrt{\frac{\rho}{\pi f \mu}}$, where ρ is resistivity and μ is the permeability) [1, 4]. Thus, to use amorphous metals at MHz frequencies, the thickness of the commercially available amorphous ribbons restricts the use of these novel alloys and hence limits the flux concentration advantage for the miniaturisation of passive components [1, 4].

Recently, we demonstrated a post-processing approach to thin the commercial ribbons to 4 μm by a wet etching route to realise the advantages of material loss performance of soft magnetic amorphous metals at high-frequencies [1, 4]. Nevertheless, wet etching of amorphous metals could be an expensive route at a mass level production as 75% of the material was wasted to reach the required material thickness [1, 4]. Furthermore, the post-processing steps significantly increase the overall cost of the material, hence limits the use of chemically etched ultra-thin ribbons for higher frequency applications. In addition to the amorphous ribbons thickness, the high materials cost of amorphous alloys, due to their high-purity constituent elements, is another challenge to replace the best-in-class ferrites [5, 7, 9]. Interestingly, the use of low-grade industrial materials has been demonstrated to significantly reduce the cost of amorphous metals without deteriorating their soft magnetic properties [10]. Further reductions

in the cost of amorphous metals, in addition to low-grade industrial compounds, by developing novel approaches of *in-situ* thinning could be advantageous to replace the ferrites with amorphous metal cores for high-frequency power conversion.

In this work, we demonstrate the rapid quenching approach of *in-situ* thinning to produce ultra-thin soft magnetic amorphous ribbons. The single step *in-situ* thinning process of amorphous ribbons provides the opportunity to produce high-performance soft magnetic amorphous ribbons at mass production at lower costs.

4.2 Fabrication

Melt-spinning is a well-known technique for making amorphous ribbons. This method uses the molten material to flow from the nozzle in the form of a jet, which comes in contact with a rotating copper wheel and procedures a melted puddle. Because of the low viscosity of the molten alloy, the shear layers extend only a few microns from the surface of the roller into the puddle, and it stays on the roller surface. The main advantages of melt-spinning are as follows; (a) production of amorphous ribbons of uniform thickness and width, (2) controlled process parameters, and (3) availability at commercial scale. Several process parameters such as the gap between nozzle and wheel, the angle of incidence of melt, the speed of rotation copper wheel, initial melt temperature, ejection pressure and material properties such as density, surface tension, viscosity, thermal conductivity influence the quality of as-spun ribbons. Among these parameters, the speed of the wheel is an important parameter in determining the thickness of the ribbon; the faster the wheel rotates, the thinner is the ribbon. For example, a $Fe_{40}Ni_{40}B_{20}$ alloy cast on a 250 mm diameter copper wheel rotating at a substrate velocity of 26.6 ms^{-1} produced a ribbon of 37 µm thickness, while at a velocity of 46.5 ms^{-1}, the ribbon thickness was only 22 µm [11]. However, it is quite challenging to produce ultrathin smooth ribbons thinner than 10 µm by conventional melt spinning. This is due to gas bubbles entrained at the melt-roller interface during casting, causing surface roughness and pockets in the ribbons.

In this work, a conventional melt-spinner was used to produce the ultra-thin ribbons. This was achieved by varying the speed of the wheel. At the first stage, the master alloy of Co-Fe-B-Si-Nb was prepared by arc-melting of pure elements Fe (99.9%), Co (99.99%), B (99.5%),

Nb (99.9%) and Si (99.9%) in a highly pure argon atmosphere with Titanium as a getter material to reduce the possibility of oxidation. The ingots (20-30 g) were re-melted at least ten times (5 times on each side) to assure a homogeneous composition of ingots. Prior to re-melting, the ingots were broken into several pieces (4-5 g) and were re-melted in quartz tubes by induction heating. After raising the temperature to the liquidus, a dwell of at least 120 seconds was used to ensure that the ingots were completely melted. A quartz tube with an orifice diameter of 0.4 mm was utilised to eject the melt onto the surface of a copper wheel with a diameter of 20 cm which was used to quench the amorphous ribbons. The chamber was evacuated down to 4×10^{-3} Pa pressure, and then Argon gas was introduced in the chamber (30 cm Hg) to avoid any possible leaks of the chamber. The gap between the quartz nozzle orifice and the surface of the Cu-wheel was maintained at 0.2 mm by a meter gauge detector. Argon was used as ejection gas, and the ejection pressure (10 kPa) was kept constant during the whole series of experiments. The speed of the Cu-wheel was increased gradually, and its effect on the thickness of the quenched ribbons was investigated. The thickness of the ribbons was measured by a micrometre and finally calibrated by the scanning electron microscopy (SEM) imaging. Thin ribbons of approximately 1 mm width and 10 cm length were fabricated. Table 1 summarises the effect of the speed of the copper wheel on the thickness of the amorphous ribbons.

Table 1. Effect of wheel speed on the thickness of the ribbons

Speed of Cu wheel (rpm)	**Thickness of ribbons (μm)**
2530	30
3550	20
4030	15
4470	11.5
4968	8
5100	5.5

A higher rotation speed of the copper wheel enables the fabrication of thinner ribbons and also means that the material experiences a higher cooling rate. It is generally accepted that the solidification rate, *R*, is inversely proportional to the square of the thickness of the solidified molten layer. For a layer of thickness, *x*, solidified at a heat transfer coefficient ∞, the solidification rate can be calculated from equation 1.

$$R = \frac{A}{x^2} \tag{1}$$

where constant A is a function of the material properties and initial temperatures but is independent of x. The value of A is 8.1×10^{-3} m^2Ks^{-1} for ideal cooling (when the heat transfer coefficient is ∞) and it is less for nonideal cooling conditions [11]. For example, assuming an average value Assuming an estimated value of $A = 10^{-3}$ m^2Ks^{-1}, the solidification rate achieved will be approximately 10^5 Ks^{-1} for $x = 100$ µm and 10^9 Ks^{-1} for $x = 1$ µm. Based on this relation, the cooling rates experienced by the ribbons as a function of their thickness were calculated and presented in Fig. 1.

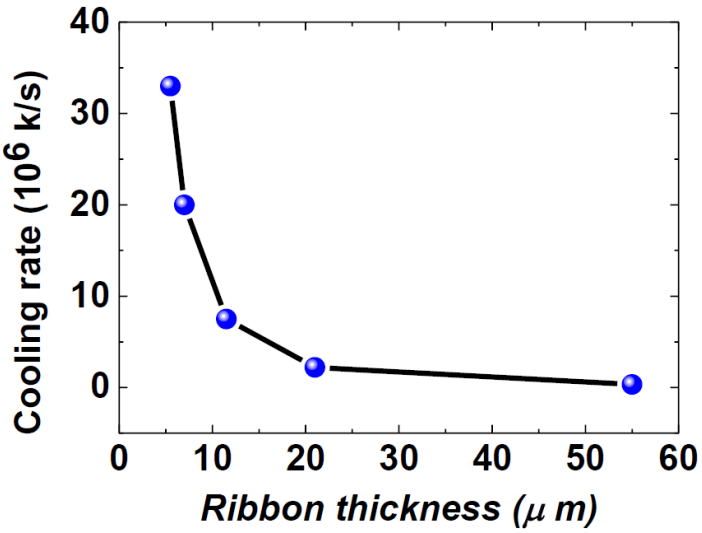

Fig. 1. Estimated cooling rates experienced by ribbons of different thicknesses.

4.3 Results and discussion

4.3.1 Atomic structure and surface morphology of ribbons

Fig. 2 presents the structural analysis of the as-quenched amorphous ribbons by X-ray diffraction (Cu-Kα radiation, λ=1.54 Å, Siemens 5000) and magneto-thermogravimetric (MTG) technique. The XRD spectrum of ultra-thin (5.5 µm) and 20 µm as-quenched ribbons shows similar diffraction patterns with a broad maxima in the range of 2θ = 40-50° (Fig. 2a). The presence of a broad hallow and the absence of Bragg's peaks in the diffraction patterns

confirm the disordered atomic structure of the ribbons. Additionally, the Curie temperature (T_C) depends on the state of the atomic structure and could be useful to trace a minimal phase precipitated during the rapid quenching process [8]. The temperature-dependent magnetisation, $M(T)$, of 5.5 µm and 20 µm ribbons, are presented in Fig. 2(b). Both samples reveal a single phase $M(T)$ behaviour without showing any "kink" before reaching the T_C (i.e., 440 $^{\circ}$C). The overlapped $M(T)$ curves of both samples show that the atomic structure of ribbons was monolithic amorphous until crystallisation at 510 ^{o}C.

The surface morphology of ribbons was investigated using scanning electron microscopy (SEM) and a profilometer as presented in Fig. 3. The cross-sectional image of the thinnest

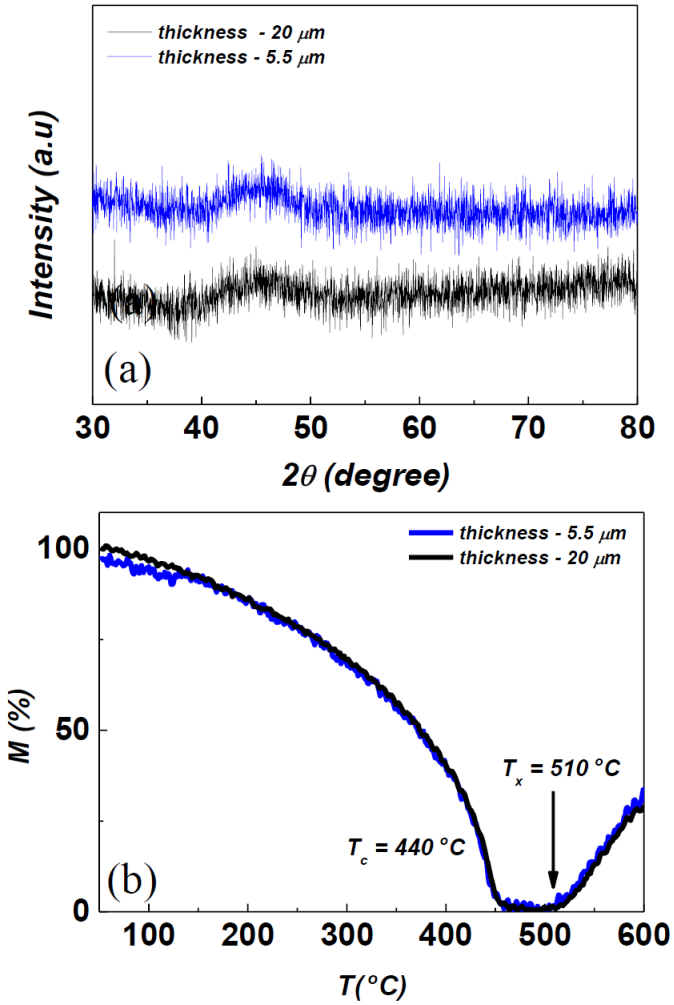

Fig. 2. (a) The X-ray diffraction patterns of 5.5 µm and 20 µm ribbons, (b) The temperature dependent magnetic behaviours, M (T), of 5.5 µm and 20 µm ribbons were measured by using a magneto-thermogravimetric technique.

ribbon is presented in Fig. 3a. The SEM micrographs of the surface of the ribbons show that surface of amorphous ribbons becomes dramatically rough when the thickness is reduced to 5.5 µm. In addition, the roughness of amorphous ribbons was evaluated by a profilometer and presented in Fig. 3f. The roughness of thinner ribbons is significantly high and in agreement with the SEM observations. Despite the very rough surface, the ultra-thin ribbons are continuous without any pores over a large scale.

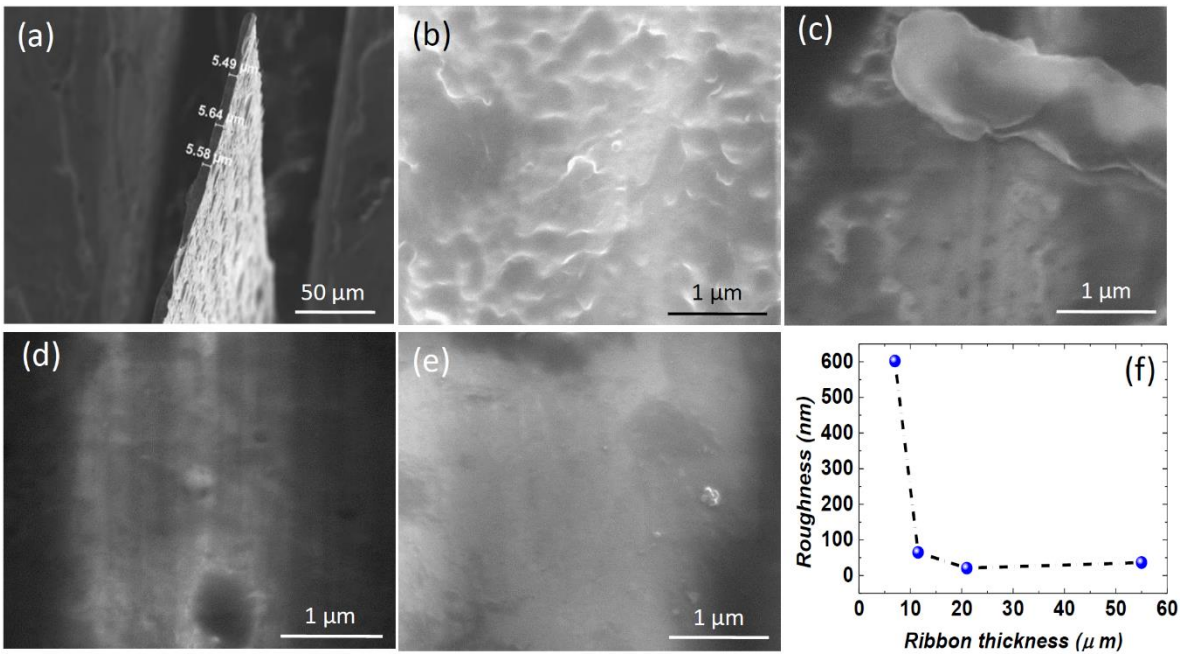

Fig. 3: (a) SEM micrograph of the cross-section of the thinnest ribbon. SEM micrographs of the surface of ribbons: (b) 5.5 µm, (c) 7 µm, (d) 11.5 µm, (e) 21 µm. (f) the surface roughness of the ribbons measured by a profilometer.

4.3.2 Magnetic properties of amorphous ribbons

Fig. 4 represents the quasistatic soft magnetic properties of the as-quenched amorphous ribbons. The in-plane magnetic hysteresis loops, illustrated in Fig. 4a, were carried out by a BH-loop tracer (SHB, MESA 200HF) along the length (25 mm) of the ribbons by applying a maximum field of 40 kA/m and were utilised to measure the coercivity (H_c) of the samples.

Fig. 4b presents the thickness-dependent H_c of amorphous ribbons, while the inset illustrates the magnetic response of the material at low magnetic fields. Ultra-low $H_c < 0.5$ A/m

of amorphous ribbons (≥ 21 μm) show the radical soft magnetic behaviour of the alloy. The exceptional soft magnetic properties of as-quenched ribbons confirmed that magnetoelastic contribution to magnetic properties was negligible and the magnetostriction constant of the amorphous alloy is close to zero. Nevertheless, the H_c gradually increased as a function of thickness and reached 5 A/m for 5.5 μm ultra-thin ribbons.

The thickness-dependent soft magnetic behaviour of amorphous ribbons can largely be explained by the contribution of surface inhomogeneities produced during the quenching

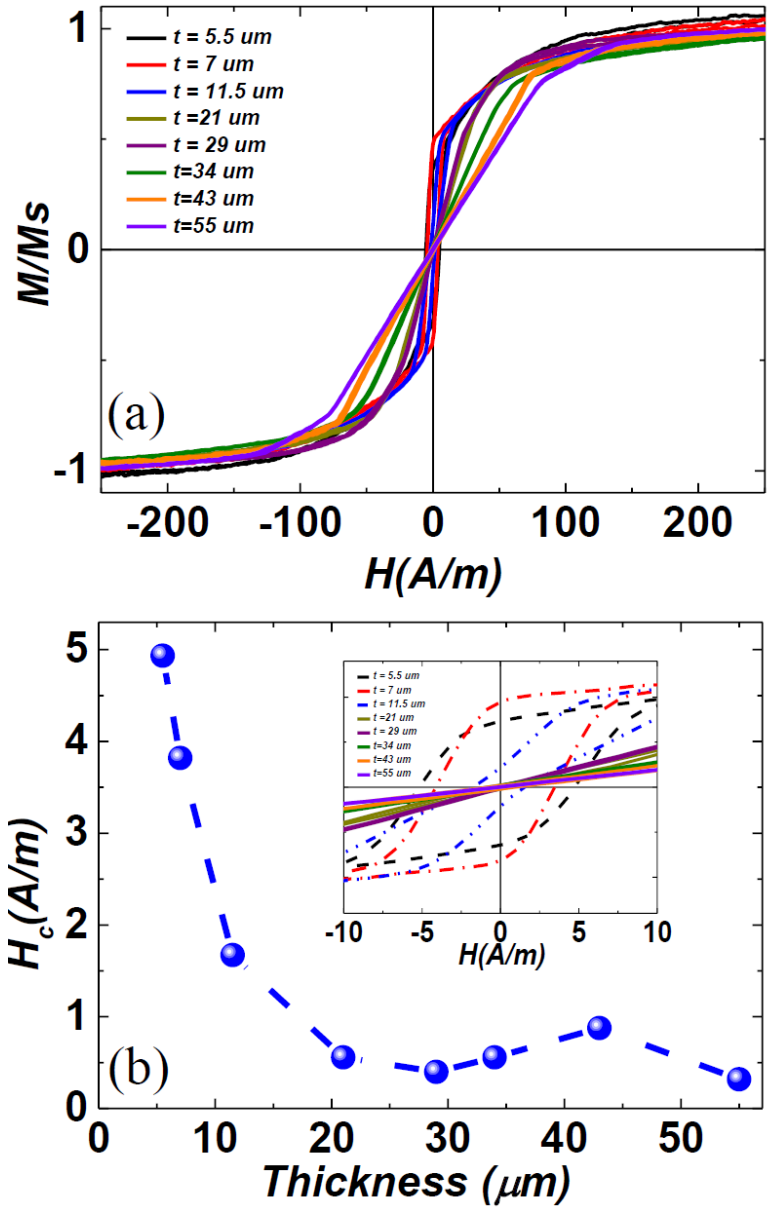

Fig. 4. (a) Hysteresis loops of the samples with different thicknesses, (b) coercivity of the amorphous ribbons as a function of their thicknesses.

process. The relatively high value of H_c is likely due to the pinning of the domain walls at the large surface irregularities observed (Fig. 3) in thinner ribbons. In such a case, when the magnetisation reversal process is dominated by the pinning of the domain walls due to thickness-dependent roughness, the H_c is inversely related to the thickness of the sample, as shown in Eq. 2.

$$H_C \propto \frac{\gamma}{t} \tag{2}$$

where t is the ribbon thickness, and γ is the domain wall energy [12]. In a multidomain regime, the magnetisation reversal process is due to the domain wall motion, and the domain wall propagates in an energy landscape influenced by some of the factors, such as grain boundaries, surface roughness, and defects. Therefore, the potential barriers and potential minima, the so-called pinning sites, inhibit the nucleation and propagation of the domain walls. Thus, in thinner ribbons, surface irregularities act as local barriers, which may inhibit the nucleation and motion of the domain wall during the magnetisation reversal. The H_c, which is required to overcome these barriers, is seen to increase with the decreasing ribbon thickness (see Fig. 4b). The contribution to H_c should be rather low for bulk cast ($\geq$ 20 μm) samples because (i) the surface upon casting is very smooth and (ii) the thickness is significantly larger than the ultra-thin ribbons resulting in a higher proportion of volume to surface area in thicker ribbons.

In addition to the surface inhomogeneities, the partial instability of free volume below the melting point in the disorder atomic structure, known as voids, are the source of pinning sites for the domain wall motion [13, 14]. The voids in amorphous metals are similar to the defects in crystalline materials and work as stress sources [14]. The possibility of originating voids is much higher at extremely high cooling rates due to an immediately frozen liquid state of the alloy, hence leads to a high level of stored internal stress in thinner ribbons. The fluctuation of internal stress or the number of voids can be reduced by annealing the amorphous alloys in the supercooled regime before crystallisation [7]. The 5.5 μm amorphous ribbons were annealed at 480 $^{\circ}$C for 600 sec and characterised for their soft magnetic properties. The coercivity (H_c = 1.6 A/m) of the ribbons is reduced by a factor of three after annealing. The improved soft magnetic properties could be attributed to the highly dense disorder atomic structure, and a reduced number of voids attained during the annealing process [7].

4.4 Conclusions

A rapid quenching approach of *in-situ* thinning was developed to produce ultra-thin amorphous ribbons of Co-Fe-B-Si-Nb alloy. The ultra-thin amorphous ribbons were continuous without any pores over a large scale and retained excellent soft magnetic properties. The thickness-dependent magnetic properties of the amorphous ribbons were largely attributed to the surface inhomogeneities and voids produced during the quenching process.

The *in-situ* thinning process of amorphous ribbons significantly reduces the cost of amorphous ribbons by consuming less amount of material. In addition, it eliminates the need for post-processing steps to reduce the thickness of ribbons to get an advantage of reduced eddy currents at high frequencies. The *in-situ* thinning process of amorphous alloys improves materials' performance, reduces material's cost and provides the opportunity for mass production of the high flux density soft magnetic amorphous materials at relatively lower costs.

Acknowledgements

The authors would like to thank CCAN and Enterprise Ireland (EI) for the financial support to perform the research work. The authors would like to thank Nuvotem Talema, Energy Limited, Excelsys Technologies for supporting the research program.

4.5 References

[1] S. Kulkarni, et al., Low loss magnetic thin films for off-line power conversion, IEEE Trans. Magn. 50 (4) (2014).

[2] A. Masood, et al., Controlling the competing magnetic anisotropy energies in FineMET amorphous thin films with ultra-soft magnetic properties, AIP Adv. 7 (5) (2017).

[3] A. Masood, et al., Tailoring the ultra-soft magnetic properties of sputtered FineMET thin films for high-frequency power applications, 8th Joint European Magnetic Symposia (Jems2016), 2017, p. 903.

[4] S. Kulkarni, et al., Low loss thin film magnetics for high frequency power supplies, 2014 16th European Conference on Power Electronics and Applications (Epe'14- Ecce Europe), (2014).

[5] A. Masood, et al., The effect of Ni-substitution on physical properties of Fe72-xB24Nb4Nix bulk metallic glassy alloys, MRS Proc. (2011) 1300.

[6] A. Masood, et al., Co-based amorphous thin films on silicon with soft magnetic properties, AIP Adv. 8 (5) (2018).

[7] A. Masood, et al., Effect of Ni-substitution on glass forming ability, mechanical, and magnetic properties of FeBNbY bulk metallic glasses, J. Appl. Phys. 113 (1) (2013).

[8] S. Lee, et al., Magneto-Thermo-Gravimetric technique to investigate the structural and magnetic properties of Fe-B-Nb-Y Bulk Metallic Glass, 13th International Conference on Rapidly Quenched and Metastable Materials, 2009, p. 144.

[9] K. Ackland, et al., Ultra-soft magnetic Co-Fe-B-Si-Nb amorphous alloys for high frequency power applications, AIP Adv. 8 (5) (2018).

[10] J.M. Silveyra, et al., High performance of low cost soft magnetic materials, Bull. Mater. Sci. 34 (7) (2011) 1407–1413.

[11] C. Suryanarayana, A. Inoue, Bulk Metallic Glasses, CRC Press, Boca Raton, 2011. [12] Y.M. Kim, et al., Thickness effects on magnetic properties and ferromagnetic re- sonance in Co-Ni-Fe-N soft magnetic thin films, J. Appl. Phys. 91 (10) (2002) 8462–8464.

[13] T. Bitoh, A. Makino, A. Inoue, Origin of low coercivity of Fe-(Al, Ga)-(P, C, B, Si, Ge) bulk glassy alloys, Mater. Trans. 44 (10) (2003) 2020–2024.

[14] T. Bitoh, A. Makino, A. Inoue, Quasi-dislocation dipole-type defects and low coer- civity of Fe-based soft magnetic glassy alloys, Metastable Mechanically Alloyed Nanocryst. Mater. 24–25 (2005) 427–430.

Chapter 5 On the mechanisms limiting power loss in amorphous CoFeB-based melt-spun ribbons

Journal of Magnetism and Magnetic Materials 502 (2020) 166535

Contents lists available at ScienceDirect

Journal of Magnetism and Magnetic Materials

journal homepage: www.elsevier.com/locate/jmmm

Research articles

On the mechanisms limiting power loss in amorphous CoFeB-based melt-spun ribbons

Hasan Ahmadian Baghbaderani[a,b,*], Ansar Masood[a], Zoran Pavlovic[a], Kenny L. Alvarez[c,d], Cian ÓMathúna[a,e], Paul McCloskey[a], Plamen Stamenov[a,b]

[a] Microsystems Centre, Tyndall National Institute, University College Cork, Cork, Ireland
[b] School of Physics and CRANN, Trinity College, Dublin 2, Ireland
[c] CEIT-IK4 and Tecnun (University of Navarra), San Sebastián, Spain
[d] Escuela de Ingeniería Mecánica, Pontificia Universidad Católica de Valparaíso, Valparaíso, Chile
[e] School of Electrical and Electronic Engineering, University College Cork, Cork, Ireland

Abstract

The mechanisms that limit the power loss performance in melt-spun amorphous ribbons have been investigated through DC and AC magnetic characterisation methods. The measured total power loss is resolved into hysteresis, eddy current, and anomalous losses. The anomalous loss is found to account for more than 90% of the total loss, which is significantly reduced by annealing in a transverse magnetic field. This is attributed to the reorientation of the preferred magnetisation axis perpendicular to the length of ribbons. Transverse magnetic annealing promotes the relative contribution of domain rotation over domain wall motion during the magnetisation reversal process. Magnetic annealing also causes a measurable decrease in the domain width, which promotes pinning and inhibits domain wall motion, thus further favouring coherent domain rotation as the primary mechanism of magnetisation. This combination accounts for a 75% decrease in the total power loss in the so-processed ribbons and renders them attractive for applications in mid- and high-frequency power supplies and inverters.

Keywords: Amorphous alloy; Magnetic properties; Magnetisation process; Magnetostructural transformations

5.1 Introduction

Power loss during electrical conversion accounts for a large percentage of the total dissipation (primarily heat) during power transmission and distribution. This is not only felt close to the end-user, resulting in a decreased efficiency of consumer-grade power electronic components [1]; but also in high-power applications such as power inverters used within photovoltaic installations [2]. The overall power loss can be attributed broadly to three different mechanisms, namely, hysteresis loss, eddy current loss, and anomalous loss. It is well understood that as the operating frequency f increases, the eddy current and anomalous losses become dominant at f > 100 kHz for metallic, high polarisation materials. On the other hand, recent advances in power conversion circuits have pushed their switching frequencies to 100s of kHz and even into the megahertz range [3, 4]. The utilization of these benefits is more readily attainable using ferrite-based low-moment materials, which are insulating. However, the low flux density typical to ferrites (0.3 – 0.4 T) requires considerable cross-sectional area, which is

massive in many deployments [5]. Thus, to put conducting and insulating core materials on a level playing field, a key metric has to be used, say for transformer applications, which work as a direct indication of the overall efficiency of the end device. One such choice is material power loss performance. Presently, ferrites, iron powder [6] and tape wound cores [7, 8] are primarily used for relatively low-power applications, where only grams of material are required per installation. An affordable, yet efficient, high-moment magnetic material, allowing for operation beyond 100 kHz, would enable mass application in higher power export-to-grid invertors (in the kW range), which are expected to become prolific in the near future as many countries are adopting new regulations with respect to renewable energy sources.

Based on related parameters to calculate the as-mentioned different kinds of losses [5], the next generation of miniaturised power electronic devices requires cores with high magnetic flux density, high resistivity, and ultra-low coercivity along with ease of manufacturability [9]. All of these characteristics are documented in amorphous materials. Furthermore, good high-frequency permeability can be observed in this type of material which is due to the combination of low coercive resulting from the homogeneous glassy structure and low eddy current loss resulting from relatively high electrical resistivity [10]. Therefore, due to the variety of applications for these materials, the largest volume usage, by far, both in dollars and tonnage, is in the cores of electrical distribution transformers [11].

Since 1995, a number of Fe- and Co-based amorphous alloys with T_C well above room temperature have been developed by different rapid cooling methods, such as copper mould casting or water quenching. The formation and properties of multicomponent Fe-based Bulk Metallic Glasses (BMGs) have attracted increasing attention because of the fundamental interests in their properties and the high industrial application potential [10]. For Co-based amorphous alloys, it is known that CoFeSiB alloys with zero magnetostriction exhibit high permeability and have been subsequently developed as ultra-low coercivity sensor materials. However, as a result of the poor glass-forming ability (GFA), high cooling rates are required, in order to obtain an amorphous phase directly from the liquid state, causing limitations in the shape and dimensions of the resulting material, limiting it to either a ribbon or a wire form [12]. One notable practical advantage of thin melt-spun ribbons is their lower eddy current loss, as compared to their crystalline counterparts, when utilised in tape wound magnetic cores.

Anomalous loss dominates the total dynamic loss in most soft magnets with a uniaxial anisotropy oriented longitudinally to the applied magnetic field. It originates from localised eddy currents around moving domain walls under the driving action of an external magnetic field. The anomalous loss can be decreased through changing the mechanism of magnetisation from predominantly domain wall motion to the coherent rotation of domains, which can be done using transverse magnetic annealing. The mechanisms of inducing magnetic anisotropy by magnetic annealing include atomic pair ordering resulting in directional order in the sample, structural relaxation, and rearrangement of free volume in amorphous materials [6].

In the present work, the effect of transverse magnetic annealing on the magnetisation reversal process and power loss mechanisms in amorphous melt-spun CoFeB-based ribbons is studied. To clarify and understand the loss-limiting mechanisms and guide a decrement in anomalous loss, Magneto-Optic Kerr Effect (MOKE) microscopy is used in parallel to bulk magnetisation measurements and model-based evaluations.

5.2 Experimental Methods

Melt-spun ribbons of 20 μm thickness and 1 mm width, with the composition of $Co_{65.88}Fe_{4.2}B_{24}Si_{1.92}Nb_4$, are obtained using fabrication conditions explained in reference [13]. X-ray powder diffraction (XRD) data of the melt-spun ribbons are collected using a Phillips PANalytical X'pert Pro diffractometer, with an operational wavelength of 1.5405 Å (Cu-Kα anode). The thermal behaviour of the ribbons before any annealing treatment is evaluated by Differential Scanning Calorimetry (DSC) in TA Instrument DSC 2920. DSC experiments are performed on 20 mg of ribbons, at the heating rate of 10 K/min in the Ar atmosphere. The ribbons are thermally annealed and magnetically annealed at 5 Tesla for one hour at three different temperatures (450, 475, and 500 °C) in a magnetic annealing oven (Model: TEL MRT5000) provided by Tokyo Electron Magnetic Solutions, Ltd. The magnetic annealing temperature was measured and controlled through a system including a thermocouple attached to the sample holder. The small coercivity (< 3 A/m) and anisotropic field of the ribbons, along its length, is accurately measured by a B-H loop tracer running at 10 Hz with a maximum applied magnetic field up to 0.1 T and with the resolvable magnetic field of 0.01 A/m. The

initial relative permeability of ribbons is calculated based on the slope of the hysteresis loop linear part. In addition, Evico Magnetics Kerr Microscope & Magnetometer is used for the visualisation of magnetic domains at $\mu_0 H$ = 0 T when the ribbons are in the remanent state of the magnetisation.

The power loss characterisation of the ribbons is performed using a custom design air-core solenoid inductor. One hundred fifty turns of 28 gauge Cu wire are wound on a 5 cm long hollow cylinder of 5 mm outer radius with near-zero spacing between the turns to create a uniform excitation field inside the solenoid. The impedance of the air core solenoid, Z_a, is measured using an LCR meter (HP4284A) at various excitation current levels. Three ribbon pieces (20 mm × 1 mm × 0.02 mm) are fixed on a sample holder and inserted inside the solenoid, along its axis, where the uniformity of the field is best (see Fig. 1). Without moving the probes from the test fixture, the ribbons are centred inside the solenoid to be at the same distance from both open ends, where the field lines are no longer parallel to the axis. In this way, the magnetic core material is exposed to a uniform excitation field along its length. The Cu turns are at a sufficient distance from the solenoid axis so that the demagnetisation field does not alter the field lines around the turns, maintaining the same AC winding resistance as in the case of air-core solenoid measurement. Therefore, the difference between the impedance measurement with and without magnetic core material, Z_c and Z_a, respectively, at different frequencies, represents the contribution of the magnetic core to the inductance and power loss at each frequency. As the cross-sectional area of the ribbons is significantly smaller than that of the solenoid, the effect of the insertion of the magnetic core on the real part of the inductance is negligible. Thus, the magnetic material power loss is calculated as [8];

$$P_{\text{loss}} = \text{Re}(Z_c - Z_a)I^2 \tag{1}$$

where $\text{Re}(Z_c - Z_a)$ is the real part of the complex impedance difference and I is the excitation current measured using the LCR meter. The induction field inside the ribbon samples is calculated by [8]:

$$B = \frac{\text{lm}(Z_c - Z_a)I}{(2\pi f S)}\pi r^2 \tag{2}$$

where f and S are the measurement frequency and the total cross-sectional area of the ribbons, and r is the radius of the coils. The power loss measurement method has been tested with commercial samples, and the results are in good agreement with the reported power loss in standard datasheets. The AC signal magnitude of 40-100 mA was used to measure the impedance and the excitation current. It should be mentioned that the values of Inductance and Resistance were measured directly by the LCR meter and no equivalent circuit was used to determine the a-mentioned values from the measured impedance and phase angle data. The PCB board in Figure 1b was only used to put the LCR meter probes in contact with the solenoid copper wire. In addition, the air core measurements let us to eliminate the effect of copper resistance.

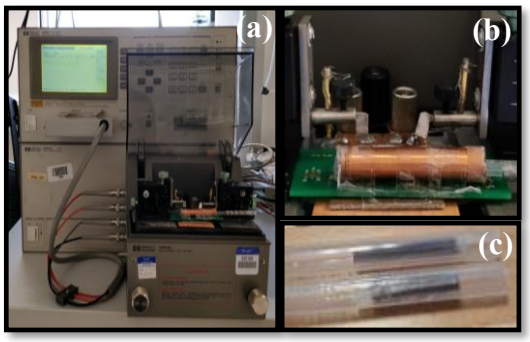

Figure 1. Power loss measurement set-up; (a) complete set-up, (b) solenoid with 150 turns of wire of gauge 28 to produce a coherent magnetic field at the centre, and (c) sample holders.

Furthermore, high-frequency permeability is derived from the inductance measurement of the single turn closed core toroidal inductor using the following equation:

$$\mu = \frac{lL_e}{\mu_0 N^2 S} \tag{3}$$

where L_e is the measured inductance, l is the magnetic path length of the toroidal core, S is the cross-sectional area of the toroidal core, N is the number of copper turns, and μ_0 is the free space permeability.

5.3 Results and discussion

5.3.1 DC Magnetic Properties

The evolution of hysteresis loops measured along the length of the ribbons as a function of magnetic annealing temperature is shown in Fig. 2. As can be seen, an increase in magnetic annealing temperature causes more sheared-over loops, which suggests that the mechanism of the magnetisation reversal process is changing from domain wall motion to rotation. Based on the DSC trace (Fig. 3) and XRD patterns (Fig. 4), up to magnetic annealing temperatures of 500 °C, the microstructure of the ribbons is still amorphous. Additionally, the important features distinguishing the hysteresis loops from each other in Fig. 2 can be explained using different parameters. First, when the field is growing from zero (Fig. 2, arrow 1), the permeability would decrease due to an increase in transverse induced anisotropy (Fig. 5), which is moving the easy axis from the length to the width of the ribbons. In addition, saturation is not achieved until $H = H_k$; this parameter, the induced anisotropy field (H_k), is increased when the annealing temperature is increased. It also represents the induced anisotropy energy (K_u) (Fig. 6) which is calculated based on:

$$K_u = \frac{H_k \mu_0 M_s}{2} \tag{4}$$

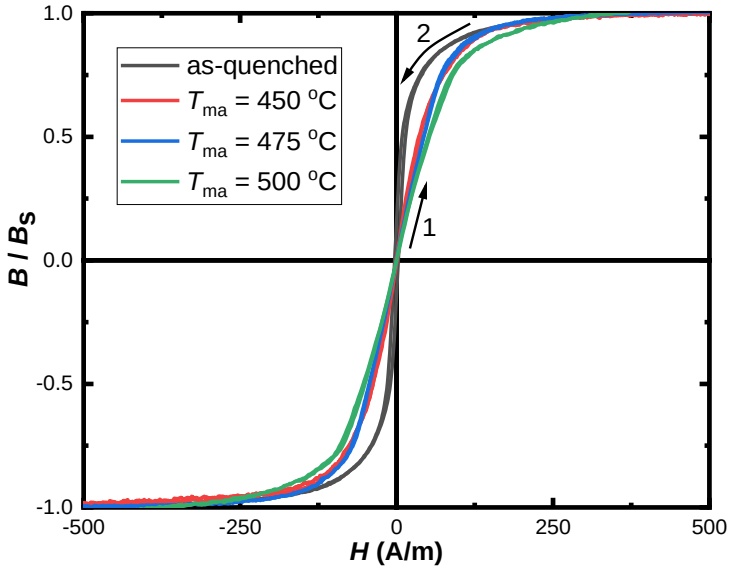

Figure 2. Hysteretic loops of as-quenched and magnetically annealed amorphous ribbons.

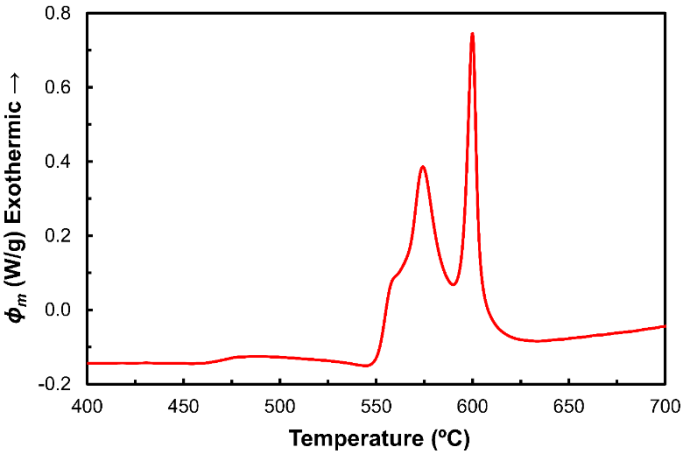

Fig. 3. DSC trace of CoFeB-based melt-spun ribbons.

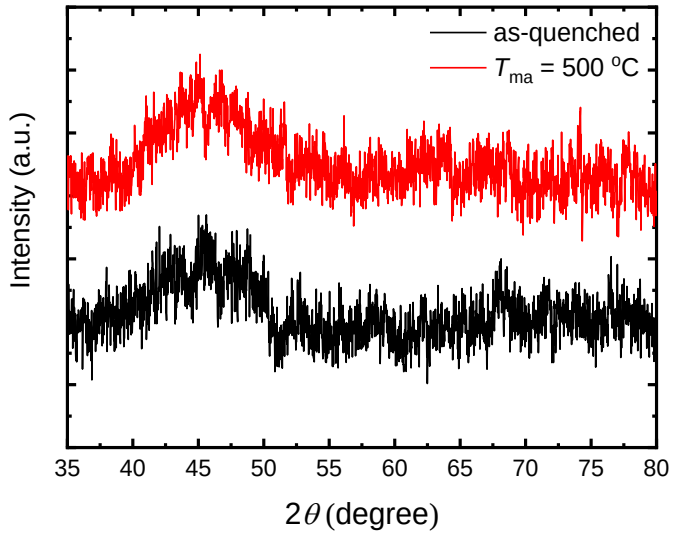

Figure 4. XRD patterns of as-quenched and magnetically annealed ribbons at 500 °C.

The high induced anisotropy at elevated temperatures could be due to larger atomic mobility, leading to a microstructure in which atomic pairs of magnetic elements are ordered [14]. By increasing the annealing temperature, as H is decreased from saturation (Fig. 2, arrow 2), the system tends to demagnetise itself more completely, which results in a decline in B_r/B_s (Fig. 5). In other words, induced anisotropy takes over as H approaches zero and rotate the magnetisation toward the nearest easy direction. As can be seen in the diminishing trend of coercivity (see Fig. 7), the magnetisation becomes more reversible as the induced anisotropy

is increased [6]. This trend can also be due to the structural relaxation and rearrangement of free volume, as well as other mechanisms of inducing anisotropy.

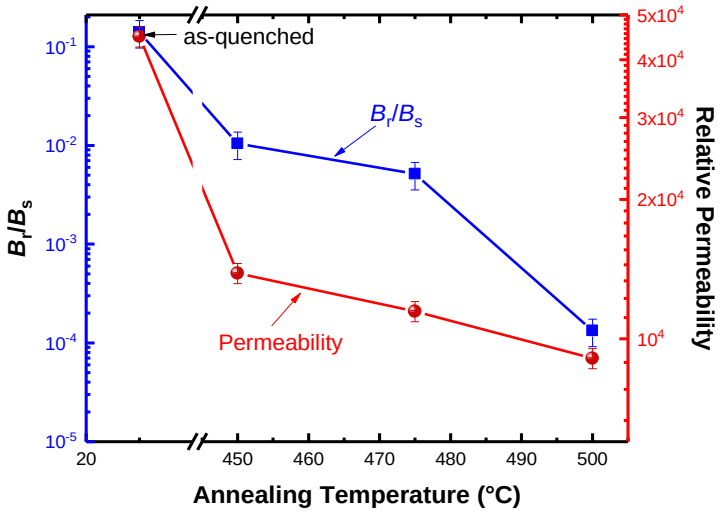

Figure 5. Relative permeability and the ratio between remnant magnetisation and saturation flux density (B_r/B_s) of the as-quenched and magnetically annealed samples at different temperatures.

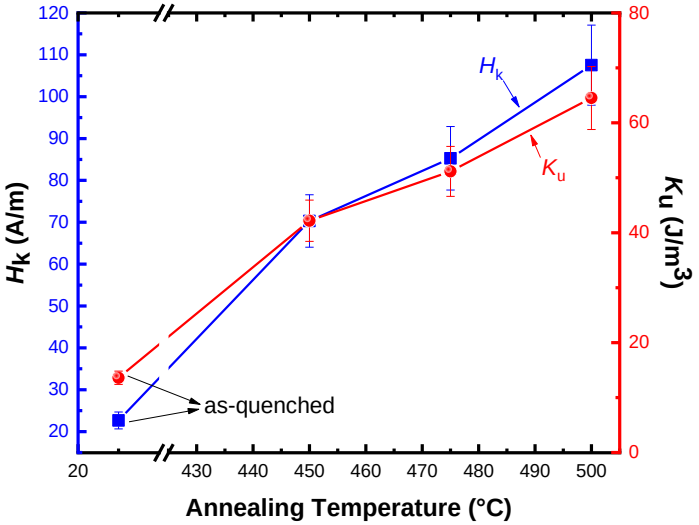

Figure 6. Magnetic anisotropy field (H_k) and Field-induced anisotropy (K_u) of the CoFeB-based ribbons annealed in a transverse magnetic field at different temperatures.

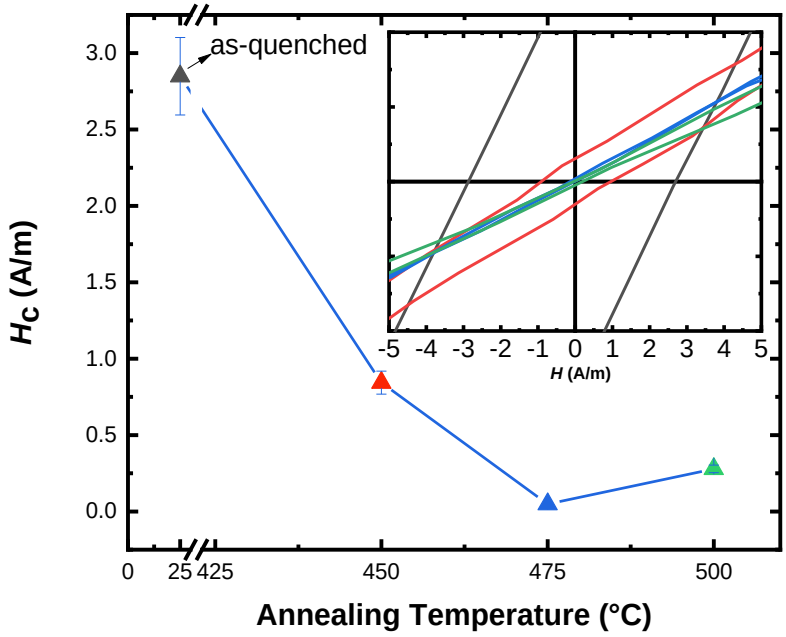

Figure 7. Coercivity of ribbons as a function of magnetic annealing temperature.

5.3.2 AC Magnetic Properties

Total power loss density increases with AC magnetic induction (B_{AC}) and frequency (Fig. 8). Samples, which have been magnetically annealed at higher temperatures, show a lower amount of power loss, a decrease of 75% after magnetic annealing at 500 °C, although the same cannot be eliminated entirely. In other words, by inducing anisotropy of an equivalent remagnetisation power density (K_u.f), the power loss density is decreasing. A linear relationship between the induced anisotropy power and the power loss holds in the system in a broad range of frequency (Fig. 9). Furthermore, the power loss is just a small fraction of the induced anisotropy power.

However, at higher levels of magnetic induction, this fraction is increasing (Fig. 9). To evaluate the effect of field annealing compared to simple annealing, ribbons are annealed in vacuum at 450, 475 and 500 °C. The power loss of the as-quenched sample is increased after simple annealing, as can be seen in Fig. 8 at three different frequencies. This effect can be

attributed to the more relaxed microstructure of the ribbons, which makes domain wall motion

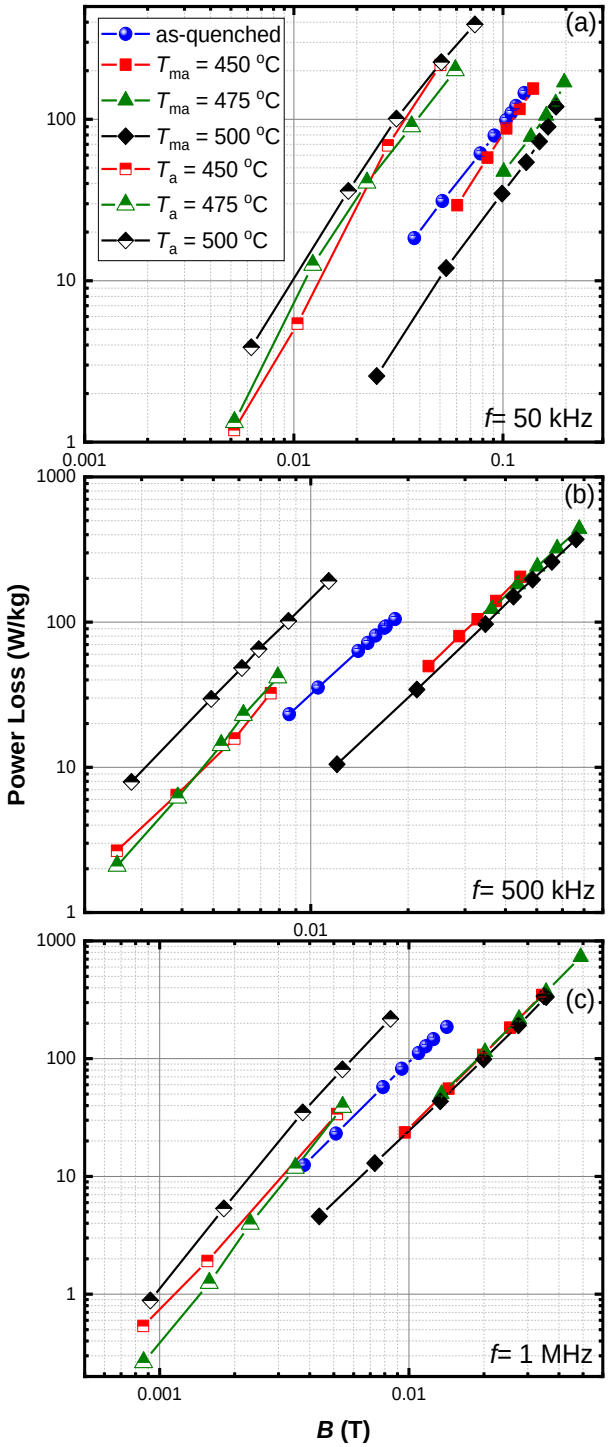

Figure 8. Power loss density of as-quenched, magnetically annealed, at T_{ma}= 450, 475 and 500 °C, and simply annealed, at T_a= 450, 475 and 500 °C, ribbons as a function of the intensity of the applied magnetic induction at different frequencies; (a) 50 kHz, (b) 500 kHz and (c) 1 MHz.

easier and as a consequence, the power loss is bigger, likely due to the micro-induction currents associated with the domain wall motion, i.e., the anomalous loss, which will be addressed accordingly.

To evaluate the contribution of different kinds of losses and their relations to microstructural and magnetic parameters, a power loss decomposition based on the analysis borrowed from reference [5] has been carried out. According to these estimates, more than 90% of total power loss is due to anomalous loss, which is in agreement with previous studies [15-17]. This contribution can be due to the low amount of hysteresis and the high permeability in the ultra-soft magnetic ribbons, which means that the primary mechanism of magnetisation is domain wall motion, instead of magnetisation rotation, which itself is mainly responsible for the anomalous part of the losses. Due to the excessiveness of this kind of loss, the relevant strategies for its minimization are discussed below in more detail.

5.3.2.1 Anomalous loss

The anomalous loss measured at 10 mT and the frequencies of 50, 500 kHz, and 1 MHz are shown in Fig. 10. It can be seen that inducing uniaxial anisotropy causes a substantial decline in the amount of anomalous loss. In other words, field annealing changes the magnetisation easy axis by inducing a transverse anisotropy, which also results in a domain size refinement, which in turn reduces the stray field energy (Fig. 11). To verify this observation, the average domain width w is estimated as [15]:

$$w \approx \sqrt{\frac{2\gamma_{\mathrm{w}} t}{K_{\mathrm{u}}.\left(N_{\mathrm{zz}} \sin^2 \beta + N_{\mathrm{yy}} \cos^2 \beta\right)}} \tag{5}$$

where γ_{w} is the domain wall energy, t is the ribbon thickness, β is the out-of-plane angle of the magnetisation vector, N_{zz} (≈ 1) is the demagnetising factor normal to the ribbon plane, while along the long axis $N_{\mathrm{xx}} \sim 0$, and N_{yy} ($\approx$0.004) is the demagnetising factor across the ribbon

width. For the ribbon with transverse anisotropy $\beta = 0$. The domain wall energy (γ_w) can be

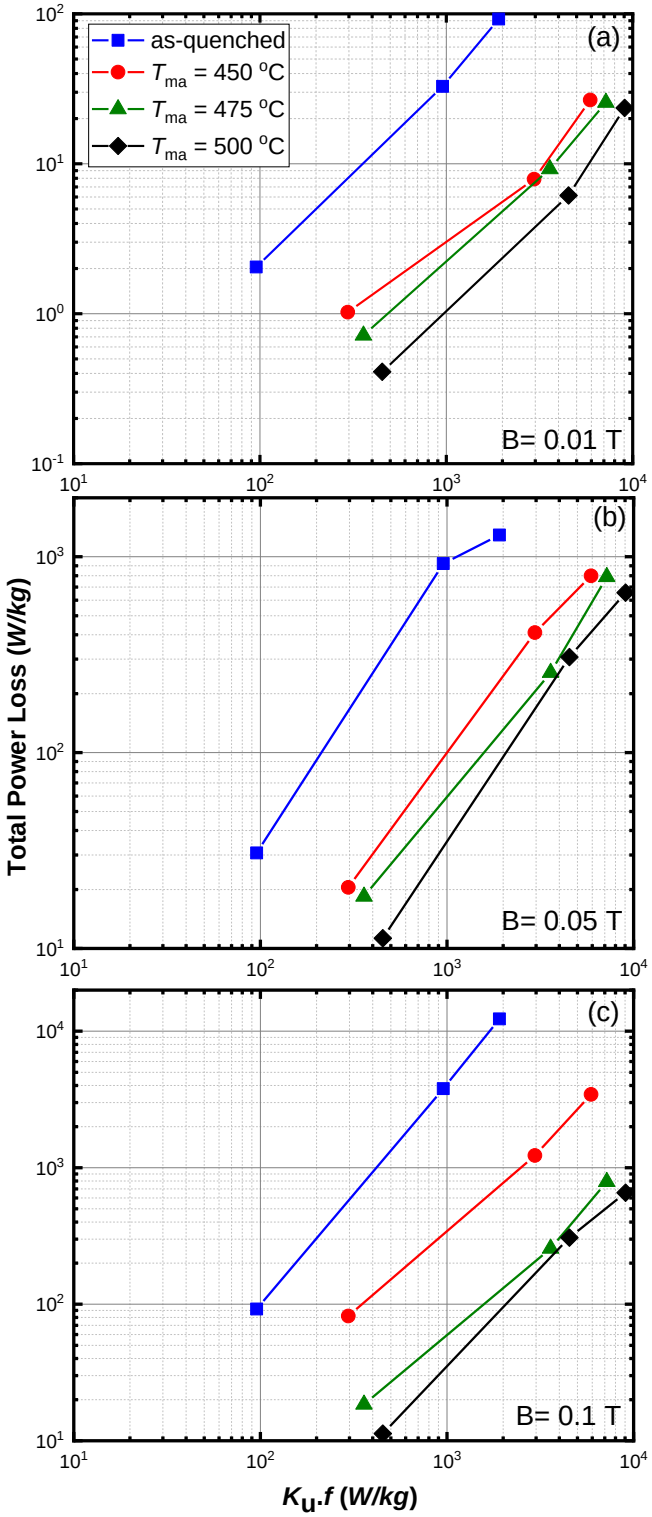

Figure 9. Total power loss as a function of induced anisotropy power for three different intensities of the magnetic induction.

calculated based on $\gamma_w = 2\pi\sqrt{AK_u}$ [18]. A is the exchange stifness constant which can be estimated based on the Curie temperature of the alloy [6]. It can be noticed that as magnetic annealing temperature is increasing, the average domain width would decrease (Fig. 11 and 12), and the domain wall energy would increase (Fig. 12), indicating that the induced anisotropy is changing the mechanism of magnetisation by making the domain wall motion harder as the domain wall energy is increasing [15]. Additionally, as can be seen in Fig. 11, the domain walls are getting smoother with increasing the magnetic annealing temperature that

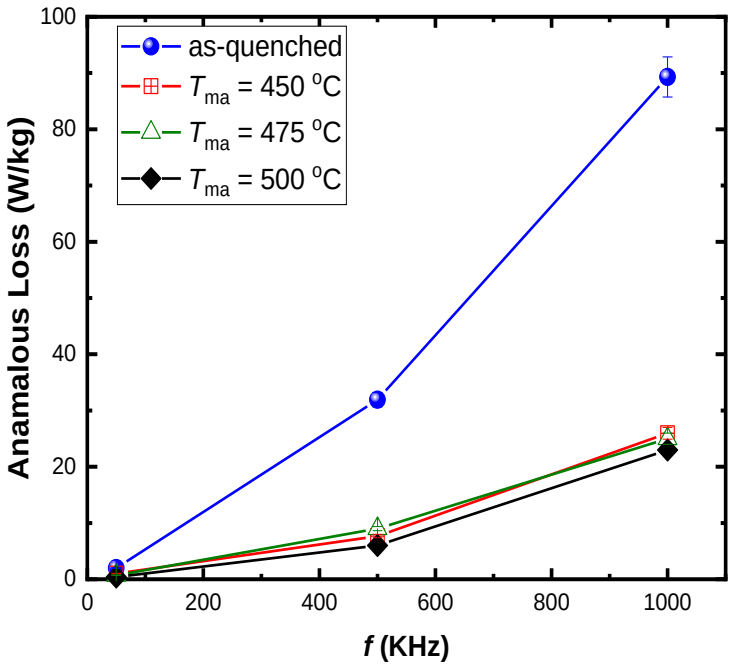

Figure 10. Anomalous loss of as-quenched and magnetic annealed samples as a function of frequency, measured at B = 0.01 T.

confirms incremental induced uniaxial anisotropy.

In addition, according to Herzer's theory [19], the relationship between total power loss and the total eddy current loss (P_{ec}), which includes classic eddy current loss and excess eddy current loss or anomalous loss, has the form as formulated in Eq. 6:

$$P_{\mathrm{t}} \approx P_{\mathrm{ec}}\left[1+\frac{w^2}{(w\cos\beta+t)^2}\frac{m^2}{1-m^2}\right] \tag{6}$$

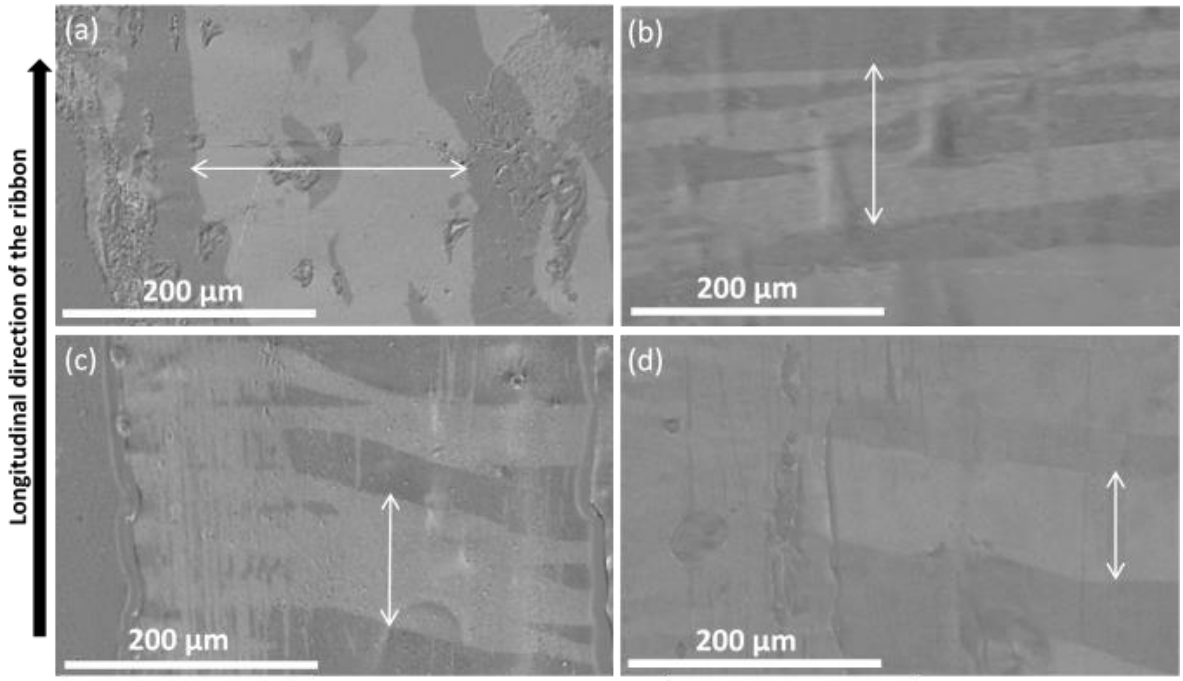

Figure 11. MOKE domain images of (a) as-quenched, and thermomagnetic annealed ribbons at (b) 450 °C, (c) 475 °C and (d) 500 °C. The domain imaging have been carried out at the remanent state of magnetisation.

where *m* denotes the average magnetisation component along the ribbon axis normalised to the saturation magnetisation. Thus, by decreasing the domain wall width (*w*) as a result of magnetic annealing, the total eddy current loss will decrease, which can be seen in Fig. 13 [15]. As it can be noticed in this figure, at B = 0.01 T, there is a reasonably good agreement between the measured and the calculated total eddy current loss based on Eq. 6. Similar behaviours are observed at higher values of B = 0.05 T and B = 0.1 T.

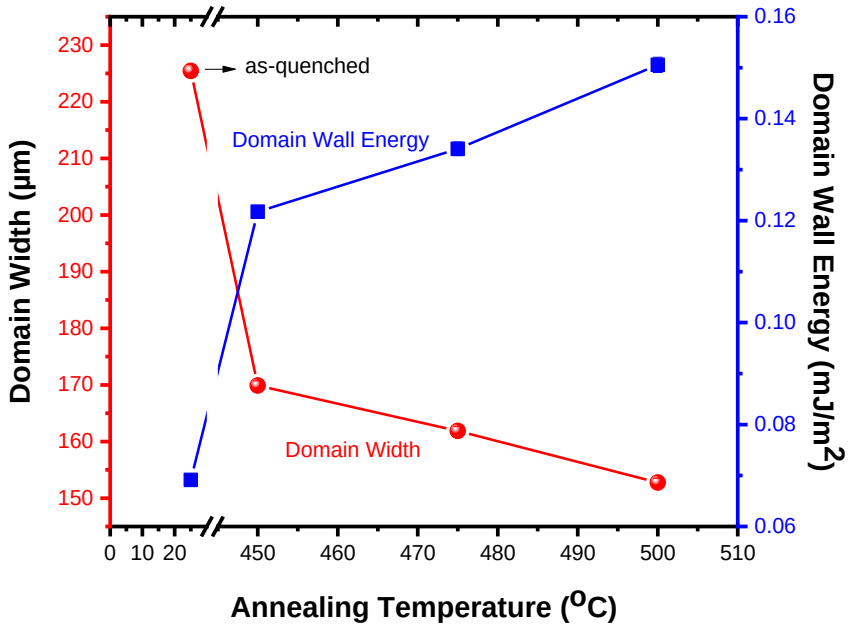

Figure 12. Calculated domain width and domain wall energy in magnetic annealed samples at different temperatures.

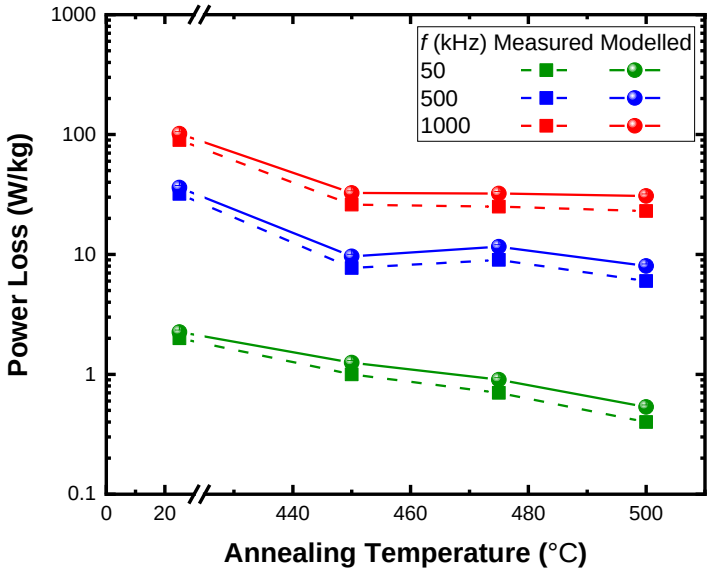

Figure 13. Measured and estimated total power loss of magnetic annealed samples at B = 0.01 T.

Additionally, to evaluate the application potential of the amorphous ribbons, the frequency spectrum of effective permeability, μ, is measured and shown in Fig. 14. The effective permeability of the as-quenched ribbons decreases steadily from 2000 to 240 in the frequency range from 50 kHz to 28 MHz, which is about 88% decrement. The permeability of the

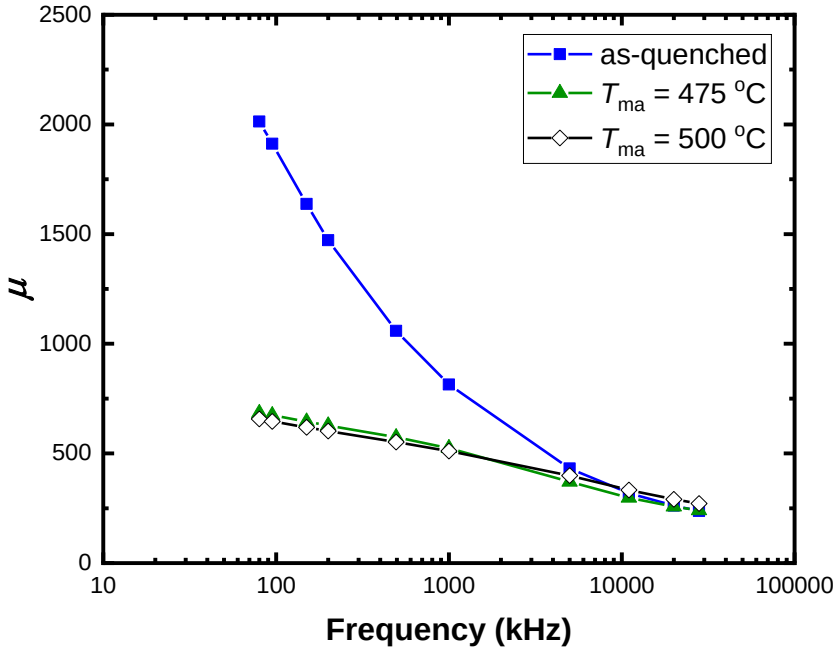

Fig. 14. Frequency dependence of the effective permeability of as-quenched and magnetic annealed ribbons at the frequency range of 50 kHz to 28 MHz.

magnetic annealed samples at 50 kHz is less than one-third of as-quenched ones, while the reduction rate of permeability for magnetic annealed samples in the as-mentioned frequency range is about 60%. At 50 kHz, the permeability of the as-quenched sample is much higher than the magnetic annealed samples because the primary mechanism of magnetisation is domain wall motion in this sample, while in the magnetic annealed samples, the dominant mechanism of magnetisation reversal is magnetisation rotation. Hence, the effective permeability in this frequency region is associated with the initial permeability of the material. Further increase in *f* causes a significant reduction in μ, which can be ascribed to a relaxation-type dispersion of the reversible bulging mechanism for which the domain walls are no longer able to follow the AC magnetic variations. Beyond the relaxation frequency,

μ becomes small, reflecting the contribution of the domain rotation as the dominant magnetisation process. Therefore, the abrupt change in the permeability of the as-quenched sample is due to a change in the mechanism of magnetisation reversal, while this change is much smaller for the magnetically-annealed samples, in which the primary mechanism of magnetisation is domain rotation, in the whole range of frequency.

5.4 Conclusions

Melt-spun ribbons have been annealed in a transverse magnetic field of 5 T, at varying temperatures of up to 500 °C. The effect of field-induced anisotropy on DC and AC magnetic properties are reported. Magnetic annealing results in ribbons with lower longitudinal coercivity and permeability (real part of permeability (μ') from 5,000 down to 1450, the imaginary part of permeability (μ'') from 100 down to 25 at 50 kHz) due to structural relaxation and a change in the easy axis of magnetisation of the ribbons, from along their length, to along their width, respectively. The latter results in the consequent predominance of domain rotation as the mechanism of magnetisation reversal. Therefore, the material-specific Q-factor (μ'/μ'') has improved from ~50 to ~58 at 50 kHz. Total power loss within the ribbons has been decomposed into hysteresis, eddy current, and anomalous losses. Based on this analysis, anomalous loss accounts for about 90% of total power loss, and through magnetic annealing and the associated decrease in the domain width, it can be reduced substantially. This mechanism is explained and verified using MOKE imaging and domain wall energy calculations based on magnetisation data. The measured behaviour of the total power loss is dominated by total eddy current loss, including eddy current and anomalous losses, and is in good agreement with Herzer's theory. Soft magnetic ribbons, of a low thickness (< 20 μm), of CoFeB-based metallic compositions, heat-treated in a transverse magnetic field of above 5 T, at a temperature in the range 450-500 ºC, therefore, hold great promise for power applications at frequencies in the range of 10 – 500 kHz, offering higher permeability alternative to ferrites.

Acknowledgement

The authors would like to thank the Science Foundation of Ireland (SFI) for the financial support to perform the research work under the grant number of 2015/SIRG/3569, Starting

Investigator Research Grant (SIRG). The authors would like to acknowledge Niclas Teichert and TEL Magnetic Solutions Company for helping in MOKE imaging and magnetic annealing.

5.5 References

[1] A.M. Leary, P.R. Ohodnicki, M.E. McHenry, Soft Magnetic Materials in High-Frequency, High-Power Conversion Applications, JOM, 64 (2012) 772-781.

[2] S.B. Kjaer, J.K. Pedersen, F. Blaabjerg, A review of single-phase grid-connected inverters for photovoltaic modules, IEEE Transactions on Industry Applications, 41 (2005) 1292-1306.

[3] J.S. Glaser, J.M. Rivas, A 500 W push-pull dc-dc power converter with a 30 MHz switching frequency, in: 2010 Twenty-Fifth Annual IEEE Applied Power Electronics Conference and Exposition (APEC), 2010, pp. 654-661.

[4] D.J. Perreault, J. Hu, J.M. Rivas, Y. Han, O. Leitermann, R.C.N. Pilawa-Podgurski, A. Sagneri, C.R. Sullivan, Opportunities and Challenges in Very High Frequency Power Conversion, in: 2009 Twenty-Fourth Annual IEEE Applied Power Electronics Conference and Exposition, 2009, pp. 1-14.

[5] S. Kulkarni, D. Li, N. Wang, S. Roy, C.Ó. Mathúna, G. Young, P. McCloskey, Low Loss Magnetic Thin Films for Off-Line Power Conversion, IEEE Transactions on Magnetics, 50 (2014) 1-4.

[6] R.C. O'Handley, Modern Magnetic Materials: Principles and Applications, Wiley, 1999.

[7] G. Herzer, Amorphous and Nanocrystalline Soft Magnets, in: G.C. Hadjipanayis (Ed.) Magnetic Hysteresis in Novel Magnetic Materials, Springer Netherlands, Dordrecht, 1997, pp. 711-730.

[8] R.W. Erickson, D. Maksimović, Fundamentals of Power Electronics, 3rd Ed., Springer, 2020.

[9] M. Ansar, M. Paul, M. Cian Ó, K. Santosh, Tailoring the ultra-soft magnetic properties of sputtered FineMET thin films for high-frequency power applications, Journal of Physics: Conference Series, 903 (2017) 012050.

[10] W.H. Wang, C. Dong, C.H. Shek, Bulk metallic glasses, Materials Science and Engineering: R: Reports, 44 (2004) 45-89.

[11] V.R.V. Ramanan, Metallic glasses in distribution transformer applications: An update, Journal of Materials Engineering, 13 (1991) 119-127.

[12] Q.K. Man, Y.Q. Dong, C.T. Chang, X.M. Wang, R.W. Li, Co-Based Bulk Metallic Glasses with Good Soft-Magnetic Properties and High Strength, Materials Science Forum, 898 (2017) 703-708.

[13] K. Ackland, A. Masood, S. Kulkarni, P. Stamenov, Ultra-soft magnetic Co-Fe-B-Si-Nb amorphous alloys for high frequency power applications, AIP Advances, 8 (2018) 056129.

[14] F. Johnson, C.Y. Um, M.E. McHenry, H. Garmestani, The influence of composition and field annealing on magnetic properties of FeCo-based amorphous and nanocrystalline alloys, Journal of Magnetism and Magnetic Materials, 297 (2006) 93-98.

[15] Z. Li, K. Yao, D. Li, X. Ni, Z. Lu, Core loss analysis of Finemet type nanocrystalline alloy ribbon with different thickness, Progress in Natural Science: Materials International, 27 (2017) 588-592.

[16] K.J. Overshott, The causes of the anomalous loss in amorphous ribbon materials, IEEE Transactions on Magnetics, 17 (1981) 2698-2700.

[17] M.A. Willard, T. Francavilla, V.G. Harris, Core-loss analysis of an (Fe, Co, Ni)-based nanocrystalline soft magnetic alloy, Journal of Applied Physics, 97 (2005) 10F502.

[18] L. Yue, S.-H. Liou, Magnetic Force Microscopy Studies of Magnetic Features and Nanostructures, in: B. Bhushan (Ed.) Scanning Probe Microscopy in Nanoscience and Nanotechnology 2, Springer Berlin Heidelberg, Berlin, Heidelberg, 2011, pp. 287-319.

[19] G. Herzer, Magnetic materials for electronic article surveillance, Journal of Magnetism and Magnetic Materials, 254-255 (2003) 598-602.

Chapter 6 Improved magnetic performance of Co-based ribbons by nanocrystallisation through magnetic annealing

Journal of Magnetism and Magnetic Materials 503 (2020) 166630

Contents lists available at ScienceDirect

Journal of Magnetism and Magnetic Materials

journal homepage: www.elsevier.com/locate/jmmm

Research articles

Improved magnetic performance of Cobalt-based ribbons by nanocrystallization through magnetic annealing

Hasan Ahmadian Baghbaderani[a,b,*], Ansar Masood[a], Zoran Pavlovic[a], Niclas Teichert[b], Cian Ó. Mathúna[a,c], Paul McCloskey[a], Plamen Stamenov[a,b]

[a] Microsystems Centre, Tyndall National Institute, University College Cork, Cork, Ireland
[b] School of Physics and CRANN, Trinity College, Dublin 2, Ireland
[c] School of Electrical and Electronic Engineering, University College Cork, Cork, Ireland

Abstract

Phase transformation driven soft magnetic properties have been correlated through different stages of nanocrystallisation of Co-based amorphous alloys, via transverse magnetic annealing, by combining structural, magnetothermal, domain imaging, AC and DC magnetometry techniques. The nanocrystallisation starts by nucleation and growth process of soft magnetic meta-stable, thermodynamically favoured, $Co_{23}B_6$ phase with less nucleation activation energy compared to other stable phases. In the second crystallisation stage, Co_2B and Co_3B, as semi-hard magnetic phases, are identified in the alloys, magnetic annealed at 525 and 550 °C, respectively. Field-induced anisotropy dominates over the residual contributions of magneto-crystalline anisotropy of the phases, precipitated after field annealing at 510, 515, and 525 °C. The anomalous loss is significantly reduced by annealing in a transverse magnetic field due to the reorientation of the preferred magnetisation axis, and consequently, the change in dominant magnetisation reversal mechanism from domain wall motion to magnetisation rotation. In addition, magnetic annealing causes a measurable decrease in the domain width, which, in turn, promotes pinning and inhibits domain wall motion, thus further favours coherent domain rotation as the primary mechanism of magnetisation. The combined mechanism of nanocrystallisation and coherent magnetisation rotation accounts for a 70% decrement in the anomalous loss in the so-processed ribbons at 525 °C, which renders them attractive for applications in mid- and high-frequency power supplies and inverters.

Keywords: Amorphous alloys, Nanocrystallisation, Magnetic annealing, Soft magnetic properties, Magnetisation reversal process, Magnetostructural transformations.

6.1 Introduction

Soft magnetic nanocomposites are generally synthesised by crystallising amorphous metal precursors that typically include large (e.g., Zr, Nb) and small atoms (e.g., B, Si) relative to the ferromagnetic transition-metal elements. In these complex multicomponent systems, constituent atoms with a significant atomic mismatch provide excellent glass forming ability and enable a composite microstructure, which consists of nanocrystals of a transition-metal-rich phase embedded within an intergranular amorphous phase, enriched in glass formers, after

the first 'primary' crystallisation event [1,2]. At higher annealing temperatures, i.e., in the range of the second exothermic event, the glass-former enriched intergranular amorphous phase crystallises as well. A large number of compounds are reported in the literature, depending on the alloy composition, including $(Fe,Co,Ni)_2B$, $(Fe,Co,Ni)_2Zr$, and $(Fe,Co,Ni)_3B$. More complex phases exist, exhibiting the $Cr_{23}C_6$ prototype structure such as $(Fe,Co,Ni)_{23}B_6$, which has a large unit cell with more than 1 nm size, containing 92 medium-sized ferromagnetic transition-metal elements and 24 small metalloid atoms [3]. This particular phase is a metastable one, which can easily decompose into $(Fe,Co,Ni)_3B$ and $(Fe,Co,Ni)_2B$. However, when the main transition metal site is partially substituted by another transition metal atom, such as Nb, Co, or Ni, the $M_{23}B_6$ phase is stabilized and more easily retained [4].

The precipitation of $M_{23}B_6$ phase throughout the amorphous matrix results in a significant improvement in the soft magnetic properties and low losses at high frequencies [5]. In addition, the network-like structure of $Co_{23}B_6$, which requires long-range atomic rearrangements of constituent elements and a large negative entropy, leads to the high stability of the supercooled liquid against crystallisation. The details of such transformations during the annealing process, inherently involving a definite sequence of compositional as well as structural ordering processes, are however still rather unclear. Furthermore, the 23:6 phases are not as well understood as other crystallisation products because they exhibit complex face-centred-cubic structures with 116 atoms per conventional unit cell that are often metastable [6]. It is, therefore, important to study the underlying structure and microstructure of these phases in order to understand the underpinning of important properties for the technical application of these materials [4].

Power loss during electrical conversion accounts for a large percentage of the total dissipation (primarily heat) during power transmission and distribution [7]. Power dissipation occurs not only close to the end-user, resulting in a decreased efficiency of the ever more ubiquitous consumer-grade power electronic components, but also in the growing share of high-power applications such as power inverters used within photovoltaic installations [8]. The overall magnetic core power loss can be attributed broadly to three different mechanisms, namely, hysteresis loss, eddy current loss, and anomalous loss. It is well understood that as the operating frequency f increases, the eddy and anomalous losses become dominant at $f > 100$

kHz, for metallic, high polarisation materials. On the other hand, recent advances in power conversion circuits have pushed switching frequencies into the 100s of kHz and even into the megahertz range (in on-chip applications) [9,10]. This minimizes the size of the passive components required but means that the magnetic material must be capable of operating at high frequency with low losses. Utilisation of these benefits is more readily attainable using ferrite-based low-moment materials, which are insulators. However, the low flux density typical to ferrites (0.3 – 0.4 T) requires considerable cross-sectional area (and volume), which is undesirable in many deployments [11]. Presently, ferrites [12], iron powder, and tape wound cores [13] are primarily used for relatively low-power applications, where only grams of material are required per installation. An affordable, yet efficient, high-moment magnetic material, allowing for operation beyond 100 kHz, would enable mass application in higher power export-to-grid invertors and power-regulation circuits (in the kW range), which are expected to become prolific in the near future as many countries are adopting new regulations with respect to renewable energy sources. Anomalous loss dominates the total dynamic loss in most soft magnetic amorphous ribbons with a uniaxial anisotropy oriented longitudinally to the applied magnetic field. It originates from localised eddy currents around moving domain walls under the driving action of an external magnetic field. The anomalous loss can be significantly reduced through changing the mechanism of magnetisation reversal from predominantly domain wall motion to coherent magnetisation rotation using transverse magnetic annealing. The mechanisms of inducing uniaxial magnetic anisotropy by magnetic annealing include spatial atomic pair ordering resulting in directional order, structural relaxation, and the rearrangement of free volume in amorphous materials [14].

The present work provides a deeper understanding of the structural phase transitions, quantifies the induced uniaxial magnetic anisotropy energies, and correlates the induced coherent magnetisation reversal process to the significantly improved high-frequency loss performance of transverse field annealed nanocrystalline ribbons. The detailed structural, magnetothermal, magnetic domain imaging and magnetisation reversal process in amorphous and nanocrystalline Co-based ribbons with different strengths of transverse field-induced anisotropies at frequencies up to 1 MHz have been investigated and discussed in detail.

6.2 Experimental methods

Melt-spun ribbons (20 μm thick and 1 mm wide) of $Co_{65.88}Fe_{4.2}B_{24}Si_{1.92}Nb_4$ alloy are obtained using rapid quenching technique; the detailed procedure is reported elsewhere [15]. The ribbons are annealed in a 5 Tesla magnetic field orientated in the transverse direction for 60 minutes at different temperatures; 510, 515, 525 and 550 °C. The equilibrium phase diagram of the alloy composition is predicted by the thermodynamic modelling approach, using Pandat^{TM} software (version 2019). This thermodynamic database is utilised to predict the possible equilibrium phases at room temperature in the current multi-component alloy system to be compared with the experimental results. X-ray powder diffraction (XRD) data of the melt-spun ribbons are collected using a Phillips PANalytical X'pert Pro diffractometer, with an operational wavelength of 1.5405 Å (Cu-Kα anode). Rietvel refinement analysis is carried out on the diffraction patterns. For transmission electron microscopy (TEM) analysis, each selected ribbon is first processed using a focused ion beam microscope (FEI Helios Nanolab 600i). A protective metallic (Pt-based) layer is deposited on the surface before milling to create an ultrathin lamella, followed by an *in-situ* micromanipulator transfer to a TEM sample holder. TEM imaging of the ultrathin lamella is performed using a JEOL-2100 TEM operating at 200 kV. In addition, the coercivity and anisotropy field of the ribbons, along its length, is measured using a B-H loop tracer (at f = 10 Hz) with the maximum magnetic field of 0.1 Tesla. In addition, an Evico Magnetics Kerr Microscope & Magnetometer is used for the visualization of magnetic domains. Thermomagnetic measurements are performed using the Magneto-thermogravimetric instrument; the detailed procedure is published elsewhere [16].

The power loss characterisation of the ribbons is performed using a custom design air-core solenoid inductor. The 150 turns of 28 gauge Cu wire are wound on a 5 cm long hollow cylinder of 5 mm outer radius with near-zero spacing between the turns to create a uniform excitation field inside the solenoid. The impedance of the air core solenoid, Z_a, is measured using an LCR meter (HP4283c) at various excitation current levels. The ribbon samples (2 cm × 1 mm × 20 μm) are inserted inside the solenoid, along its axis, where the uniformity of the field is best (see Fig. 1). Without moving the probes from the test fixture, the ribbons are centred inside the solenoid to be at the same distance from both open ends, where the magnetic field lines are no

longer parallel to the axis. In this way, the magnetic core material is exposed to a uniform excitation field along its length. The Cu turns are at a sufficient distance from the solenoid axis so that the demagnetisation field does not alter the field lines around the turns, maintaining the same AC winding resistance as in the case of air-core solenoid measurement. Therefore, the difference between the impedance measurement with and without magnetic core material, Z_c and Z_a, respectively, represents the contribution of the magnetic core to the inductance and power loss at each frequency. As the cross-sectional area of the ribbons is significantly smaller than that of the solenoid, the effect of the insertion of the magnetic core on the real part of the inductance is negligible. Therefore, the magnetic material power loss is calculated as:

$$P_{\text{loss}} = \text{Re}(Z_c - Z_a)I^2 \quad (1)$$

where Re(Z_c-Z_a) is the real part of the complex impedance difference, and I is the excitation current measured using the LCR meter. The induction field inside the ribbon samples is calculated by;

$$B = \frac{\text{lm}(Z_c - Z_a)I}{(2\pi f S)}\pi r^2 \quad (2)$$

where f and S are the measurement frequency and the total cross-sectional area of the ribbons, and r is the radius of the coils. The power loss measurement method has been tested with commercial samples, and the results are in good agreement with the reported power loss in standard datasheets.

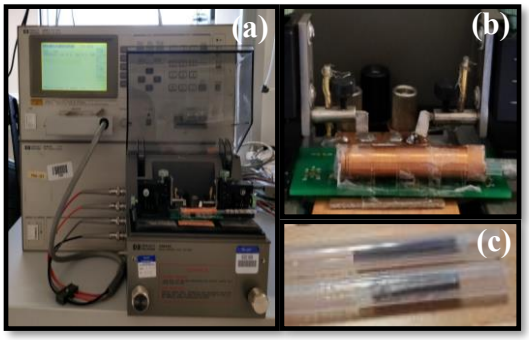

Figure 1. Power loss measurement set-up; (a) complete set-up, (b) solenoid with 150 turns of wire of guage 28 to produce a coherent magnetic field at the centre, and (c) sample holders.

6.3 Results and discussions

6.3.1 Structural characterization

Figure 2 shows the XRD patterns of the ribbons as a function of magnetic annealing temperature up to 550 °C. The XRD pattern of the as-quenched ribbons exhibits a broad diffuse peak at 2θ = 44.40°, which represents the amorphous atomic structure of the ribbons before any heat treatment. Although no significant peak can be observed in the magnetic annealed sample at 510 °C, TEM investigations show the nucleation of nanocrystals with an average size of 5 nm in an amorphous matrix, see Fig. 3a and 3c. As the distance between atomic planes of crystallites in three directions is the same and is equal to 6.057 Å (Fig. 3c), these planes may be {111} planes of a crystal with a lattice parameter of 10.49 Å, which is in agreement with the reported lattice parameter of the metastable $Co_{23}B_6$ phase [5]. By increasing the temperature to 525 °C, several additional peaks appear in the XRD patterns belonging to $Co_{23}B_6$ and Co_2B, an orthorhombic equilibrium phase. Annealing the ribbons at 550 °C further increases the intensity of the peaks corresponding to $Co_{23}B_6$ and Co_2B phases. Simultaneously, the appearance of a new orthorhombic equilibrium phase, i.e., Co_3B, is suspected as hinted by the presence of overlapped peaks at 2θ = 41.79°, 44.67°, and 48.68°, in addition to a low-intensity peak at 73.9°. The formation of Co_3B is confirmed by the Rietveld refinement method, and the percentage of the phase is estimated as 12%.

The detailed crystallisation process is investigated by TEM micrographs of ribbons annealed at 510 and 525 °C, as shown in Fig. 3. The distance between lattice planes in three different directions is equal (6.057 Å), see Fig. 3c, which corresponds to {111} planes. This lattice spacing is in good agreement with the calculated distance based on the lattice parameter of $Co_{23}B_6$ phase, estimated from Rietveld refinement analysis of XRD patterns. In addition, the refined lattice parameter, i.e., 10.54 Å, is in good agreement with the reported lattice parameter of this metastable phase [5]. The atomic planes attributed to $Co_{23}B_6$ phase in the samples annealed at 510 °C and 525 °C can be seen in Fig. 3c and 3d, respectively. Additionally, based on the lattice parameter of different phases mentioned in Table 1 and calculated atomic planes spacing, the sets of {100} and {110} planes of Co_2B phase are identified in 525 °C annealed

ribbons (see Fig. 3e and 3f). As can be seen in Fig. 3a and b, the size of nanocrystals increases with annealing temperature and nanocrystals with different atomic orientations (Fig. 3 d-f) are formed at the expense of the amorphous matrix, which forms the main part of the microstructure of the magnetic annealed sample at 510 °C (Fig. 3a and 3c). Furthermore, the crystallite size of the ribbons annealed at 525 and 550°C, which is calculated by the Rietveld refinement method, is 33.53 and 33.54 nm, respectively. For the former, the size of crystallites is in good agreement with the apparent TEM images (Fig. 3b and Fig. 3d-f).

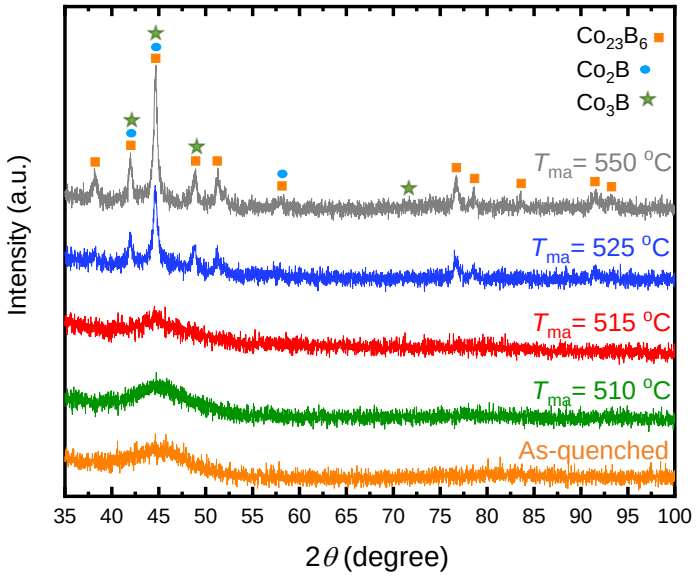

Figure 2. XRD patterns of as-quenched and magnetically annealed samples at 510, 515, 525 and 550 °C.

The thermodynamic and kinetic aspects of the phase transitions, as mentioned above, are investigated in detail. The phase transitions are studied by evaluating the equilibrium phase diagram of the system using Pandat^{TM} software. The thermodynamic calculations reveal three main phases, including Co_2B, Co (hcp), and Co_3B, that are stable from room temperature to 780 °C. Contrary to that, the microstructure analysis of the magnetically annealed ribbons, see Fig. 2 and 3, confirmed the presence of the metastable $Co_{23}B_6$ phase at 510 °C, Co_2B phase at 525 °C, and finally, Co_3B phase at 550 °C. Therefore, the discrepancy between experimental observations and thermodynamic modelling needs to be addressed accordingly.

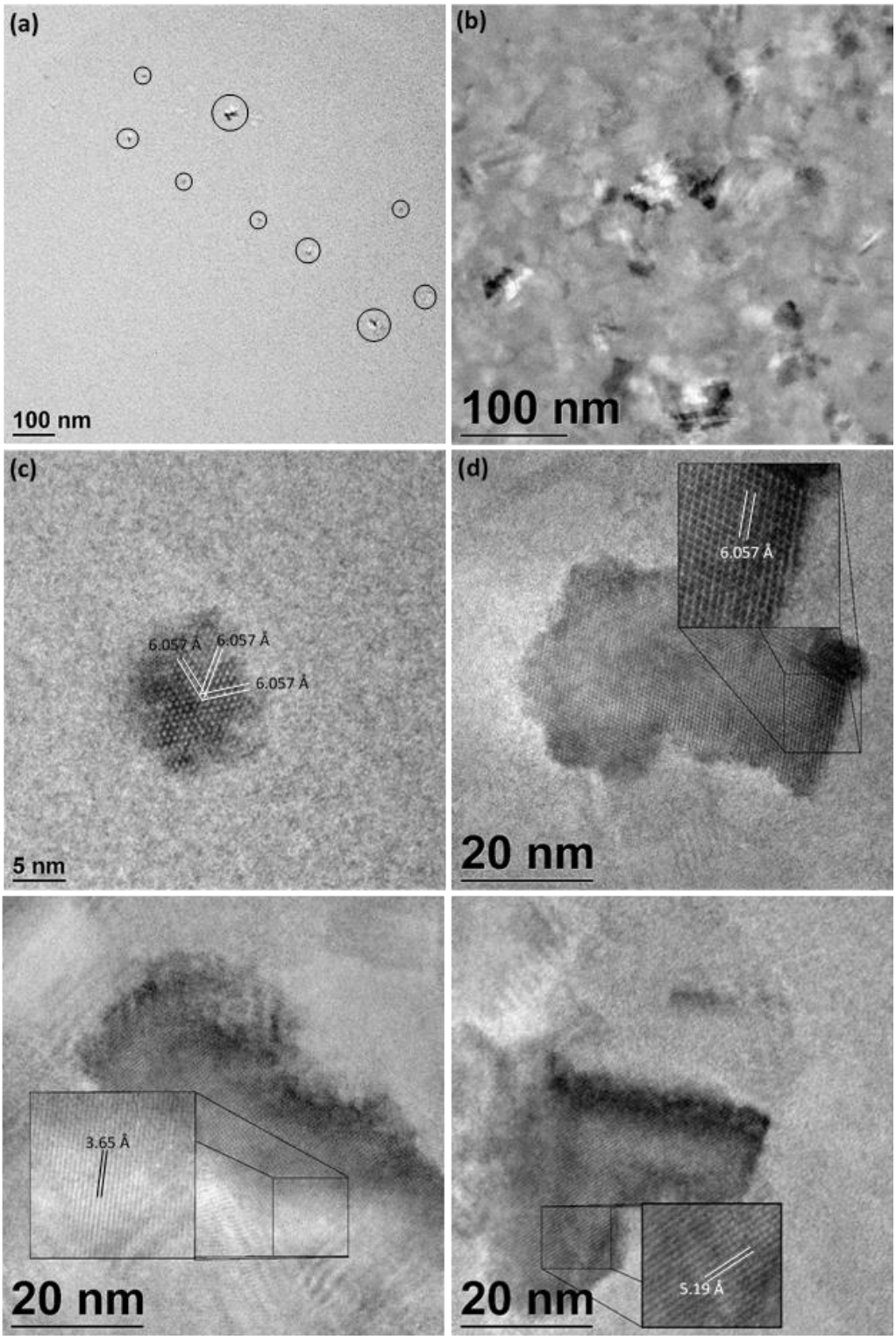

Figure 3. TEM micrographs of magnetically annealed samples at: (a) 510 °C (circles indicate nano-crystallites) and (b) 525 °C; {111} planes in $Co_{23}B_6$ in magnetically annealed samples at: (c) 510°C and (d) 525°C; (e) {110} and (f) {100} planes of Co_2B in the magnetically annealed sample at 525 °C.

Table 1. Crystal structure, lattice parameter, Gibbs free energy and interface energy difference between the liquid and solid; ΔG_{v} and σ, the activation threshold for formation of a critical nucleus ΔG^* of different phases at 510 °C.

Phase	**Space group**	**Lattice Parameter (Å)**			**ΔG_{v} (kJ/mol)**	**σ (J/m^2) ×10^5**	**ΔG^* (J) ×10^{23}**	**ΔG^* (meV)**
$Co_{23}B_6$	$Fm\bar{3}m$	10.54			155	3.71	3.55	0.355
Co	$P63/mmc$	2.5	4.06		9.03	1.12	29.2	2.92
Co_2B	I42m	5.19	4.32		7.95	1.62	114	11.4
Co_3B	Pnma	5.22	6.63	4.41	29.4	5.4	304.8	30.48

The nucleation of a metastable phase is likely to be kinetically favoured compared to that of the stable phase [5]. According to classical nucleation theory [17], the activation threshold for the formation of a critical nucleus is ΔG^*, which is the free energy required to form the critical nucleus, that can be expressed as;

$$\Delta G^* = \frac{16\pi\sigma^3}{3\Delta G_{\mathrm{v}}^2} f(\theta) \tag{3}$$

where $f(\theta)$ is the catalytic potency factor for heterogeneous nucleation, which depends on the wetting angle θ. ΔG_{v} is the Gibbs free energy difference between the liquid and the solid:

$$\Delta G_{\mathrm{v}} = \Delta H_{\mathrm{f}} \frac{T_{\mathrm{m}} - T_{\mathrm{ma}}}{T_{\mathrm{m}}} \tag{4}$$

where ΔH_{f}, T_{m}, and T_{ma} denote the enthalpy of fusion, melting temperature, and magnetic annealing temperature, respectively. In addition, the interface energy, σ, can be estimated by the model developed by Spaepen and Meyer [18]:

$$\sigma = \alpha \frac{\Delta S_{\mathrm{f}} T_{\mathrm{ma}}}{(N_{\mathrm{L}} V_{\mathrm{m}}^2)^{1/3}} \tag{5}$$

where α is a factor dependent on the structure of the solid nucleus and ΔS_{f}, N_{L}, and V_{m} are the entropy of fusion, Avogadro's number, and molar volume of the phase, respectively. Without the knowledge of the contact angle θ of the crystal nucleus to the substrate, the nucleation is

assumed to be homogenous. Based on this theory, the activation threshold of the stable and metastable phases in this system is estimated, as summarised in Table 1. As can be seen, the necessary activation energy for the formation of $Co_{23}B_6$ at 510 °C is much less than other stable phases, and hence the nucleation of this phase is favoured kinetically.

6.3.2 DC magnetic properties

Transverse magnetic field annealing is used to reorient the magnetisation axis by inducing uniaxial magnetic anisotropy. Reorientation of the magnetic axis is confirmed by comparing the preferred orientation of domains, observed by MOKE, in as-quenched and magnetic annealed ribbons at 510 and 525 °C, as illustrated in Fig. 4. It can be seen that the preferred magnetisation axis in the as-quenched ribbons is aligned to the longitudinal direction (Fig. 4a), as is well-anticipated by the dominant shape anisotropy. However, the magnetisation alignment was reoriented to the width of the ribbon by transverse magnetic annealing at 510 °C (Fig. 4b), along with the limited growth of $Co_{23}B_6$ in the amorphous matrix (Fig. 3c). The type and fraction of nanocrystallites increase after magnetic annealing at 525 °C (Fig. 2 and 3), which results in a more complex atomic and magnetic structure (Fig. 4c). Simultaneously, the magnetic domain structure transformed from wider irregular domains (Fig 4a and 4b) to a pattern of small but smoother domains (Fig. 4c).

The evolution of hysteresis loops, measured along the length of the ribbons, as a function of magnetic annealing temperature is presented in Fig. 5. It can be seen that the shape of hysteresis loops becomes sheared by increasing the magnetic annealing temperature. The emerged shape of the sheared hysteresis loops could be attributed to the effect of transverse induced anisotropy in the preferred magnetisation direction. The as-mentioned effect can be measured quantitatively by the induced anisotropy energy (K_u) (see Fig. 6), which is calculated based on the following equation [19]:

$$K_u = \frac{H_k \mu_0 M_s}{2} \tag{6}$$

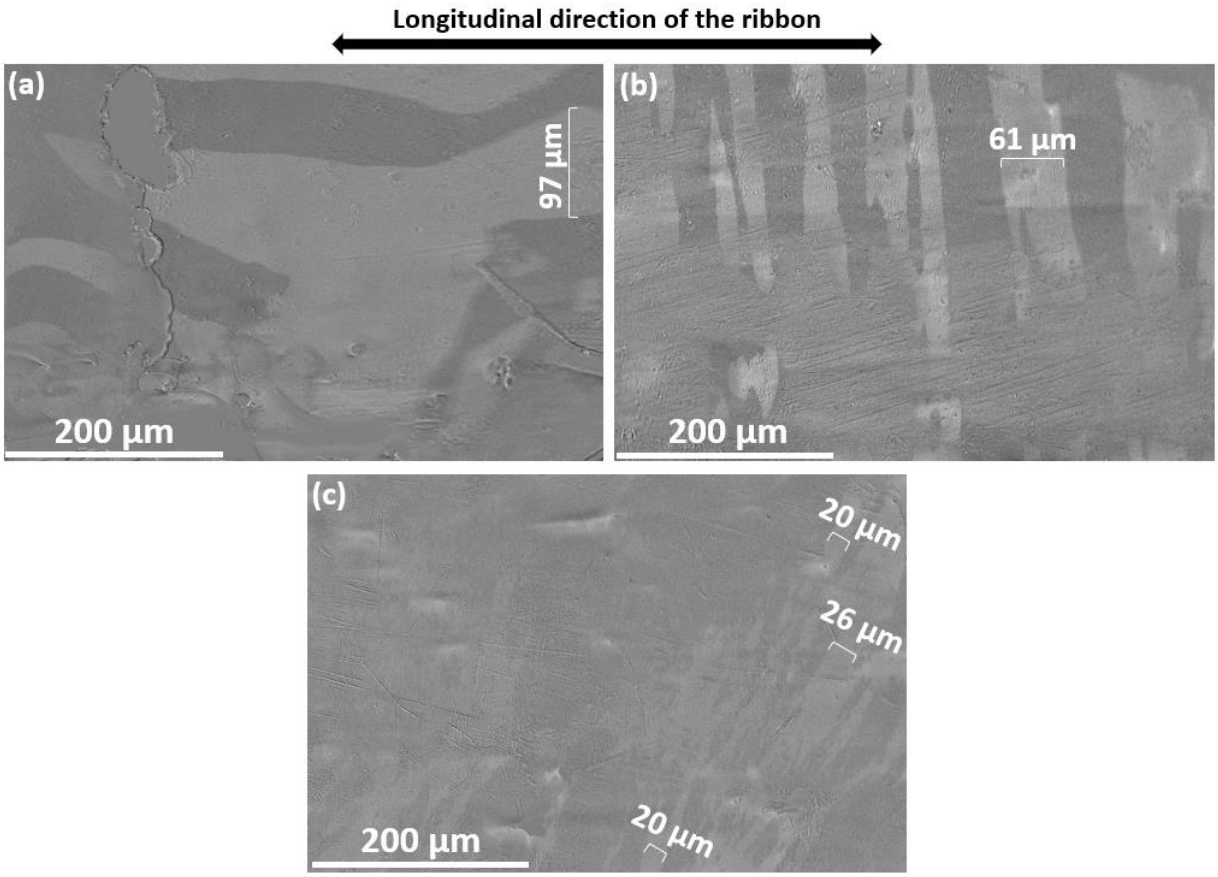

Figure 4. Domain images during the magnetisation of as-quenched (a), magnetically annealed at 510 °C (b) and 525 °C (c) ribbons at $\mu_0 H$ = 0 T. The domain imaging have been carried out at the remanent state of magnetisation.

where μ_0 is the free space permeability, and M_s is saturation magnetisation. The uniaxial induced anisotropy is related to directional atomic ordering along the direction of the local magnetisation in order to minimise the spin-orbit coupling energy [12]. The directional ordering of solute atoms originates by the local spontaneous magnetisation during heating of the sample; hence, K_u is only induced when the field annealing temperature is lower than Curie temperature (T_C). Thus, a crucial factor influencing the field-induced K_u in the multiple-phase nanocrystalline soft magnetic alloys is the T_C of the different phases. In order to determine the T_C of the precipitated phases, thermomagnetic measurements, M(T), are carried out on magnetic annealed ribbons, as shown in Fig. 7. As can be seen, the T_C of the amorphous phase is ~ 310°C, while the T_C of $Co_{23}B_6$ is more than 600 °C. It is worth mentioning that optimum

annealing temperature, for realizing the 'magnetically softest' microstructure, of the nanocrystalline soft magnetic alloys often lies in a range between the Curie points of the two constituent phases [20], so amorphous ribbons are magnetically annealed at temperatures between these two Curie points.

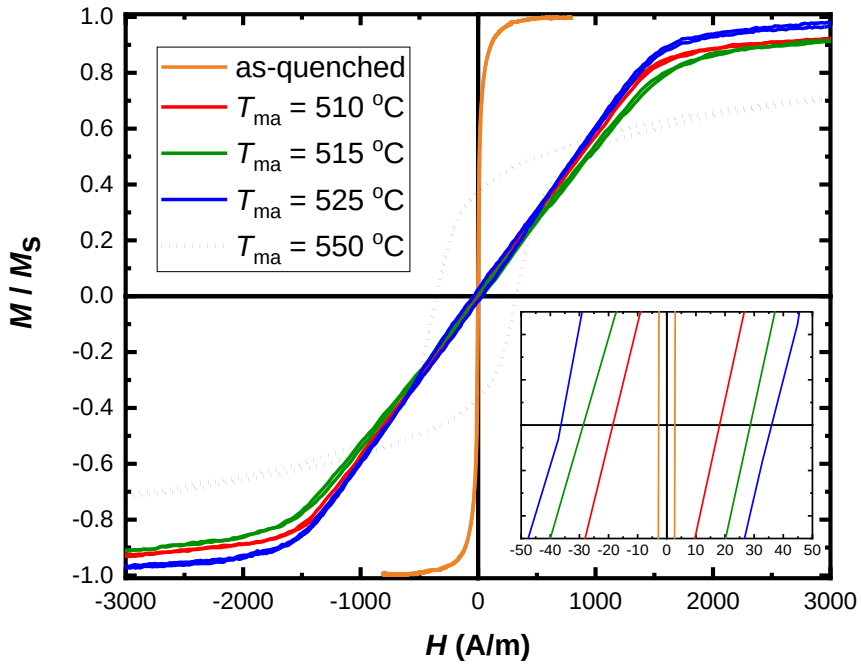

Figure 5. Hysteresis loops of as-quenched and magnetic annealed ribbons at 510, 515, 525 and 550 °C.

Additionally, the effect of the microstructural evolution of ribbons during magnetic annealing can be observed as in *M*(T) curves (Fig. 7). First of all, due to the monolithic phase of the amorphous as-quenched ribbons, just a single phase with a T_C = 310 °C can be observed. However, in magnetically annealed samples at 510, 515, and 525 °C, in addition to the amorphous matrix phase, another phase with the T_C = 610 °C, which is possibly related to $Co_{23}B_6$, can be distinguished. In addition, the decreasing fraction of the amorphous phase produced from a higher magnetic annealing temperature (as previously confirmed by XRD and TEM, see Fig. 2 and 3) can be ascribed to the *M*(T) behaviour of magnetic annealed samples. In other words, at the point shown by the arrow in Fig. 7, the *M*(T) curves of magnetic annealed

samples at 525, 515 and 510 °C respectively, diverge, indicating that the amorphous phase transforms to $Co_{23}B_6$ at different temperatures in the samples which are magnetically annealed at different temperatures. Thus, in the samples which are annealed at higher temperatures, the required energy to perform the as-mentioned transition is lower.

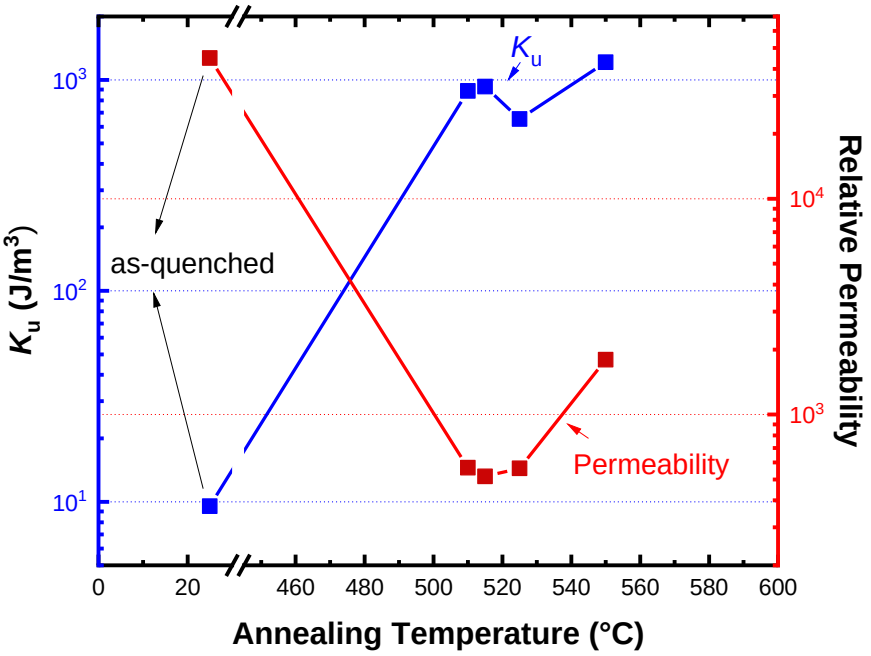

Figure 6. Induced anisotropy energy and relative permeability of ribbons as a function of magnetic annealing temperature (the size of the symbols represents the measurements uncertainty).

The metastable equilibrium between $Co_{23}B_6$, as a primary bcc phase, and the residual amorphous phases is maintained in the nanocrystalline soft magnetic alloy. An obvious consequence of this two-phase microstructure is that the bulk field-induced K_u of the sample reflects the volume-weighted average of the two local K_u contributions from the two constituent phases. Thus, as the annealing temperature is less than the T_C of $Co_{23}B_6$ phase and higher than the T_C of the amorphous phase, the anisotropy induced by an applied magnetic field during nanocrystallisation (Fig. 2 and 3), primarily originates from the $Co_{23}B_6$ grains, which results in an abrupt increase in K_u after magnetic annealing at 510 °C, as compared to as-quenched ribbons (Fig. 6).

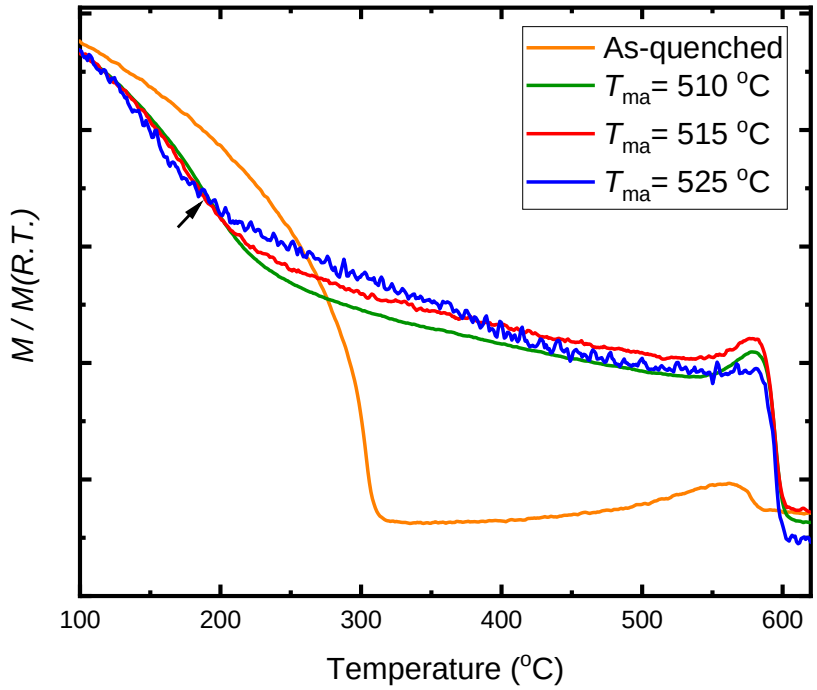

Figure 7. Temperature dependence of normalised magnetisation for as-quenched and magnetically annealed samples.

The average anisotropy constant $\langle K \rangle$ of a coupled multiphase system with anisotropies randomly oriented on a scale smaller than a magnetic correlation length, L_{ex}, can be described by Eq. 7 [21]:

$$\langle K \rangle = \sqrt{K_{\mathrm{u}}^2 + \sum_{\mathrm{v}} x_{\mathrm{v}} \beta_{\mathrm{v}}^2 K_{1,\mathrm{v}}^2 \,.\, (D_{\mathrm{v}}/L_{\mathrm{ex}})^3} \tag{7}$$

where K_{u} denotes a uniaxial anisotropy, which is uniform on a scale much larger than L_{ex}. The random contributions are represented by the local anisotropy constants, $K_{1,\mathrm{v}}$, the grain sizes, D_{v}, and the volume fractions, x_{v}, of the individual structural phases labelled by the index v. The parameters β_{v} mainly involve conventions used to define the anisotropy constants for different symmetries. Therefore, two different parameters lead to an increase in $\langle K \rangle$. First of

all, increasing K_u, as a result of higher temperature annealing (see Fig. 6) and nanocrystallisation of the sample (see Fig. 2 and 3), results in a contribution of the local anisotropy constant of the crystalline phases to the average anisotropy constant, as demonstrated in Eq. 7. Thus, the local density of induced anisotropy in the residual amorphous phase becomes negligible or considerably smaller than that in the primary bcc phase and the anisotropy induced by annealing at $T_{C,amorph} < T_{ma} < T_{C,Co_{23}B_6}$, in a magnetic field applied during nanocrystallisation, mainly due to the bcc grains of $Co_{23}B_6$ phase.

The subsequent decrease and then increase in K_u with increasing the annealing temperature to 525 and 550 °C can be related to the formation of octahedral crystals of Co_2B and, in particular, to the superlattice structure of orthorhombic Co_3B in an annealed sample at 550 °C. The induction of an extra magnetic anisotropy in a crystal by the directional ordering of solute atoms is due to the change in the crystal symmetry. This means that the effectiveness of the solute atoms on the induction of K_u depends on the type of solid solution and its crystalline system. This effect can also be seen in the completely different shape of the hysteresis loop, and high coercivity of the sample annealed at 550 °C (see Fig. 5), which is due to the limited formation of Co_3B as a semi-hard magnetic phase with anisotropy energy of 507 kJ/m^3 [22]. In other words, the perfect sheared hysteresis loops after field annealing at 510, 515, and 525°C indicate that field-induced anisotropy dominates over the residual contributions from the random magneto-crystalline anisotropies. Contrary to that, the domination of extrinsic magnetocrystalline anisotropy over field-induced anisotropy is noticeable in ribbons which are magnetically annealed at 550 °C, which could be attributed to the strong magneto-crystalline anisotropy and higher relative concentration of Co_3B.

Therefore, although the grain size of the $Co_{23}B_6$ in the ribbons annealed at 525 and 550 °C remains almost unchanged and it is expected that, based on random anisotropy model [21], ferromagnetic exchange interaction between these small grains force the magnetic moments more and more to align parallel, simultaneously precipitation of semi-hard Co_3B phase significantly deteriorates the soft magnetic properties in the sample annealed at 550 °C. Consequently, a small volume fraction of a phase with high anisotropy can change the magnetic behaviour of the whole sample.

Transverse magnetic annealing at 510 °C results in rather a substantial decrease in permeability (Fig. 6). However, annealing at a higher temperature does not further reduce the permeability. In particular, the permeability is sensitive to the angle between the applied magnetic field and macroscopic anisotropy direction. As the samples are magnetised along their length, during DC magnetic measurements, and this direction is perpendicular to the induced K_u axis, the permeability is determined by magnetisation rotation and, hence, is inversely proportional to the induced anisotropy energy, based on equations 7 and 8 (see Fig. 6) [23].

$$\mu = \frac{J_s^2}{2\mu_0\langle K\rangle} \tag{8}$$

where J_s is the average saturation polarization of the material. Figure 8 shows the change in the coercivity of samples as a function of magnetic annealing temperature. The coercivity of as-quenched ribbons is 2.9 A/m and increases to 355 A/m for ribbons magnetically annealed at 550 °C (Fig. 5 and 8). Limited crystallisation of $Co_{23}B_6$ phase in the sample annealed at 510 °C (Fig. 3a and 3c) results in increased coercivity due to magneto-crystalline anisotropy. In addition, coercivity is directly related to the average anisotropy constant $\langle K\rangle$ by [23]:

$$H_c = p_c \frac{\langle K\rangle}{J_s} \tag{9}$$

where p_c is the dimensionless pre-factor of the order of unity. Thus, by increasing the average anisotropy constant, (see Eq. 7), the H_c of the ribbons increases (Fig. 8). Furthermore, the substantial increase in the coercivity of the sample magnetically annealed at 550 °C compared to one magnetically annealed at 525 °C may be due to the formation of Co_3B as a semi-hard magnetic phase.

Figure 8 also shows the change in the saturation magnetisation of ribbons versus magnetic annealing temperature. First, there is an increase in M_s from 0.84 to more than 1 T after magnetic annealing the amorphous ribbons at 510 °C. However, a further increase in the magnetic annealing temperature results in an abrupt decrease in the M_s of the samples. The evolution of saturation magnetisation was correlated with the growth of the crystalline phases

during magnetic annealing. The ~ 40% decrement is accounted for the amount of weak magnetic crystalline phases, as evidenced in Fig. 3b.

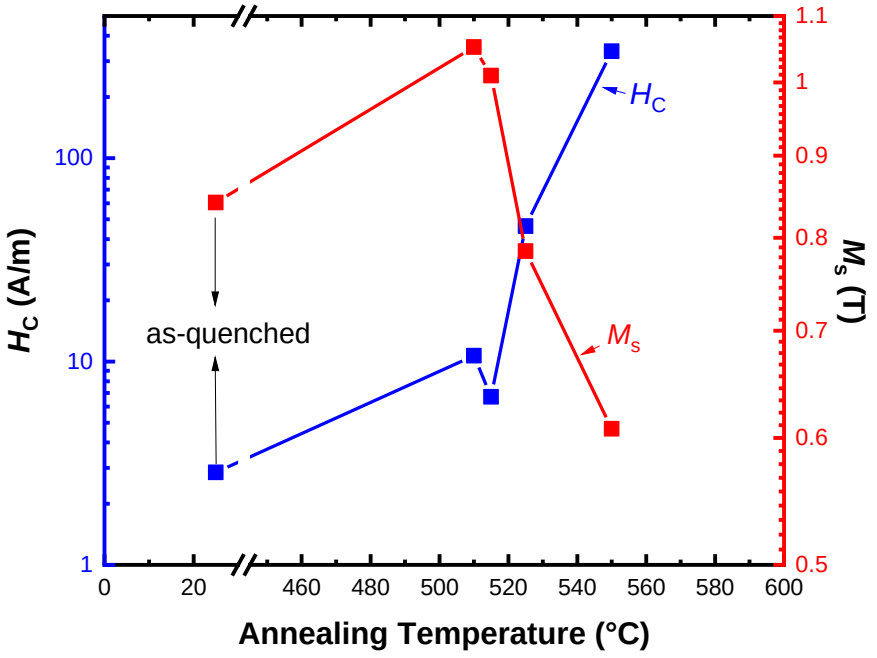

Figure 8. Coercivity and saturation magnetisation of ribbons versus magnetic annealing temperature.

First, as Cobalt atoms occupy four different types of positions in the cubic $Co_{23}B_6$ structure with unique symmetries and neighbouring atomic configurations, an effective localized moment can be attributed to each type of site. Ohodnicki *et al.* [6] showed that the largest local moments are at the 4a and 8c sites in $Co_{23}B_6$ structure. As has been pointed out previously in theoretical calculations for the $(Fe,Co)_{23}B_6$ structures [24], large local moments are observed for some of the transition-metal atoms at these sites (Fe at 4b sites = 2.64 μ_B, Fe at 8c sites = 2.60 μ_B, Co at 8c sites = 1.91 μ_B relative to those calculated for pure bcc Fe = 2.17 μ_B and fcc Co = 1.60 μ_B). Thus, larger local moments of Cobalt atoms in $Co_{23}B_6$ atomic structure compared to Cobalt atoms in pure Cobalt results in an increase in the M_s of the magnetic annealed sample at 510 °C compared to the as-quenched sample. Further magnetic annealing

results in the formation of a Co_2B phase with a magnetic moment of 0.76 $\mu_{B/f.a.}$, leading to a substantial decrease in M_s for magnetically annealed samples at elevated temperatures (Fig. 8).

6.3.3 AC magnetic properties

The total power loss of samples measured at three different frequencies may be decomposed into three different power loss mechanisms; hysteresis, eddy current, and anomalous, using the analysis outlined in reference [11]. By applying a similar approach, it was shown that anomalous loss is the main contributor to the total power loss [25–27]. Magnetic annealing may be used to decrease this main mechanism of power loss, and hence this type of power loss is investigated in more detail as follows.

Figure 9 represents anomalous loss behaviour of different samples as a function of magnetic induction at different frequencies; 50 kHz, 500 kHz, and 1 MHz. The anomalous loss of nanocrystalline ribbons is higher than that of as-quenched ribbons at 50 kHz (Fig. 9a). However, upon increasing the frequency to 500 kHz, the performance of the T_{ma} = 525 °C sample is better than the as-quenched sample, which could be due to the fact that the contribution of anomalous loss is more significant at higher frequencies. Magnetic annealing as a method of decreasing this kind of power loss becomes even more effective. Thus, in addition to T_{ma}= 525 °C sample, nanocrystalline ribbons annealed at 510 °C also show lower anomalous loss compared to the as-quenched sample at 1 MHz. As a case in point, magnetic annealing at 525°C decreases the anomalous loss of as-quenched ribbons by 70%, at f = 1 MHz and B = 5 mT. Although more anisotropy is induced in the samples with T_{ma}= 510 and 515 °C, it seems that a sufficient amount of anisotropy energy is induced in the sample magnetically annealed at 525 °C. At higher temperatures, the crystallisation of the secondary phase leads to a worse compromise between permeability and power loss. In addition, these results are in agreement with the studies of Flohrer *et al.* [28,29] in which the excess loss contribution increases with increasing strength of the induced anisotropy. The lower excess loss in cores

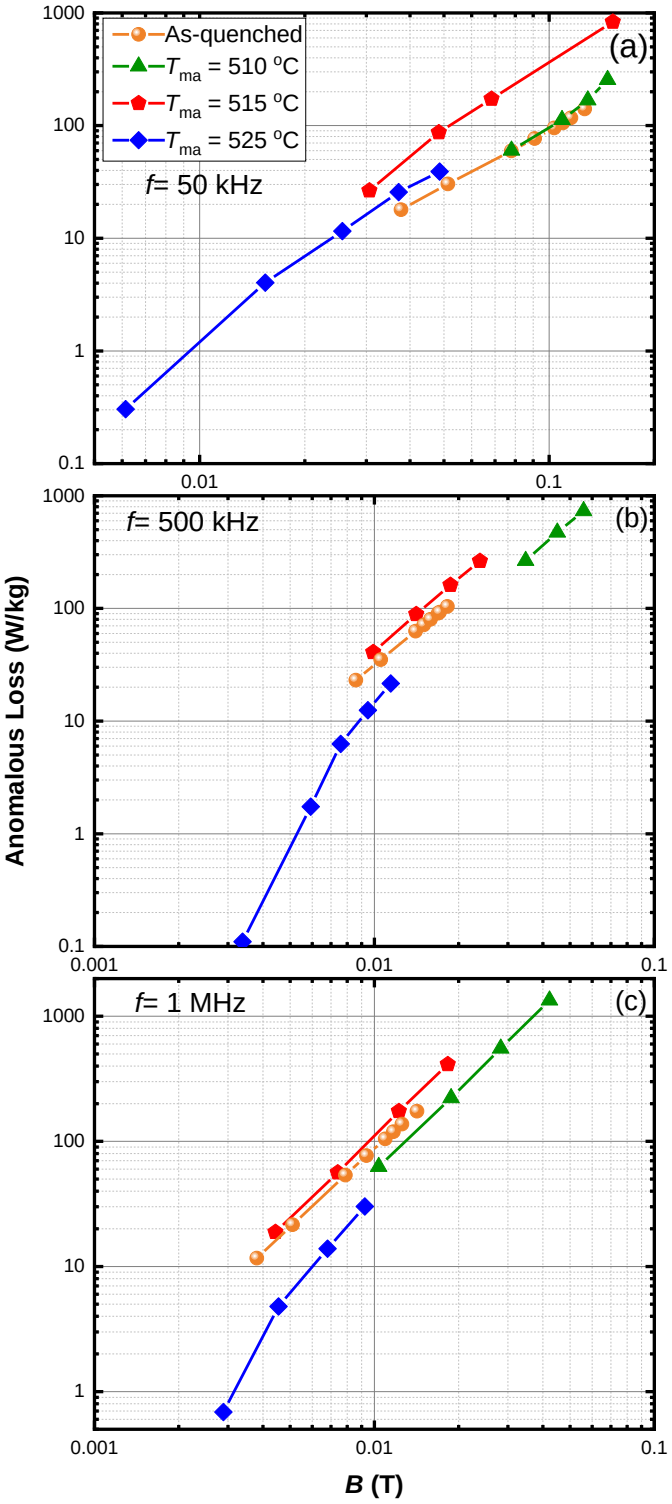

Figure 9. Anomalous loss of as-quenched and magnetically annealed ribbons as a function of magnetic induction at (a) 50 kHz, (b) 500 kHz and (c) 1 MHz.

with weak induced anisotropy, in [28], is ascribed to a larger number of active domain walls

compared to cores with higher induced anisotropy. However, it is mentioned, in [29], that with rising frequency and decreasing induced anisotropy, the magnetisation process changes from wall displacement to domain nucleation, which limits the mean surface wall velocity.

Additionally, according to Herzer's theory [30], the relationship between total power loss (P_t) and the total eddy current loss (P_{ec}), which includes classic and excess eddy current (anomalous) loss has the form of:

$$P_t \approx P_{ec}\left[1 + \frac{w^2}{(w\cos\beta + t)^2}\frac{m^2}{1-m^2}\right] \tag{10}$$

where w denotes the average domain width, t is the ribbon thickness, β is the out-of-plane angle of the magnetisation vector, and m denotes the average magnetisation component along the ribbon axis normalised to the saturation magnetisation. First, by changing the mechanism of magnetisation from domain wall motion to domain rotation, the movement of domain walls is limited substantially, resulting in lower excess eddy current loss or anomalous loss (Fig. 9b and 9c). Finally, the demagnetisation energy is lower in samples with narrower domain width (w) (Fig. 4), and as can be concluded from Eq. 10, the total power loss decreases in such samples due to the prohibited domain propagation. Thus, different mechanisms are effective on the decrement of total power loss during transverse magnetic annealing.

6.4 Conclusions

In this work, we develop a better understanding of nanocrystallisation, phase transformation, and soft magnetic behaviour of Co-based melt-spun ribbons through magnetic annealing at temperatures between the Curie points of the amorphous and the main nanocrystalline phase. XRD and TEM are used to investigate the atomic structure of the ribbons magnetically annealed at different temperatures. In addition, structural features are correlated with magnetic properties investigated by Kerr microscopy, DC magnetometry, and thermomagnetic measurements. Magnetic annealing at 510 °C results in the formation of the metastable $Co_{23}B_6$ phase, which has not been anticipated by thermodynamic models. Thus, $Co_{23}B_6$ nucleates at lower temperatures compared to Co_2B and Co_3B phases, owing to its lower nucleation

activation energy. The perfect sheared hysteresis loops after magnetic field annealing at 510, 515, and 525 °C indicate that field-induced anisotropy dominates over the residual contributions from magnetocrystalline anisotropy. However, magnetocrystalline anisotropy dominates over field-induced anisotropy in the sample, which is magnetically annealed at 550 °C, due to the formation of Co_3B, a semi-hard magnetic phase. The anomalous loss, as the primary mechanism of power loss, can be reduced by 70% by annealing at 525 °C in a transverse magnetic field, which results in an increase in the relative contribution of domain rotation in comparison to domain wall motion. Another contributing factor is the decrement of the domain width by increasing the magnetic annealing temperature, and it contributes to a further decrease in the anomalous loss by promoting the pinning of domain walls. Therefore, nanocrystalline Co-based systems offer an interesting engineering tradeoff between the extreme properties of amorphous and fully crystalline soft magnets.

Acknowledgement

The authors would like to thank the Science Foundation of Ireland (SFI) for the financial support to perform the research work under the grant number of 2015/SIRG/3569, Starting Investigator Research Grant (SIRG). The authors also thank Professor Dr. Valter Ström and Ms. Esmat Dastanpoor from The Royal Institute of Technology – KTH for the MTG experiments. N. Teichert would like to acknowledge funding from the European Union's Horizon 2020 research and innovation programme under the Marie Skłodowska-Curie EDGE grant agreement No 713567.

6.5 References

[1] B. Idzikowski, P. Švec, M. Miglierini, eds., Properties and Applications of Nanocrystalline Alloys from Amorphous Precursors, Springer Netherlands, 2005. doi:10.1007/1-4020-2965-9.

[2] A.I. C. Suryanarayana, Bulk Metallic Glasses, Second Edition, CRC, New York, 2012.

[3] A. Hirata, Y. Hirotsu, K. Amiya, N. Nishiyama, A. Inoue, Nanocrystallisation of complex Fe23B6-type structure in glassy Fe-Co-B-Si-Nb alloy, Intermetallics. 16 (2008) 491–497. doi:10.1016/j.intermet.2007.11.006.

[4] J. Long, P.R. Ohodnicki, D.E. Laughlin, M.E. McHenry, T. Ohkubo, K. Hono, Structural studies of secondary crystallisation products of the Fe23 B6 -type in a nanocrystalline FeCoB-

based alloy, J. Appl. Phys. 101 (2007) 114–117. doi:10.1063/1.2714250.

[5] X.X. Wei, W. Xu, J.L. Kang, M. Ferry, J.F. Li, Metastable Co23B6 phase solidified from deeply undercooled Co79.3B20.7 alloy melt, J. Mater. Sci. 51 (2016) 6436–6443. doi:10.1007/s10853-016-9941-4.

[6] P.R. Ohodnicki, N.C. Cates, D.E. Laughlin, M.E. McHenry, M. Widom, Ab initio theoretical study of magnetisation and phase stability of the (Fe,Co,Ni)23B6 and (Fe,Co,Ni)23Zr6 structures of Cr23C6 and Mn23Th6 prototypes, Phys. Rev. B - Condens. Matter Mater. Phys. 78 (2008) 1–13. doi:10.1103/PhysRevB.78.144414.

[7] A.M. Leary, P.R. Ohodnicki, M.E. McHenry, Soft Magnetic Materials in High-Frequency, High-Power Conversion Applications, JOM. 64 (2012) 772–781. doi:10.1007/s11837-012-0350-0.

[8] S.B. Kjaer, J.K. Pedersen, F. Blaabjerg, A review of single-phase grid-connected inverters for photovoltaic modules, IEEE Trans. Ind. Appl. 41 (2005) 1292–1306. doi:10.1109/TIA.2005.853371.

[9] J.S. Glaser, J.M. Rivas, A 500 W push-pull dc-dc power converter with a 30 MHz switching frequency, in: 2010 Twenty-Fifth Annu. IEEE Appl. Power Electron. Conf. Expo., 2010: pp. 654–661. doi:10.1109/APEC.2010.5433602.

[10] D.J. Perreault, J. Hu, J.M. Rivas, Y. Han, O. Leitermann, R.C.N. Pilawa-Podgurski, A. Sagneri, C.R. Sullivan, Opportunities and Challenges in Very High Frequency Power Conversion, in: 2009 Twenty-Fourth Annu. IEEE Appl. Power Electron. Conf. Expo., 2009: pp. 1–14. doi:10.1109/APEC.2009.4802625.

[11] S. Kulkarni, D. Li, N. Wang, S. Roy, C.Ó. Mathúna, G. Young, P. McCloskey, Low Loss Magnetic Thin Films for Off-Line Power Conversion, IEEE Trans. Magn. 50 (2014) 1–4. doi:10.1109/TMAG.2013.2288791.

[12] R.C. O'Handley, Modern Magnetic Materials: Principles and Applications, Wiley, 1999. https://books.google.ie/books?id=RKV1QgAACAAJ.

[13] G. Herzer, Modern soft magnets: Amorphous and nanocrystalline materials, Acta Mater. 61 (2013) 718–734. doi:https://doi.org/10.1016/j.actamat.2012.10.040.

[14] M.E. McHenry, M.A. Willard, D.E. Laughlin, Amorphous and nanocrystalline materials for applications as soft magnets, Prog. Mater. Sci. 44 (1999) 291–433. doi:https://doi.org/10.1016/S0079-6425(99)00002-X.

[15] K. Ackland, A. Masood, S. Kulkarni, P. Stamenov, Ultra-soft magnetic Co-Fe-B-Si-Nb amorphous alloys for high frequency power applications, AIP Adv. 8 (2018) 56129. doi:10.1063/1.5007707.

[16] S. Lee, A. Masood, T. Tamaki, S. Valter, K. V Rao, A. Makino, A. Inoue, Magneto-thermo-gravimetric technique to investigate the structural and magnetic properties of Fe-B-Nb-Y Bulk Metallic Glass, J. Phys. Conf. Ser. 144 (2009) 12074. doi:10.1088/1742-

6596/144/1/012074.

[17] D.A. Porter, K.E. Easterling, M.Y. Sherif, Phase transformations in metals and alloys, third edition, 2009.

[18] F. Spaepen, R.B. Meyer, The surface tension in a structural model for the solid-liquid interface, Scr. Metall. 10 (1976) 37–43. doi:10.1016/0036-9748(76)90323-9.

[19] F. Johnson, C.Y. Um, M.E. McHenry, H. Garmestani, The influence of composition and field annealing on magnetic properties of FeCo-based amorphous and nanocrystalline alloys, J. Magn. Magn. Mater. 297 (2006) 93–98. doi:https://doi.org/10.1016/j.jmmm.2005.02.056.

[20] G. Herzer, Amorphous and Nanocrystalline Soft Magnets, in: G.C. Hadjipanayis (Ed.), Magn. Hysteresis Nov. Magn. Mater., Springer Netherlands, Dordrecht, 1997: pp. 711–730. doi:10.1007/978-94-011-5478-9_77.

[21] G. Herzer, The Random Anisotropy Model, Prop. Appl. Nanocrystalline Alloy. from Amorph. Precursors. 184 (2005) 15–34. doi:10.1007/1-4020-2965-9_2.

[22] S.K. Pal, K.P. Skokov, T. Groeb, S. Ener, O. Gutfleisch, Properties of magnetically semi-hard (FexCo1−x)3B compounds, J. Alloys Compd. 696 (2017) 543–547. doi:10.1016/j.jallcom.2016.11.226.

[23] G. Herzer, On the theoretical understanding of nanocrystalline soft magnetic materials, J. Mater. Eng. Perform. 2 (1993) 193–197. doi:10.1007/BF02660285.

[24] B. Idzikowski, A. Szajek, Nanogranular phase formation during devitrification of Fe(NiCo)ZrB amorphous alloys, Czechoslov. J. Phys. 54 (2004) 12–15. doi:10.1007/s10582-004-0031-5.

[25] Z. Li, K. Yao, D. Li, X. Ni, Z. Lu, Core loss analysis of Finemet type nanocrystalline alloy ribbon with different thickness, Prog. Nat. Sci. Mater. Int. 27 (2017) 588–592. doi:https://doi.org/10.1016/j.pnsc.2017.09.002.

[26] K.J. Overshott, The causes of the anomalous loss in amorphous ribbon materials, IEEE Trans. Magn. 17 (1981) 2698–2700. doi:10.1109/TMAG.1981.1061648.

[27] M.A. Willard, T. Francavilla, V.G. Harris, Core-loss analysis of an (Fe, Co, Ni)-based nanocrystalline soft magnetic alloy, J. Appl. Phys. 97 (2005) 10F502. doi:10.1063/1.1847333.

[28] S. Flohrer, R. Schäfer, J. McCord, S. Roth, L. Schultz, F. Fiorillo, W. Günther, G. Herzer, Dynamic magnetisation process of nanocrystalline tape wound cores with transverse field-induced anisotropy, Acta Mater. 54 (2006) 4693–4698. doi:https://doi.org/10.1016/j.actamat.2006.04.040.

[29] S. Flohrer, R. Schäfer, J. McCord, S. Roth, L. Schultz, G. Herzer, Magnetisation loss and domain refinement in nanocrystalline tape wound cores, Acta Mater. 54 (2006) 3253–3259. doi:https://doi.org/10.1016/j.actamat.2006.03.011.

[30] G. Herzer, Magnetic materials for electronic article surveillance, J. Magn. Magn. Mater.

254–255 (2003) 598–602. doi:https://doi.org/10.1016/S0304-8853(02)00930-7.

Chapter 7 Conclusion and Outlook

Chapter 7 highlights the contribution of this thesis to the state of knowledge, the concluding remarks, and the ideas for future research in the field. Design, fabrication and optimisation of Cobalt-based amorphous alloys have been outlined in this research. The amorphisation capability of the alloys is predicted using an efficient multi-faceted model. The fabricated alloys exhibit excellent soft magnetic properties. The magnetic properties of melt-spun ribbons are improved by transverse magnetic annealing. In addition, ultra-thin amorphous ribbons have been fabricated using high-speed melt spinning. The power loss behaviour of the ribbons has been optimised by magnetic annealing, and the optimisation has been investigated in detail through decomposing the power loss into three main components and evaluating the contribution of each mechanism to the total power loss. In the following paragraphs, state of the art in current research is discussed.

After outlining the background and rationale for the present study in the first Chapter, the second Chapter [1] proposes a new approach to designing amorphous soft magnetic alloys. Three different factors, including the liquidus temperature, mixing enthalpy, and atomic mismatch factor are used to predict the amorphisation capability of Co-Fe-B alloys. Then, the alloys are fabricated by melt spinning. Based on this approach, five out of seven alloys have an amorphous structure, confirming the capability of the proposed model in predicting the alloy compositions with higher amorphisation ability in a ternary alloy system in the absence of any costly elements, such as Nb, Mo and Zr. Despite the interest in amorphous soft magnets, no one, to the best of our knowledge, has utilised such a multi-faceted model in predicting the amorphisation capability of this class of alloys.

Further, the output of the alloy design process is five amorphous alloys compositions, among which one is magnetically ultra-soft, H_c = 2.9 A/m; a surface crystalline alloy, with low H_c and 50% lower power loss, at high frequencies, compared to the best amorphous ribbons,

due to the *in-situ* induced out-of-plane anisotropy of the crystalline phase on the surface; and a nanocrystalline sample with a very high saturation flux density. Therefore, the Chapter sheds new light on novel soft magnetic alloys in which different structural features leads to excellent DC and AC soft magnetic properties. The mechanism behind the low power loss of the surface-crystalline alloy is studied in detail which has not been done before for Co-based alloys. We believe that we have found an innovative solution to the high power loss of amorphous ribbons, with no need for any post-processing to induce transverse anisotropy.

As far as we know, no one has used the moderate values of the parameters used in the as-mentioned model to design an *in-situ* nanocrystalline alloy, which is the focus of Chapter 3 [2]. The fabricated alloy exhibit exceptionally high B_s = 1.57 T, which is attributed to the precipitation of the metastable Co_7Fe_3 nanocrystalline phase dispersed heterogeneously in the amorphous matrix. This paper also takes a new look at the application of Mössbauer spectroscopy in characterising the nanocomposites. First, high M_s of Co_7Fe_3 phase can be inferred from the high hyperfine magnetic field of the Fe nuclei deduced from Mössbauer spectra. In addition, generally, our knowledge of the atomic structure of the amorphous phase is largely based on very limited data from, for example, TEM images, whereas, in this study, Mössbauer spectroscopy and the extracted distribution of the hyperfine magnetic field are used to scrutinise the atomic structure of the amorphous phase. It is found that cobalt atoms form clusters, as they attract each other to form ordered structures, and boron atoms undergo only short-range ordering, likely due to covalent bond formation, governed by the size and electronegativity differences with the atoms in the amorphous matrix.

To use amorphous metals at MHz frequencies, the thickness of the commercially available amorphous ribbons restricts the use of these alloys and hence limits the flux concentration advantage for the miniaturisation of passive components [3]. In Chapter 4 [4], we have found a novel solution for this issue which is the fabrication of *in-situ* thinned Co-based amorphous ribbons through high-speed melt spinning. It is proven that the *in-situ* thinning process of amorphous ribbons can substantially decrease the precursors' cost, increase the application frequency of the ribbons and eliminates the need for post-processing steps; hence it provides the opportunity for mass production of high-performance ultra-soft magnetic amorphous ribbons at relatively lower costs.

The mechanisms that limit the power loss performance in melt-spun amorphous ribbons have been investigated through DC and AC magnetic characterisation methods in Chapter 5 [5]. These findings add substantially to our understanding of the significant contribution of anomalous loss to the total loss and the effect of magnetic annealing in decreasing this effect. To clarify and understand the loss-limiting mechanisms and guide a decrement in anomalous loss, an innovative model-based evaluation coupled with Magneto-Optic Kerr Effect (MOKE) microscopy and bulk magnetisation measurements are used.

Although several studies have been carried out on the fabrication and characterisation of Fe-based nanocrystalline alloys as excellent candidates to make the cores of power converters [6], few researchers have focused on Co-based nanocrystalline soft magnetic alloys. This can be due to the complications in fabricating the nanocrystalline Co-based alloys with good soft magnetic properties, as the majority of CoB-based crystalline phases (Boron is one of the main glass formers in the amorphous systems) show semi-hard magnetic properties [7]. However, as an innovative approach, it has been shown in Chapter 6 [8] that the limited precipitation of the meta-stable $Co_{23}B_6$ phase throughout the amorphous matrix results in a significant improvement in the soft magnetic properties and low losses at high frequencies. The nanocrystallisation starts by nucleation and growth process of soft magnetic meta-stable, $Co_{23}B_6$ phase with less nucleation activation energy compared to other stable phases through magnetic annealing. The combined mechanism of nanocrystallisation and coherent magnetisation rotation accounts for a 70% decrement in the anomalous loss in the so-processed ribbons at 525 °C, which renders them attractive for applications in mid- and high-frequency power supplies and inverters.

The main conclusions of the chapters in this thesis are summarised as follows:

- The formation of an amorphous phase depends on multiple topological, kinetic and thermodynamic parameters. To predict the amorphisation capability of alloys, different criteria representing those properties should be taken into account, and no single parameter is sufficient to achieve this. The liquidus temperature, mixing enthalpy, and atomic mismatch factor can be the as-mentioned set of factors, which are successfully used to predict the amorphisation capability of Co-Fe-B alloys. This

prediction is imperically predicted by having five amorphous alloys out of seven designed compositions.

- A multi-faceted model to predict the amorphisation capability can be used as a guide to fabricate amorphous alloys with desired properties. For example, the alloy composition can be tuned to have high amorphisation ability even without introducing any costly elements and hence decrease the cost of initial materials used in the alloy production. This can also give an opportunity for material scientists to design alloys with a higher percentage of magnetic components in order to increase saturation magnetisation of the fabricated alloy for further device miniaturisation.
- Evaluating and manipulating amorphisation capability parameters do not only lead to finding the optimised compositions with high amorphisation capability, but can also result in fabricating partially crystallised amorphous ribbons. The surface or bulk crystallised alloys can have very interesting magnetic properties, superior to their amorphous counterparts, such as high saturation magnetisation (~ 1.57 T), ultra-low coercivity (~ 8 A/m), and low power loss, especially at high frequencies, which is crucial for power converters. As a case in point, the surface crystalline ribbons offer 50% lower power loss at 2 MHz compared to the best investigated amorphous alloy. Thus, designing alloy compositions with different amorphisation capabilities can be really useful in the development of functional materials for a broad range of applications.
- Evaluating the crystallisation behaviour of amorphous alloys by DSC and heat treatment can be helpful in scrutinising the amorphisation behaviour of alloys. It shows evidence that the alloys, which crystalise in the eutectic mode, show higher amorphisation capability.
- The atomic structure of amorphous and nanocrystalline alloys can be evaluated by analysing the distribution of hyperfine magnetic field, characterised by Mössbauer spectroscopy. This suggests opportunities for correlating the properties of these alloys and their atomic structure.
- In-situ thinning of amorphous ribbons can result in the fabrication of significantly cheaper amorphous ribbons by consuming less material than post-thinned

or post-magnetically-annealed ribbons and at the same time achieve very interesting magnetic properties, particularly for high-frequency applications.

- Power loss decomposition shows that among the different mechanisms of power loss, the anomalous loss contributed the most to the total power loss of melt-spun ribbons from 50 kHz to 1 MHz. Anomalous loss can be reduced substantially by magnetic annealing, which is associated with a decrease in the domain width. This mechanism is explained and verified using MOKE imaging and domain wall energy calculations based on magnetisation data. Thus, amorphous < 20 μm Co-based ribbons, heat-treated in a transverse magnetic field, at a temperature in the range 450 – 500 °C hold great promise for power applications at frequencies in the range 50 kHz - 1 MHz, as a higher-permeability alternative to ferrites.
- Limited and controlled nanocrystallisation of Co-based alloys during magnetic annealing offers an interesting engineering trade-off between the properties of amorphous and fully crystalline soft magnets. This can result in a more than 70% reduction in the power loss of the alloy as a result of limited nanocrystallisation of soft magnetic metastable $Co_{23}B_6$. The formation of such phases is evaluated and predicted using kinetic analysis.

The work presented in this thesis shows how to design more cost-effective novel alloys with tuned amorphisation capability. Secondly, it demonstrates that a reduction of the fabrication cost can be achieved by *in-situ* thinning the melt-spun ribbons. Finally, the mechanism of improving the soft magnetic properties of amorphous and nanocrystalline ribbons through magnetic annealing is discussed. The prospect of being able to optimise the magnetic properties of the RSP alloys through design, fabrication and heat treatment serves as a continuous impulse for future research. Therefore, this research has given rise to many ideas and questions in need of further investigation, which is addressed accordingly.

- The predictive parameters can be quantified more and then combined to form a single factor. Thermodynamic, kinetic and topological parameters have been taken into account to predict the AMC of alloys in this thesis. By introducing more parameters

into this model and overlapping their optimum value to have a high AMC, can this result in an algorithm by which the AMC can be estimated?

- Can atomistic magnetic modelling be carried out to establish a more comprehensive predictive model to engineer the alloy compositions with desired magnetic properties? To benefit from the interaction between magnetic components so as to maximise the magnetisation and minimise the coercivity by changing the structure of the domains, the applied predictive parameters in this thesis can be coupled with magnetic modelling outputs to design magnetic alloys.

- Can the magnetic softness of amorphous alloys be correlated with their magnetic structure and their composition? The different values of coercivity of fully amorphous ribbons can be explained by their domain structure observed using MOKE. The correlation between the alloy composition (the portion of magnetic components and glass formers), the atomistic information about the amorphous structure (extracted using Mössbauer spectroscopy) and the domain structure can be used as a guide to design the amorphous alloys with optimised soft magnetic properties.

- Inducing transverse anisotropy during the melt spinning procedure on various alloys is going to be a subject of future study. This can be done by attaching two discs of permanent magnets on each side of the melt spinner wheel. This procedure can eliminate the need for post-process heat treatment which causes embrittlement of the ribbon. In addition, post-process heat treatment increases the likelihood of crystallisation and oxidation, both of which can deteriorate the soft magnetic properties of the ribbons.

- In-plane and out-of-plane crystallisation of melt-spun ribbons inside a high-intensity magnetic field can be investigated. The effect of magnetic field annealing on the crystallisation behaviour of melt-spun ribbons can be evaluated and compared with the samples which are traditionally annealed. The magnetic field can accelerate the crystallisation of some specific phases with soft and hard magnetic properties, which might be desirable for particular applications.

- Rapid annealing of melt-spun ribbons can also be suggested as future work. It would be interesting to heat treat the as-quenched ribbons in a non-equilibrium condition to find out more about the kinetics of crystallisation in different heating rates,

which can help to correlate this behaviour with their AMC. In addition, rapid transverse annealing in a magnetic field would be interesting to investigate.

7.1 References

[1] Hasan Ahmadian Baghbaderani, Ansar Masood, Kenny L. Alvarez, Cian Ó Mathúna, Paul McCloskey, Composition engineering of ultra-soft-magnetic Co-based alloys, Ready for Submission (2021).

[2] H. Ahmadian Baghbaderani, A. Masood, K.L. Alvarez, C.Ó. Mathúna, P. McCloskey, P. Stamenov, CALPHAD-assisted development of in-situ nanocrystallised melt-spun Co-Fe-B alloy with high B (1.57 T), J. Alloys Compd. 877 (2021) 160194. doi:10.1016/j.jallcom.2021.160194.

[3] S. Kulkarni, D. Li, N. Wang, S. Roy, C.O. Mathuna, G. Young, P. McCloskey, Low Loss Magnetic Thin Films for Off-Line Power Conversion, IEEE Trans. Magn. 50 (2014) 1–4. doi:10.1109/TMAG.2013.2288791.

[4] A. Masood, H.A. Baghbaderani, V. Ström, P. Stamenov, P. McCloskey, C. Mathúna, S. Kulkarni, Fabrication and soft magnetic properties of rapidly quenched Co-Fe-B-Si-Nb ultra-thin amorphous ribbons, J. Magn. Magn. Mater. 483 (2019) 54–58. doi:10.1016/j.jmmm.2019.03.079.

[5] H. Ahmadian Baghbaderani, A. Masood, Z. Pavlovic, K. L. Alvarez, C. ÓMathúna, P. McCloskey, P. Stamenov, On the mechanisms limiting power loss in amorphous CoFeB-based melt-spun ribbons, J. Magn. Magn. Mater. 502 (2020) 166535. doi:10.1016/j.jmmm.2020.166535.

[6] C. Suryanarayana, A. Inoue, Iron-based bulk metallic glasses, Int. Mater. Rev. 58 (2013) 131–166. doi:10.1179/1743280412Y.0000000007.

[7] J.M.D. Coey, Magnetism and magnetic materials, Cambridge University Press, Cambridge, 2010. doi:10.1017/CBO9780511845000.

[8] H. Ahmadian Baghbaderani, A. Masood, Z. Pavlovic, N. Teichert, C. Ó. Mathúna, P. McCloskey, P. Stamenov, Improved magnetic performance of Cobalt-based ribbons by nanocrystallization through magnetic annealing, J. Magn. Magn. Mater. 503 (2020) 166630. doi:10.1016/j.jmmm.2020.166630.

Appendix A

Journal of Non-Crystalline Solids 574 (2021) 121151

Contents lists available at ScienceDirect

Journal of Non-Crystalline Solids

journal homepage: www.elsevier.com/locate/jnoncrysol

Novel predictive methodology of amorphisation of gas-atomised Fe-Si-B alloy powders

Kenny L. Alvarez [a,*], Hasan Ahmadian Baghbaderani [b,c], José M. Martín [a], Nerea Burgos [a], Paul McCloskey [b], Julián González [d], Ansar Masood [b]

[a] CEIT-Basque Research and Technology Alliance (BRTA), Paseo de Manuel Lardizabal 15, 20018, Donostia San Sebastián, Spain
[b] Tyndall National Institute, University College Cork, Lee Maltings, Dyke Parade, T12 R5CP, Cork, Ireland
[c] School of Physics and CRANN, Trinity College, D02 PN40, Dublin 2, Ireland
[d] Dept. of Materials Physics, University of the Basque Country, Pº de Manuel Lardizabal 3, 20018, Donostia San Sebastián, Spain

Abstract

Large amorphisation capability is an essential attribute to vitrify amorphous alloys, especially when lower cooling rates are the fundamental constraint in the synthesis process. The present work is focused on developing amorphisation capability criteria to predict rich regions of amorphous forming ability (AFA), in the Fe-Si-B phase diagram, of alloys to be produced by gas-atomisation. In the first step, the AFA of Fe-Si-B powders was evaluated by conventional empirical glass forming parameters that eventually did not guide to the best AFA alloy. In a second step, AFA analysis was extended to the ternary phase diagram, calculated using computational CALPHAD methodology, along with superimposed mathematical model based on the topological instability factor (λ), the estimated critical cooling rate (R_C) and critical particle size (d_C) to confine the phase diagram regions with larger AFA. The alloy with the highest amorphisation capability shows optimum atomic size mismatch in the vicinity of λ = 0.204. Not all regions in the phase diagram were optimal to design an alloy with high AFA, except where Fe_2B is the first solid phase under equilibrium solidification. Within the above two limits, the alloys with lower liquidus temperatures, *i.e.,* closer to the eutectic point, show the highest amorphisation capability (100%) for the gas-atomised powders. We suggest the proposed predictive methodology can be adopted as a guide to design novel amorphous alloys of high amorphisation capability for a broader range of powder metallurgical applications.

Keywords: Amorphous materials, Amorphous forming ability, Glass forming ability, Metallic glass, Gas-atomization, Soft magnetic powders.

1. Introduction

Since the discovery of disordered alloys by Duwez *et al.* [1] in the 1960s, amorphous metals have been extensively investigated for fundamental as well as technological applications, including structural, biomedical, aerospace, and energy conversion [2]. Amorphous metals are metastable materials, conventionally solidified in ~ 20 - 30 μm thick ribbons at ultra-high cooling rates (~ 10^6 K/s) to maintain short-range order atomic structure. If the short-range atomic order of amorphous alloys is similar to the precursor melt and concurrently reveals a

distinct glass transition temperature (T_g) well below the crystallisation temperature (T_X), the alloys are known as "metallic glasses" (MGs) [3,4]. Contrary to the amorphous metals, MGs can sometimes be solidified at phenomenally low cooling rates (as low as natural cooling) [5,6]. The functionality of MGs can be remarkably augmented if the glass forming ability (GFA) (*i.e.,* ease of glass formation, which determines the critical cooling rate) is substantially increased. Glass formation involves the thermal stability of the liquid phase and the suppression of crystallisation kinetics upon the cooling of melts [7]. To synthesise MGs at modest cooling rates, the kinetics of phase transformation and the mechanism of glass formation has emerged as an intriguing subject [8]. Why only specific alloys retain significant amorphisation capability, while others show a high degree of crystallisation during solidification, remains an open question to the material science community [8,9].

A large number of empirical glass forming parameters have been proposed to predict the GFA of alloys, though the origin of most criteria relies on the classical nucleation and growth theory [7]. For example, Turnbull demonstrated that when the reduced glass transition temperature ($T_{rg} = T_g/T_l$, being T_l the liquidus temperature) is higher than 2/3, the homogenous crystal nucleation rate decreases and, as a result, the crystallisation kinetics becomes more sluggish [10,11]. Similarly, Donald & Davies [12] proposed a simple way to estimate the GFA of alloys with two or more elements using the rule of mixture liquidus temperature (ΔT^*). Furthermore, Inoue formulated three empirical rules to predict the GFA, stating that: (i) the alloy must contain at least three elements, (ii) the constituents should include a significant atomic size difference (≥ 12%), and (iii) a negative heat of mixing among the major constituents is preferable [13,14]. Several other GFA parameters have been proposed, including ΔT_X [15], S [16], γ [17], δ [18], $\varnothing$ [19], γ_m [20], ω [21] and new β [22]. All these parameters use T_g to estimate the GFA. Despite that all these parameters have been demonstrated to be sufficiently accurate to measure the GFA of alloys, the critical cooling rate, R_c, and critical diameter, D_{max}, are still the most direct and quantifiable parameters. Since R_c and D_{max} are challenging to be measured, other criteria like P' [23], σ [24], λ [25], α (= T_X/T_l) and β (= 1 + α) [26] have been developed, which can be applied even for conventional amorphous alloys where T_g is not obvious. However, none of these criteria is valid for a broad range of MGs. Conventionally, the design of amorphous metals is frequently based on empirical rules, that is, a trial-and-error

approach, which is time-consuming and costly, hence designing alloys with a high amorphous forming ability (AFA) using thermodynamic modelling would be a step forward [27,28].

Among the broad range of amorphous metals, Fe-based alloys are of significant importance for their high demand in power conversion applications [29–31]. One of the most investigated systems is Fe-Si-B, thanks to its unique capability to retain exceptional soft magnetic properties, high corrosion resistance, and excellent mechanical properties [32]. Fe-Si-B alloys are generally melt-spun into amorphous ribbons of ~ 20 μm in thickness at ultra-high cooling rates (~ 10^6 K/s) [33]. One of the fundamental drawbacks of melt-spun ribbons is their shape; the very thin thickness and long length limit the fabrication of devices with complex geometries. Contrary to that, amorphous powders provide the flexibility to make complex shapes and, after coating with an electrical insulator layer, are considered an excellent material for high-frequency technological applications [34–36]. Amorphous powders are usually produced by gas-atomisation, which is a well-industrialised mass production technique to produce micron size powders. This process consists of breaking the liquid melt stream into droplets by using a supersonic gas flow. However, one of the fundamental limitations of gas-atomisation is the relatively low cooling rate (~ 10^4 - 10^5 K/s) as compared to the melt-spinning [37]. If the GFA of the alloys is not sufficiently high, the powders could exhibit a crystalline structure, deteriorating the soft magnetic performance and making them unsuitable for power conversion applications. Therefore, designing Fe-based alloys with high AFA that can be atomised as amorphous powders is essential to take advantage of the capabilities of these novel materials.

The present work is focused on establishing amorphisation capability criteria for Fe-Si-B powders by combining the CALPHAD (CALculation of PHAse Diagram) methodology with the topological instability factor (λ). The new criteria were confirmed by selecting Fe-Si-B alloys within the high GFA region of the ternary phase diagram (Fe-rich). These alloys were gas-atomised into powders. Initially, the amorphisation capability of the alloys was evaluated using conventional empirical parameters, such as enthalpy of mixing, ΔH^{mix}, α-, and β-parameters, but the trends predicted by these parameters were inconsistent with the experimental observations. Finally, the CALPHAD methodology was combined with λ-factor to obtain the highest amorphisation capability region inside the ternary Fe-Si-B system.

2. Materials and methods

The compositions of Fe-Si-B alloys were selected within the glass-forming region of the ternary phase diagram, as reported in the bibliography [38–40]. The gas atomisation experiments were carried out using a convergent-divergent, close-coupled atomiser in an atomisation unit PSI model Hermiga 75/3VI. Eleven different compositions of the ternary Fe-Si-B system were atomised (see compositions in Table 1). Regarding the raw materials, iron (supplied by Allied Metal Corp.), silicon (supplied by Cometal S.A.), and boron (supplied by H.C. Starck) of commercial purity were melted in an induction furnace. First, the chamber was purged with helium in order to evacuate the oxygen and avoid oxidation. Then, the temperature was increased by induction heating up to 1700 ºC. The amount of powder produced per batch was nearly 2.5 kg. Helium at a pressure of 60 bar was used as atomising gas.

Thermal transitions were analysed by Differential Scanning Calorimetry (DSC). The powders were analysed using a TA Instrument DSC 2920. The experiments were performed using a sample of about 10 mg on a copper pan with a lid, at a heating rate of 10 ºC/min up to 700 ºC and under an argon atmosphere. The crystallisation temperatures (T_X), crystallisation enthalpies (ΔH_C), and energy released by partially amorphous powders (as-atomised, ΔH) were obtained from these experiments.

Additionally, the structural characterisation of the powders was carried out via X-ray diffraction (XRD), using a diffractometer (Philips PW1825) and the characteristic wavelength of the K_α line for Cu (λ = 1.542 Å). The diffraction angle (2θ) varied from 25 º to 90 º at a scanning rate of 0.005 º/s, in steps of 0.02 º with a holding time of 4 s at each diffraction angle. The particle size distribution of the powders was measured by laser diffraction in an instrument Sympatec Helos (H0852). The true density was measured in a He pycnometer Micrometrics Accupyc 1330.

Thermodynamic calculations and modelling have been carried out using PANDAT^{TM} version 2019, using the thermodynamic database for multi-component Fe-rich alloys, PanIron. PANDAT^{TM} is an integrated computational tool developed based on the CALPHAD (CALculation of PHAse Diagram) approach for multi-component phase diagram calculations and materials properties simulations. The Fe-Si-B equilibrium phase diagram, including the

liquidus temperatures (T_l) and the solidified phases from the melt under equilibrium conditions, were calculated using this software.

3. Results and discussions

3.1 Structural analysis of the powders

XRD patterns of the as-atomised powders, presented in Fig. 1, show the precipitation of different crystalline phases during the solidification process, which were identified as α-Fe(Si), Fe_2B, and Fe_3Si. As can be seen in Fig. 1, α-Fe(Si) and Fe_3Si have similar XRD patterns. However, there are two additional diffraction peaks at $2\theta \approx 27$ and 31º corresponding to (111) and (200), which distinguish Fe_3Si [41] from α-Fe(Si). In addition, as the lattice parameter of Fe_3Si [41] is twice that of α-Fe(Si) [42], Fe_3Si shows diffraction peaks at slightly higher 2θ. A broad peak between $2\theta = 35$ and 55º along with sharp Bragg's peaks indicate the simultaneous formation of amorphous and crystalline phases on gas-atomisation of alloys #1 to #10. Nevertheless, alloy #11 shows only sharp Bragg's peaks without a broad halo, demonstrating the full crystalline state of the powder. Interestingly, the relative area of the broad halo and the broadening of the crystalline peaks is different in each alloy, indicating the varying volume fraction of amorphous and crystalline structures in each composition. For instance, alloy #3 shows a single broad peak at 45º (2θ) with a little shoulder kink, demonstrating the highest volume fraction of the amorphous phase in the investigated alloys. The small peak in alloy #3 is due to surface crystallisation in the largest particles (*i.e.*, > 100 μm) due to the nature of the production process [43,44].

The cooling rate in gas atomisation is inversely proportional to the particle size (see APPENDIX A) [37], suggesting that the amorphisation is more likely in the smallest particle size fraction in each alloy. Accordingly, the as-atomised powders were sieved to separate the fraction < 20 μm. The XRD patterns of the sieved powders (< 20 μm) of alloys #1, #3, #6 and #7 show only a broad halo between 35 and 55 ° (2θ) (Fig. 2 (a)), confirming the amorphous nature of these alloys. Contrary to that, the other alloys (alloys #2, #4, #5, #8, #9, and #10) reveal Bragg's peaks of the crystalline phases, identified as α-Fe(Si), Fe_2B, and Fe_3Si. Interestingly, the relative intensity of the crystalline peaks in the sieved powders (< 20 μm) was significantly smaller than the ones in the as-atomised powders (see Fig. 1), confirming the

higher weight fraction of amorphous phase in the fraction < 20 µm as compared to as-atomised powder. The higher amorphous fraction of sieved powders can be utilised as an "amorphisation capability indicator" for the alloys. On the other hand, the absence of the broad peak between 35 and 55° (2θ) in the fraction < 20 µm of alloy #11 confirms its fully crystalline structure.

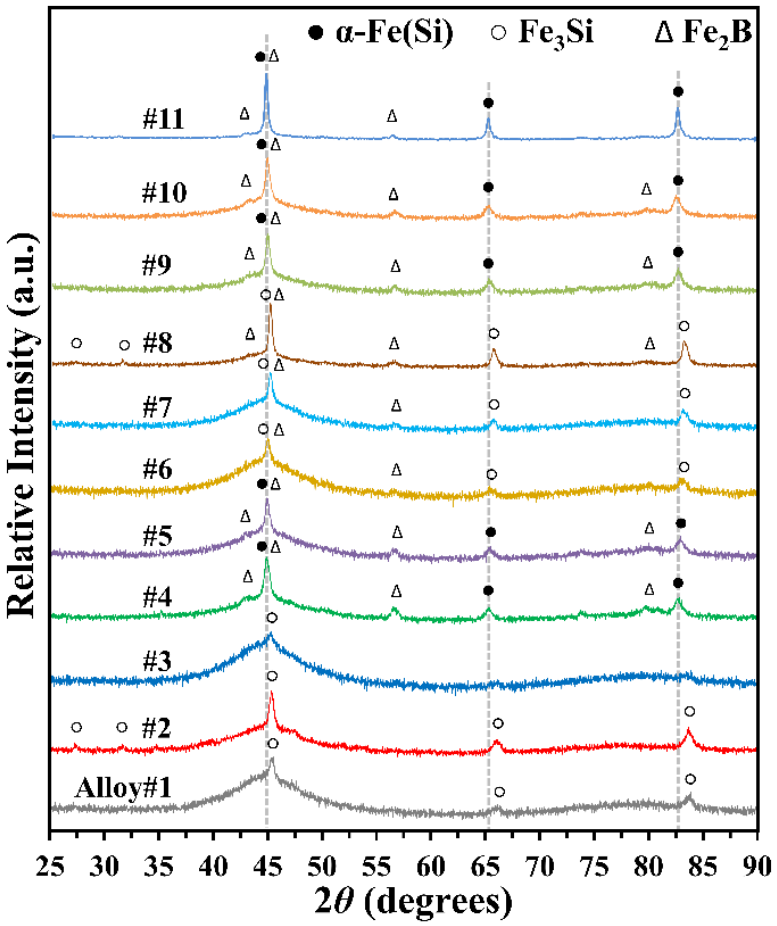

Fig. 1. XRD patterns of the as-atomised powders of alloys #1 to #11. Dashed grey lines correspond to the positions of the peaks of the phase α-Fe(Si).

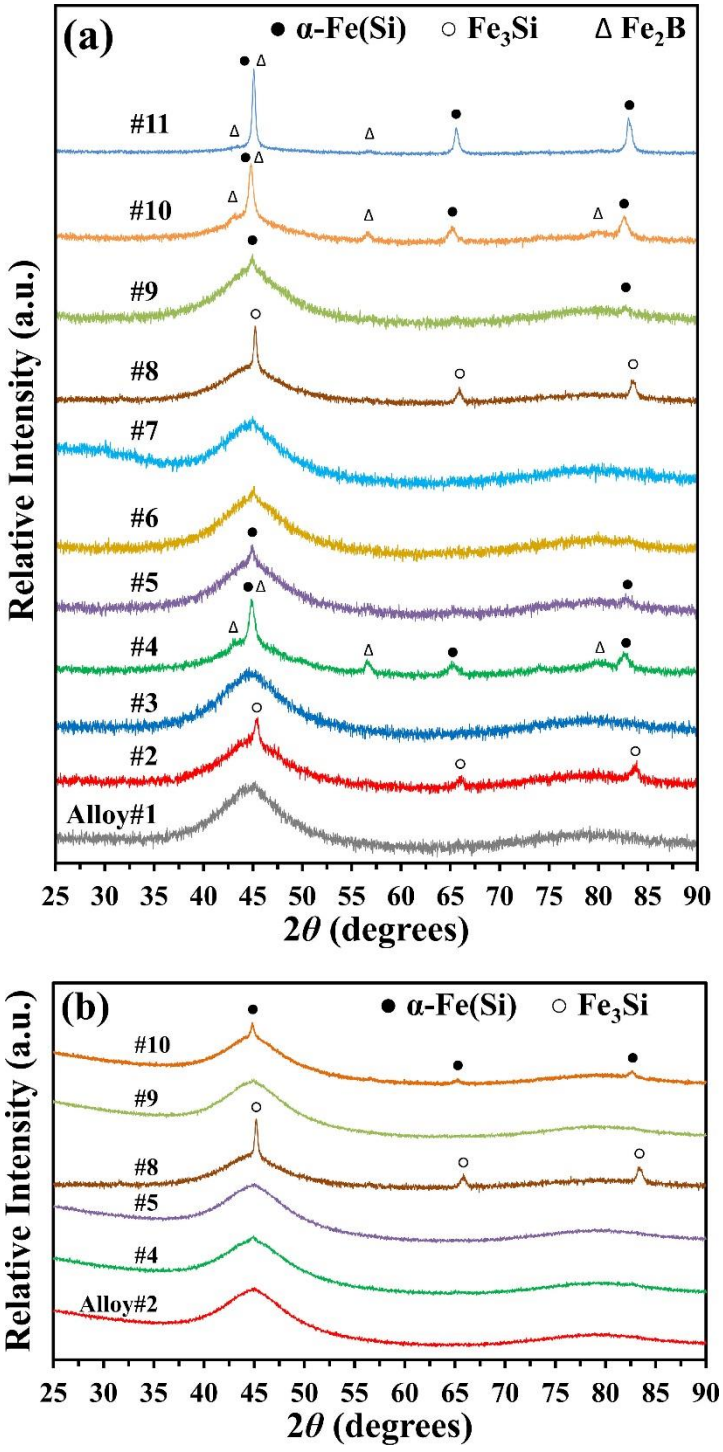

Fig. 2. a) XRD patterns of the sieved powders (<20 μm) of alloys #1 to #11 and (b) XRD patterns of the sieved powders (<10 μm) of alloys #2, #4, #5 and #8 to #10.

Furthermore, in order to find the particle size below which fully amorphous structure can be found, the partially crystalline powders in the fraction < 20 µm (Fig. 2 (a)) were further sieved to separate the fraction < 10 µm. As can be seen in the XRD patterns shown in Fig. 2 (b), the absence of Bragg's peaks in the fraction < 10 µm of alloys #2, #4, #5, and #9 confirms the amorphous nature of the particles below 10 µm. Conversely, alloys #8 and #10 exhibit crystalline structure even in the particles < 10 µm, which indicates the low amorphisation capability of these alloys.

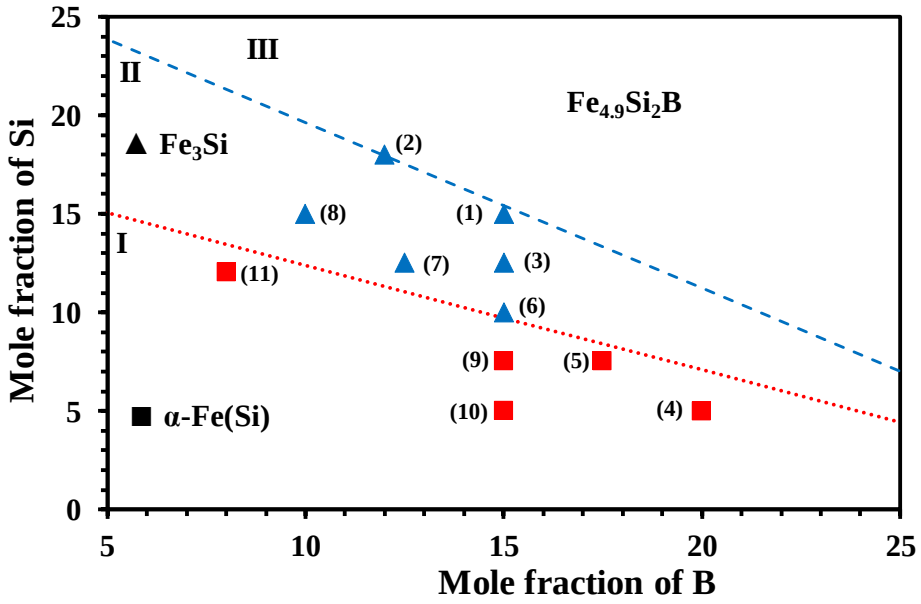

Fig. 3. Fe-rich corner of the ternary Fe-Si-B system showing the limits for the formation of the phases α-Fe(Si) (■) and Fe_3Si (▲), according to the XRD results shown in Fig. 1 of the as-atomised alloys (alloys #1 to #11).

Fig. 3 presents the nature of the crystalline phases formed as a function of Si and B content. The Fe-rich corner of the ternary Fe-Si-B system has been divided into three regions: below the dotted line (region-I), between dotted and dashed line (region-II) and above the dashed line (region-III). It is evident that the crystallisation of the α-Fe(Si) (B2) phase takes place in region-I, and the ordered Fe_3Si (DO_3) phase crystallises in region-II, which agrees with a previous report [45]. Even if this work does not include any composition in region-III, it has been demonstrated that the phase $Fe_{4.9}Si_2B$ precipitates when Si and B contents exceed 30 at.% [45,46]. Consequently, it can establish an upper and lower limit for the formation of

α-Fe(Si) and Fe_3Si considering the amount of Si and B. In addition, Fe_2B phase precipitates in some as-atomised alloys (see Fig. 1), though no correlation between the Fe_2B and Si and B content can be established.

3.2 Amorphous fraction (AF) of as-atomised powders

The thermal transitions in the as-atomised powders were analysed using DSC presented in Fig. 4. The crystallisation starts in a broad temperature range, *i.e.*, T_X of different alloys are between

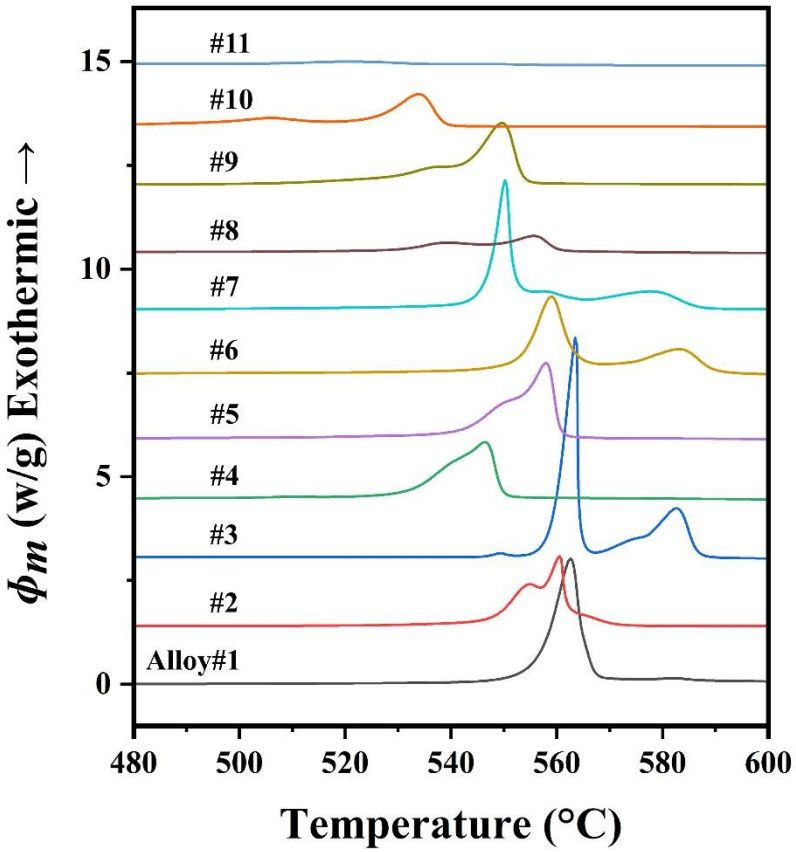

Fig. 4. DSC traces of the as-atomised powders of alloys #1 to #11.

489 and 553 ºC, as summarised in Table 1. The powders reveal one, two, or three exothermic events, depending on the crystallisation mode of the alloys (*i.e.*, polymorphous, primary, or eutectic crystallisation [14]). Although alloy #1 exhibits only one crystallisation peak, the multi-crystallisation peak characteristic observed in alloys #2 to #10 can be attributed to the primary crystallisation mode [14,47]. Moreover, overlapped exothermic peaks in some alloys show that the crystallisation of the second and/or third phase starts even before the completion

of the precipitation of the previous phase. The sharp peak characteristic observed in alloys #1, #3 and #7 indicates the compositional homogeneity of the crystallites precipitated during heating. Finally, it can be noted that the DSC trace of alloy #11 does not show any measurable crystallisation peak, confirming the fully crystalline microstructure of this alloy.

Table 1. DSC results of the as-atomised and sieved powders[a].

Alloy #	Composition (at.%)	T_X (°C)	ΔH_C (J/g)	ΔH (J/g) (as-atomised powder)	AF (%)
1	$Fe_{70}Si_{15}B_{15}$	557	161.0	132.0	82
2	$Fe_{70}Si_{18}B_{12}$	547	166.0	91.0	55
3	$Fe_{72.5}Si_{12.5}B_{15}$	547	170.0	170.0	100
4	$Fe_{75}Si_5B_{20}$	530	178.8	95.5	54
5	$Fe_{75}Si_{7.5}B_{17.5}$	542	178.0	113.0	63
6	$Fe_{75}Si_{10}B_{15}$	553	179.0	146.0	82
7	$Fe_{75}Si_{12.5}B_{12.5}$	547	164.0	134.0	82
8	$Fe_{75}Si_{15}B_{10}$	528	184[b]	49.4	27
9	$Fe_{77.50}Si_{7.5}B_{15}$	525	173.0	111.0	64
10	$Fe_{80}Si_5B_{15}$	489	---	70.6	<27
11	$Fe_{80}Si_{12}B_8$	---	---	---	0

[a] T_X: crystallisation temperature; ΔH_C: crystallisation enthalpy; ΔH: area of exothermic peak of partially amorphous powders (as-atomised); AF: amorphous fraction calculated with Eq. (A. 2) shown in APPENDIX A.

[b] Value obtained from Ref [49,50].

The heat released during crystallisation, *i.e.*, the area under the crystallisation peaks, was used to calculate the amorphous fraction of the powders in the as-atomised state [48]. The crystallisation enthalpy (ΔH_C) of the amorphous phase of each alloy was obtained from the DSC trace of fully amorphous particles, separated by sieving and whose amorphous structure was confirmed by XRD (see Fig. 2). A partially amorphous structure results in the reduction of the energy released during crystallisation and, consequently, the area of the exothermic peaks is reduced. This area is proportional to the weight fraction (%) of the amorphous phase existing in the sample. The area of the exothermic peaks of partially amorphous as-atomised powders (ΔH) was divided by the crystallisation enthalpy (ΔH_C) to obtain the amorphous fractions (AF) in the as-atomised powders, as shown by Eq. (A. 2) (see APPENDIX A). Since

alloys #8 and #10 exhibited Bragg's peaks even in the fraction < 10 μm (see Fig. 2 (b)), ΔH_C could not be measured for these compositions. The ΔH_C of alloy #8 was obtained from the literature [49,50], while for alloy #10, ΔH_C was approximated by the area of the exothermic peak of partially amorphous particles of the fraction < 10 μm; consequently, AF of alloy #10 is not an exact value, but an upper boundary. The amorphous fraction (AF) in the as-atomised powders is summarised in Table 1. Alloy #3 reveals a 100% of amorphous fraction, which is in good agreement with XRD results (see Fig. 1). Furthermore, alloys #1, #6, and #7 revealed AF = 82%, which is the second-highest AF among the investigated alloys. The AF of alloys #2, #4, #5, and #9 remained in the range of 54 to 64%. On the other hand, the AF of alloys #8 and #10 were estimated as 27% and < 27%, respectively, denoting the low amorphisation capability of these alloys. The AF of alloy #11 was found zero since it did not show any measurable exothermic peak (see Fig. 4).

3.3 Evaluation of amorphisation capability of the alloys

The AF is a good indicator of the amorphisation capability of the alloys, and other parameters can be derived using AF, such as the critical particle size, d_C, and the critical cooling rate, R_C (see APPENDIX A for the calculation procedure). AF, d_C, and R_C can be used to gauge how useful conventional empirical criteria are to predict the amorphisation capability of gas-atomised powders. Different conventional amorphisation capability parameters of the investigated alloys were calculated and are summarised in Table 2. Since some of the alloys were amorphous and did not reveal any glass transition (or supercooled liquid region), only parameters that do not use T_g were analysed to estimate the AFA. Alloy #3 ($Fe_{72.5}Si_{12.5}B_{15}$) has the highest amorphisation capability within the series of investigated alloys since it has the largest AF ~ 100%, the largest d_C ~ 96 μm, and the lowest $R_C \sim 6.3 \times 10^4$ K/s.

According to Inoue's empirical rules [13], the enthalpy of mixing, ΔH^{mix}, significantly favours the formation of the amorphous structure and is a good indicator of the AFA. The more negative the ΔH^{mix} is, the higher the AFA of an alloy. The enthalpy of mixing of the alloys is summarised in Table 2; the detailed calculation procedure is reported elsewhere [51]. Interestingly, ΔH^{mix} does not correlate with the AF; the most negative ΔH^{mix} was observed for alloy #2, which was partially amorphous (AF = 55%). In addition, the most negative ΔH^{mix}

coincides with the alloys showing the lowest T_l and, consequently, is the closest one to the deepest eutectic point (see Table 2). Similarly, no correlation was identified for α- and β-parameters with the AF of the alloys [26], being the largest values of $\alpha \sim 0.480$ and $\beta \sim 1.480$ for the alloy #2, which has low AF = 55%, along with a small $d_C \sim 16.7$ μm and a high $R_C \sim 2.1 \times 10^6$ K/s.

Table 2. Amorphisation capability parameters[a].

Alloy #	Composition (at.%)	AF (%)	ΔH^{mix} (kJ/mol)	α (= T_X/T_l)	β (= 1 + α)	d_C (μm)	R_C (K/s)	T_l (°C)	λ-factor
1	$Fe_{70}Si_{15}B_{15}$	82	-268800	0.469	1.469	43.6	3.0E+05	1188	0.220
2	$Fe_{70}Si_{18}B_{12}$	55	-275856	0.480	1.480	16.7	2.1E+06	1139	0.214
3	$Fe_{72.5}Si_{12.5}B_{15}$	100	-250475	0.452	1.452	96.1	6.3E+04	1210	0.204
4	$Fe_{75}Si_5B_{20}$	54	-214100	0.411	1.411	21.5	1.2E+06	1290	0.197
5	$Fe_{75}Si_{7.5}B_{17.5}$	63	-222600	0.431	1.431	30.9	6.0E+05	1257	0.193
6	$Fe_{75}Si_{10}B_{15}$	82	-230400	0.453	1.453	43.3	3.1E+05	1220	0.188
7	$Fe_{75}Si_{12.5}B_{12.5}$	82	-237500	0.465	1.465	55.4	1.9E+05	1177	0.183
8	$Fe_{75}Si_{15}B_{10}$	27[b]	-243900	0.447	1.447	8.8[b)]	7.6E+06[b)]	1180	0.179
9	$Fe_{77.50}Si_{7.5}B_{15}$	64	-208575	0.431	1.431	31.8	5.8E+05	1217	0.172
10	$Fe_{80}Si_5B_{15}$	<27	-185000	0.407	1.407	<10.0	>5.8E+06	1202	0.156
11	$Fe_{80}Si_{12}B_8$	0	-206336	---	---	---	---	1261	0.143

[a] AF: amorphous fraction calculated with Eq. (A. 2) shown in APPENDIX A; ΔH^{mix} enthalpy of mixing calculated by the procedure shown in Ref. [51]; α and β: GFA parameters [26]; d_C: critical particle size calculated following the procedure shown in APPENDIX A; R_C: critical cooling rate estimated with Eq. (A. 3) shown in APPENDIX A; T_l: liquidus temperature calculated by PANDAT™; λ-factor: calculated by Eq. (1).

[b] Values calculated based on the crystallisation enthalpy obtained from amorphous wires from Ref [49,50] (see also Table 1).

3.4 Establishing the amorphisation criteria for the alloys

The AFA was evaluated by combining thermodynamic modelling and the topological instability factor (λ) of the Fe-Si-B alloys. The liquidus surface projection (blue dotted lines) of the Fe-Si-B phase diagram in the vicinity of the Fe-rich zone is presented in Fig. 5 (a). Isothermal lines (solid green) are drawn to show how T_l decreases towards the eutectic point

E1 (red dot). In addition, it displays the primary stable phases just below the liquidus temperature. The position of the Fe-Si-B alloys investigated in the present study is indicated with numbered black spots.

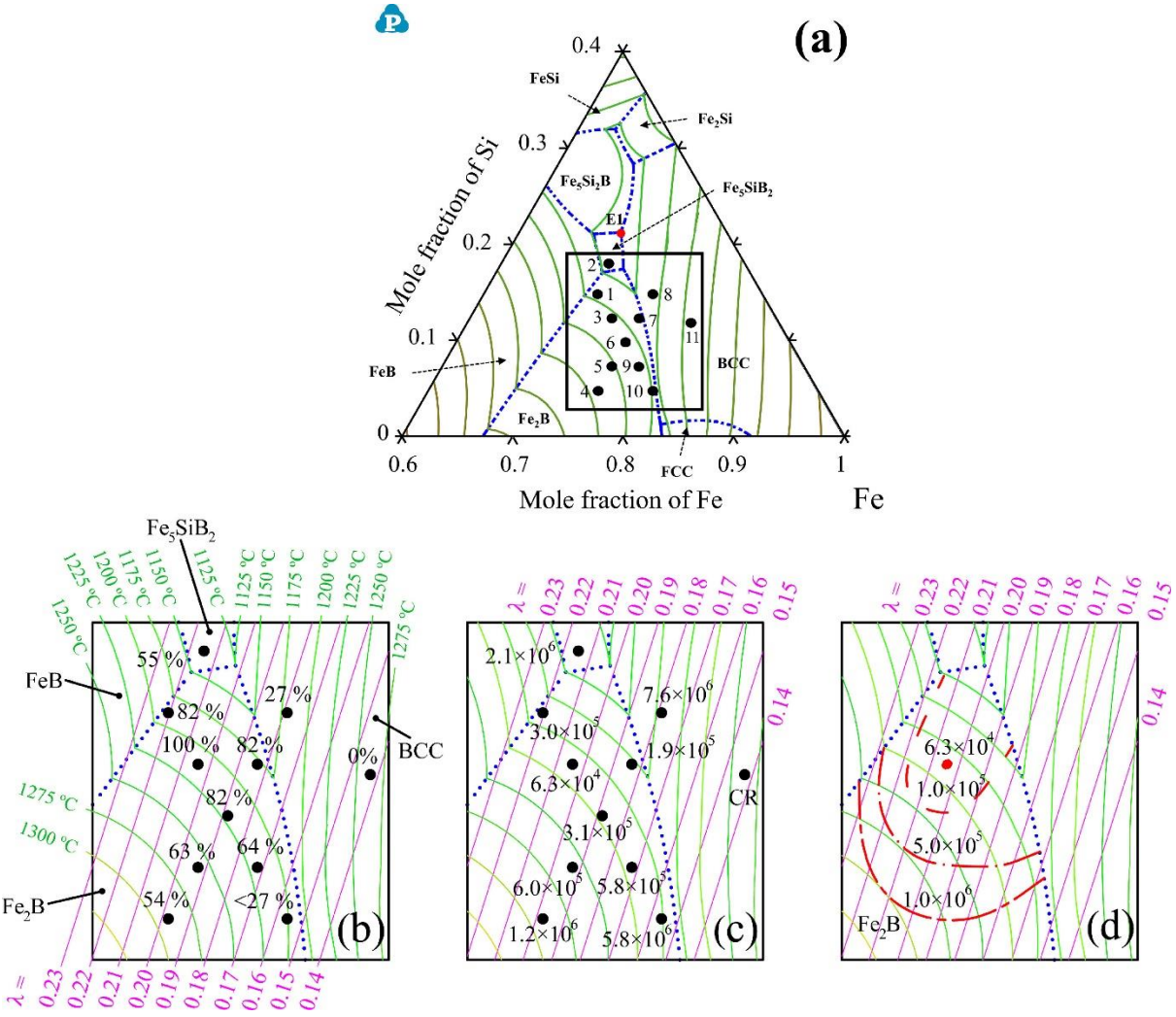

Fig. 5. a) Liquidus surface projection (blue dotted line) of the ternary Fe-Si-B diagram in the Fe-rich zone showing the investigated alloys (numbered black dots), eutectic point E1 (red dot), and the first equilibrium solid phase formed upon solidification; b) Magnified region showing λ-factor lines (solid magenta straight lines), AF (%) of all the investigated alloys and isotherms every 25 °C (green curved lines); c) R_C for all the investigated alloys; d) Estimated locus of constant R_C for 1.0 × 10^5 K/s (red dashed line), 5.0 × 10^5 K/s (red dash-dotted line) and 1.0 × 10^6 K/s (red two-dashed line).

The λ-factor of the Fe-Si-B alloys was calculated using Eq. (1), which only considers topological aspects and was initially proposed for binary alloys [25] and later extended to

multi-component systems by Yan *et al.* [52]. This parameter describes the minimum solute concentration needed for producing material as amorphous and is defined as:

$$\lambda = \sum_{i=B}^{Z} C_i \cdot |(r_i/r_A)^3 - 1| \quad (1)$$

where C_i is the solute atomic concentration (at.%), r_i is the solute atomic radius (nm), and r_A is the solvent atomic radius (nm). Assuming that the structure of amorphous metals can be modelled as an arrangement of icosahedral clusters, it has been proven that the optimal glass structure for numerous multi-component alloys is acquired when $\lambda \simeq 0.18$ [52]. Recently, the use of λ-factor, along with CALPHAD methodology, was reported to predict the glass forming ability of ternary Zr-Fe-Al [53], Fe-Nb-B [54] and Co-Fe-B [55] bulk metallic glasses produced by Cu-mould casting and melt spinning, showing that the optimal value of λ can change from 0.14 to 0.22 depending on the composition. Consequently, in order to determine the optimal λ-factor for a given ternary system, this parameter should be validated experimentally.

Table 2 shows the λ-factor calculated for all the investigated alloys. The values range between 0.143 and 0.220. On the other hand, Fig. 5 (b) to (d) display magnified zone of Fig. 5 (a) inside the black rectangle; in these enlarged figures, λ-factor lines and isothermal lines have been superimposed on the liquidus surface projection. The following information has been added in each one of these figures: i) AF (see Fig. 5 (b), ii) R_C (see Fig. 5 (c)), and iii) locus of constant R_C for 1.0×10^5 K/s (red dashed line), 5.0×10^5 K/s (red dash-dotted line) and 1.0×10^6 K/s (red two-dashed line) (see Fig. 5 (d)).

The AFA of Fe-Si-B alloys has been analysed considering the information displayed in Fig. 5. The amorphisation criteria have been established as follow, depending on the first solid phase formed upon equilibrium solidification (*i.e.*, BCC, Fe_5SiB_2 and Fe_2B), T_l and λ-parameter:

i. **BCC (Fe-Si solid solution with BCC structure)**: two alloys were atomised within this region, being one fully crystalline (alloy #11) and the other with AF = 27% (alloy #8). Lowering the T_l plays a significant role in the amorphisation capability of alloys in this region; reducing T_l from 1261 ºC (alloy #11) to 1180 ºC (alloy #8) increased AF from

0 to ~27% (see Table 2). Interestingly, it is possible to obtain melt-spun amorphous ribbons of compositions belonging to this region, as reported elsewhere [38–40]. The lower cooling rates in gas atomisation as compared to melt-spinning, however, do not allow producing a high fraction of amorphous phase in powders. The low AFA of alloy #11 could be attributed to the low $\lambda = 0.143$, compared to the optimal value (*i.e.*, $\lambda = 0.18$), and the high T_l (= 1261 ºC). On the other hand, alloy #8 with a good combination of $\lambda = 0.179$ and low $T_l = 1180$ ºC was expected to reveal high AF. Nevertheless, the low AF (= 27%) of alloy #8 suggests that the cooling rates in gas atomisation are not high enough to synthesise fully amorphous powders within this region. It seems that the region of the phase diagram where compositions are selected has a significant influence on the AFA. This can be easily pointed out by comparing alloy #8 with alloy #7; alloy #7 has similar λ-factor (= 0.183) and T_l (= 1177 ºC), but AF of this alloy is 82%, *i.e.*, three times higher than in the case of alloy #8.

ii. **Fe_5SiB_2**: only one composition (alloy #2, $Fe_{70}Si_{18}B_{12}$) was produced within this region, corresponding to the lowest $T_l = 1139$ ºC (see Table 2). According to the bibliography, AFA significantly improves when T_l is lower or closer to the eutectic composition [14]. However, alloy #2 was only partially amorphous (AF = 55%), and R_C was as high as ~ 2.1×10^6 K/s, suggesting that a low T_l is not enough to produce the high AFA. The λ-factor of this alloy was calculated to be 0.214, which is significantly higher than the optimal value (*i.e.*, $\lambda = 0.18$).

iii. **Fe_2B**: most of the compositions were produced within this region (8 samples), where AF varied from 54 to 100%. The results showed before suggest that this region is highly favourable for the formation of amorphous Fe-Si-B alloys. The best combination of T_l and λ-factor was found for alloy #7 (*i.e.*, the lowest $T_l = 1177$ ºC in the region and $\lambda = 0.183$ close to the optimal theoretical value). However, alloy #7 only retained an AF = 82%. Interestingly, alloy #3 revealed 100% of amorphous structure, suggesting that the optimal experimental value of λ-factor for Fe-Si-B alloys is approximately 0.204. It seems that the AF of Fe-Si-B compositions systematically converges to 100% when they approach the composition of alloy #3 (see Fig. 5 (b)). For instance, alloy #3 is encircled by alloys #1 ($\lambda = 0.220$), #6 ($\lambda = 0.188$) and #7 ($\lambda = 0.183$), which revealed an

AF = 82%. More interestingly, whereas alloys #9 (T_l = 1217 ºC) and #6 (T_l = 1220 ºC) possess similar T_l values and are in the same Fe_2B region, AF rose from 64% in alloy #9 to 82% in alloy #6. This significant increase in AF can be attributed to the rise of λ-factor from 0.172 (alloy #9) to 0.188 (alloy #6), thus approaching the optimal experimental value of 0.204. This suggests that the λ-factor is one of the most critical parameters for the amorphisation capability criteria of the Fe-Si-B alloys.

These results can be used as an instrument to carefully select compositions of the ternary Fe-Si-B system with high AFA. For example, Fig. 5 (c) can be used to select compositions whose critical cooling rate (R_C) is just below the average cooling rate characteristic of the technique used to synthesise the alloy. Furthermore, the proposed methodology to establish the optimum AFA region, combining CALPHAD, the topological instability factor (λ), and gas atomisation for experimental validation could be extended to other systems where the formation of amorphous phases is challenging.

4. Conclusions

According to the presented results, alloys with high amorphisation capability in the Fe-Si-B system can be designed using the following rules:

i. Not all regions of the phase diagram are suitable to obtain amorphous alloys. For the Fe-Si-B system, the compositions in the region where Fe_2B is the first solid phase formed upon equilibrium solidification have higher AFA as compared to others.

ii. The relative solute/solvent concentration should be such that λ-factor values vary in the range of 0.18 to 0.22. More specifically, the highest AFA is achieved when the λ-factor is approximately 0.204.

iii. Within limits fixed by the two previous criteria, the alloys with lower liquidus temperature (*i.e.*, closer to the eutectic composition) will have higher amorphisation capability.

Given a production method with a characteristic average cooling rate, these criteria can be used to design ternary Fe-Si-B alloys with a high enough AFA (*i.e.*, with a low enough critical cooling rate) to be obtained with an amorphous structure.

Appendix A

The average cooling rate of non-crystalline alloy particles during gas atomisation ($\left|\frac{\Delta T_d}{\Delta t}\right|$) can be estimated using the following simplified equation [56,57]:

$$\left|\frac{\Delta T_d}{\Delta t}\right| \approx \left|\frac{12}{\rho \cdot C_p} \cdot \left(T_d - T_f\right) \cdot \frac{k_g}{d^2}\right| \quad \text{(A. 1)}$$

where ρ is the density of the alloy, C_p the heat capacity, T_d the ambience temperature, T_f the furnace temperature, k_g the thermal conductivity of the atomising gas, and d the diameter of the particle.

Eq. (A. 1) indicates that the cooling rate of a particle is inversely proportional to the square of its diameter, so small particles experience high cooling rates during gas atomisation, which consequently increases the fraction of the amorphous phase. Based on this fact, the fully amorphous particles were separated from as-atomised powders using sieves with different opening meshes in order to find a particle size below which the powder is completely amorphous according to its XRD pattern. Then, the energy released upon heating by fully amorphous particles (*i.e.*, the crystallisation enthalpy, ΔH_C) and by the as-atomised powder (*i.e.*, ΔH) were measured by DSC. Finally, the amorphous fraction (AF) was calculated using the following equation [46,48,58]:

$$AF = \frac{\Delta H}{\Delta H_C} \quad \text{(A. 2)}$$

The possibility of amorphisation is higher in the smallest particles, but in general, it is not possible to affirm that every particle containing an amorphous phase is fully amorphous [58]. Particles with size near the critical diameter may possess a mixture of amorphous and crystalline structures. In the particular case of Fe-Si-B powders, the amount of crystallites in the particles with an amorphous phase is minimal [44]; therefore, it can be neglected. Thus, the fraction of the amorphous phase calculated from Eq. (A. 2) can be considered equal to the fraction of amorphous particles. The critical diameter (d_C) was obtained from the cumulative particle size distribution of the as-atomised powder, determined by laser diffraction, using the AF calculated with Eq. (A. 2), as explained in reference [46]. The critical diameter values are

reported in Table 2. The critical cooling rate (R_C), also reported in Table 2, was calculated by substituting the critical diameter (d_C) into Eq. (A. 1):

$$R_C \approx \left| \frac{12}{\rho \cdot C_p} \cdot \left(T_d - T_f\right) \frac{k_g}{d_c^2} \right| \quad \text{(A. 3)}$$

The numerical values used in this calculation were C_p = 35 J/(mol·K) [59], T_d = 300 K, T_f = 1973 K, k_g = 0.150 W/(m·K) for He [57] and the density of the alloys (ρ) measured by He pycnometry (see Table A. 1).

Table A. 1 Density (ρ) of alloys #1 to 11.

Alloy	Compositions (at.%)	ρ (g/cm^3)
1	$Fe_{70}Si_{15}B_{15}$	6.89
2	$Fe_{70}Si_{18}B_{12}$	6.84
3	$Fe_{72.5}Si_{12.5}B_{15}$	6.96
4	$Fe_{75}Si_5B_{20}$	7.20
5	$Fe_{75}Si_{7.5}B_{17.5}$	7.07
6	$Fe_{75}Si_{10}B_{15}$	7.05
7	$Fe_{75}Si_{12.5}B_{12.5}$	7.02
8	$Fe_{75}Si_{15}B_{10}$	7.04
9	$Fe_{77.50}Si_{7.5}B_{15}$	7.13
10	$Fe_{80}Si_5B_{15}$	7.26
11	$Fe_{80}Si_{12}B_8$	7.26

References

[1] P. Duwez, R.H. Willens, W. Klement, Continuous series of metastable solid solutions in silver-copper alloys, J. Appl. Phys. 31 (1960) 1136–1137. https://doi.org/10.1063/1.1735777.

[2] H.X. Li, Z.C. Lu, S.L. Wang, Y. Wu, Z.P. Lu, Fe-based bulk metallic glasses: Glass formation, fabrication, properties and applications, Prog. Mater. Sci. 103 (2019) 235–318. https://doi.org/10.1016/j.pmatsci.2019.01.003.

[3] C.A. Queiroz, J. Šesták, Aspects of the non-crystalline state, Phys. Chem. Glas. Eur. J. Og Glas. Sci. Technol. Part B. 51 (2010) 165–172.

[4] P.K. Gupta, Non-crystalline solids: glasses and amorphous solids, J. Non. Cryst. Solids.

195 (1996) 158–164. https://doi.org/10.1016/0022-3093(95)00502-1.

[5] I.-R. Lu, G. Wilde, G.P. Görler, R. Willnecker, Thermodynamic properties of Pd-based glass-forming alloys, J. Non. Cryst. Solids. 250–252 (1999) 577–581. https://doi.org/10.1016/S0022-3093(99)00135-0.

[6] Z. Mahbooba, L. Thorsson, M. Unosson, P. Skoglund, H. West, T. Horn, C. Rock, E. Vogli, O. Harrysson, Additive manufacturing of an iron-based bulk metallic glass larger than the critical casting thickness, Appl. Mater. Today. 11 (2018) 264–269. https://doi.org/10.1016/j.apmt.2018.02.011.

[7] A. Masood, V. Ström, L. Belova, K. V. Rao, J. Ågren, Effect of Ni-substitution on glass forming ability, mechanical, and magnetic properties of FeBNbY bulk metallic glasses, J. Appl. Phys. 113 (2013) 013505. https://doi.org/10.1063/1.4772753.

[8] A. Masood, L. Belova, V. Ström, On the correlation between glass forming ability (GFA) and soft magnetism of Ni-substituted Fe-based metallic glassy alloys, J. Magn. Magn. Mater. 504 (2020) 166667. https://doi.org/10.1016/j.jmmm.2020.166667.

[9] E. Dastanpour, M.H. Enayati, A. Masood, V. Ström, On the glass forming ability (GFA), crystallization behavior and soft magnetic properties of nanomet-substituted alloys, J. Non. Cryst. Solids. 529 (2020) 119774. https://doi.org/10.1016/j.jnoncrysol.2019.119774.

[10] D. Turnbull, Under What Conditions Can A Glass Be Formed?, Contemp. Phys. 10 (1969) 473–488. https://doi.org/10.1080/00107516908204405.

[11] Z.P. Lu, Y. Li, S.C. Ng, Reduced glass transition temperature and glass forming ability of bulk glass forming alloys, J. Non. Cryst. Solids. 270 (2000) 103–114. https://doi.org/10.1016/S0022-3093(00)00064-8.

[12] I.W. Donald, H.A. Davies, Prediction of glass-forming ability for metallic systems, J. Non. Cryst. Solids. 30 (1978) 77–85. https://doi.org/10.1016/0022-3093(78)90058-3.

[13] A. Takeuchi, A. Inoue, Classification of bulk metallic glasses by atomic size difference, heat of mixing and period of constituent elements and its application to characterization of the main alloying element, Mater. Trans. 46 (2005) 2817–2829. https://doi.org/10.2320/matertrans.46.2817.

[14] C. Suryanarayana, A. Inoue, Bulk Metallic Glasses, CRC/Taylor & Francis, US, 2011.

[15] A. Inoue, T. Zhang, T. Masumoto, Glass-forming ability of alloys, J. Non. Cryst. Solids. 156–158 (1993) 473–480. https://doi.org/10.1016/0022-3093(93)90003-G.

[16] M. Saad, M. Poulain, Glass forming ability criterion, Mater. Sci. Forum. 19–20 (1987) 11–18. https://doi.org/10.4028/www.scientific.net/msf.19-20.11.

[17] Z.P. Lu, C.T. Liu, A new glass-forming ability criterion for bulk metallic glasses, Acta Mater. 50 (2002) 3501–3512. https://doi.org/10.1016/S1359-6454(02)00166-0.

[18] Q. Chen, J. Shen, D. Zhang, H. Fan, J. Sun, D.G. McCartney, A new criterion for evaluating the glass-forming ability of bulk metallic glasses, Mater. Sci. Eng. A. 433 (2006) 155–160. https://doi.org/10.1016/j.msea.2006.06.053.

[19] G.J. Fan, H. Choo, P.K. Liaw, A new criterion for the glass-forming ability of liquids, J. Non. Cryst. Solids. 353 (2007) 102–107. https://doi.org/10.1016/j.jnoncrysol.2006.08.049.

[20] X.H. Du, J.C. Huang, C.T. Liu, Z.P. Lu, New criterion of glass forming ability for bulk metallic glasses, J. Appl. Phys. 101 (2007) 23–25. https://doi.org/10.1063/1.2718286.

[21] Z. Long, H. Wei, Y. Ding, P. Zhang, G. Xie, A. Inoue, A new criterion for predicting the glass-forming ability of bulk metallic glasses, J. Alloys Compd. 475 (2009) 207–219. https://doi.org/10.1016/j.jallcom.2008.07.087.

[22] Z.Z. Yuan, S.L. Bao, Y. Lu, D.P. Zhang, L. Yao, A new criterion for evaluating the glass-forming ability of bulk glass forming alloys, J. Alloys Compd. 459 (2008) 251–260. https://doi.org/10.1016/j.jallcom.2007.05.037.

[23] E.S. Park, W.T. Kim, D.H. Kim, A simple model for determining alloy composition with large glass forming ability in ternary alloys, Metall. Mater. Trans. A Phys. Metall. Mater. Sci. 32 (2001) 200–202. https://doi.org/10.1007/s11661-998-0334-4.

[24] E.S. Park, D.H. Kim, W.T. Kim, Parameter for glass forming ability of ternary alloy systems, Appl. Phys. Lett. 86 (2005) 061907. https://doi.org/10.1063/1.1862790.

[25] T. Egami, Y. Waseda, Atomic size effect on the glass forming ability of metallic alloys, J. Non. Cryst. Solids. 64 (1984) 113–134.

[26] K. Mondal, B.S. Murty, On the parameters to assess the glass forming ability of liquids, J. Non. Cryst. Solids. 351 (2005) 1366–1371. https://doi.org/10.1016/j.jnoncrysol.2005.03.006.

[27] J.J. Han, C.P. Wang, J. Wang, X.J. Liu, Y. Wang, Z.K. Liu, Compositional design of Fe-based multi-component bulk metallic glass based on CALPHAD method, Mater. Des. 126 (2017) 47–56. https://doi.org/10.1016/j.matdes.2017.04.030.

[28] L. Shi, K. Yao, Composition design for Fe-based soft magnetic amorphous and nanocrystalline alloys with high Fe content, Mater. Des. 189 (2020) 108511. https://doi.org/10.1016/j.matdes.2020.108511.

[29] K. Ackland, A. Masood, S. Kulkarni, P. Stamenov, Ultra-soft magnetic Co-Fe-B-Si-Nb amorphous alloys for high frequency power applications, AIP Adv. 8 (2018). https://doi.org/10.1063/1.5007707.

[30] H. Ahmadian, A. Masood, Z. Pavlovic, K.L. Alvarez, C. Ómathúna, P. Mccloskey, P. Stamenov, On the mechanisms limiting power loss in amorphous CoFeB-based melt-spun ribbons, J. Magn. Magn. Mater. 502 (2020) 166535. https://doi.org/10.1016/j.jmmm.2020.166535.

[31] A. Masood, H.A. Baghbaderani, K.L. Alvarez, J.M. Blanco, Z. Pavlovic, V. Ström, P. Stamenov, C.O. Mathuna, P. Mccloskey, High-frequency power loss mechanisms in ultra-thin amorphous ribbons, J. Magn. Magn. Mater. 519 (2021) 167469. https://doi.org/10.1016/j.jmmm.2020.167469.

[32] M. Hagiwara, A. Inoue, T. Masumoto, Mechanical properties of Fe-Si-B amorphous wires produced by in-rotating-water spinning method, Metall. Trans. A. 13 (1982) 373–382. https://doi.org/10.1007/BF02643346.

[33] G. Herzer, Modern soft magnets: Amorphous and nanocrystalline materials, Acta Mater. 61 (2013) 718–734. https://doi.org/10.1016/j.actamat.2012.10.040.

[34] R.M. German, Powder Metallurgy and Particulate Materials Processing, Metal Powder Industries Federation (MPIF), Princeton, NJ, USA, 2005.

[35] K.L. Alvarez, H.A. Baghbaderani, J.M. Martín, N. Burgos, M. Ipatov, Z. Pavlovic, P. Mccloskey, A. Masood, J. Gonzalez, Novel Fe-based amorphous and nanocrystalline powder cores for high- frequency power conversion, J. Magn. Magn. Mater. 501 (2020) 166457. https://doi.org/10.1016/j.jmmm.2020.166457.

[36] Z. Guo, J. Wang, W. Chen, D. Chen, H. Sun, Z. Xue, C. Wang, Crystal-like microstructural Finemet/FeSi compound powder core with excellent soft magnetic properties and its loss separation analysis, Mater. Des. 192 (2020) 108769. https://doi.org/10.1016/j.matdes.2020.108769.

[37] A.J. Yule, J.J. Dunkley, Atomization of Melts for Powder Production and Spray Deposition, Oxford University Press, UK Oxford, 1994.

[38] T. Sato, Study on powder properties of Fe-P-C and Fe-B-Si alloy powders prepared by water atomization, J. Mater. Sci. 26 (1991) 2329–2336. https://doi.org/10.1007/BF01130177.

[39] M. Hagiwara, A. Inoue, T. Masumoto, The critical thickness for the formation of Fe-, Ni- and Co-based amorphous alloys with metalloids, Sci. Reports Res. Institutes Tohoku Univ. Ser. a-Physics Chem. Metall. 29 (1981) 351–358.

[40] F.E. Luborsky, I. Reeve, H.A. Davies, H.H. Liebermann, Effect of Fe-B-Si composition on maximum thickness for casting amorphous metals, IEEE Trans. Magn. 18 (1982) 1385–1387. https://doi.org/10.1109/TMAG.1982.1062025.

[41] M. Schütte, R. Wartchow, M. Binnewies, Shape controlling synthesis - Formation of Fe_3Si by the reaction of iron with silicon tetrachloride and crystal structure refinement, Zeitschrift Fur Anorg. Und Allg. Chemie. 629 (2003) 1846–1850. https://doi.org/10.1002/zaac.200300125.

[42] M. Polcarová, K. Godwod, J. Bąk-Misiuk, S. Kadečková, J. Brádler, Lattice parameters of Fe-Si alloy single crystals, Phys. Status Solidi. 106 (1988) 17–23. https://doi.org/10.1002/pssa.2211060103.

[43] K.L. Alvarez, J.M. Martin, M. Ipatov, L. Dominguez, J. Gonzalez, Magnetic Properties of Annealed Amorphous $Fe_{72.5}Si_{12.5}B_{15}$ Alloy Obtained by Gas Atomization Technique, IEEE Trans. Magn. 54 (2018) 2002405. https://doi.org/10.1109/TMAG.2018.2839258.

[44] K.L. Alvarez, J.M. Martín, M. Ipatov, L. Dominguez, J. Gonzalez, Effect of Composition and Particle Size on the Soft Magnetic Character of Fe-Rich Amorphous Alloys Obtained by Gas Atomization, in: Euro PM2019, European Powder Metallurgy Association (EPMA), Maastricht, The Netherlands, 2019: pp. 1–6.

[45] A. Załuska, H. Matyja, Crystallization characteristics of amorphous Fe-Si-B alloys, J. Mater. Sci. 18 (1983) 2163–2172. https://doi.org/10.1007/BF00555011.

[46] K.L. Alvarez, J.M. Martín, M. Ipatov, J. Gonzalez, Soft magnetic amorphous alloys (Fe-rich) obtained by gas atomisation technique, J. Alloys Compd. 735 (2018) 2646–2652. https://doi.org/10.1016/j.jallcom.2017.11.272.

[47] Burton, Amorphous metallic alloys, 1st ed., Butterworths, UK, 1983.

[48] M.E. Brown, Introduction to Thermal Analysis: Techniques and Applications, 2001. https://doi.org/10.1017/CBO9781107415324.004.

[49] M. Hagiwara, A. Inoue, T. Masumoto, Production of amorphous CoSiB and CoMSiB (M ≡ Group IV - VIII transition metals) wires by a method employing melt spinning into rotating water and some properties of the wires, Mater. Sci. Eng. 54 (1982) 197–207. https://doi.org/10.1016/0025-5416(82)90114-8.

[50] U. Carow-Watamura, D.V. Louzguine, A. Takeuchi, B-Fe-Si (144), in: Y. Kawazoe, U. Carow-Watamura, J.Z. Yu (Eds.), Phys. Prop. Ternary Amorph. Alloy. Part 2 Syst. from B-Be-Fe to Co-W-Zr. Landolt-Börnstein - Gr. III Condens. Matter (Numerical Data Funct. Relationships Sci. Technol., Springer, Berlin, Heidelberg, 2011: pp. 200–253. https://doi.org/https://doi.org/10.1007/978-3-642-13850-8_44.

[51] A. Takeuchi, A. Inoue, Calculations of mixing enthalpy and mismatch entropy for ternary amorphous alloys, Mater. Trans. JIM. 41 (2000) 1372–1378. https://doi.org/10.2320/matertrans1989.41.1372.

[52] Z.J. Yan, J.F. Li, S.R. He, Y.H. Zhou, Evaluation of the optimum solute concentration for good glass forming ability in multicomponent metallic glasses, Mater. Res. Bull. 38 (2003) 681–689. https://doi.org/10.1016/S0025-5408(03)00010-2.

[53] A. Tabeshian, H. Mao, L. Arnberg, R.E. Aune, Investigation of glass forming ability in the Zr-rich part of the Zr-Fe-Al ternary system, J. Appl. Phys. 125 (2019) 065101. https://doi.org/10.1063/1.5066554.

[54] D.D.E. Brennhaugen, H. Mao, D. V. Louzguine-Luzgin, L. Arnberg, R.E. Aune, Predictive modeling of glass forming ability in the Fe-Nb-B system using the CALPHAD approach, J. Alloys Compd. 707 (2017) 120–125. https://doi.org/10.1016/j.jallcom.2016.12.049.

[55] H.A. Baghbaderani, A. Masood, K.L. Alvarez, C.Ó. Mathúna, P. McCloskey, P. Stamenov, CALPHAD-assisted development of in-situ nanocrystallised melt-spun Co-Fe-B alloy with high Bs (1.57T), J. Alloys Compd. 877 (2021) 160194. https://doi.org/https://doi.org/10.1016/j.jallcom.2021.160194.

[56] H. Shiwen, L. Yong, G. Sheng, Cooling rate calculation of non-equilibrium aluminum alloy powders prepared by gas atomization, Rare Met. Mater. Eng. 38 (2009) 353–356.

[57] A. Inoue, Light-metal based amorphous alloys, in: Curr. Top. Amorph. Mater., Elsevier B.V., 1993: pp. 159–166. https://doi.org/10.1016/B978-0-444-81576-7.50023-X.

[58] N. Ciftci, N. Ellendt, R. Von Bargen, H. Henein, L. Mädler, V. Uhlenwinkel, Atomization and characterization of a glass forming alloy $\{(Fe_{0.6}Co_{0.4})_{0.75}B_{0.2}Si_{0.05}\}_{96}Nb_4$, J. Non. Cryst. Solids. 394–395 (2014) 36–42. https://doi.org/10.1016/j.jnoncrysol.2014.03.023.

[59] J. Zhang, H. Fujimori, A. Inoue, T. Masumoto, Specific heat behaviour on soft magnetic thick amorphous ribbons of an Fe-B-Si alloy, Mater. Sci. Eng. 99 (1988) 35–38. https://doi.org/10.1016/0025-5416(88)90286-8.

Appendix B

Journal of Magnetism and Magnetic Materials 501 (2020) 166457

Contents lists available at ScienceDirect

Journal of Magnetism and Magnetic Materials

journal homepage: www.elsevier.com/locate/jmmm

Research articles

Novel Fe-based amorphous and nanocrystalline powder cores for high-frequency power conversion

Kenny L. Alvarez[a,b,*], H.A. Baghbaderani[c], J.M. Martín[a], N. Burgos[a], M. Ipatov[d], Z. Pavlovic[c], P. McCloskey[c], A. Masood[c], J. Gonzalez[e]

[a] CEIT and Tecnun (University of Navarra), Pº de Manuel Lardizabal 15, 20018 San Sebastián, Spain
[b] Escuela de Ingeniería Mecánica, Pontificia Universidad Católica de Valparaíso, Av. Brasil 2950, Valparaíso, Chile
[c] Tyndall National Institute, University College Cork, Lee Maltings Complex, Dyke Parade T12R5CP, Cork, Ireland
[d] SGIker (Magnetic Measurements), University of the Basque Country, Av. Tolosa 72, 20018 San Sebastián, Spain
[e] Dept. of Materials Physics, University of the Basque Country, Pº de Manuel Lardizabal 3, 20018 San Sebastián, Spain

Abstract

The present work demonstrates the high-frequency core loss performance of Fe-based amorphous and nanocrystalline powder cores, initially produced by gas atomised powder, consolidated using sieved particles ≤ 20 μm, and isolated by a precise insulating layer of polymer to limit the inter- and intra-particle eddy currents to attain enhanced performance. The large glass forming ability (GFA) of the gas atomised powder, reflected by different glass forming instruments, such as the supercooled region (ΔT_X = 54 ºC) and the reduced glass transition temperature (T_{rg}= 0.56), is consistent with the substantial amorphisation capability of the alloy. To the best of our knowledge, this is the first-ever report to reveal a large ΔT_X in the Finemet-type alloy powders, an essential parameter to gas-atomise the amorphous powders with significantly lower cooling rates compared to the melt-spun ribbons. Further, subsequent annealing of the amorphous powders, between the exothermic events guided by differential scanning calorimetry (DSC), lead to the growth of a fine nanocrystalline structure of grains ≤ 15 nm, thanks to the positive enthalpy of mixing of Cu with the constituents to act as a nucleation agent, to retain the excellent soft magnetic properties. The DC soft magnetic properties of the powders were significantly improved on thermal annealing, confirmed by hysteretic loops, quantified by reduced coercivity H_c < 80 A/m of annealed powder at < 575 ºC, and attributed to the reduced magnetoelastic contribution due to zero/near-zero magnetostriction anisotropy, attained due to the homogenous nanocrystalline structure. The amorphous and nanocrystalline powder cores, consolidated by compression moulding, show ultra-high loss performance, due to the ultra-low coercivity attained on nanocrystallisation, and negligible eddy currents loss, owning to efficient insulation of small particles, for high-frequency power conversion applications, such as voltage regulator (VR), and resonant converters, in automotive industry and data storage centres.

Keywords: Gas Atomization, Amorphous and Nanocrystalline Powders, Powder Cores, Core Loss, High-frequency.

1. Introduction

The high-saturation flux density (B_s > 1.5 T), ultra-low coercivity (H_c < 1 A/m) and high-permeability (μ_r > 10^5) of amorphous and nanocrystalline materials, as compared to soft-

ferrites (B_s < 0.5 T), makes them a potential candidate for device miniaturisation in high-frequency power converters, such as voltage regulator (VR) and resonant converters, for applications in automotive industry and data storage centres [1,2]. Amorphous and nanocrystalline alloys are generally produced in melt-spun ribbon form, well investigated for their soft magnetic properties, and commercially available for low-frequency power conversion. However, as the device operating frequency (f) approaches MHz range, the eddy current loss (P_e α f^2) abruptly increases, as compared to the hysteresis loss (P_h α f), and consequently, the total core loss (P_{CV}) is dominated by P_e at f > 100 kHz [3]. The large P_e significantly deteriorates the soft magnetic properties, resulting in a substantial amount of joule heating, that restricts the device design freedom, and hence, limits the high flux concentration advantage of amorphous and nanocrystalline materials for high-frequency power applications [4]. To overcome the challenge of eddy current loss at MHz switching frequencies, magnetic cores made by insulated amorphous and nanocrystalline powders are one of the possible solutions, where inter-particle eddy currents can be limited using insulated particles. The efficiency of magnetic cores can be further enhanced if ultra-small powder particles (≤ 20 μm) are used to avoid the eddy currents inside insulated particles [5–7].

Soft magnetic amorphous powders are generally produced by gas atomisation which emerged as a novel route for bulk scale amorphous powder production to form complex geometries using different consolidation techniques and hence, provides a unique solution to overcome the intrinsic problem of low glass forming ability (GFA) of amorphous metals to produce in bulk dimensions [8–10]. The gas atomisation consists of breaking a metal stream into droplets using a high-velocity gas flow and is a well industrialised mass production method [11]. The high velocity of the gas and the small diameter of the droplets (microns range) allow rapid solidification of the melt with reasonably high cooling rates to produce amorphous powders [12,13]. However, if GFA of the alloys, which is a measure of critical cooling rates to produce alloys into amorphous form, is not large enough, it is challenging to produce amorphous powders [14]. The production of amorphous metal powders by gas atomisation, while retaining their excellent soft magnetic properties, is rather a new area of research and hence, provides a potential route to utilise this novel class of materials for a broader range of applications, including high-frequency power conversion [15].

The purpose of the present work is as follows; it demonstrates the production of amorphous powders by gas atomisation, reveals the high amorphisation capability of the alloy powders, shows the grain growth mechanisms of nanocrystallisation, and correlates the structural and soft magnetic properties. Finally, it demonstrates the high-frequency core loss mechanisms of amorphous and nanocrystalline powder cores, consolidated by compression moulding, using precisely isolated ultra-small (≤ 20 μm) powders to overcome the inter- and intra-particle eddy currents at various excitation fields.

2. Materials and methods

Amorphous $(Fe_{0.725}Si_{0.125}B_{0.150})_{96.5}Nb_{3.0}Cu_{0.5}$ (atomic %) composition is based on the ternary Fe-Si-B alloy obtained in our previous work [13]. The powder was produced via gas atomisation using a convergent-divergent, close-coupled atomiser in an atomisation unit PSI model Hermiga 75/3VI. The amount of powder produced was nearly 2.5 kg. Fe (Allied Metal Corp.), Si (Cometal S.A.), B (H.C. Starck), Nb and Cu (AMPERE alloys S.A.) of commercial purity were melted in an induction furnace under a high purity argon atmosphere. The atomisation chamber was evacuated and purged with helium to minimise oxidation. The melt pouring temperature was 1700 ºC. The atomising gas was helium at a pressure of 60 bar. The particle size distribution of the powders was measured by Sympatec Helos (H 0852) laser diffractometer. The true density was measured in a He pycnometer Micromeritics AccuPyc 1330.

Isothermal heat treatment of powder was carried out in a conventional laboratory furnace (CARBOLITE, RHF 14/35). The powder was sieved ≤ 20 μm, and a 15 g sample was used for annealing in an alumina crucible. Before annealing, the chamber was purged with high purity argon ($H_2O \leq 3$ ppm, $O_2 \leq 3$ ppm $C_nH_m \leq 3$ ppm). The temperature was precisely controlled, using a thermocouple, to anneal samples at three different temperatures (525, 575 and 625 ºC) for 30 minutes dwell time.

The isothermally annealed powder of ≤ 20 μm was uniformly mixed with 20 vol.% of Araldite AT 1-1 epoxy resin. Toroidal powder cores (~ Ø 22 × ~ Ø 10 × ~t 6.5 mm) were prepared by compression moulding. The samples were pressed uniaxially in a Tinius-Olsen 30T press at 200 MPa using a floating die. Then, the temperature was raised to 120 ºC for 10

min. Finally, the sample was cooled down to room temperature, the pressure was released, and the compact was ejected from the die by pushing with the upper punch. After shaping the toroidal cores, the organic binder was completely cured for 24 hours at 120 ºC under an ambient atmosphere. The homogeneous distribution of particles and binder was analysed on a fracture surface using field emission gun scanning electron microscopy (FEI Quanta 3D FEG). The geometric density of the compacts was calculated from their weight and dimensions.

Differential scanning calorimetry (DSC) was used to identify the thermal transitions of the powders. The DSC experiments were conducted in a TA Instruments DSC 2920, at a heating rate of 10 ºC/min under an argon atmosphere, using a powder of ~ 10 mg on a copper pan, covered with a copper lid. Particle shape was studied using scanning electron microscopy (SEM, Philips XL30CP). The constituent phases were identified via X-ray diffraction (XRD, Philips X´pert MRD, Cu-K_α, λ = 1.542 Å). The diffraction angle (2θ) varied from 25º to 90º (scanning rate of 0.005 º/s, step size = 0.02º, holding time = 4 sec). Furthermore, the Rietveld refinement method was performed, using another refined XRD pattern obtained from Bruker D8 Advance A25 diffractometer, to estimate the size and the volume fraction of crystalline phases, the detailed procedure is published elsewhere [16]. Thin foils from powders were prepared using a focused ion beam (FIB, FEI Quanta 3D FEG) milling instrument by lift-out technique. In the first step, a particle of ~ 20 µm was selected, and a Pt line was deposited on the surface. Two stair-step FIB trenches were cut on both sides of the Pt line. In the second step, the specimen was further thinned to less than 1 µm, and a slice of the specimen was cut free. The obtained lamella was removed using a micromanipulator and welded with Pt to a Cu grid that was suitable for transmission electron microscopy (TEM) analysis. Final milling < 100 nm was conducted by employing successively lower voltages of up to 2 kV. The obtained specimen was examined by a conventional bright-field imaging TEM microscope (JEOL JEM-2100F), operated at 200 kV with LaB_6 filament.

The DC magnetic properties of the powders were evaluated using a vibrating sample magnetometer (VSM, Quantum Design PPMS-9T, Model P525), calibrated with a paramagnetic Dy_2O_3 standard. The temperature dependence of magnetisation $M(T)$, was measured using the magneto-thermo-gravimetric (MTG) technique, and the Curie temperature (T_C) was calculated using the steepest temperature derivative, $dM(T)/dT$, the detailed procedure

is published elsewhere [17]. The P_{CV} and μ_r were calculated based on resistance and inductance measurements, respectively, of an inductor prototype using LCR meter (Agilent E4980A). The prototype windings consist of 30 uniformly distributed copper turns. The measurements were conducted at frequencies from 50 kHz to 1 MHz and at four different current levels (25, 50, 75, and 100 mA). The power loss and permeability of the hollow toroidal plastic core, with the same dimensions as air-core, was also measured in order to subtract the copper winding loss. Additionally, the high-frequency permeameter (PMM 9G, Ryowa Electronics) was used to measure the μ_r spectrum in the 10-9000 MHz frequency range, using a square sample (4 mm × 4 mm × 0.5 mm) diced from a consolidated specimen (80 vol.% of powder mixed with 20 vol.% of epoxy resin).

3. Results and discussion

a. Thermal and structural characterisation of the powders

The gas-atomisation parameters and physical properties of the as-atomised powders (i.e., as received after atomisation, before sieving or annealing) are summarised in Table I. A broad distribution of particle size was obtained with a 10th percent percentile D_{10} = 5.1 μm and a 90th percent percentile D_{90} = 60.0 μm. The powder particle was obtained with a median size (D_{50}) of 17.5 μm. The apparent density (defined as the mass per unit of volume of loose-packed powders) was measured as 35.3% of the true density. The tap density, i.e., the powder's packing ability without applying any pressure, was 68.5% of the true density.

The fine particle size of atomised powder could be attributed to the high gas pressure during the atomisation and use of helium gas (for example, helium velocity is about three times higher than argon velocity for the same atomisation pressure) [11]. The high thermal conductivity of helium as compared to argon enhances the cooling rate by one order of magnitude, helping to obtain the amorphous structure of the powders [12]. The low apparent density of powder could be attributed to the ultra-fine nature of the particles due to high inter-particle friction. The high relative tap density (i.e., the tap density expressed as a percentage of the true density) demonstrates that vibrating the powder was significantly effective in improving powder packing, which, in other words, indicates the spherical nature of the powder produced during the present study.

Table I. Atomisation parameters and thermal and physical properties of the as-atomised powder.

Property		Value
Mass flow rate of melt (g/s)		17.24
Mass flow rate of gas (g/s)		12.63
Gas-metal mass flow rate ratio (GMR)		0.73
Liquidus temperature (ºC)		1124
Melt superheat (ºC)		576
Particle size distribution of as-atomised powder (μm)	D_{10}	5.1
	D_{50}	17.5
	D_{90}	60.0
Particle size distribution of the fraction ≤ 20 μm (μm)	D_{10}	4.3
	D_{50}	9.2
	D_{90}	19.6
Apparent density (% of true density)		35.3
Tap density (% of true density)		68.5
True density (g/cm^3)		7.02

D_{10}: 10th percent percentile; D_{50}: median particle size; D_{90}: 90th percent percentile.

Fig. 1 presents the XRD pattern of the as-atomised powder. A typical broad halo pattern in the range 2θ = 35 - 55º, with no distinguishable narrow diffraction peaks, which confirms the amorphous nature of the powder. Fig. 1 (inset) shows a secondary electrons image of the as-atomised powder. The particles were spherical, which is a typical characteristic of the powders produced via inert gas atomisation. In addition, the SEM reveals the broad size distribution range of the particles. It is worth mentioning that Cu, in the present alloy, has a positive enthalpy of mixing with the constituent elements and has a high tendency to start nucleation of

crystallites if cooling rates are insufficient during the atomisation process [18]. The XRD and SEM confirm that Fe-Si-B-Nb-Cu alloy preserves a tremendous capacity to be produced in amorphous spherical particles with a broad particle size (5 - 60 μm) distribution via helium gas atomisation with high productivity (1 kg/min) and yield (100%).

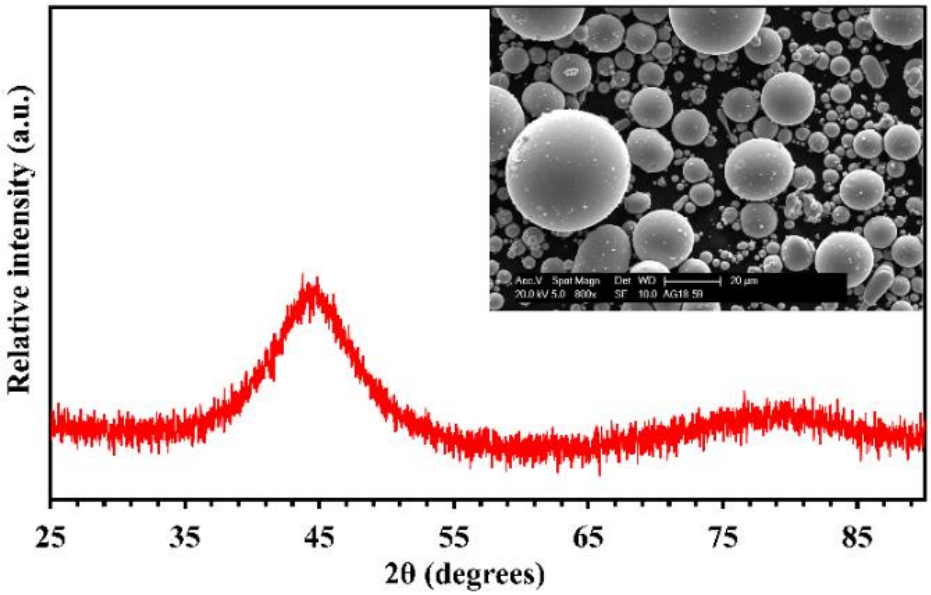

Fig. 1. X-ray diffraction pattern (XRD) of the as-atomised $(Fe_{0.725}Si_{0.125}B_{0.150})_{96.5}Nb_{3.0}Cu_{0.5}$ powder. The inset shows the SEM image of the as-atomised powder.

Fig. 2 shows the DSC trace of the as-atomised powder. The small endothermic peak observed at 335 ºC corresponds to the T_C of the alloy. The change observed in the heat capacity at the glass transition temperature T_g = 504 ºC is due to the glass transition. Two different exothermic events were distinguished in DSC, where the first peak corresponds to the crystallisation of Fe_3Si at T_{X1} = 558 ºC, and the second peak can be ascribed to the precipitation of Fe_2B at T_{X2} = 656 ºC [19]. In order to evaluate the GFA of the powders, two different parameters, such as supercooled liquid region ΔT_X *(*= T_{X1} - T_g) and the reduced glass transition temperature T_{rg} (= T_g/T_l, T_l = liquidus temperature), were calculated from the DSC [20]. The large ΔT_X = 54 ºC and high T_{rg} = 0.56 confirm the high GFA of the alloy, which is essentially required to quench the amorphous alloys at low cooling rates [21,22]. In addition, the

amorphous structure of the large particles (60 μm) further justifies the substantial amorphisation capability of the alloy. The large ΔT_X (i.e., 54 ºC) of Fe-Si-B-Nb-Cu shows high thermal stability against crystallisation, which is of significant importance to retain the amorphous atomic structure under robust working conditions. To the best of our knowledge, this is the first-ever report to reveal a large ΔT_X in a Finemet-type powder alloy.

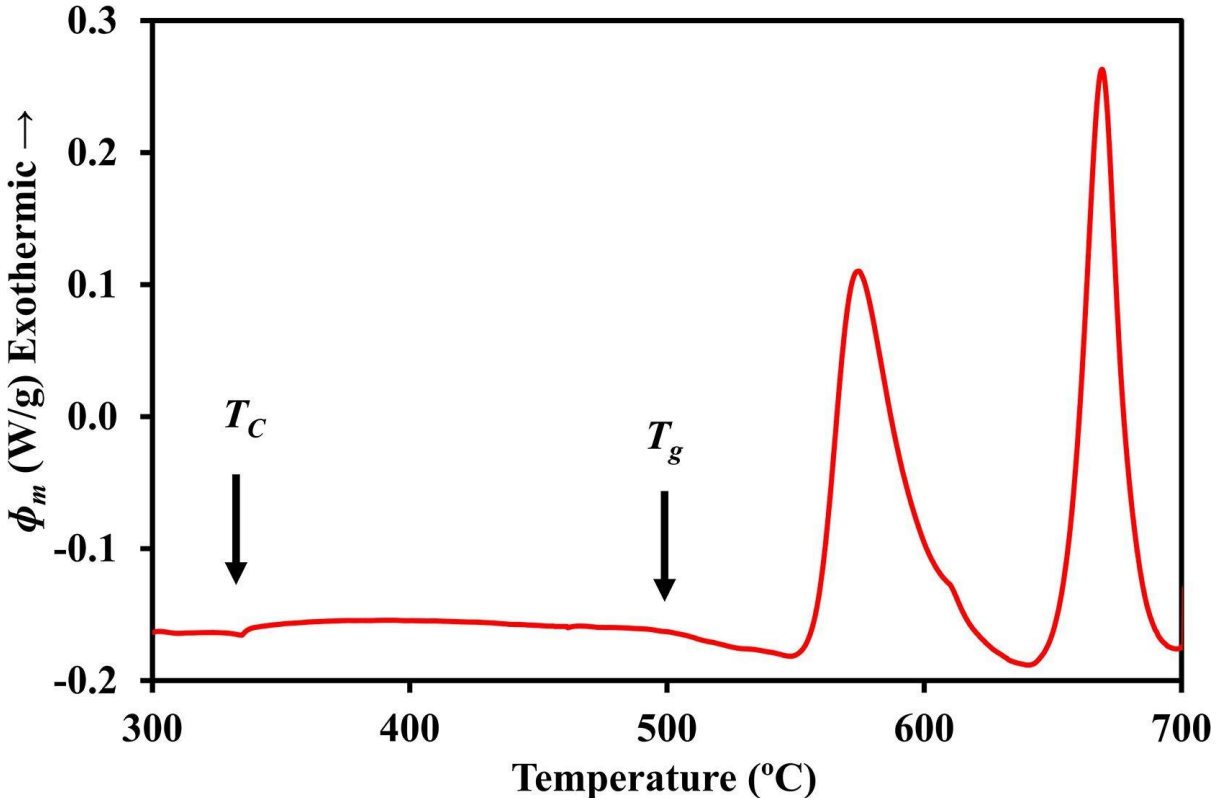

Fig. 2. Differential scanning calorimetry (DSC) trace of as-atomised sieved $(Fe_{0.725}Si_{0.125}B_{0.150})_{96.5}Nb_{3.0}Cu_{0.5}$ powder (≤ 20 μm).

In order to investigate the effect of structural relaxation and nanocrystallisation on the soft magnetic properties, the sieved powders ≤ 20 μm were annealed at three different temperatures, based on DSC, such as; (a) 525 ºC (below the onset of first crystallisation peak,), (b) 575 ºC (at the peak of first exothermic event) and (c) 625 ºC (between first and second exothermic event). Fig. 3 shows the XRD patterns of the annealed powders. The XRD analysis of the powders annealed at 525 ºC (i.e., the supercooled liquid region) did not show any sign of crystallisation; rather, it showed a broad maximum of amorphous structure. The powders

annealed at 575 ºC and 625 ºC revealed sharp Bragg's peaks, corresponding to the crystalline phase Fe_3Si (DO_3). The precipitation of Fe_3Si phase has been observed in similar alloys and reported elsewhere [23]. The size of nanocrystalline grains D, as well as the weight fraction X_D of Fe_3Si phase, were calculated by the Rietveld refinement method and summarised in Table II. Annealing at 575 ºC resulted in crystallisation of 23 wt.% of the as-atomised amorphous structure, where the precipitated phase was confirmed as Fe_3Si with a crystal size of 11.7 nm. Increasing the annealing temperature to 625 ºC leads to a slight increment of the crystal size (up to 13.4 nm), while the amount of Fe_3Si phase increased to ~ 47 wt.%.

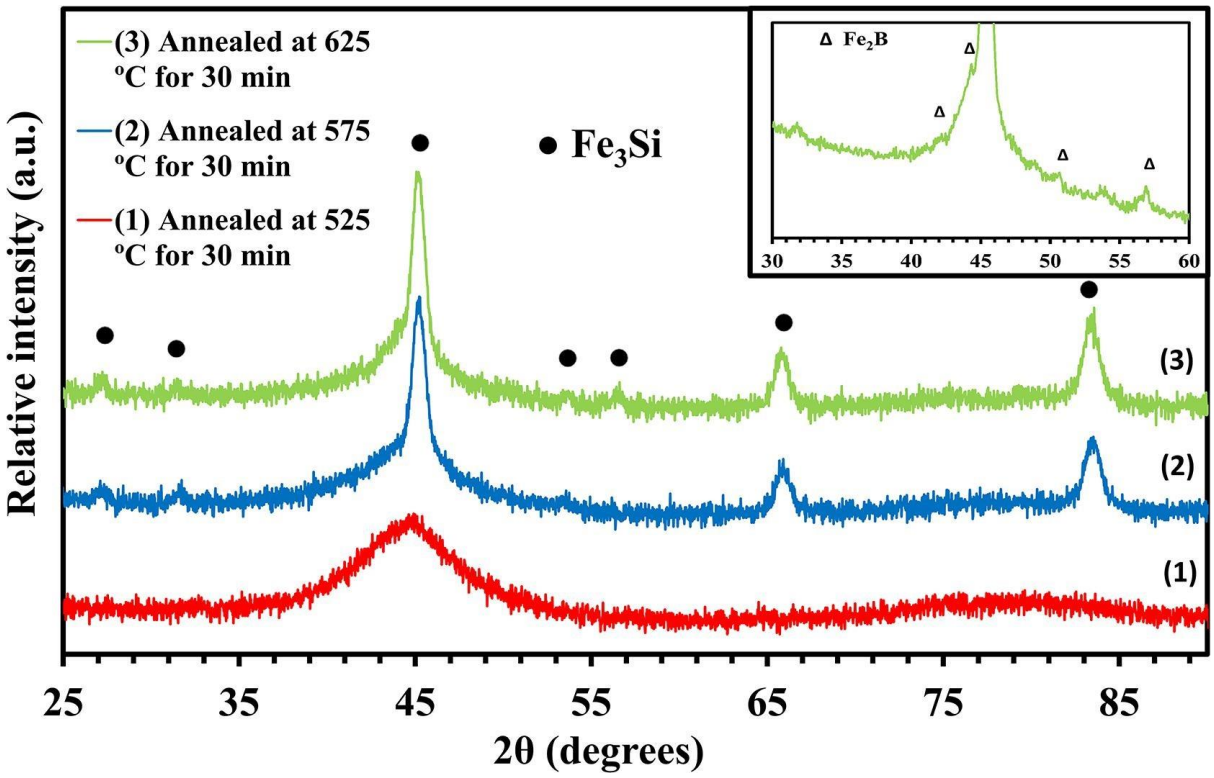

Fig. 3. X-ray diffraction pattern (XRD) of ≤ 20 μm powders annealed at 525 ºC, 575 ºC, and 625 ºC temperatures for 30 min. Inset shows XRD pattern of high quality of the sample annealed

Fig. 4 shows the bright field TEM image of 525 ºC, 575 ºC, and 625 ºC annealed powders, whereas the inset presents the selected area electron diffraction (SAED) patterns. The TEM of the 525 ºC annealed sample revealed a minimal volume fraction of nanocrystals of size ≤ 10 nm. The anomalous precipitation of the nanocrystalline phase below T_X (i.e., 558 ºC) was surprising, as a highly dense amorphous atomic structure was anticipated upon structural

relaxation. Furthermore, no signs of crystallisation were visible for the 525 ºC annealed powders by the XRD and SAED patterns, see Fig. 3 and the inset of Fig. 4(a). The 575 and 625 ºC annealed samples revealed the nanocrystallisation of the Fe_3Si phase, and SAED patterns from the randomly oriented Fe_3Si nanocrystals. Since the alloy contains Cu and Nb, this nanocrystallisation was expected after annealing the powder at the first crystallisation peak. Cu helps to increase the nucleation sites because Cu-rich clusters are formed during the sample heating, and, as a result, a homogeneous crystallisation randomly distributed in the amorphous matrix, takes place in Cu depleted zones. On the other hand, Nb hinders nanocrystals growth [24] and is so effective that crystal size barely grows even if the annealing temperature is increased to 50 ºC above the crystallisation peak temperature (from 575 to 625 ºC). The size of the nanocrystals and volume fraction measured by TEM was in good agreement with the XRD analysis of the powders shown in Table II.

The Curie temperature (T_C) intrinsically depends on the atomic structure of the magnetic material and is a useful instrument to investigate any small structural changes appearing during the annealing process of the amorphous alloys. Fig. 5 shows the $M(T)$ of the as-atomised and annealed powders. The magnetisation of the as-atomised powders approached zero at T_C = 335 ºC. The single-phase monolithic behaviour of $M(T)$, without showing any "kink" before the evolution of the 2nd magnetic phase on crystallisation, confirms the amorphous nature of the as-atomised powders [3,17]. The $M(T)$ of the 525 ºC annealed powders exhibited T_C = 369 ºC, higher than the T_C of as-atomised powder. The higher T_C of annealed powder could be attributed to the enhanced exchange interaction between Fe-Fe atoms, due to the highly-dense atomic packing achieved on the structural relaxation of the amorphous phase [13,17,25]. More interestingly, the magnetisation of 525 ºC annealed powder never reached zero at T_C = 369 ºC; rather it approached the temperature where a new magnetic phase precipitated after the 2nd exothermic event (see Fig. 2). This behaviour of $M(T)$ is well-known for two-phase magnetic materials, where the area under the curve can be utilised to quantify the volume fraction of the precipitated phases [17]. The anomalous precipitation of the nanocrystalline phase at 525 ºC was not expected since it is well below the crystallisation temperature (T_X = 558 ºC, see Fig. 2) of the powders. The existence of small crystallites observed by the $M(T)$ of 525 ºC annealed powder is in good agreement with the high-resolution TEM imaging (see Fig. 4), thanks to the

ultra-high sensitivity of the MTG technique to detect the minimal volume fraction of nanocrystals, which otherwise is not obvious from conventional diffraction techniques (i.e., XRD, SAED).

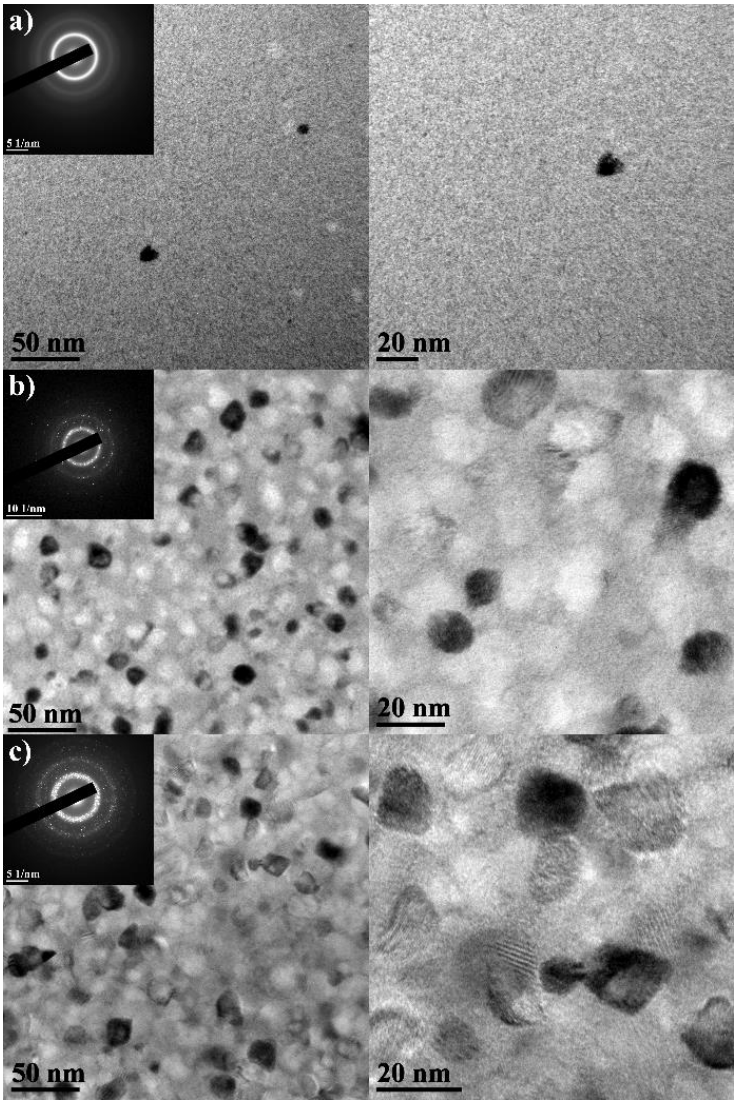

Fig. 4. Bright-field TEM images of the samples annealed at a) 525 ºC, b) 575 ºC and c) 625 ºC. Insets show the selected area electron diffraction (SAED).

Moreover, the *M(T)* of the 575 ºC annealed powder showed two-phase magnetic behaviour by revealing the significant volume fraction of the nanocrystalline phase in the amorphous matrix. The T_C = 380 ºC of the remaining amorphous matrix was slightly higher than that of

the 525 ºC annealed powders. The T_C of the nanocrystalline phase in 575 ºC annealed powders was measured as 567 ºC. The direct measurement of T_C = 567 ºC from the *M(T)* further confirms the presence of the Fe_3Si phase, which was initially observed by structural investigations (see Fig. 3 and Fog. 4) and agrees with theoretically estimated values for the Fe_3Si phase [26]. Furthermore, a small peak in the *M(T)* of 575 ºC annealed powders was observed after the T_C of Fe_3Si phase, which is the same temperature (~ 610 ºC) at which a small overlapped peak was emerged in DSC curve (see Fig. 2). The contribution of the new phase precipitated at 610 ºC is distinct from *M(T)* of 625 ºC annealed powders, suggesting a new magnetic phase as compared to 525 ºC and 575 ºC annealed powders.

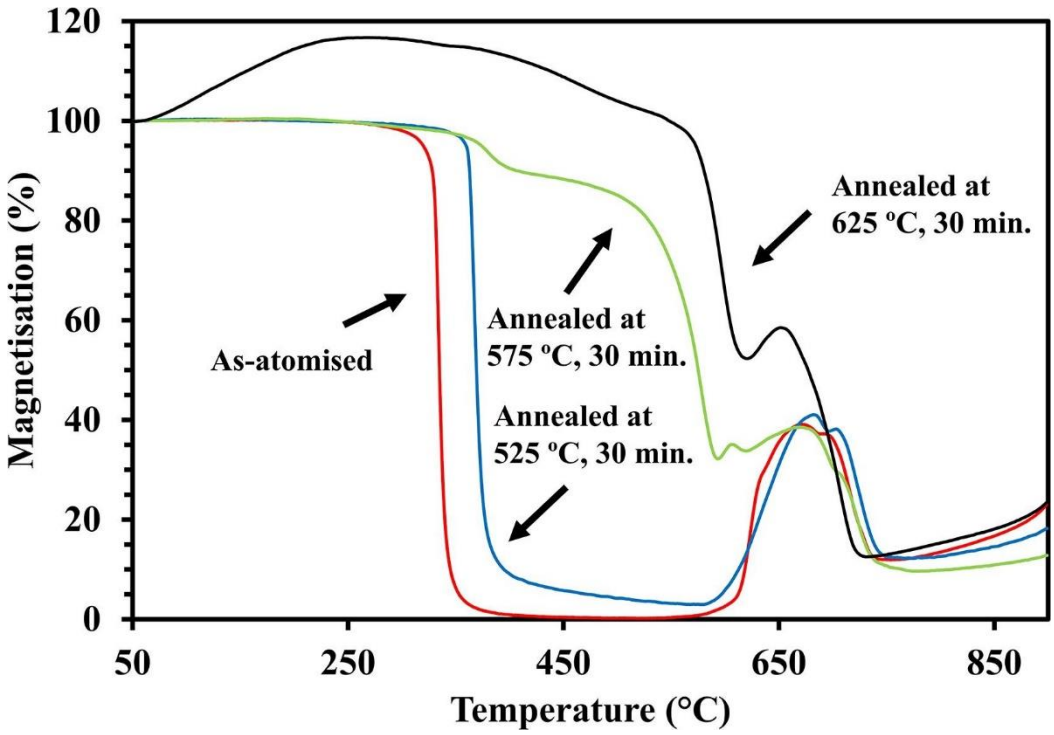

Fig. 5. Temperature dependence of magnetisation behaviour *M(T)* of powders annealed at 525 ºC, 575 ºC, and 625 ºC for 30 min. The *M(T)* of the as-atomised powder was presented for

b. DC soft magnetic properties of amorphous and nanocrystalline powders

Fig. 6 shows the hysteresis loop of as-atomised and annealed powders measured at room temperature. The soft magnetic behaviour of as-atomised and annealed powders was confirmed by the small H_c (see inset in Fig. 6). The magnetic properties obtained from the hysteresis loops are summarised in Table III. The H_c of the as-quenched amorphous powder was measured as 136 A/m, which was reduced to 70 A/m on annealing at 525 ºC (i.e., the temperature in the supercooled liquid region). The H_c of powders slightly increased to 72.42 A/m after annealing at 575 ºC (i.e., the first crystallisation peak temperature). However, an abrupt increase in the H_c = 1153.6 A/m was observed after annealing at 625 ºC. Despite the low H_c of powders annealed below 525 ºC, the coercivity is still higher as compared to melt-spun amorphous ribbons. The higher H_c of powders could be ascribed to a magnetic surface effect due to the large specific surface of gas-atomised powders.

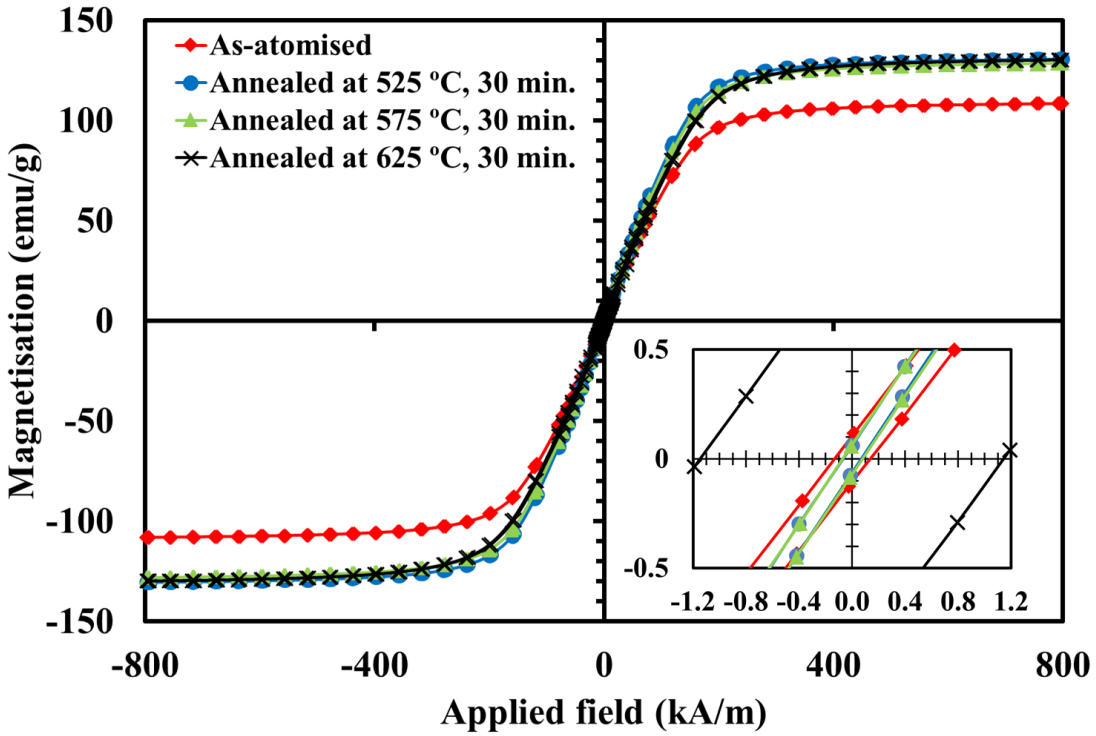

Fig. 6. Hysteresis loop measured at room temperature of the as-atomised and annealed powders ≤ 20 µm. Inset shows the magnification at the origin of coordinates.

Table II The structural and AC magnetic properties of different magnetic cores.

Property	As-atomised	Annealed 30 min		
		525 ºC	575 ºC	625 ºC
ρ_{core} (g/cm^3)	5.19	5.11	5.06	5.09
ρ_{core} (% of theor. dens.)	88.5	87.2	86.3	86.8
$X_{v\text{-}powder}$ (%)	70.8	69.7	69.0	69.5
$X_{v\text{-}epoxy}$ (%)	17.7	17.4	17.3	17.4
$X_{v\text{-}porosity}$ (%)	11.5	12.9	13.7	13.1
X_D (wt. %)	-	-	23	~ 47
D (nm)	-	-	11.7	13.4
Core loss (mW/cm^3)	1.41	0.64	0.62	0.58
μ_r (-)	16.09	15.85	15.30	13.97

ρ_{core}: core density; $X_{v\text{-}powder}$: volume fraction of magnetic powder; $X_{v\text{-}epoxy}$: volume fraction of epoxy resin; $X_{v\text{-}porosity}$: volume fraction of porosity; X_D: weight percentage of Fe_3Si phase; D: Fe_3Si crystallite size; Core loss (P_{CV}) at 1 MHz for B_m = 1 mT; μ_r: relative permeability.

The H_c of amorphous and nanocrystalline materials depends on effective magnetic anisotropy [28]. The high H_c (136 A/m) of the as-atomised powders could be attributed to the large residual stress induced due to the nature of the production process. In addition, the large magnetostriction constant (λ) of Fe-based amorphous alloys play a vital role in defining the high H_c. The soft magnetic properties of amorphous materials can be significantly improved by the thermal treatment of the alloys. The annealing can either relax the amorphous atomic structure by releasing the residual stress or grow a nanocrystalline structure inside the amorphous matrix. The reduced H_c of 525 ºC and 575 ºC annealed powders can be explained by the reduction of magnetoelastic anisotropy energy, due to structural relaxation of the amorphous phase or precipitation of significant volume fraction of nanocrystalline phase, which consequently makes the $\lambda \approx 0$, as confirmed by XRD, TEM, and $M(T)$ analysis (see Fig. 3, Fig. 4 and Fig. 5). In the case of the nanocrystalline materials, the magnetic softening depends on the size, volume fraction, and homogenous distribution of the nanocrystals. In the present alloy system, Cu works as a nucleation agent, due to the positive enthalpy of mixing with constituent elements, while the Nb works as an inhibitor, due to its large atomic size, to control the grain growth process. The nucleation and grain growth process in gas-atomised powders resulted in precisely controlled crystallites of $\leq$ 20 nm grains homogenously

distributed in the amorphous matrix, which is of significant importance to attain excellent soft magnetic properties and is well explained by Herzer's random anisotropy model (RAM). According to the RAM model, the local magnetic anisotropies (mainly of magnetocrystalline nature) of nanocrystalline grains are randomly averaged out since the ferromagnetic correlation exchange length (L_{ex} ~ 35 nm for α-Fe grains) is larger than the size of nanocrystals (D) embedded homogeneously in the amorphous matrix. The RAM model was initially proposed for amorphous materials [29], and later extended to nanocrystalline alloys under the assumption that $L_{ex} > D$ [28]. Further, deterioration in soft magnetic properties of the powders annealed at 625 ºC (i.e., H_c = 1153.6 A/m) could be ascribed to the precipitation of borides. The DSC trace in Fig. 2 shows a small overlapped peak at ~ 610 ºC that could be due to the precipitation of the metastable phase Fe_3B or the stable phase Fe_2B [30]. The precipitation of borides in powders annealed at 625 ºC was also observed in $M(T)$ curves (see Fig. 5). Furthermore, a high-resolution XRD was performed on the 625 ºC annealed powders, where the formation of a stable Fe_2B phase was confirmed (see inset in Fig. 3) [31]. It was believed that the high H_c of the 625 ºC annealed powders is due to the Fe_2B phase, which contains significantly high magnetocrystalline anisotropy and cannot be averaged out even though the grain size of Fe_3Si remains 13.4 nm and hence, does not follow the RAM model [32].

Moreover, the distribution of the anisotropy field was analysed to confirm the magnetic softening of amorphous and annealed powders [27]. The average anisotropy field, $<H_k>$, of as-atomised powders reduced from 165.6 to 161.6 kA/m after annealing at 525 ºC and then increased to 163.2 kA/m for 575 ºC annealed powders (see Table III). The full width at half maximum (FWHM) of the anisotropy field distribution of amorphous and annealed powders are summarised in Table III. The smaller FWHM of 525 ºC and 575 ºC annealed powders, as compared to as-atomised, confirmed the magnetic softening achieved after annealing. However, large $<H_k>$ and FWHM of 625 ºC annealed powders could be associated with the deteriorated soft magnetic properties due to the precipitation of borides during the annealing.

The hysteresis loops presented in Fig. 6 were used to measure the saturation magnetisation M_s of the powders. The M_s = 112 emu/g of the as-atomised powder increased to 132 - 134 emu/g after annealing. The increase in M_s values can be understood in terms of the two different contributions coming from the relative volume fractions of the crystalline phase Fe_3Si and the

remaining amorphous phase [33]. The three annealed powders have a close value of M_s, despite that the weight fraction of Fe_3Si ranges between 0 and 47 wt.%, which shows that M_s is somewhat similar to the amorphous relaxed phase and Fe_3Si.

c. Core fabrication and high-frequency soft magnetic properties

The magnetic cores were fabricated by mixing the as-atomised or annealed powder (≤ 20 μm) with 20 vol.% of the resin, the detailed procedure is explained in section 2. Fig. 7 shows a typical SEM image of the fractured surface of the core, while the inset illustrates an optical image of the core. The SEM analysis confirmed the homogeneous distribution of organic binder and powder particles. In fact, a thin layer of epoxy worked as an insulating coating around particles. The presence of an organic insulating film at the contact area between magnetic particles, compressed at high pressure (200 MPa) and temperature (120 ºC), cannot be directly observed with SEM technique. However, its presence with a thickness of < 100 Å has been demonstrated by X-ray photoelectron spectroscopy during the uniaxial pressing of iron compacts at 600 MPa [34]. Consequently, it appears that such an insulating film subsists in the present case. The insulating layer helps to reduce the inter-particle eddy current and, consequently, the associated core loss.

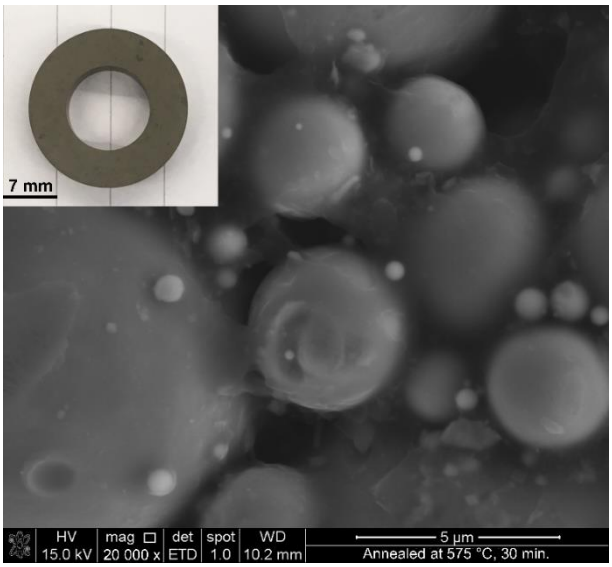

Fig. 7. Representative SEM image of magnetic core annealed at 575 ºC for 30 min. The inset shows an optical image of the core.

From the true density of the magnetic powder (7.02 g/cm^3) and epoxy resin (1.25 g/cm^3), the theoretical density of the mix with 20 vol.% of the organic binder was calculated to be 5.87 g/cm^3. The geometric density of the cores (ρ_{core}, in g/cm^3 and as % of the theoretical density of the mix), as well as the volume fraction of magnetic powder ($X_{v\text{-}powder}$), resin ($X_{v\text{-}epoxy}$) and porosity ($X_{v\text{-}porosity}$), are summarised in Table II. The volume fraction of magnetic powder was higher than the relative tap density due to the applied pressure during moulding. The brittle nature of the amorphous powders does not allow particles to flow plastically, and consequently, only a marginal increment of the volume fraction of magnetic powder above the relative tap density was observed.

Table III Magnetic properties of as-atomised and annealed powers.

Property	**As-atomised**	**Annealed 30 min**		
		525 ºC	**575 ºC**	**625 ºC**
H_c (A/m)	136	70	72.42	1153.6
M_s (emu/g)	112	134	132	133
$<H_k>$ (kA/m)	165.6	161.6	163.2	172
FWHM (kA/m)	94.30	76	78.94	98.84

H_C: coercivity obtained from the hysteresis loop; M_S: saturation magnetisation; $<H_k>$: average anisotropy field, calculated as the H field of the maximum value of the anisotropy field distribution $P(H_K)$ [27]; FWHM: full width at half maximum of the anisotropy field distribution.

Fig. 8 shows the materials loss performance at different frequencies and excitation fields of cores made by as-atomised and annealed powders. The materials loss can be broadly divided into three categories, such as hysteresis loss (P_h), eddy current loss (P_e), and anomalous loss (P_{an}) [5]. The total P_{CV} can be written as:

$$P_{CV} = P_h + P_e + P_{an} \quad (1)$$

The P_h in powder cores is generally dominant at low frequencies, whereas the P_e and P_{an} become significant at higher frequencies [35]. Fig. 8 (a) shows the core loss performance of

the as-atomised and annealed cores as a function of frequency at different excitations (B_m = 0.5 - 1 mT). The core loss of as-atomised powder cores was significantly higher in the entire frequency spectrum (50 kHz - 1000 kHz). The high core loss of the as-atomised powder core can be associated with the dominant P_h due to the substantial magnetoelastic contributions, intrinsically associated with the high saturation magnetostriction (λ = 10 - 30 × 10^{-6}) of Fe-based amorphous alloys [36]. In addition, a marginal increment in the frequency-dependent slope of core loss suggests the dominant loss appears from the hysteresis contributions at low frequencies and remained significant up to the MHz range. The core loss performance significantly improved after annealing at 525 ºC, 575 ºC, and 625 ºC. The improved loss performance of annealed cores can be associated with the reduced magnetoelastic contributions, due to zero/near-zero λ, achieved on the growth of homogeneously dispersed nanocrystalline structure [32,37]. The slopes of the core loss behaviour of annealed cores became steeper as compared to as-atomised cores, suggesting the frequency dependent dynamic mode of the aforementioned loss components.

The dynamic mode of loss components in powder cores is evident from the crossover and immediate increase in the slope of core loss when frequency approaches the MHz range. For example, 525 ºC annealed cores exhibit the best loss performance, as compared to the other nanocrystalline cores, at f = 50 - 200 kHz (B_m = 0.5 T), could be associated with the ultra-low P_h due to small H_c = 70 A/m (see Table II and Fig. 6). However, when f approaches ≥ 200 kHz, the loss of the 525 ºC core increases and becomes higher than the loss of 625 ºC annealed cores (see Fig. 8). The higher core loss of 525 ºC annealed cores, as compared to 625 ºC, at $f \geq$ 200 kHz could be attributed to the transition in dominant loss mechanisms as a function of frequency. It is believed that the intra-particle P_e in 525 ºC annealed cores was higher as compared to 625 ºC annealed cores at $f \geq$ 200 kHz, and hence, the overall loss of 525 ºC cores increased. The eddy current loss depends on the resistivity and size of the powder particles. While having a similar size of powder for both cores, it seems that the resistivity of the nanocrystalline powder was higher than 525 ºC annealed powders. The high resistivity of two-phase nanocrystalline materials, as compared to amorphous metals, is expected due to the complex electron scattering mechanism at the interface of grain boundaries between amorphous and nanocrystalline phases. A similar crossover was observed in the loss

performance of the 525 and 625 ºC annealed cores at B_m = 0.1 T, but at a comparatively lower frequency (f = 110 kHz). Furthermore, an abrupt change in the slopes of the core loss performance of all cores was observed at 500 kHz. The change in the slopes might be due to a capacitive coupling effect that promotes displacement currents between the particles through the resin so that the overall material loss is abruptly increased. It is suggested that the inter-particle displacement current, which emerged due to capacitive coupling, can be reduced by the coating of individual powder particles or by increasing the volume fraction of the resin [38].

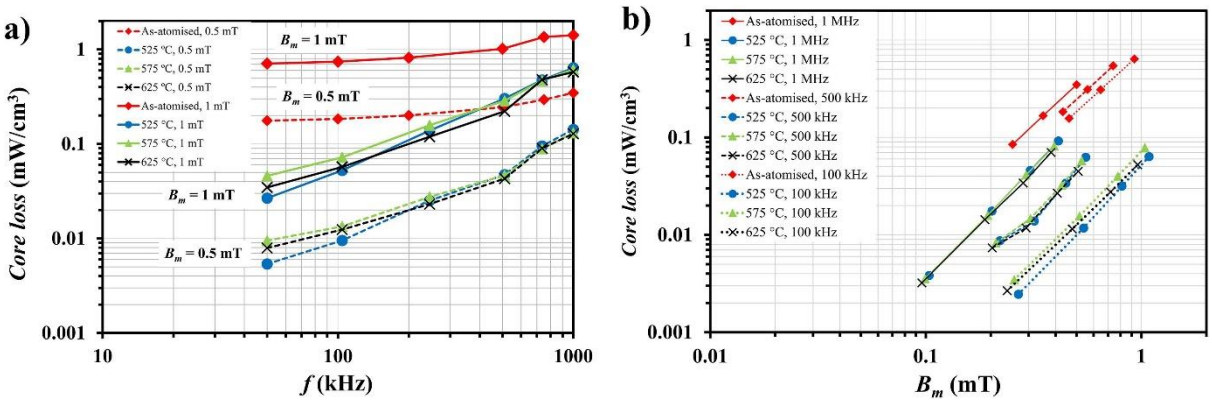

Fig. 8. Core loss (P_{cv}) of the samples as-atomised and annealed at 525, 575, and 625 ºC for 30 min. a) Core loss for different frequencies (f) at two magnetic flux densities (B_m = 1 and 0.5 mT); b) Core loss for different magnetic flux densities at three different frequencies (f = 100 kHz, 500 kHz and 1 MHz).

Fig. 8 shows the high-frequency permeability spectrum of 575 ºC annealed powders. Remarkably, 575 ºC annealed powders revealed a very stable permeability behaviour with a ferromagnetic resonance at f = 3 GHz, which suggests that the operational frequency range of these cores can reach up to several hundreds of MHz.

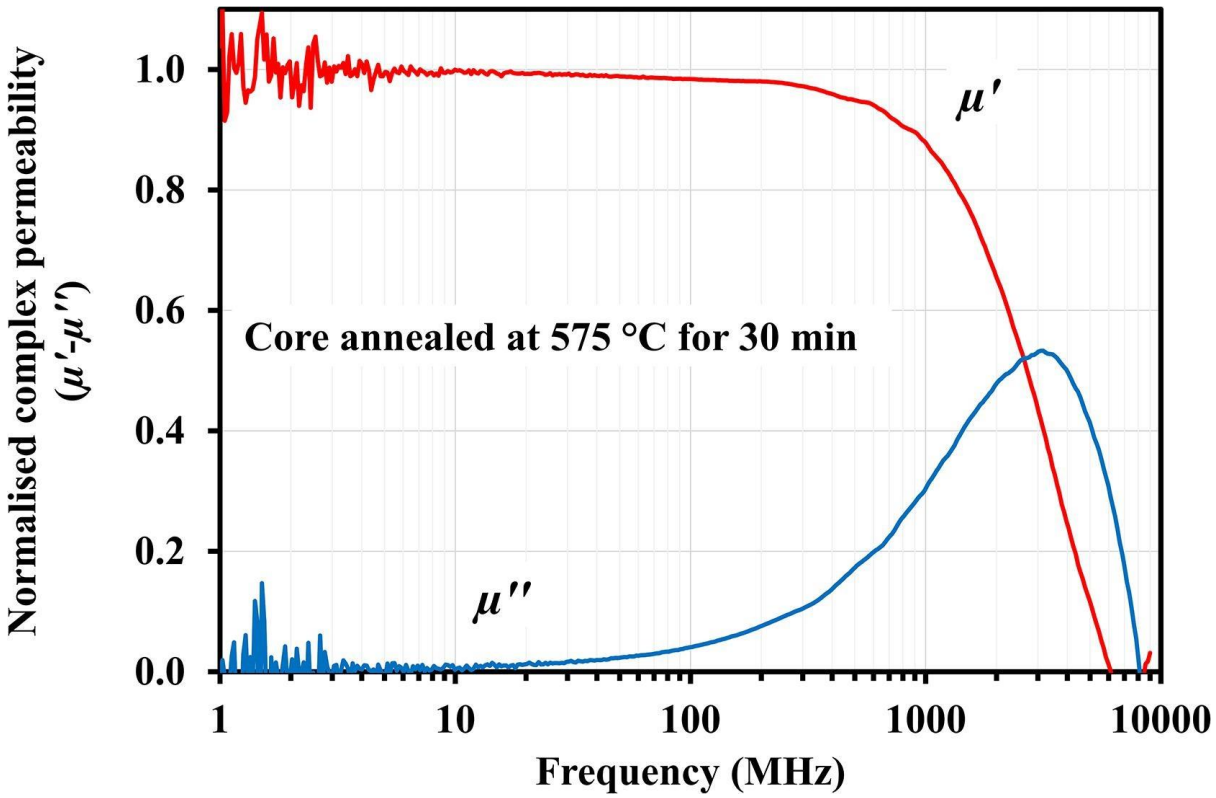

Fig. 9. Normalised complex permeability (μ'-μ'') at high frequencies of the core annealed at 575 ºC for 30 min.

4. Conclusions

Amorphous powders of $(Fe_{0.725}Si_{0.125}B_{0.150})_{96.5}Nb_{3.0}Cu_{0.5}$ alloy were successfully produced via helium gas atomisation, and subsequently annealed to grow nanocrystalline structures to attain excellent core loss performance. The thermal analysis of the amorphous powders showed high GFA, as confirmed by different glass forming parameters such as supercooled region (ΔT_X = 54 ºC) and reduced glass transition temperature (T_{rg} = 0.56). The high amorphisation capability of the alloy was further justified by the amorphous nature of the broad size distribution (5 - 60 µm) of the powder. Two exothermic events in the DSC were used as a guide for the selection of the annealing temperatures to grow the soft magnetic nanocrystalline structure. The annealing at 525 ºC (i.e., < T_{X1}) resulted in the anomalous crystallisation, which was unexpected due to the large ΔT_X of the alloy, and experimentally confirmed by $M(T)$

experiments, thanks to its ultra-high sensitivity, which otherwise is challenging by conventional diffraction techniques (i.e., XRD, SAED). Further annealing of powders at 575 ºC (i.e., > T_{X1}) precipitated the nanocrystalline Fe_3Si phase of 23 wt.%, being the average crystallite size of 11.7 nm. The homogeneous distribution of nanocrystalline grains in the amorphous matrix, confirmed by XRD and TEM, revealed the effective role of Cu, as a nucleation agent, and Nb, as an inhibitor, to control the nucleation and grain growth dynamic in the powders.

The DC soft magnetic properties of the powders were significantly improved on thermal annealing, confirmed by hysteretic loops, quantified by reduced H_c < 80 A/m of powders annealed at ≤ 575 ºC, and hence, attributed to the reduced magnetoelastic contribution due to zero/near-zero magnetostriction anisotropy attained due to the homogenous nanocrystalline structure. A degradation in H_c = 1153.6 A/m after annealing at 625 ºC, despite having ultra-fine nanocrystalline grains (< 15 nm) to follow the Herzer's RAM, shows the non-vanishing effective magnetocrystalline anisotropy of minimal boride phases. Last but not least, high-frequency core loss performance of the nanocrystalline cores significantly improved, as compared to as-atomised powder cores, and ascribed to the significant reduction of the hysteresis loss contribution due to aforementioned vanishing magnetoelastic anisotropy energies. The dynamic mode of loss components in nanocrystalline powder cores revealed the change of dominant loss mechanism as a function of frequency, and hence, displacement currents, due to capacitive coupling, abruptly increase the loss when frequency approaches MHz range. The ease of powder atomisation, high GFA of the alloy composition, and controlled nanocrystallisation capability to retain excellent core loss performance makes the materials ideal candidates for high-frequency power conversions, such as voltage regulators and resonant converters, for the automotive industry and data centres.

Acknowledgements

Author Kenny L. Alvarez thanks to Becas Chile (CONICYT) for the financial support. The authors thank for technical and human support provided by SGIker Medidas Magneticas Gipuzkoa (UPV/EHU/ERDF, EU), and for the MTG experimental support by the Professor Dr. Valter Ström and Ms. Esmat Dastanpoor from The Royal Institute of Technology - KTH.

References

[1] Y. Zhang, P. Sharma, A. Makino, Fe-Rich Fe-Si-B-P-Cu powder cores for high-frequency power electronic applications, IEEE Trans. Magn. 50 (2014) 2006804. doi:10.1371/journal.pcbi.1000729.

[2] R. Hasegawa, Applications of amorphous magnetic alloys in electronic devices, J. Non. Cryst. Solids. 287 (2001) 405–412. doi:10.1016/S0022-3093(01)00633-0.

[3] A. Masood, H.A. Baghbaderani, V. Ström, P. Stamenov, P. McCloskey, C. Mathúna, S. Kulkarni, Fabrication and soft magnetic properties of rapidly quenched Co-Fe-B-Si-Nb ultra-thin amorphous ribbons, J. Magn. Magn. Mater. 483 (2019) 54–58. doi:10.1016/j.jmmm.2019.03.079.

[4] K. J. Sunday, M.L. Taheri, Soft magnetic composites: recent advancements in the technology, Met. Powder Rep. 72 (2017) 425–429. doi:10.1016/j.mprp.2016.08.003.

[5] P. Kollár, Z. Bircáková, J. Füzer, R. Bures, M. Fáberová, Power loss separation in Fe-based composite materials, J. Magn. Magn. Mater. 327 (2013) 146–150. doi:10.1016/j.jmmm.2012.09.055.

[6] H. Shokrollahi, K. Janghorban, Soft magnetic composite materials (SMCs), J. Mater. Process. Technol. 189 (2007) 1–12. doi:10.1016/j.jmatprotec.2007.02.034.

[7] M. De Wulf, L. Anestiev, L. Dupré, L. Froyen, J. Melkebeek, Magnetic properties and loss separation in iron powder soft magnetic composite materials, J. Appl. Phys. 91 (2002) 7845–7847. doi:10.1063/1.1446115.

[8] T. Suzuki, P. Sharma, L. Jiang, Y. Zhang, A. Makino, Fabrication and properties of under 10 μm sized amorphous powders of high B_s soft magnetic alloy for high-frequency applications, IEEE Trans. Magn. 54 (2018) 2801705. doi:10.1109/TMAG.2018.2833138.

[9] L. Chang, L. Xie, M. Liu, Q. Li, Y. Dong, C. Chang, X.M. Wang, A. Inoue, Novel Fe-based nanocrystalline powder cores with excellent magnetic properties produced using gas-atomized powder, J. Magn. Magn. Mater. 452 (2018) 442–446. doi:10.1016/j.jmmm.2017.12.049.

[10] Y.B. Kim, D.H. Jang, H.K. Seok, K.Y. Kim, Fabrication of Fe–Si–B based amorphous powder cores by cold pressing and their magnetic properties, Mater. Sci. Eng. A Struct. Mater. Prop. Microstruct. Process. 449–451 (2007) 389–393. doi:10.1016/j.msea.2006.02.394.

[11] A.J. Yule, J.J. Dunkley, Atomization of Melts for Powder Production and Spray Deposition, Oxford University Press, UK Oxford, 1994.

[12] K.L. Alvarez, J.M. Martín, M. Ipatov, J. Gonzalez, Soft magnetic amorphous alloys (Fe-rich) obtained by gas atomisation technique, J. Alloys Compd. 735 (2018) 2646–2652. doi:10.1016/j.jallcom.2017.11.272.

[13] K.L. Alvarez, J.M. Martin, M. Ipatov, L. Dominguez, J. Gonzalez, Magnetic properties of annealed amorphous $Fe_{72.5}Si_{12.5}B_{15}$ alloy obtained by gas atomization technique, IEEE Trans. Magn. 54 (2018) 2002405. doi:10.1109/TMAG.2018.2839258.

[14] A. García-Escorial, M. Lieblich, A. Hernando, A. Aragón, P. Marín, Temperature dependence of the coercive field of gas atomized $Fe_{73.5}Si_{13.5}B_9Nb_3Cu_1$, J. Alloys Compd. 536 (2012) S300–S303. doi:10.1016/j.jallcom.2011.11.015.

[15] A.M. Leary, P.R. Ohodnicki, M.E. Mchenry, Soft magnetic materials in high-frequency, high-power conversion applications, Jom. 64 (2012) 772–781. doi:10.1007/s11837-012-0350-0.

[16] K.L. Alvarez, J.M. Martín, N. Burgos, M. Ipatov, L. Dominguez, J. Gonzalez, Structural and magnetic properties of amorphous and nanocrystalline Fe–Si–B–P–Nb–Cu alloys produced by gas atomization, J. Alloys Compd. 810 (2019) 151754. doi:10.1016/j.jallcom.2019.151754.

[17] S. Lee, A. Masood, T. Tamaki, S. Valter, K. V. Rao, A. Makino, A. Inoue, Magneto-thermo-gravimetric technique to investigate the structural and magnetic properties of Fe-B-Nb-Y Bulk Metallic Glass, J. Phys. Conf. Ser. 144 (2009) 8–12. doi:10.1088/1742-6596/144/1/012074.

[18] A. Takeuchi, A. Inoue, Classification of bulk metallic glasses by atomic size difference, heat of mixing and period of constituent elements and its application to characterization of the main alloying element, Mater. Trans. 46 (2005) 2817–2829. doi:10.2320/matertrans.46.2817.

[19] P. Duhaj, I. Maťko, P. Švec, D. Janičkovič, Structural characterization of the finemet type alloys, J. Non. Cryst. Solids. 192–193 (1995) 561–564. doi:10.1016/0022-3093(95)00407-6.

[20] C. Suryanarayana, A. Inoue, Bulk Metallic Glasses, CRC/Taylor & Francis, US, 2011.

[21] A. Masood, A. Biswas, V. Ström, L. Belova, J. Ågren, K. V. Rao, The effect of Ni-substitution on physical properties of $Fe_{72-x}B_{24}Nb_4Ni_x$ bulk metallic glassy alloys, Mater. Res. Soc. Symp. Proc. 1300 (2011) 52–57. doi:10.1557/opl.2011.304.

[22] A. Masood, V. Ström, L. Belova, K. V. Rao, J. Ågren, Effect of Ni-substitution on glass forming ability, mechanical, and magnetic properties of FeBNbY bulk metallic glasses, J. Appl. Phys. 113 (2013) 013505. doi:10.1063/1.4772753.

[23] N. Mattern, Structure of nanocrystalline soft-magnetic materials, Mater. Sci. Forum. 79–82 (1991) 607–612. doi:10.4028/www.scientific.net/MSF.79-82.607.

[24] Y. Yoshizawa, K. Yamauachi, Fe-based soft magnetic alloys composed of ultrafine grain structure, Mater. Trans. JIM. 31 (1990) 307–314. doi:10.2320/matertrans1989.31.307.

[25] S. Kaloshkin, M. Churyukanova, V. Zadorozhnyi, I. Shchetinin, R.K. Roy, Curie temperature behaviour at relaxation and nanocrystallisation of Finemet alloys, J. Alloys Compd. 509 (2011) S400–S403. doi:10.1016/j.jallcom.2011.01.090.

[26] I. Ohnuma, S. Abe, S. Shimenouchi, T. Omori, R. Kainuma, K. Ishida, Experimental and thermodynamic studies of the Fe-Si binary system, ISIJ Int. 52 (2012) 540–548. doi:10.2355/isijinternational.52.540.

[27] J.M. Barandiarán, M. Vazquez, A. Hernando, J. Gonzalez, G. Rivero, Distribution of the magnetic anisotropy in amorphous alloys ribbons, IEEE Trans. Magn. 25 (1989) 3330–3332. doi:10.1109/20.42293.

[28] G. Herzer, Grain size dependence of coercivity and permeability in nanocrystalline ferromagnets, IEEE Trans. Magn. 26 (1990) 1397–1402. doi:10.1109/20.104389.

[29] R. Alben, J.J. Becker, M.C. Chi, Random anisotropy in amorphous ferromagnets, J. Appl. Phys. 49 (1978) 1653–1658. doi:10.1063/1.324881.

[30] C. Yang, F. Liu, S. Ren, G. Yang, Microstructure and magnetic properties of a two-phase alloy of α-Fe and metastable Fe_3B, J. Magn. Magn. Mater. 321 (2009) 91–94. doi:10.1016/j.jmmm.2008.08.041.

[31] X. Luo, Y. Wu, M. Han, L. Deng, High frequency permeability of Fe-Cu-Nb-Si-B nanocrystalline flakes with the distribution of shape anisotropy fields, J. Magn. Magn. Mater. 451 (2018) 5–10. doi:10.1016/j.jmmm.2017.10.113.

[32] G. Herzer, Modern soft magnets: Amorphous and nanocrystalline materials, Acta Mater. 61 (2013) 718–734. doi:10.1016/j.actamat.2012.10.040.

[33] J. González, Magnetic properties arising from two additive contributions in soft magnetic nanocrystalline alloys, Appl. Phys. Lett. 85 (2004) 5944–5946. doi:10.1063/1.1833583.

[34] E. Hjortsberg, L. Nyborg, H. Vidarsson, Microscopic characterisation of topography and lubricant distribution on surface of powder compacts, Powder Metall. 48 (2005) 345–353. doi:10.1179/174329005X73711.

[35] Y. Liu, Y. Yi, W. Shao, Y. Shao, Microstructure and magnetic properties of soft magnetic powder cores of amorphous and nanocrystalline alloys, J. Magn. Magn. Mater. 330 (2013) 119–133. doi:10.1016/j.jmmm.2012.10.043.

[36] S. Ito, K. Aso, Y. Makino, S. Uedaira, Magnetostriction and magnetisation of iron-based amorphous alloys, Appl. Phys. Lett. 37 (1980) 665–666. doi:10.1063/1.92029.

[37] A. Ślawska-Waniewska, H.K. Lachowicz, Magnetostriction in soft magnetic nanocrystalline materials, Scr. Mater. 48 (2003) 889–894. doi:10.1016/s1359-6462(02)00623-1.

[38] T. Suzuki, P. Sharma, A. Makino, Extending the operational frequency range of high B_s – FeSiBP amorphous alloy to GHz by coating the powder surface with silicon oxide, J. Magn. Magn. Mater. 491 (2019) 165641. doi:10.1016/j.jmmm.2019.165641.